University of Nottingham

The use of protective structures to reduce tunnelling induced damage to buildings

Geyang Song



This dissertation is submitted for the degree of Doctor of Philosophy

Nottingham Centre for Geomechanics
Faculty of Engineering

October 2019

Declaration of Authorship

I, Geyang SONG, declare that this dissertation titled, 'The use of protective structures to reduce tunnelling induced damage to buildings' and the work presented in it are my own. I confirm that:

- This work was done wholly or mainly while in candidature for a research degree at this University.
- Where any part of this thesis has previously been submitted for a degree or any other qualification at this University or any other institution, this has been clearly stated.
- Where I have consulted the published work of others, this is always clearly attributed.
- Where I have quoted from the work of others, the source is always given. With the exception of such quotations, this thesis is entirely my own work.
- I have acknowledged all main sources of help.
- Where the thesis is based on work done by myself jointly with others, I have made clear exactly what was done by others and what I have contributed myself.

Signed: Geyang Song

Date: October 2019

“ Sincerity of heart, kindness and patience ”

Tao Song

Abstract

In urban areas, due to the limited underground space, tunnels are being built close to or underneath existing buried foundations. As a result, it is essential to understand the effect of tunnelling on nearby structures and buried foundations. Tunnel-structure interaction problems have been widely investigated via numerical and physical modelling as well as with field monitoring. However, the use of protective measures, such as protective walls, to reduce the effect of tunnelling on structures have received much less research attention. Protective measures are often very costly and designed in an overly conservative way. A better understanding of tunnel, soil, piled structure and protective wall interaction (TSPPWI) problems would enable more efficient and cost-effective protective measures to be adopted.

In general, this thesis involves the study of three main areas, with centrifuge models developed to study each area: (1) greenfield tunnelling in sand, (2) effect of tunnelling on piled structures, and (3) the use of protective walls to protect buildings from tunnelling induced damage. The centrifuge models focus on the two-dimensional plane-strain case where the tunnel runs transversely to the structure. A newly developed mechanical model tunnel was used to simulate tunnel volume loss within the centrifuge tests. The research makes the use of the novel coupled centrifuge-numerical modelling (CCNM) hybrid testing equipment and methodologies developed at the University of Nottingham to simulate the tunnel-structure interaction problem within the centrifuge tests. The CCNM process allows more accurate simulation of the tunnel-structure interactions by adjusting the loads applied to the foundation piles within the centrifuge model according to outcomes of a numerical model that is used to simulate the structure domain simultaneously with the centrifuge model domain. In addition, to measure the axial force along the foundation piles and bending moment of the protective walls, optical fibre Bragg grating (FBG) sensors were used during the centrifuge tests. This research represents the one of the first applications of FBG sensors in a geotechnical centrifuge.

Greenfield tunnelling centrifuge tests were carried out using the newly developed rigid boundary mechanical model tunnel. The result showed good consistency in terms of soil displacement mechanisms with data from conventional flexible membrane model tunnels. An available empirical method for describing the variation of settlement trough shape in sand was modified based on the current centrifuge results. The outcomes of this work provide a more in-depth understanding of the effect of model tunnel boundary condition and will benefit future researchers considering which type of model tunnel to adopt when developing centrifuge tests related to tunnelling.

The tunnel structure interaction tests using the CCNM approach considered two cases of structure stiffness: a zero stiffness structure (constant pile head load), and full structure stiffness (based on a five storey steel frame building with four foundation piles running transverse to the tunnel direction). These tests served as a baseline for comparison with the protective wall tests. The structure stiffness affects pile head settlement and the variation in the pile head load with tunnel volume loss. The pile located closest to the tunnel showed the most significant pile head settlement with tunnelling, and FBG data indicated the loss of end bearing force and shaft resistance along the pile during tunnel volume loss. Post-tunnelling pile jacking tests were performed and indicated that the amount of displacement required to re-mobilise the shaft resistance along the pile depends on the amount of loss in shaft resistance during tunnelling.

In the tunnel-building interaction tests including protective walls (TSPPWI), two protective walls (made out of aluminium plate) were used with different embedded depths, referred to as 'short' (toe of the wall located at the tunnel spring line) and 'long' (toe of the wall located below the tunnel invert). The use of a protective wall can reduce the soil movements on the building side of the wall. Results demonstrate that the 'long' wall provides a more significant reduction in soil movements with tunnelling than the 'short' wall. During tunnelling, the protective walls reduced the amount of settlement of the building foundation piles, as well as the change in pile head load. The efficiency of the walls was quantified using the settlement of the piles with respect to the case without a protective wall. Results indicate that the 'long' protective wall provides higher efficiency, but the efficiency reduces for the piles located further away from the tunnel. Despite the use of protective walls, the FBG sensors indicated that the pile shaft resistance reduced with tunnelling, and during post-tunnelling pile jacking, a more significant pile head displacement was required to fully re-mobilise the shaft resistance for the piles that lost most of their shaft resistance during tunnel volume loss. The outcomes from these tests will help engineers to refine their design of protective walls in practice, and enable more efficient and cost-effective protective measures to be adopted.

Acknowledgements

I would like to thank my main supervisor, Dr Alec Marshall, sincerely. I thank for his help, advise, and most importantly, thank for his encouragement. I would like to sincerely thank my secondary supervisor Dr Charles Heron, thank for his help and advises in related to centrifuge testing methods.

I want to thank all the technicians in Nottingham Centre for Geomechanics research group. I want to thank Dr Solomon Idinyang, Mr Luke Bedford and Dr Mir Hashemi Afrapoli, thank for their contributions to my research work. I want to thank Mr Lee Hickling, Mr Steven Lawton, Mr Andrew Maddison and Mr Jim Meakin; I would like to thank for their professional help and support.

I want to thank all of my fellow researchers in Nottingham Centre for Geomechanics research group. Many thanks also to Dr Andrea Franza, Mr Jingmin Xu, Mr KunKun Chen and Mr Ge Cui for their help and friendship.

Finally, thanks to my parents, wife and family. In particular, I would like to thank my dad, thank for his continued support and love.

Contents

Declaration of Authorship i

Acknowledgements v

Contents vi

List of Figures ix

List of Tables xiii

Symbols xiv

1 Introduction 1
- 1.1 Description of the problems . . . 1
- 1.2 Aims and objectives of the research . . . 2
- 1.3 Structure of the thesis . . . 3

2 Background 5
- 2.1 Greenfield tunnelling . . . 5
  - 2.1.1 Ground movements . . . 5
  - 2.1.2 Surface and subsurface transverse settlement . . . 7
- 2.2 Tunnelling effect on piles and piled structures . . . 11
  - 2.2.1 Building damage assessment . . . 11
  - 2.2.2 Pile settlement due to tunnelling . . . 13
  - 2.2.3 Single pile load transfer due to tunnelling . . . 19
  - 2.2.4 Piled structure settlement and deformation due to tunnelling . . . 22
  - 2.2.5 Piled structure load transfer with tunnelling . . . 26
- 2.3 The use of protective structures to reduce tunnelling-induced ground movements . . . 27
  - 2.3.1 Centrifuge study of using protective wall to control ground movements . . . 28
  - 2.3.2 The use of pile walls in practice to protect buildings from tunnelling-induced movements . . . 29
- 2.4 Summary of the chapter . . . 30

3 Review of centrifuge modelling technique 32
- 3.1 Geotechnical centrifuge technology . . . 32

3.1.1 Scaling concepts . . . 33
3.1.2 Scaling effects . . . 34
3.1.3 Boundary effect . . . 35
3.2 Centrifuge modelling technology . . . 35
3.2.1 Modelling of tunnel volume loss . . . 36
3.2.2 Modelling of piles . . . 39
3.2.3 Principle of FBG sensors . . . 40
3.3 Summary of the chapter . . . 42

4 Experimental methods, equipment, and testing configurations 44
4.1 Introduction . . . 44
4.2 Greenfield tunnelling in sand . . . 45
4.2.1 Experimental programme . . . 45
4.2.2 Simulation of tunnel volume loss . . . 46
4.2.3 Measuring displacements . . . 49
4.2.4 Testing material and model preparations . . . 52
4.2.5 Testing procedures . . . 53
4.3 The effects of tunnelling on piled structures . . . 53
4.3.1 Experimental programme . . . 54
4.3.2 Coupled centrifuge-numerical modelling (CCNM) . . . 54
4.3.3 Pile loading system . . . 56
4.3.4 Steel frame structure model . . . 57
4.3.5 Model piles and instrumentation . . . 57
4.3.6 Testing material and model preparation . . . 64
4.3.7 Testing procedures . . . 65
4.4 The use of protective structures to protect buildings from tunnelling-induced damage . . . 66
4.4.1 Experimental programme . . . 66
4.4.2 Model piles and instrumentation . . . 67
4.4.3 Model walls and instrumentation . . . 69
4.4.4 Soil displacements measurement . . . 73
4.4.5 Model preparation . . . 75
4.4.6 Testing procedure . . . 76
4.5 Chapter summary . . . 77

5 Tunnelling in sandy ground 79
5.1 Introduction . . . 79
5.2 Interpretation of measured results . . . 81
5.2.1 Effect of model tunnel on initial conditions . . . 81
5.2.2 Effect of soil deformation mechanism . . . 82
5.2.3 Settlement troughs . . . 84
5.2.4 Change in trough width parameter . . . 84
5.2.5 Effect of model tunnel on settlement trough shape characteristics . . . 89
5.2.6 Relationship between soil and tunnel volume loss . . . 90
5.3 Conclusions . . . 94

6 The effect of tunnelling on piled structures 97

6.1 Introduction . . . 97
6.2 Interpretation of measured results . . . 98
6.2.1 Axial force along the pile after centrifuge acceleration . . . 98
6.2.2 Determination of pile axial load capacity . . . 99
6.2.3 Pile loading . . . 101
6.2.4 Effect of structure stiffness on pile settlement due to tunnel volume loss . . . 103
6.2.5 Effect of structure stiffness on pile head load distribution with tunnel volume loss . . . 106
6.2.6 Axial force redistribution along piles and change in mobilised pile shaft friction during tunnelling . . . 108
6.2.7 Determination of post-tunnelling pile axial capacity . . . 113
6.3 Summary and conclusions . . . 117

7 The use of protective walls to reduce buildings from tunnelling-induced damage 119
7.1 Introduction . . . 119
7.2 Interpretation of measured results . . . 121
7.2.1 Axial force along the piles and pile settlement after centrifuge acceleration . . . 121
7.2.2 Pile loading . . . 123
7.2.3 The effect of protective walls on tunnelling-induced ground movements . . . 126
7.2.4 Protective wall response to tunnelling . . . 129
7.2.5 The effect of protective walls on pile settlement and pile head load distribution with tunnelling . . . 133
7.2.6 Settlement and deformation of structures . . . 138
7.2.7 The effect of protective walls on the axial force distribution along the piles and change in pile shaft resistance with tunnelling . . . 141
7.2.8 The effect of protective walls on post-tunnelling pile jacking response 146
7.3 Summary and conclusions . . . 150

8 Conclusions and recommendations for further research 154
8.1 Conclusions . . . 155
8.1.1 Experimental methods, equipment, and testing configurations . . . 155
8.1.2 Tunnelling in sandy ground . . . 155
8.1.3 The effect of tunnelling on piled structures . . . 156
8.1.4 The use of protective structures to reduce buildings from tunnelling-induced damage . . . 158
8.2 Guidance for practical application . . . 160
8.3 Recommendations for future work . . . 161

Bibliography 163

List of Figures

2.1 Main components of ground movement due to shield tunnelling after Cording (1991) . . . 6
2.2 Greenfield settlement trough features after Attewell and Yeates (1984) . . 6
2.3 Relation between settlement trough width parameter and depth of tunnel for different ground conditions after Peck (1969) . . . 7
2.4 Underground structures in urban environment (Mair, 2008) . . . 11
2.5 Definition of deflection ratios by Potts and Addenbrooke (1997),Goh and Mair (2012) and Franza and Marshall (2017) . . . 12
2.6 Centrifuge model test configuration (Loganathan et al., 2000) (unit in mm) 14
2.7 Centrifuge model test configuration by Jacobsz (2003) (unit in mm) . . . 15
2.8 Influence zone identify by Jacobsz (2003) that large settlement is expected 16
2.9 Position of pile and instrumentation by Selemetas (2005) . . . 16
2.10 Zones of influence identified by Selemetas (2005) and Kaalberg et al. (2005) from Franza (2016) . . . 17
2.11 Testing layout and strain gauge position from Lee and Chiang (2007) (unit in prototype scale) . . . 18
2.12 Tested piles location in related to the zone of influence provided by Jacobsz (2003) from Marshall (2009) . . . 18
2.13 Testing layout of the centrifuge tested by Ng and Lu (2013) . . . 19
2.14 Load transfer mechanism for pile with 3200kN working load (Lee and Chiang, 2007) (Unit in prototype scale) . . . 21
2.15 Pile group base locations for centrifuge tests conducted by Jacobsz (2003)) 23
2.16 Pile group tests layout by Ng et al. (2014) . . . 23
2.17 Pile group tests layout by Boonsiri and Takemura (2015a) . . . 24
2.18 Pile group tests layout by Franza and Marshall (2017) . . . 25
2.19 The computed M^{DR} in (a) sagging (b) hogging from centrifuge test and design lines provided by Franza and Marshall (2017) . . . 26
2.20 Model geometry tested by Bilotta (2008) . . . 28
2.21 Geometry of the case given by Ledesma and Alonso (2017) . . . 29
2.22 Measured and computed vertical settlement given by Ledesma and Alonso (2017) . . . 30

3.1 The effect of side boundary given by Bolton et al. (1999) . . . 35
3.2 Details of the model tunnel used by Bolton et al. (1999) . . . 36
3.3 Details of the model tunnel used by Marshall (2009) . . . 37
3.4 Details of the model tunnel used by Boonyarak and Ng (2015) . . . 37
3.5 Details of the model tunnel used by Boonsiri and Takemura (2015b) . . . 38

3.6 Model piles used by Loganathan et al. (2000): (a) "bending pile", (b)"axial force pile" . . . 39
3.7 Axial force and radial stress load cell (Jacobsz, 2003) . . . 40
3.8 Model pile used by Marshall (2009) . . . 41
3.9 Basic Bragg grating process based on Kersey et al. (1997) . . . 42

4.1 Strong box for greenfield tunnelling . . . 46
4.2 Eccentric rigid boundary mechanical model tunnel . . . 47
4.3 Eccentric rigid boundary mechanical model tunnel deformed shape . . . 48
4.4 Cross check the tunnel volume loss measurement . . . 48
4.5 Standard error for tracking with subset size in pixel space . . . 50
4.6 'stitch' process using Solidworks . . . 51
4.7 Histograms of displacement errors on (a) horizontal displacement and (b) vertical displacement . . . 52
4.8 Test layout in model scale : (a) Pile jacking tests, and (b) tunnelling next to piled frame . . . 54
4.9 CCNM simulation process for a framed building with a pile foundation . . . 55
4.10 Pile loading system layout . . . 56
4.11 The load control response time under centrifuge environment . . . 57
4.12 FBG sensor installation procedure . . . 59
4.13 Model pile axial force calibration . . . 60
4.14 Model pile axial force calibration: (a) loading sequence; (b) Pile 3 B_4 result 61
4.15 Centrifuge setup for FBG sensors and interrogator . . . 63
4.16 Verify FBG sensors under centrifuge environment . . . 63
4.17 FBG sensors' reading under centrifuge environment . . . 64
4.18 Model pile installation procedure . . . 65
4.19 Testing layout in model scale . . . 67
4.20 Strong box for protective wall centrifuge tests . . . 68
4.21 FBG calibration results . . . 69
4.22 FBG sensor installation for aluminium plate . . . 70
4.23 Bending moment calibration for FBG sensors . . . 72
4.24 Change in wavelength $\Delta\lambda_B P_3$ with bending moment . . . 73
4.25 Locations of the FBG sensors for both model walls . . . 73
4.26 Interface between the acrylic window and aluminium model wall . . . 74
4.27 Standard error for tracking with subset size in pixel space using new camera (Dalsa nano-m4020) . . . 74
4.28 Histograms of displacement errors on (a) horizontal displacement and (b) vertical displacement using new camera . . . 75
4.29 Sand sample preparation and the location of the model wall . . . 76
4.30 Locations of the two interrogators . . . 77

5.1 Test layout in model scale . . . 81
5.2 Soil movements around FM and eRBM model tunnels during centrifuge spin-up: (a) vertical displacements, (b) horizontal displacements . . . 82
5.3 Centrifuge test results of vertical and horizontal soil displacements for FM and eRBM model tunnels: $C/D = 2$ and $V_{l,t} = 2\%$ . . . 83
5.4 Settlement trough data at surface and subsurface for $V_{l,t} \approx 2\%$ . . . 85

5.5 Variation of x^* and x^{**} with depth at $V_{l,t} \approx 2\%$ for (a) centrifuge test; (b) finite element analysis . . . 86
5.6 Centrifuge test fitted curve parameters with volume loss: (a) slope of x^* and x^{**} with depth; (b) surface trough width parameter . . . 87
5.7 (a) relationship between intercept of $\partial x^*/\partial z$ or $\partial x^{**}/\partial z$ and $K^*{}_s$ or K^{**} at tunnel volume loss $V_{l,t} = 0\%$ with C/D ratio; (b) slope of the fitted line with C/D ratio . . . 88
5.8 Goodness of fit of modified Gaussian curves to centrifuge data . . . 90
5.9 K^* and K^{**} with depth for centrifuge tests at $V_{l,t} \approx 2.0\%$ . . . 91
5.10 Variation of surface soil volume loss with tunnel volume loss for both FM and eRBM model tunnels . . . 92
5.11 Variation of $V_{l,s}$ with depth at $V_{l,t} \approx 2.0\%$ . . . 93
5.12 Contours of shear and volumetric strain for centrifuge test $C/D = 2.0$ at $V_{l,t} = 2.0\%$ . . . 94
5.13 Illustration of soil strains due to tunnel volume loss based on the observations in Figure 5.12 . . . 95

6.1 Axial force along the pile after centrifuge acceleration . . . 99
6.2 Load settlement curve for pile jacking test . . . 100
6.3 Shaft resistance during pile jacking test: pile 2 . . . 100
6.4 Global pile stiffness versus pile head load for test pile jacking . . . 101
6.5 Axial force along the pile before and after pile loading . . . 102
6.6 Load settlement curve for piles during pile loading . . . 103
6.7 Load settlement curve for piles 2 and 3 during pile loading . . . 103
6.8 (a) Pile 3 settlement during pile 2 installation (b) Change in axial force along the pile 3 after pile 2 installation . . . 104
6.9 Pile settlement with tunnel volume loss: (a) pile 1, (b) pile 2, (c) pile 3, (d) pile 4 . . . 105
6.10 Contribution of structure stiffness to pile settlement . . . 106
6.11 Pile head load with tunnel volume loss: (a) pile 1, (b) pile 2, (c) pile 3, (d) pile 4 . . . 107
6.12 The pile settlement due to change in pile head load during tunnel volume loss for test CCNM2 . . . 108
6.13 Pile axial load at $V_{l,t} = 1,\ 2,$ and 3% : (a) pile 1, (b) pile 2, (c) pile3, (d) pile 4 . . . 109
6.14 Change in unit shaft resistance at $V_{l,t} = 1,\ 2,$ and 3% : (a) pile 1, (b) pile 2, (c) pile3, (d) pile 4 . . . 111
6.15 Pile 2 settlement and head load change with pile 1 jacking . . . 114
6.16 Load-displacement curves for all the tests . . . 114
6.17 Post-tunnelling pile global stiffness with pile head load . . . 115
6.18 shaft resistance of piles in all the tests . . . 116
6.19 Post-tunnelling pile axial capacity . . . 117

7.1 Location of the protective wall, piles and the field of view for geoPIV-RG 121
7.2 Axial force along the pile after centrifuge acceleration . . . 122
7.3 Vertical settlement of the soil and piles after centrifuge acceleration . . . 123
7.4 Illustration of the pile and soil settlements after centrifuge acceleration . . 123
7.5 Pile head settlement after centrifuge acceleration . . . 124

7.6 Axial force distribution before and after pile loading 124
7.7 Pile head settlement during pile loading 125
7.8 (a) Pile head settlement and (b) change in axial force for pile 4 during pile 3 loading 125
7.9 Bending moment along the protective wall after pile loading 126
7.10 Measured surface displacement: (a) vertical settlement, (b) horizontal displacement (positive value is moving downwards or towards right) . . . 127
7.11 Contours of vertical and horizontal settlement (mm) at $V_{l,t}$=2.0 % for all tests (soil moving downwards is positive) 130
7.12 Contours of horizontal movement (mm) at $V_{l,t}$=2.0 % for all tests (soil moving to the right is positive) 131
7.13 Horizontal displacement and bending moment along the wall with tunnel volume loss: (a) horizontal displacement, (b) bending moment 132
7.14 Pile head settlement with tunnel volume loss 134
7.15 The difference in pile settlement with tunnelling between tests CCNM2 and CCNM3 135
7.16 Efficiency parameter $\eta^{rs}_{V_{l,t}}$ with tunnel volume loss 136
7.17 Average efficiency parameter $\overline{\eta^{rs}}$ with respect to pile location 137
7.18 Pile head load with tunnel volume loss 138
7.19 Structure settlement at $V_{l,t} = 2.8\%$ 139
7.20 Illustrate of the structure layout and angular distortion calculation 139
7.21 Angular distortion of the frames in a bay at a tunnel volume loss of $V_{l,t} = 2.8\%$ 140
7.22 Angular distortion of the frame at level 1 with tunnelling 141
7.23 Pile axial load at $V_{l,t} = 0,\ 1,\ 2,$ and 2.8 % : (a) CCNM3 1, (b) CCNM-R-S, (c) CCNM-R-L 142
7.24 Change in unit shaft resistance at $V_{l,t} = 0,\ 1,\ 2,$ and 2.8% : (a) CCNM3, (b) CCNM-R-S, (c) CCNM-R-L 145
7.25 Soil settlements with respect to the pile along the depth of the pile at a tunnel volume loss of $V_{l,t} = 2.8\%$ 146
7.26 Load-displacement curves: test PJ, CCNM3, CCNM-R-S and CCNM-R-L 147
7.27 Post-tunnelling pile global stiffness with pile head load 148
7.28 Shaft resistance of piles: test PJ, CCNM3, CCNM-R-S and CCNM-R-L . 149
7.29 Load-settlement path history for piles 151

List of Tables

3.1 Centrifuge scaling laws by Taylor (1994) 33
3.2 Pile properties in model scale and prototype scale (Boonsiri and Takemura, 2015b) 41

4.1 Summary of the centrifuge tests performed at 80 g for greenfield tunnelling 45
4.2 Summary of the centrifuge tests performed at 80 g 55
4.3 Pile properties in model and prototype scale 58
4.4 Summary of the centrifuge tests performed at 80 g 67
4.5 Protective wall properties in model and prototype scale 70

Symbols

a	Length dimension for yield density curve fitting
At	Tunnel cross-sectional area
b	The dimensionless coefficient for yield density curve fitting
B	Full width of the building/effect cone diameter
B_i	The spacing of the building column / FBG sensor index for pile
C	Depth of cover above the tunnel
C_u	Coefficient of uniformity
d_e	Distance between the pile and tunnel (Pile 1)
d_p	Diameter of the pile
d_w	Horizontal distance between the protective wall and tunnel
D	Diameter of the tunnel (D_t)
D_{50}	Average size of the soil particle
D_{ci}	Diameter of the cavity
D_h	Horizontal displacement of the protective wall along its depth
$DR_{hog,bldg}$	Hogging deflection section of the building
$DR_{hog,gf}$	Hogging deflection section of the greenfield surface settlements
$DR_{sag,bldg}$	Sagging deflection section of the building
$DR_{sag,gf}$	Sagging deflection section of the greenfield surface settlements
e_{c0}	Maximum void ratio at zero pressure
e_{d0}	Minimum void ratio at zero pressure
e_d	Void ratio depends on C_u
e_{i0}	Critical void ratio at zero pressure
e_{max}	Maximum void ratio
e_{min}	Minimum void ratio
e_{p0}	Initial void ratio of compression test at zero pressure
EI^*	Elastic building stiffness per running meter
E_s	Secant stiffness of the soil at $z_t/2$ under 0.01% axial strain
F_i	Axial force along the pile for a particular FBG sensor B_i
G_s	Specific gravity

h_m	Height of the soil model
h_s	Granular hardness
H	Half width of the building / height of the frame
H_i	Height of the building storey in prototype scale
i or i_g	Horizontal distance between tunnel and inflection point
I_d	Relative density
K	Trough width parameter
$K^{**slope}_{s,V_{l,t}}$	Slope of the line fitted to K_s^{**}
$K^{*slope}_{s,V_{l,t}}$	Slope of the line fitted to K_s^{*}
$K^{**int}_{s,V_{l,t}}$	Intercept of the fitted line at $V_{l,t} = 0\%$ for K_s^{**}
$K^{*int}_{s,V_{l,t}}$	Intercept of the fitted line at $V_{l,t} = 0\%$ for K_s^{*}
$K_B P_i$	Coefficient of FBG sensor location P_i for bending calculation
K_{B_i}	Coefficient of the FBG sensor B_i for axial force calculation
K_0	Static state lateral earth pressure coefficient
K_P	Coefficient of wavelength sensitive to pressure P
K_ε	Coefficient of wavelength sensitive to strain ε
K_T	Coefficient of wavelength sensitive to temperature T
$K^{**slope,ln}_{s,V_{l,t}}$	Curve fitting coefficient from Franza (2016)
$K^{*slope,ln}_{s,V_{l,t}}$	Curve fitting coefficient from Franza (2016)
$K^{**int,ln}_{s,V_{l,t}}$	Curve fitting coefficient from Franza (2016)
$K^{*int,ln}_{s,V_{l,t}}$	Curve fitting coefficient from Franza (2016)
K^{**}	Trough width parameter based on x^{**}
K_s^*	Surface trough width parameter based on x^*
K_s^{**}	Surface trough width parameter based on $x{**}$
$K^{*int}_{s,V_{l,t}}$	K_s^* at zero tunnel volume loss
$K^{**int}_{s,V_{l,t}}$	K_s^{**} at zero tunnel volume loss
$K^{*slope}_{s,V_{l,t}}$	Slope of the K_s^* with tunnelling
$K^{**slope}_{s,V_{l,t}}$	Slope of the K_s^{**} with tunnelling
L_p	Depth of the pile
L^g_{sag}	Length in greenfield to the building under sagging zone
L^g_{hog}	Length in greenfield to the building under hogging zone
L	Length of the building in longitudinal direction
l_w	Length of the protective wall
M^*	Curve fitting coefficient from Franza (2016)
$M^{DR_{sag}}$	Sagging modification factor for deflection ratio
$M^{DR_{hog}}$	Hogging modification factor for deflection ratio
M^{**}	Curve fitting coefficient from Franza (2016)
$M^{\varepsilon_{gc}}$	Modification factor for compression horizontal strain

$M^{\varepsilon_{gt}}$	Modification factor for tensile horizontal strain
M_i	Bending moment for a particular FBG location P_i
n	Controls curve/core effective index/ fitting parameter
N	Gravity scale factor
P	Pressure applied to the sensor
p'	Mean effective stress
P_i	Initial pile head load/ FBG measurement location index
P_i'	Modified pile head load
Q_t	Pile head load
Q_s	Shaft resistance
Q_b	Pile end-bearing force
R	Ratio between pile head and ground surface settlement
R^2	Coefficient of determination
R_e	Effective centrifuge radius
R_t	Distance between soil surface to centrifuge rotation axis
S Slope of the frame S_t	Spacing between the piles
S_v	Settlement of soil / vertical displacement of frame joint
S_{max}	Maximum soil settlement
S_{lg}	Longitudinal spacing of transverse pile rows
S_{bw}	Surface settlement of the soil at the retained side of the wall
S_{ref}	Greenfield surface settlement to S_{bw}
S	Distance between the side of the wall to the location of the cone
S_h	Horizontal displacement of the frame joint / protective wall
S_p	Settlement of the pile
$S_{p,t}$	Settlement of the pile due to tunnelling
$S_{p,s}$	Settlement of the pile due to structure stiffness
$S^s_{V_{l,t}}$	Settlement of the pile without protective wall
$S^{rs}_{V_{l,t}}$	Settlement of the pile for the pile at the retained side of the wall
t_w	Thickness of the protective wall
T	Temperature applied to the sensor
v_i	Pile displacement
$V_{l,s}$	Soil volume loss normalised by the tunnel cross-sectional area
$V_{l,t}$	Tunnel volume loss normalised by the tunnel cross-sectional area
V_s	Volume of the settlement trough per meter length
V_t	Tunnel volume loss per meter length
V_{cr}	Volume loss of the crater created
V_{ci}	Volume loss of the cavity
x	Horizontal distance from the tunnel centre line

x^*	Horizontal distance of $S_v(i_g)$
x^{**}	Horizontal distance of $0.5S_v(i_g)$
$X_{CP_i,image_i}$	Horizontal overlapping objective space coordinate
$Y_{CP_i,image_i}$	Vertical overlapping objective space coordinate
z_t	Depth of the tunnel
z	Depth of the soil level interested
α	Ensure i in distance/ govern the peak friction angle of the soil
α^*	relative axial stiffness parameter
β	Govern the soil stiffness or angular distortion
$\Delta\lambda$	Change in wavelength
$\Delta\lambda_B P_i$	Change in wavelength at the measurement location P_i
ΔQ_t	Change in pile head load
$\Delta f_{vl}(z)$	Change in unit shaft resistance with tunnelling
$\Delta Q_s^f(z)$	Change in shaft resistance after tunnel volume loss
$\Delta Q_s^i(z)$	Change in shaft resistance before tunnel volume loss a
Δz	Distance between the two measurement points
$\Delta V_{l,t}$	Increment of tunnel volume loss
ε	Elongation strain of sensor or the PIV-RG 'stitching' error
ε_t	Strain of the aluminium pile
$\varepsilon_{hc,bldg}$	Building compression horizontal strain in sagging zone
$\varepsilon_{ht,bldg}$	Building tensile horizontal strain in sagging zone
$\varepsilon_{hc,gf}$	Greenfield compression horizontal strain in sagging zone
$\varepsilon_{ht,gf}$	Greenfield tensile horizontal strain in sagging zone
$\eta_{V_{l,t}}^{rs}$	Efficiency of the protective wall for each pile
$\overline{\eta^{rs}}$	Average of $\eta_{V_{l,t}}^{rs}$ regardless of tunnel volume loss
$\eta_{bw}^{V_{l,t}}$	Effectiveness of wall in reducing ground movements
θ	Tilt of the frame
λ_B	Bragg wavelength
Λ	Grating pitch
λ_{OS_i}	Wavelength offset during axial force calibration for a pile
μ	Poisson's ratio
ρ^*	relative bending stiffness parameter
ρ_{sag}^p	Sagging piled building stiffness
ρ_{hog}^p	Hogging piled building stiffness
ω	Angular velocity
ρ	Soil density

σ_{vm}	Model scale vertical soil stress
σ_{vp}	Prototype scale vertical soil stress
ϕ_c	Critical state friction angle

$\partial x/\partial z^{*slope}_{V_{l,t}}$	Gradient of the $\partial x^*/\partial z$
$\partial x/\partial z^{**slope}_{V_{l,t}}$	Gradient of the $\partial x^{**}/\partial z$
$\partial x^*/\partial z^{int}_{V_{l,t}}$	Intercept of the fitted line at zero tunnel volume for $\partial x^*/\partial z$
$\partial x^{**}/\partial z^{int}_{V_{l,t}}$	Intercept of the fitted line at zero tunnel volume for $\partial x^{**}/\partial z$

Chapter 1

Introduction

1.1 Description of the problems

According to DeSA et al. (2013), in the next 40 years, the world population is about to increase to 10 billion, and by 2050, 70% of the world population will live in the urban environment. The rapid development in cities requires to meet the demand for infrastructure. Transport infrastructure plays a vital role to accommodate the rapid increase in urban population. Without an efficient urban transport system, cites are likely to create more traffic congestion and travel time. Probably the most recognised solution to reduce the congestion of a city is by utilising underground infrastructure systems.

A large part of these underground systems is made up of tunnels. Tunnels are being built close to, underneath or even clashing with, existing buried infrastructure and building foundations. As a result, to protect the existing assets from potential damage caused by tunnelling, protective measures have been used in practice, which includes compensation grouting, structure jacking and the use of a protective walls. However, because of the high uncertainty regarding the consequence of tunnelling on existing assets, and the limited understanding of the effect of the protective measures on existing assets, the protective measures are generally costly. In order to achieve more sustainable cities and enable more efficient and cost-effective protective measures to be adopted, it is vital to improve the understanding of tunnel, soil, piled structures and protective walls interaction (TSPPWI) problems.

1.2 Aims and objectives of the research

Numerical modelling has been widely used as a tool to study tunnel-structure interaction problems. However numerical analysis needs to be verified and tested against experimental data or field measurements. Invaluable insights and data for verifying analytical and numerical simulation on the problem of tunnel interaction have been provided by physical modelling with a geotechnical centrifuge. For physical modelling, some degree of simplification is necessary compared with real case: the piled structures are simplified to plates with the piles rigidly connected or constant load was applied to pile foundations to simulate the self-weight of the structure. The use of simplified models could over- or under-predict (eg. the use of rigid connected beam or constant loaded piles) the contribution of superstructure effects to the global tunnel pile structure interaction (TPSI) problems.

This research is intended to develop experimental applications and to obtain previously unattainable results, which will enable a better understanding of the complex tunnel, soil, piled structures and protective walls interaction (TSPPWI) problems. In addition, the scope of the research is limited to dry sand. This research aims to use hybrid testing apparatus and methods developed at the University of Nottingham to address the limitations stated above, known as coupled centrifuge-numeric modelling (CCNM) (Franza et al., 2019). This research also aims to apply optical Fibre Bragg Grating (FBG) sensing techniques within the CCNM application, which offers several benefits over conventional strain gauges, including electric noise insensitivity, better resolution and very small instrument size.

The aims stated above were achieved through the following objectives, as well as the novel experimental developments within this research are highlighted:

- Develop a new centrifuge model container and a **rigid boundary mechanical model tunnel** to simulate eccentric shape tunnel volume loss; conduct greenfield tests to validate the performance of the newly developed model tunnel. Compare the results against other centrifuge tests using fluid filled flexible membrane model tunnel to identify the difference in resultant soil displacement mechanism.
- Develop a **modular actuator** with a load/displacement control system; improve the current **CCNM system** and ensure a more realistic numerical steel frame structure to be adopted. Obtain the data and interpret the tunnel-soil-pile-structure interaction mechanisms, as well as evaluate the effect of structure stiffness on this interaction problem.

- Develop model piles and protective walls for centrifuge tests, and **integrate FBG sensors within these model piles and walls.** Identify the effect of protective walls in reducing tunnelling induced damage on piled structures, and produce normalised data to quantify the efficiency of the protective walls. By achieving above items, it is believed that the complex soil structure interaction problems can be better understand, therefore, the development of guidance or design chart for engineering practice purpose can aided from this work.

1.3 Structure of the thesis

This thesis consists of seven chapters, and can be described as follows:

Chapter 2 presented the review of greenfield tunnelling, the effect of tunnelling on piles and piled structures, the use of protective structures to protect buildings from tunnelling induced damage. In addition, the geotechnical centrifuge technology, and the development of centrifuge model tunnels, piles and instrumentation were reviewed. The basic principle of fibre Bragg Grating (FBG) was reviewed as well.

Chapter 3 presented the review of geotechnical centrifuge technology, and the development of centrifuge model tunnels, piles and instrumentation. The basic principle of fibre Bragg Grating (FBG) was reviewed as well.

Chapter 4 provided the detailed development of centrifuge testing facilities as well as the testing procedures and methodology. Three centrifuge test packages were presented in this chapter: 1) greenfield tunnelling in sand, 2) effects of tunnelling on piled structures, 3) the use of protective walls to protect buildings from tunnelling induced damage.

In **Chapter 5** three centrifuge tests were conducted using newly developed eccentric rigid boundary mechanical (eRBM) model tunnel with three cover to diameter ratios (C/D). Experimental and numerical model results were used to explore the effect of different tunnel boundary conditions on resulting ground deformations. Empirical methods developed by Marshall (2012) to describe the variation of settlement trough shape in sands were modified based on the eRBM model tunnel centrifuge results.

In **Chapter 6**, the tunnel-pile-structure interaction (TPSI) problems were investigated using a novel coupled numerical-centrifuge method (CCNM) approach. The outcomes from four centrifuge tests were presented. Two different structure stiffness were investigated, which are fully flexible (constant load on each pile) and full structure stiffness (structure stiffness simulated using a numerical model within the CCNM application).

FBG sensors were used to measure the axial force along the four piles. After tunnel volume loss, pile jacking tests were conducted to investigate the post-tunnelling pile capacity.

In **Chapter 7**, four centrifuge tests were carried out under 80g to study the performance of protective walls in reducing piled structures from tunnelling induced damage. Two protective walls were used and had an embedded depth of 207 mm and 297 mm, respectively. The testing results presented in this chapter also included bending moment along with the depth of the wall, which was measured by the FBG sensors.

Chapter 8 summarised the major findings of this research, and made some suggestions for further research.

Chapter 2

Background

This chapter presents a review of greenfield tunnelling, the effect of tunnelling on structures, the use of protective structures to protect buildings from tunnelling-induced damage, as well as geotechnical centrifuge technology. Greenfield tunnel volume loss and the resulting soil movements are discussed first, followed by the surface and subsurface tunnelling-induced transverse settlements and prediction methods developed by various authors. The influence of tunnelling-induced soil movements on structures such as pile foundations and surface structures are presented. Finally, the use of protective structures to control ground movements was then reviewed, as well as the use of protective walls in practice to protect assets from tunnelling-induced damage.

2.1 Greenfield tunnelling

2.1.1 Ground movements

The main components that could cause ground movements for shield tunnelling are summarised by Mair and Taylor (1997), which are shown in Figure 2.1. The excavation face stress relief during tunnelling is the main reason to cause ground movements. The radial ground movement as suggested by Mair and Taylor (1997) is caused by the passage of the over-cutting front face, and the soil behind tends to contract radially. The tail void is the gap between the shield tail-skin and the tunnel lining outer surface that causes radial ground movement towards the tunnel centre line. With the development of ground loading, which is applied to the tunnel lining, the tunnel lining deforms towards the tunnel centre line (common assumption). In addition, long-term soil consolidation can cause ground movements and is particularly significant in soft clay tunnelling due to its low permeability.

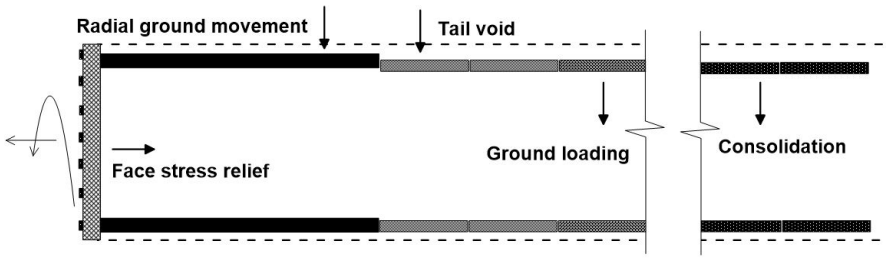


FIGURE 2.1: Main components of ground movement due to shield tunnelling after Cording (1991)

tunnelling-induced ground movements are three-dimensional; the typical greenfield longitude/transverse surface and subsurface settlement trough shape with key features are showed in Figure 2.2. The prediction of the greenfield surface and subsurface transverse settlement trough from various authors will be discussed in the next section.

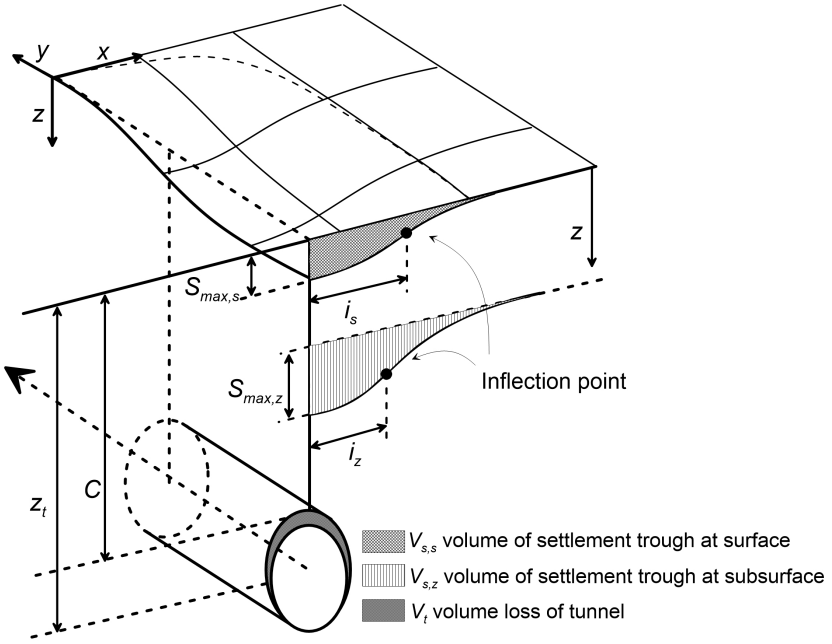


FIGURE 2.2: Greenfield settlement trough features after Attewell and Yeates (1984)

Greenfield displacements can be defined as the soil is naturally formed and has been "touched" by any engineering work, and the soil has no interactions between surrounding structures such as pile foundations or pipelines. Volume loss is one of the key elements when considering ground displacements. The soil volume loss can be described as $V_{l,s} = V_s/A_t$, where V_s is the volume of the settlement trough per meter length (longitude direction has a unit length of 1m), and A_t is the nominal tunnel cross-sectional area. Tunnel volume loss V_t is the amount of soil loss close to the tunnel region due to tunnel excavation and was discussed previously (Figure 2.2). It can be described as $V_t = V_{l,t} \times A_t$, where $V_{l,t}$ is the tunnel volume loss. For tunnelling in clay in the short-term (undrained case with zero change in soil volume), tunnel volume loss $V_{l,t}$ equals to the

soil volume loss $V_{l,s}$. For tunnelling in the sand, $V_{l,s}$ is not constrained and will not necessarily equal $V_{l,t}$; this topic will be further discussed in chapter 4.

2.1.2 Surface and subsurface transverse settlement

Peck (1969) showed that the Gaussian distribution curve can well describe the tunnelling-induced transverse settlement trough for clay under the undrained condition:

$$S_v = S_{max} \cdot exp(\frac{-x^2}{2i^2}) \tag{2.1}$$

where S_{max} is the maximum settlement at the tunnel centre line, x is the horizontal distance from tunnel centre line, and i is the horizontal distance from tunnel centre line to the inflection point of the curve (see Figure 2.2). The parameter i is influenced by tunnel depth, tunnel diameter and ground conditions (Peck, 1969). Mair and Taylor (1997) summarised the data provided by Peck (1969) and produced a graph (Figure 2.3) to indicate the relationship between width parameter (i) and depth of tunnel under different ground conditions.

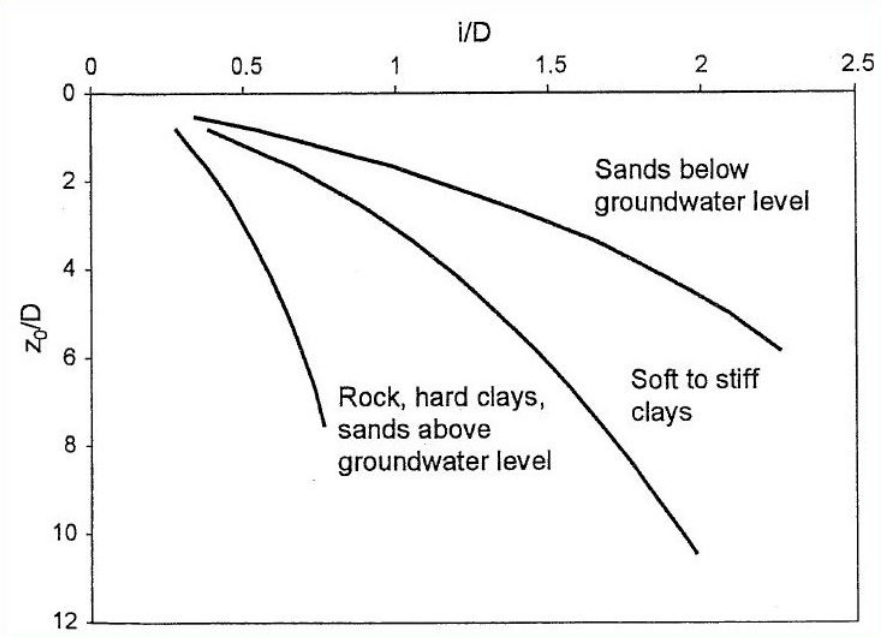


FIGURE 2.3: Relation between settlement trough width parameter and depth of tunnel for different ground conditions after Peck (1969)

Clough and Schmidt (1981) stated that with a given ground loss, the maximum soil settlement can either be defined by i or S_{max} (the integration of equation 2.1, $V_s = \int_{-\infty}^{+\infty} S_v(x)\,\mathrm{d}x = \sqrt{2\pi}\ i\ S_{max}$). Based on the field measurement data of tunnel excavation in clay, Clough and Schmidt (1981) produced the following equation to describe the

parameter i:

$$i = 0.5 D_t^{0.2} {z_t}^{0.8} \tag{2.2}$$

Where D_t is the diameter of the tunnel and z_t is the depth of the tunnel. Unlike the equation proposed by Clough and Schmidt (1981) (Equation 2.2) , O'reilly and New (1981) stated that there is no significant correlation between i and tunnel diameter. As a result, the following equation was proposed:

$$i = K z_t \tag{2.3}$$

where the K is the trough width parameter. Mair and Taylor (1997) suggested that for practical purposes, K could be taken as 0.5 for clay and 0.25 for sands and gravels.

Celestino et al. (2000) pointed out that the Gaussian curve does not always predict a good fit to the settlement troughs, and proposed a yield density curve to describe the settlement which contains three curve parameters (one additional degree of freedom compared with standard Gaussian curve), which can be expressed as:

$$S_v = \frac{S_{max}}{1 + (\frac{x}{a})^b} \tag{2.4}$$

Where S_{max} is the maximum settlement, a is length parameter and b is dimensionless, and horizontal distance from the tunnel centre line to the inflection point of the curve i can be expressed as $i = a(\frac{b-1}{b+1})^{1/b}$.

Jacobsz (2003) conducted a series of centrifuge tests in sand and developed a new equation to estimate the transverse surface settlement trough for tunnelling in sand:

$$S_v = S_{max} exp\{-\frac{1}{3}(\frac{|x|}{i})^{1.5}\} \tag{2.5}$$

Centrifuge tests were conducted at various volume losses, and the data were curve fitted using Equation 2.5. Compared with the Gaussian curve, results indicated that Equation 2.5 fits the experimental data better than the Gaussian.

Vorster et al. (2005) proposed the modified Gaussian equation to fit the observed transverses soil settlements from centrifuge experiments:

$$\begin{aligned} S_v &= \frac{n}{(n+1) + exp(\alpha \frac{x^2}{i^2})} S_{max} \\ n &= e^{\alpha} \cdot \frac{2\alpha - 1}{2\alpha + 1} + 1 \end{aligned} \tag{2.6}$$

where the n is the parameter that controls the width of the settlement trough, and α is the parameter to ensure that i remains the distance to the inflexion point. Like the yield density function, the modified Gaussian curve contains an additional degree of freedom compared to the standard Gaussian curve and it allows the curve to fit narrow settlement troughs. The centrifuge tests conducted by Marshall (2009) confirmed the goodness of fit of the modified Gaussian curve.

The subsurface settlement trough as suggested by Mair et al. (1993), can also be similarly characterised by Gaussian distribution as those for surface settlement. As a result, the equation used for surface settlement trough to determine the inflexion point (Equation 2.3) can also be applied to sub-surface by substituting the distance above the tunnel axis $z_t - z$:

$$i = K(z_t - z) \tag{2.7}$$

The value of K shows a non-linear relation with depth z. By reviewing field measurements and centrifuge tests data in clay, Mair et al. (1993) proposed the equation as follows:

$$K = \frac{0.175 + 0.325 \times (1 - z/z_t)}{(1 - z/z_t)} \tag{2.8}$$

Marshall et al. (2012) found that the standard parameters i and K were not sufficient to describe the settlement trough shape compared with other equations that use three degrees of freedom such as modified Gaussian. Marshall et al. (2012) suggested to use three points on the Gaussian curve which are S_{max}, $S_v(i_g) = 0.606S_{max}$ and the half settlement of $S_v(i_g)$ ($0.5S_v(i_g) = 0.303S_{max}$) to characterise the settlement trough shape. The horizontal distance of $S_v(i_g)$ and $0.5S_v(i_g)$ from the tunnel centre line are referred as x^* and x^{**}. The trough width parameter K based on x^* and x^{**} can also be expressed as $K^* = x^*/(z_t - z)$ and $K^{**} = x^{**}/(z_t - z)$. Based on the centrifuge results, Marshall et al. (2012) proposed the following equations to predict the settlement trough shape in dry dense sand:

$$\begin{aligned}
K^* &= \frac{K_s^* + \partial x^*/\partial z(z/z_t)}{1 - z/z_t} \\
K^{**} &= \frac{K_s^{**} + \partial x^{**}/\partial z(z/z_t)}{1 - z/z_t} \\
K_s^* &= K_{s,V_{l,t}}^{*int} + K^{*slope}_{s,V_{l,t}}(V_{l,t}) \\
K_s^{**} &= K_{s,V_{l,t}}^{**int} + K^{**slope}_{s,V_{l,t}}(V_{l,t})
\end{aligned} \tag{2.9}$$

Based on three centrifuge tests with different cover to diameter ratios ($C/D = 1.3,\ 2.4$ and 4.4), Marshall et al. (2012) summarised that the $K^{*int}_{s,V_{l,t}} = 0.44 + 0.055\ C/D$, $K^{*slope}_{s,V_{l,t}} = -0.041$, $\partial x^*/\partial z = -0.436$, $K^{**}_s = K^*_s + 0.29$ and $\partial x^{**}/\partial z = \partial x^*/\partial z - 0.20$. Assumption was made that the trough shape parameter have a linear variation against tunnel volume loss and cover to diameter ratio. Franza (2016) pointed out that equation 2.9 did not considered the transition between shallow to deep tunnels and may lead to an overestimation of the settlement width.

Based on centrifuge tests conducted by Franza (2016), Zhou (2015) and Marshall et al. (2012), a new set of equations to estimate the settlement trough width parameter that accounting for the variation in soil relative density (I_d), cover to diameter ratio (C/D), subsurface soil depth (z/z_t) and tunnel volume loss ($V_{l.t}$) is developed by Franza et al. (2019):

$$\begin{aligned} K^*_s &= K^{*int,ln}_{s,V_{l,t}} + K^{*slope,ln}_{s,V_{l,t}} \ln(V_{l,t}) \\ K^{**}_s &= K^{**int,ln}_{s,V_{l,t}} + K^{**slope,ln}_{s,V_{l,t}} \ln(V_{l,t}) \\ \frac{\partial x^*}{\partial z} &= \frac{M^*}{1 + z/z_t};\ \frac{\partial x^{**}}{\partial z} = \frac{M^{**}}{1 + z/z_t} \end{aligned} \tag{2.10}$$

In Equation 2.10, there are six parameters that need to be determined by the variation of I_d and C/D , which are $K^{*int,ln}_{s,V_{l,t}}$, $K^{*slope,ln}_{s,V_{l,t}}$, $K^{**int,ln}_{s,V_{l,t}}$, $K^{**slope,ln}_{s,V_{l,t}}$, M^* and M^{**}. The parameters stated above were calculated by regression analyses using logarithmic reflection equation as given by Franza et al. (2019), and the results are as follows:

$$\begin{aligned} K^{*int,ln}_{s,V_{l,t}} &= (-0.84I_d + 0.95)\ln(C/D) + 0.45I_d + 0.07 \\ K^{**int,ln}_{s,V_{l,t}} &= (-1.16I_d + 1.36)\ln(C/D) + 0.47I_d + 0.42 \\ K^{*slope,ln}_{s,V_{l,t}} &= (0.35I_d - 0.30)\ln(C/D) - 0.22I_d + 0.07 \\ K^{**slope,ln}_{s,V_{l,t}} &= (0.41I_d - 0.35)\ln(C/D) - 0.22I_d - 0.01 \\ M^* &= (0.81I_d - 0.93)\ln(C/D) - 0.60I_d - 0.07 \\ M^{**} &= (1.50I_d - 1.55)\ln(C/D) - 0.96I_d - 0.28 \end{aligned} \tag{2.11}$$

The overall performance of Equation 2.10 and 2.11 show a relatively good match with centrifuge measurements for both K^* and K^{**} as indicated by Franza (2016).

2.2 Tunnelling effect on piles and piled structures

Excavation of a tunnel is often close to or underneath existing structures. It is important for the engineers and researchers to understand the tunnelling effect on existing structures. The structures and the associated infrastructure elements that could potentially be affected by nearby tunnelling-induced ground movements include: pipelines, single or groups of piles, existing tunnels, and surface buildings, see Figure 2.4. In this section, the review is mainly focused on the interactions between tunnel, piles and piled structures. The single pile settlement and deformation due to tunnelling is first reviewed, followed by the pile load transfer due to tunnelling, and the piled structure deformations.



FIGURE 2.4: Underground structures in urban environment (Mair, 2008)

2.2.1 Building damage assessment

Potts and Addenbrooke (1997) proposed the modification factor approach to determine the deformation, the parameters are deflection ratio and horizontal strain (Boscardin and Cording, 1989, Burland, 1995). The definition of the deflection ratios are given in

Figure 2.5. As a result, the modification factors for deflection ratio as suggested by Potts and Addenbrooke (1997) can be defined as:

$$\begin{aligned} M^{DR_{sag}} &= DR_{sag,bldg}/DR_{sag,gf} \\ M^{DR_{hog}} &= DR_{hog,bldg}/DR_{hog,gf} \end{aligned} \tag{2.12}$$

where $DR_{hog,gf}$ and $DR_{sag,gf}$ are the hogging and sagging deflection ratio for the section of the building with respect to the greenfield ground surface settlements. In a similar fashion, Potts and Addenbrooke (1997) suggested that the modification factors for compressive and tensile horizontal strain are defined as:

$$\begin{aligned} M^{\varepsilon_{gc}} &= \varepsilon_{hc,bldg}/\varepsilon_{hc,gf} \\ M^{\varepsilon_{gt}} &= \varepsilon_{ht,bldg}/\varepsilon_{ht,gf} \end{aligned} \tag{2.13}$$

and $\varepsilon_{ht,gf}$ and $\varepsilon_{hc,gf}$ is the maximum horizontal tensile and compressive strain for the section of the building located in sagging and hogging zone with respect to the greenfield ground surface settlements.

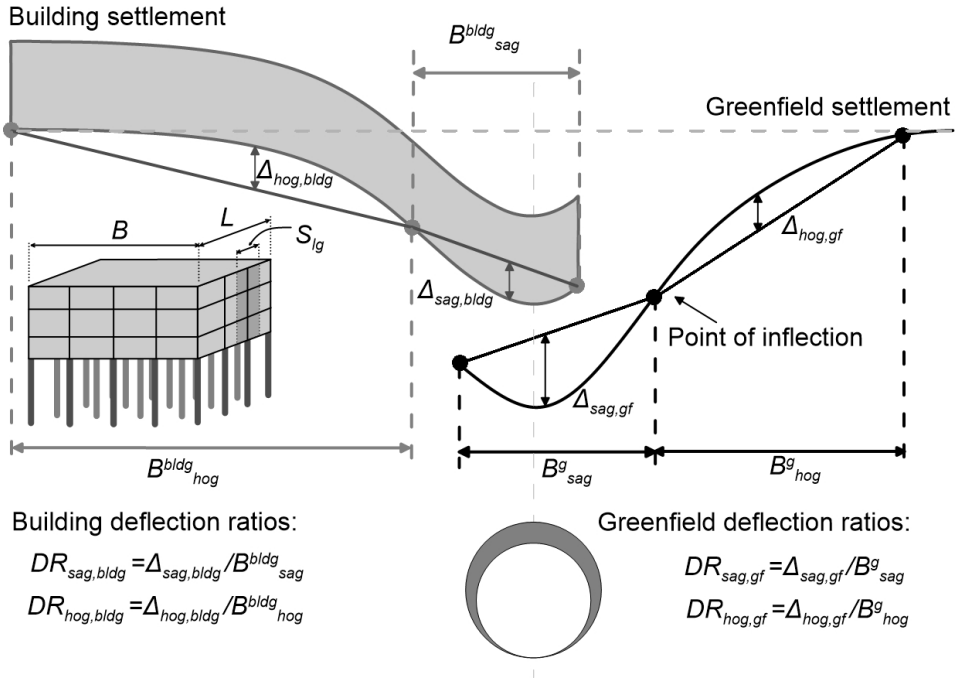


FIGURE 2.5: Definition of deflection ratios by Potts and Addenbrooke (1997),Goh and Mair (2012) and Franza and Marshall (2017)

In addition, to quantify the stiffness of the structure, Potts and Addenbrooke (1997) proposed the relative bending (ρ^*) and axial (α^*) stiffness parameters, which can be

defined as:

$$\begin{aligned} \rho^* &= \mathrm{EI}/\mathrm{E}_s H^4 \\ \alpha^* &= \mathrm{EA}/\mathrm{E}_s H \end{aligned} \tag{2.14}$$

where H is the half width of the building (B), and E_s is the soil stiffness. Potts and Addenbrooke (1997) suggested E_s is the secant stiffness of the soil located at a depth of $z_t/2$ under 0.01% axial strain. Goh and Mair (2012) modified Equation 2.14, and defined a new equation to calculate relative bending stiffness as:

$$\begin{aligned} \rho_{sag} &= \frac{\mathrm{EI}^*}{\mathrm{E}_s (B^g_{hog})^3} \\ \rho_{hog} &= \frac{\mathrm{EI}^*}{\mathrm{E}_s (B^g_{hog})^3} \end{aligned} \tag{2.15}$$

EI^* is the elastic building stiffnesses per running metre (kNm^2/m run). L^g_{sag} and L^g_{hog} are the lengths in greenfield condition corresponding to the building's location in sagging and hogging, respectively.

Franza and Marshall (2017) extended the building stiffness parameter to account for piled structures:

$$\begin{aligned} \rho^p_{sag} &= \frac{\mathrm{EI}}{\mathrm{E}_s (B^g_{sag})^3} \frac{S_{lg}}{L} \\ \rho^p_{hog} &= \frac{\mathrm{EI}}{\mathrm{E}_s (B^g_{hog})^3} \frac{S_{lg}}{L} \end{aligned} \tag{2.16}$$

where S_{lg} is the longitudinal spacing of transverse pile rows, and L is the length of the building in longitudinal direction, see Figure 2.5.

2.2.2 Pile settlement due to tunnelling

It has been well established that pile installation method (such as driven pile and bored pile) has a significant effect on the performance of the pile (during tunnel volume loss). This is because the different installation methods cause different pile working load distribution along the pile. The focus of the research is on dry sand, therefore, for non-displacement piles in sand (bored pile), pile working loads are mainly taken by the pile end bearing resistance. For displacement piles in sand (jacked or driven pile), the pile working load is mainly taken by shaft resistance. Therefore, during tunnel volume loss, the axial force along the two types of the pile is different, this is because the initial stress conditions are different (effect of installation method).

Loganathan et al. (2000) conducted three centrifuge tests in clay using non-displacement single piles and pile groups (2 × 2) to investigate the tunnelling-induced ground movements and pile deformations by varying the depth of the tunnel. The centrifuge model configuration is shown in Figure 2.6. The diameter of the single pile is 9 mm and has a horizontal distance of 55 mm from the tunnel centre line. The single pile was pushed into the clay at a rate of 0.5 mm/s to allow excess pore water pressure dissipation prior to the centrifuge acceleration. Due to the fact that the pile was pushed into the soil at 1g, the ground stress did not replicate the real soil disturbance occurred during pile installation. As a result, the pile is assumed as a non-displacement pile. From the single pile centrifuge test results, Loganathan et al. (2000) pointed out that the maximum pile head settlement is expected for tunnels located at the pile tip level (z_t=180 mm, C/D=2.5). The tests conducted by Loganathan et al. (2000) provided an insight into pile settlement response to tunnelling-induced ground movement at various pile base locations with respect to the depth of the tunnel.

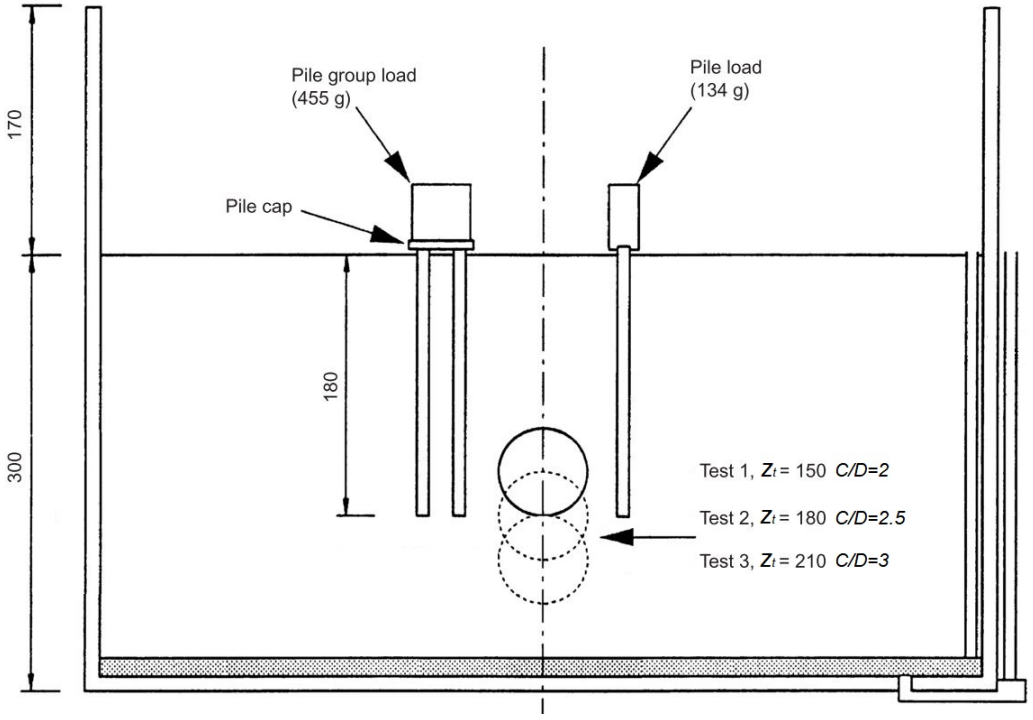


FIGURE 2.6: Centrifuge model test configuration (Loganathan et al., 2000) (unit in mm)

Jacobsz (2003) carried out a series of centrifuge tests in dry Fraction E silica sand using single displacement piles located at various positions. Jacobsz (2003) identified four influence zones where the pile could experience different settlement and mobilised shaft friction at a given tunnel volume loss. During centrifuge tests, piles with a diameter of 12 mm fitted with a 60° conical tip were pushed into the sandy ground by 25 mm (to ensure the based load was fully mobilised) after the designated g-level was reached

(75 g). This pile driving process under the required g-level (replicating the real ground stress profile) will cause significant surrounding soil disturbance when compared with the method used by Loganathan et al. (2000), so the process cab be assumed as a displacement pile. Figure 2.7 shows the tests layout and experiment configuration for the tests conducted by Jacobsz (2003).

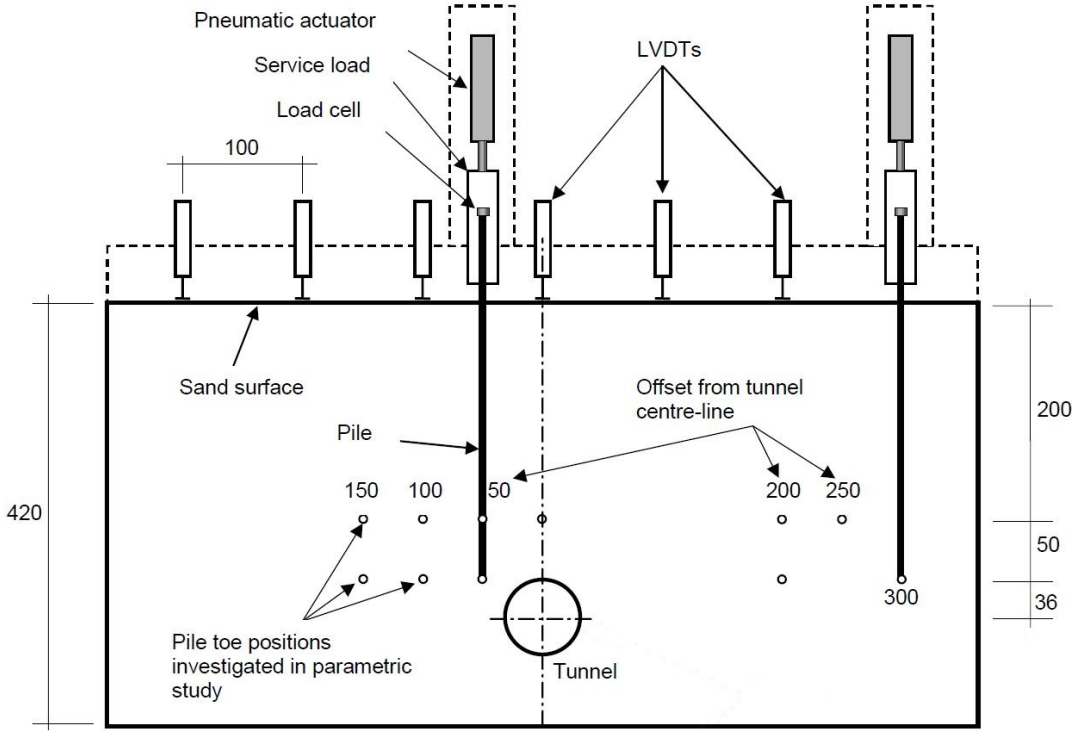


FIGURE 2.7: Centrifuge model test configuration by Jacobsz (2003) (unit in mm)

Based on the pile settlement data obtained from centrifuge tests at a volume loss of 1.5%, four different influence zones were identified by Jacobsz (2003), see Figure 2.8. The piles with their base located in Zone D settle less than the surface and subsurface greenfield settlement, piles with their base located in Zone C show relatively similar settlement to surface and subsurface settlement, and in Zone B piles settle more than the greenfield soil settlements. For piles with their base located in Zone A, pile settlement shows a similar value to surface and subsurface soil settlements with a tunnel volume loss less than 1.5%.

During the construction of London to the Channel Tunnel Rail Link (CTRL), Selemetas (2005) conducted a series of full-scale trials to investigate the response of single piles and piled structures due to tunnelling-induced ground movement. The tunnel excavation was carried out by two 8 m diameter earth pressure balance machines (EPBM) at a depth of 19.5 m with a spacing of 16 m, and the ground contains London clay, sandy gravel and alluvium deposits. The test layout and instruments are showed in Figure 2.9.

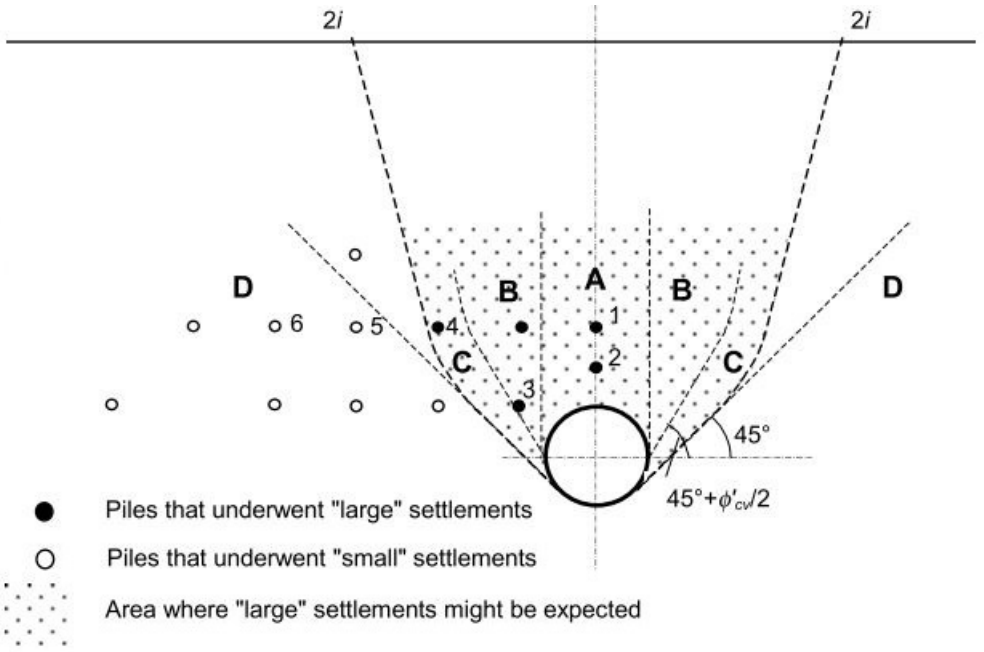


FIGURE 2.8: Influence zone identify by Jacobsz (2003) that large settlement is expected

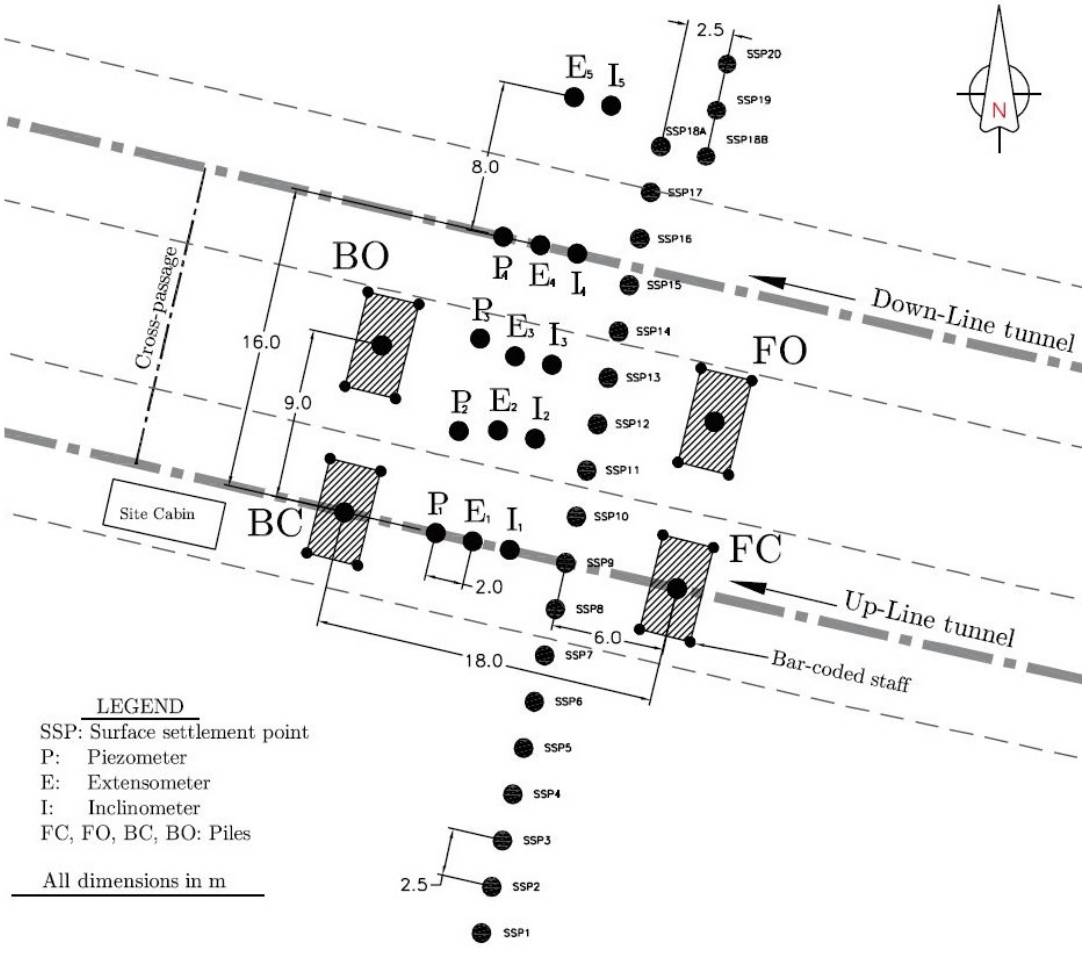


FIGURE 2.9: Position of pile and instrumentation by Selemetas (2005)

Selemetas (2005) suggested to use R value to compare the pile head settlement against the ground surface settlement, which is the ratio between absolute pile head displacement and nearby ground surface soil displacement ($R = \frac{pile\ head\ settlement}{ground\ surface\ settlement}$). Based on the measured pile settlement and nearby greenfield surface soil settlement, three influence zones are identified by Selemetas (2005) (see Figure 2.10). $R > 1$ for the pile with their base located in Zone A. Piles with their base located in Zone B settle a similar amount as the surface siuk and piles with their base located in Zone C settle less than the surface soil ($R < 1$). Similar zones of influence were identified by Kaalberg et al. (2005) with a slightly wider zone of influence A (the cutoff line between zone A and B: inclined angle of 60° from tunnel spring line to surface rather than a vertical line, see Figure 2.10).

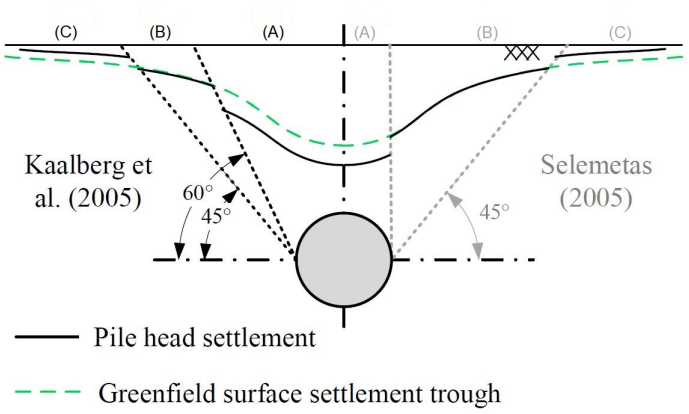


FIGURE 2.10: Zones of influence identified by Selemetas (2005) and Kaalberg et al. (2005) from Franza (2016)

Lee and Chiang (2007) conducted a series of centrifuge tests to investigate the response of single piles to tunnelling-induced soil movements. The tests were carried out with fully saturated quartz sand. Piles were fixed at the predetermined positions prior to sand pluviation in order to replicate bored piles (non-displacement pile). Figure 2.11 shows the test layout. By varying the pile working load and the horizontal distance between the pile and the tunnel, Lee and Chiang (2007) found that pile settlement increases significantly when the piles are located closer to the tunnel.

Marshall (2009) conducted two groups of centrifuge tests (Tunpile1 and Tunpile2) to investigate the pile settlement, pile strain change and resultant ground displacements due to tunnelling in dry dense silica sand ($I_d = 90\%$). The piles tested in the centrifuge were jacked into the ground after the target g-level (75 g) was reached. As a result, piles can be assumed as displacement piles. The measured pile settlement for the pile with their base located in Zone A ,influence zone defined by (Jacobsz, 2003) shows a similar value to the greenfield soil settlement at a volume loss below 0.9%. The pile head starts to settle more than the soil with further increase in tunnel volume loss; these results match the outcomes from Zone A defined by Selemetas (2005) and Kaalberg et al.

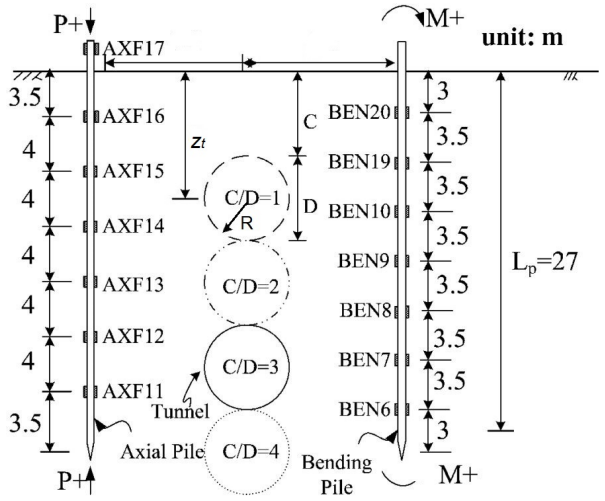


FIGURE 2.11: Testing layout and strain gauge position from Lee and Chiang (2007) (unit in prototype scale)

(2005). For piles with their base located in Zone B, zone of influence defined by (Jacobsz, 2003), centrifuge results showed that the measured pile settlements are greater than soil displacements, which confirmed the finding from Jacobsz (2003), see Figure 2.12.

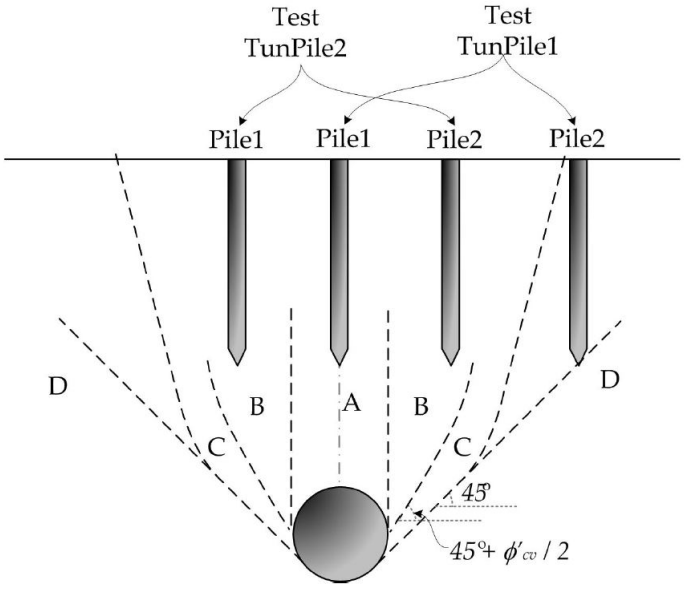


FIGURE 2.12: Tested piles location in related to the zone of influence provided by Jacobsz (2003) from Marshall (2009)

Ng and Lu (2013) carried out centrifuge tests to investigate the behaviour of a single pile due to twin tunnelling that considered the tunnel excavation sequence. The detailed review of the model tunnel which has the ability to simulate tunnel excavation sequence is presented in Section 3.2. The testing layout is shown in Figure 2.13. The piles were installed to the predefined position prior to sand pluviation and piles can be assumed as non-displacement piles. Linear variable differential transformers (LVDTs)

were mounted at the pile head to measure the pile settlement due to twin tunnelling. After the application of the 1200 N working load to the pile via a hydraulic jack, tunnel volume loss was carried out (tunnel volume loss up to 1%) and piles settlement and axial force along the piles were measured. Two tunnel construction sequences were tested: 1) excavation carried out from the tunnel located near the pile base followed by the tunnel at the middle depth of the pile (test TS); 2) excavation carried out from the tunnel located at the middle depth of the pile followed by the tunnel located at the pile base (test ST). Based on the test TS, Ng and Lu (2013) concluded that the pile settlement induced by the second tunnel (tunnel located at the middle of the pile) is only 40% of the settlement induced by the first tunnel excavation (tunnel located at pile base). For test ST, Ng and Lu (2013) summarised that pile settlement induced by the second tunnel (tunnel located at pile base) excavation is 40% more than the settlement caused by the first tunnel excavation (tunnel located at pile base) in test TS. This is due to the stress release along the pile shaft that occurred during the excavation of the first tunnel in Test TS, where pile load is transferred to the pile base, therefore, additional tunnel excavation near the pile base causes greater pile settlement (detailed load transfer along the pile during test ST will be discussed in Section 2.2.3). As a result, Ng and Lu (2013) suggested that the tunnel construction sequence has a significant effect on the pile settlement induced by twin tunnelling at different depths.

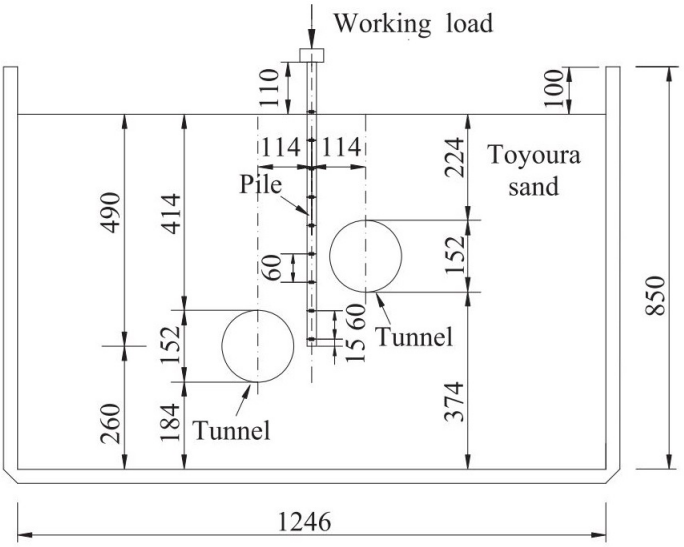


FIGURE 2.13: Testing layout of the centrifuge tested by Ng and Lu (2013)

2.2.3 Single pile load transfer due to tunnelling

For the centrifuge tests conducted by Loganathan et al. (2000) (testing layout described in the previous section), strain gauges were located on the outer surface of the pile with eight different locations to measure both bending moment and axial force along the pile.

Loganathan et al. (2000) summarised that the maximum bending moment is expected to occur at the bottom of the pile, and a tunnel located at the pile base will cause greater bending moment along the pile than other tunnel locations. The induced maximum axial force for a pile is located at the tunnel depth for the tunnel located above the pile base; otherwise the maximum axial force of the pile will be located at the pile base (for the case where tunnel is located below the pile base).

The centrifuge tests conducted by Jacobsz (2003) used full Wheatstone bridge strain gauge configuration (temperature compensation considered) to measure axial force along the pile and lateral stress (a separate gauge specifically designed for lateral stress measurement). Detailed instrument configuration will be discussed in Section 3.2. A load cell was located at the base of the pile, which enabled the measurement of the end bearing force during tunnel volume loss, and strain gauges located along the pile allowed the measurement of the shaft resistance. As suggested by Jacobsz (2003), for piles located in Zone A, with an increase in tunnel volume loss, the pile experienced a sudden reduction in pile end bearing resistance, in the same time, pile shaft friction was mobilised in order to maintain the equilibrium of the pile head load. Piles located in Zone B showed similar load transfer behaviour between the pile base and shaft resistance to the piles located in Zone A. For piles located in Zone C, the pile end bearing resistance increased with tunnel volume loss (tunnel volume loss less than 0.5%), and to balance the pile head load, shaft friction along the pile reduced. With further increase in tunnel volume loss (greater than 0.5%), shaft resistance increased, and the pile end bearing load started to decrease. For piles located outside the zone of influence defined by Jacobsz (2003), shaft resistance along the pile was reduced with tunnel volume loss.

The full-scale pile response due to tunnelling was investigated by Selemetas (2005). Four driven cast-in-situ piles located directly above or with an offset of 9 m from the tunnel centre line were used (see Figure 2.9). The piles were installed by firstly driving a steel tube equipped with a based plate to the required depth, and then the steel tube was filled with grout. Then, the steel tube was pulled out, and the reinforcement cage equipped with vibrating wire strain gauges was inserted into the wet concrete. Four vibrating wire strain gauges were grouped as a cluster located along the reinforcement cage every 2 m, which allow the measurement of the axial load along the four piles. Based on the measured data, the change in axial load due to tunnelling can be divided into four different stages which are: 1) arrival of the EPBM face, 2) during the passage of the shield, 3) the completion of tail-skin grouting and 4) long term after the tunnel excavation. Based on the axial force measurement, Selemetas (2005) pointed out that the axial compression load of the pile directly above the tunnel centre line increased during the arrival of the EPBM (earth pressure balance machine) excavation face. Significant pile load reduction is observed during the passage of the EPBM. During the tail-skin

grouting, pile load distribution matches well with the initial pile load prior to tunnelling, and with time, the axial load reduced along the pile and the pile located close to the tunnel centre line experienced an increase in base load and reduction in shaft friction.

Strain gauges were used to measure axial force (full Wheatstone bridge) and bending moment (half Wheatstone bridge) along the depth of the pile for the centrifuge tests carried by Lee and Chiang (2007). Based on the measured results, the depth ratio (L_p/z_t, see Figure 2.11) and working load have a significant effect on the axial force along the pile. Figure 2.14 shows a typical axial load transfer and skin friction mobilisation mechanism during tunnel volume loss for a single pile with 3200 kN working load that was located 4.5 m away from the tunnel centre line (units are in prototype scale). With the increase in tunnel volume loss, pile end bearing load decreased, and to balance the pile working load equilibrium, pile shaft friction is mobilised.

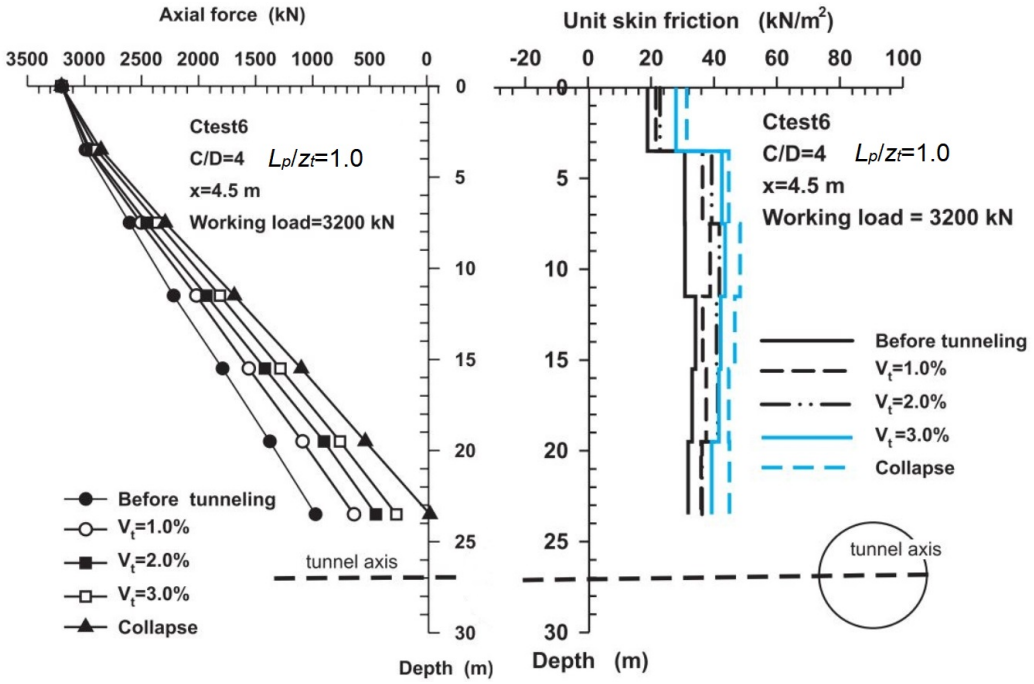


FIGURE 2.14: Load transfer mechanism for pile with 3200kN working load (Lee and Chiang, 2007) (Unit in prototype scale)

The axial load distribution of a single pile due to twin tunnelling was investigated by Ng and Lu (2013). Before tunnelling, 85% of the working load applied to the pile was carried by pile shaft (shaft resistance) and only 15% of the pile working load was transferred to the pile base (end bearing load). For test TS, as the first tunnel excavation face (tunnel located at pile base) approached the pile, pile end bearing force decreased, and to balance the pile working load equilibrium, shaft resistance along the pile increased. Further advancement of the tunnel excavation face caused the reduction of shaft resistance and increase in pile end bearing force. After the second tunnel excavation (tunnel located at

the middle of the pile), reduction in shaft resistance was identified at the upper portion of the pile, which was caused by the downwards soil movements as well as the nearby soil stress release. For test ST, after the excavation of the first tunnel (tunnel located at the middle of the pile), the pile shaft resistance reduced at the upper portion of the pile and an increase in shaft resistance was observed at the lower portion of the pile as well as the end bearing load. When the second tunnel was excavated (tunnel located at the pile base), shaft resistance reduced at the lower portion of the pile as well as the end bearing force, which caused greater pile settlement than test TS.

2.2.4 Piled structure settlement and deformation due to tunnelling

For piled structure simulation within the centrifuge, a pile cap was often used to connect the piles. For the centrifuge tests reviewed in this section, it is important to notice that pile cap was not in contact with the soil. As a result, the load (self-weight) of the piled structure was only carried by the pile shaft friction and end bearing capacity.

A 2 $\times$ 2 pile group (spacing of 25 mm in both directions) was used for the centrifuge tests conducted by Loganathan et al. (2000). A 10 mm thick aluminium plate was used as a pile cap to hold the piles in position. The pile group was located at an offset distance of 67.5 mm from the centre of the pile group to the tunnel centre line. Detailed testing configurations are discussed in Section 2.2.2. By varying the cover to diameter ratio (C/D), Loganathan et al. (2000) concluded that the maximum pile settlement and lateral displacement occurred when the tunnel was located at the pile base (C/D=2.5).

Jacobsz (2003) tested pile groups with service load on the piles. The weight on the pile groups was rigidly connected to the pile cap. Figure 2.15 shows the pile base locations within the centrifuge strong box. Based on the pile settlement data, Jacobsz (2003) pointed out that with the increase in offset distance between the pile group and tunnel centre line, pile group settlement and rotation reduced. In addition, to achieve the same magnitude of settlement to a single pile, higher volume loss is required for a pile group.

By using the flexible membrane model tunnel which has the ability to simulate tunnel excavation sequence in the centrifuge, Ng et al. (2014) studied the pile group response to a side-by-side twin tunnelling. Figure 2.16 shows the centrifuge test configuration; three centrifuge tests were carried out with different cover to diameter ratios. During the model preparation stage, the pile group was fixed at the predefined location prior to sand pluviation, and piles can be assumed as a non-displacement. From the measured pile settlement, Ng et al. (2014) suggested that the rate of the pile group settlement is increased when the first tunnel excavation face is approaching the pile group centre line, and the settlement rate is decreased when the excavation face passed the pile group

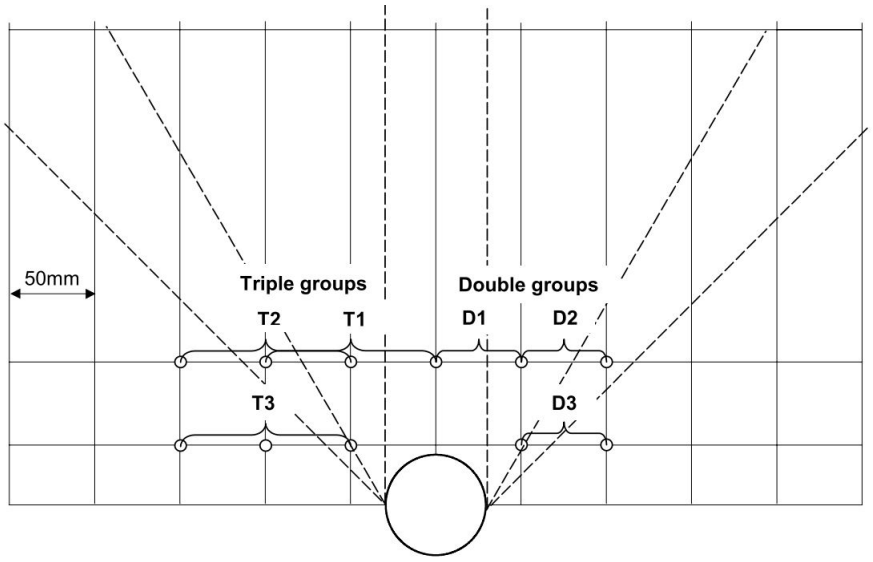


FIGURE 2.15: Pile group base locations for centrifuge tests conducted by Jacobsz (2003)

centre line. By comparing the final pile group settlement in all three centrifuge tests, Ng et al. (2014) indicated that the maximum pile group settlement is observed for the case that the tunnels are excavated below the pile base (C/D=3.72).

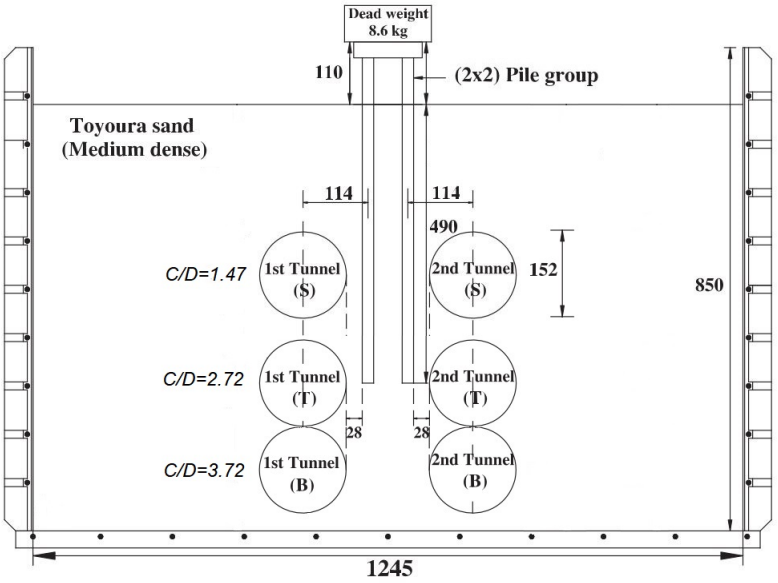


FIGURE 2.16: Pile group tests layout by Ng et al. (2014)

Boonsiri and Takemura (2015a) used a concentric rigid boundary mechanical (RBM) model tunnel within the centrifuge to study the pile group response to adjacent tunnelling in sand. The concentric rigid boundary mechanical model tunnel has the ability to impose concentric uniform displacements around its circumference. 2 × 2 pile groups with different pile lengths were used in the centrifuge tests, with a centre to centre pile spacing of 50 mm. 20 mm thick stainless steel plate (pile cap) were used to connect the

piles rigidly. The pile groups were held in place first, and then the sand was pluviated to achieve a relative density of 80%. Figure 2.17 shows the test configuration by Boonsiri and Takemura (2015a). Pile groups with different length, offset from the tunnel and working load were tested under two C/D ratios (C/D=1.5 and 2.5). Based on the measured pile settlement data, Boonsiri and Takemura (2015a) found that for all the tests, the pile group located close to the tunnel settles more than the pile group located further away from the tunnel. In addition, a pile group with a heavy working load shows more settlement to the pile group with less working load under a given tunnel volume loss.

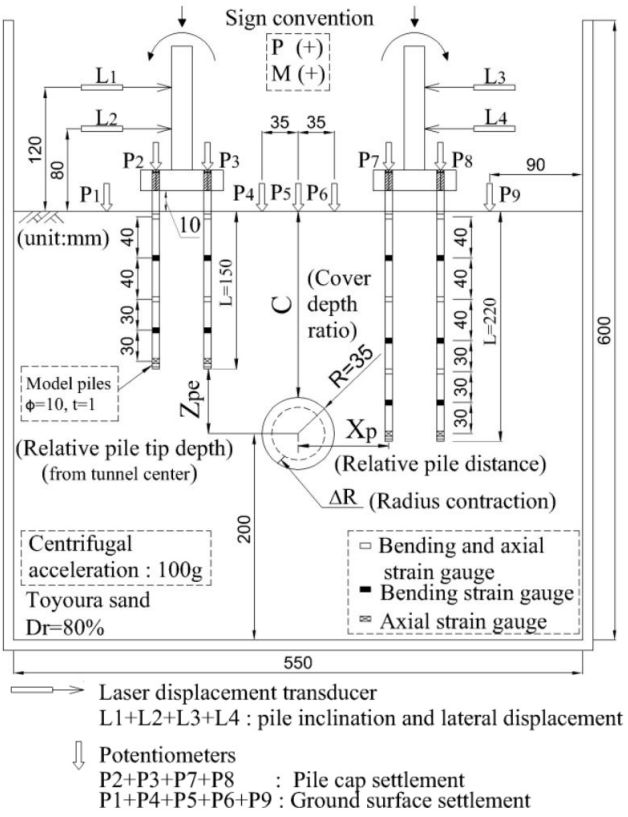


FIGURE 2.17: Pile group tests layout by Boonsiri and Takemura (2015a)

In practice, a precise levelling monitoring technique was carried out by Selemetas (2005) to measure the response of two piled structures due to tunnelling-induced ground movements. The first structure is a three-storey steel-framed masonry building located between the two tunnel lines and the second structure is a reinforced concrete double box piled structure located perpendicular to tunnel excavation direction. Based on the measured data and by comparing the piled structure settlement against the surrounding ground surface settlements, Selemetas (2005) summarised that the magnitude of the pile settlement is affected by the relative position of the pile base to the tunnel and the induced tunnel volume loss. In addition, for the pile located in Zone A (defined by Selemetas (2005), see Figure 2.10), the pile shows a similar magnitude in settlement to

the subsurface settlement at pile base level under small tunnel volume loss. For piles located outside Zone A defined by Selemetas (2005), piles showed a similar or lesser settlement than the surrounding ground surface settlements.

So far, the reviews of piled structures tested within the centrifuge are mainly based on pile groups that were rigidly connected via a solid pile cap. However, studies of the structure stiffness effects on the response of the piled structure due to tunnelling are limited. Centrifuge tests conducted by Franza and Marshall (2017) considered the pile structure stiffness effects and the piled structure was replicated using an equivalent aluminium plate. Figure 2.18 shows the testing configurations. The piled structure dis-

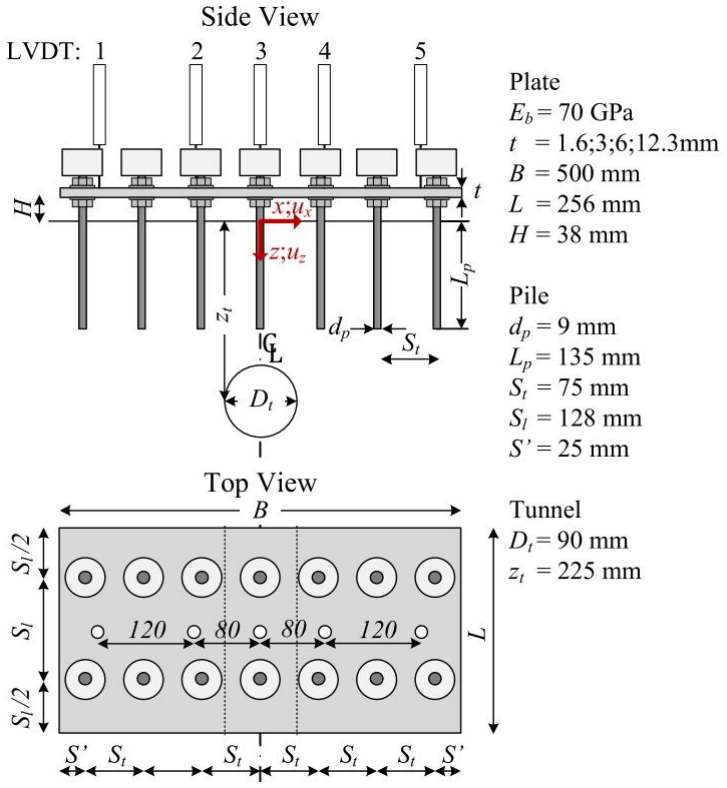


FIGURE 2.18: Pile group tests layout by Franza and Marshall (2017)

placement was measured from GeoPIV (Particle Image Velocimetry) and LVDTs. To vary the structure stiffness, different thickness of the aluminium plates were selected. The piled structures were pushed into the soil under 1 g condition and can be assumed as a non-displacement pile (surrounding soil disturbances are small due to soil stress is relatively small). Franza and Marshall (2017) summarised that the structure settlement is affected by the relationship between structure stiffness and weight. At a given structure stiffness, an increase in structure weight will cause higher distortion. Figure 2.19 shows the modification factors in sagging and hogging zone against relative bending stiffness ρ^p. From Figure 2.19, Franza and Marshall (2017) indicated that the increase in structure stiffness or decrease in structure weight will cause less structure deformation.

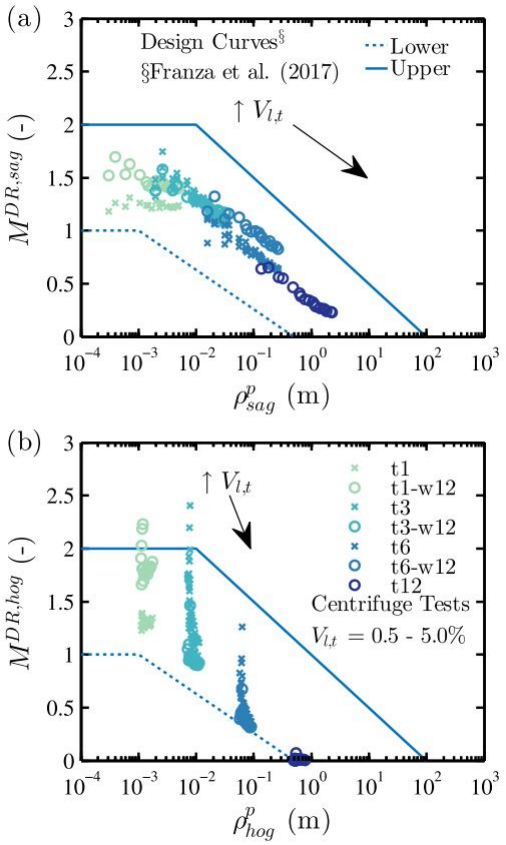


FIGURE 2.19: The computed M^{DR} in (a) sagging (b) hogging from centrifuge test and design lines provided by Franza and Marshall (2017)

2.2.5 Piled structure load transfer with tunnelling

Pile groups consisting of 2 × 1 (double pile group) and 3 × 1 (triple pile group) piles were tested by Jacobsz (2003) in a geotechnical centrifuge in dry silica sand. The tests configuration is shown in Figure 2.15. With the increase in tunnel volume loss, the pile group starts to transfer the load from the pile base to shaft (mobilisation of the pile shaft resistance), with further increase in tunnel volume loss, the shaft resistance reached the maximum and the working load from the piles started to transfer from one to another. This load transfer between the piles will cause the global pile to rotate and accelerate the base load reduction for the pile located close to the tunnel.

Strain gauges were used for the centrifuge tests given by Ng et al. (2014) to measure the axial force and bending moment along the pile during tunnel volume loss. For the test of a tunnel excavated near the middle depth of the pile group (test SS C/D=1.47, see Figure 2.16), shaft resistance at the upper portion of the pile reduced as the first tunnel excavation face reached the pile group centre line, the pile load was then transferred to the lower portion of the pile as well as the adjacent piles. A similar load transfer mechanism was also identified in test TT (C/D=2.72). For test BB (C/D=3.72), after

the first tunnel excavation face reached the pile group centre line, the pile located close to the first excavated tunnel reduced pile end bearing capacity significantly, and shaft resistance was mobilised at the upper portion of the pile.

For the centrifuge tests conducted by Boonsiri and Takemura (2015a), the measured data suggested that the pile located close to the tunnel has a larger pile end bearing load variation than the pile located further away from the tunnel during tunnel volume loss. For piles with their base located in Zone B (zone defined by Jacobsz (2003)), the end bearing load decreased with tunnelling. Boonsiri and Takemura (2015a) also indicated that for the piles with their base located in Zone B and C (zone defined by Jacobsz (2003)) negative skin friction is developed (pile settles less than the surrounding soil) during tunnel volume loss.

So far, the reviews are focused on the centrifuge modelling of tunnelling underneath or adjacent to piles. The piled structure described above was simplified as 1) an equivalent beam, 2) rigidly connected, 3) individually loaded with no physical connections. Theses simplifications could over or under-predicted the effect of structure stiffness on associated pile settlement due to tunnelling. Therefore a more accurate approach to simulate superstructure is required within the centrifuge modelling field, which is one of the purpose of this research.

2.3 The use of protective structures to reduce tunnelling-induced ground movements

As discussed from the previous sections, structures located close to the tunnels are likely to be affected during the excavation of a tunnel. The ground movements due to tunnelling have a high potential to damage existing nearby superstructures or threaten the serviceability of buildings. Therefore, it is vital to reduce structures from tunnelling induced ground movements (uneven settlement of the structure due to tunnelling subsidence). Various techniques are available for this purpose, such as compensation grouting, cutoff walls, and structural jacking. For the research presented in this thesis, the focus is on the cutoff walls (protective walls) are used to protect buildings from tunnelling-induced damage, hence the review presented here is limited to this protective measure.

2.3.1 Centrifuge study of using protective wall to control ground movements

Bilotta (2008) used a series of aluminium diaphragm walls in centrifuge tests to assess the effectiveness of diaphragm wall to reduce tunnelling-induced ground movements in clay. The length, location and thickness of the wall, as well as the roughness of the soil-wall interface was varied. Figure 2.20 shows the testing model geometry. The distance between the tunnel invert and the base of the model box is one diameter of the tunnel (50 mm), Bilotta (2008) suggests that such distance should be sufficient to have minimal effect to the results. The aluminium mode wall has a unit weight of γ=27 kN/m^3, which is similar to the unit weight of the reinforced concrete. The walls are installed into the soil as a "wished in place" wall, and the effect of the installation is out of the scope of the work.

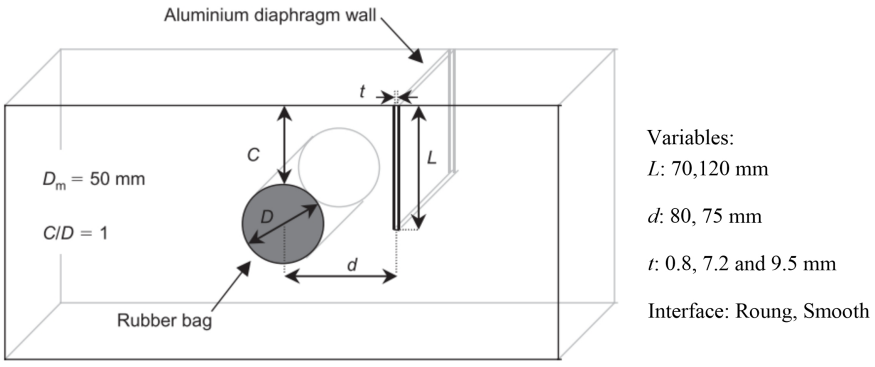


FIGURE 2.20: Model geometry tested by Bilotta (2008)

To quantify the effectiveness of the wall in reducing tunnelling-induced ground movements, a dimensionless ratio $\eta_{bw}^{V_{l,t}}$ was defined by Bilotta (2008) as:

$$\eta_{bw}^{V_{l,t}} = \frac{S_{ref} - S_{bw}}{S_{ref}} \times 100\% \tag{2.17}$$

where S_{bw} is surface settlement immediately behind the wall (at the retained side of the wall), and S_{ref} is the greenfield settlement at the same location and tunnel volume loss $V_{l,t}$.

Based on the centrifuge results, Bilotta (2008) summarised that the use of a diaphragm wall could effectively reduce the soil settlements due to tunnelling, and the effectiveness of the wall $\eta_{bw}^{V_{l,t}}$ is mainly affected by its length.

2.3.2 The use of pile walls in practice to protect buildings from tunnelling-induced movements

In practice, a stiff pile wall has been used to protect sensitive buildings from tunnelling-induced ground movements (Ledesma and Alonso, 2017). Based on the observation of the building, as suggested by Ledesma and Alonso (2017) that with the use of stiff pile wall, the effect of tunnelling on the sensitive structures is negligible. The geometry of the tunnel, pile wall and structure is shown in Figure 2.21.

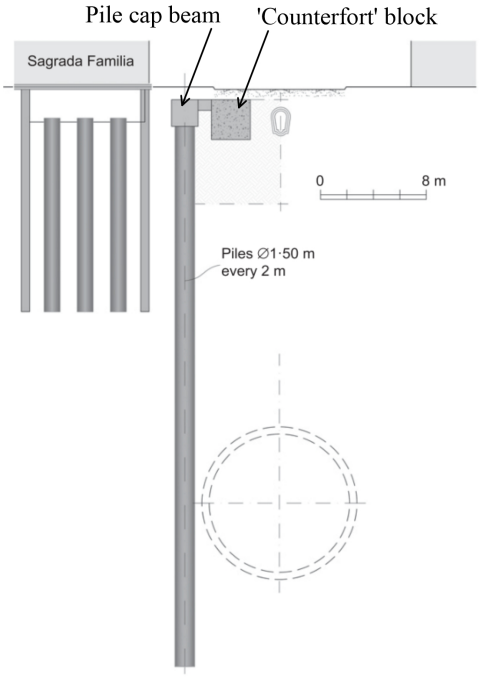


FIGURE 2.21: Geometry of the case given by Ledesma and Alonso (2017)

1.5 m diameter reinforced concrete piles were used to form the stiff pile wall, which has a length of 41 m. The distance between the piles is 2.0 m, which leads to a 0.5 m gap between the piles. A rigid pile cap beam was used to connect the piles. In addition, a "counterfort" block was placed next to the pile cap beam, in order to reduce the lateral movement of the pile cap beam, see Figure 2.21.

The tunnel volume loss due to the excavation of the tunnel using EPB is around $V_{l,t} = 0.5\%$, and Figure 2.22 shows the vertical settlement trough including the field measurement data after the passage of the EPB and "long-term" measurement data. In addition, the numerical model results are presented, where case A (solid black line) does not consider the weight of the structure as well as the buildings on the other side of the street, whereas case B (dashed black line) takes the weight of the structure and buildings into consideration. Ledesma and Alonso (2017) pointed out that most of the

measured ground movements were below the range of instruments accuracy, and the impact of tunnelling-induced ground movements on sensitive structure was negligible.

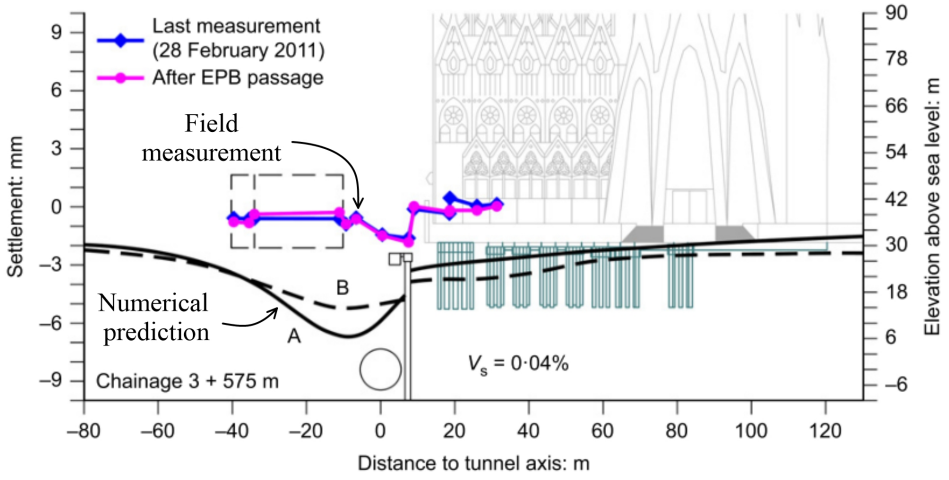


FIGURE 2.22: Measured and computed vertical settlement given by Ledesma and Alonso (2017)

2.4 Summary of the chapter

As discussed in Section 1.2, the scope of this research is limited to sand, and the literature reviewed in this chapter is mainly based on sand. Greenfield tunnelling was reviewed first (Section 2.1). As discussed, the excavation of a tunnel will cause ground movements, which are three-dimensional (see Figure 2.2). It is important to predict and understand the ground movements, and this research is focused on the transverse settlement. Several researchers have developed different methods (equations) to predict the surface and subsurface transverse settlement based on field measurement data and centrifuge test results. For centrifuge tests, tunnel volume loss is commonly simulated by a flexible membrane (FM) model tunnel (Divall, 2013, Farrell, 2010, Franza, 2016, Jacobsz, 2003, Loganathan et al., 2000, Marshall, 2009, Vorster, 2006, Williamson, 2014, Zhou, 2015). Based on the equations developed by Marshall (2012), Franza et al. (2019) further developed these equations, which considered the effect of soil relative density and C/D, and the results showed great match with their centrifuge results (using FM model tunnel). Another approach to simulate the tunnel volume loss is by using rigid boundary mechanical (RBM) model tunnel (Katoh et al., 1998), and has been used to study soil-structure interaction problems by Boonsiri and Takemura (2015a,b). Marshall and Franza (2017) showed, based on the data from Boonsiri and Takemura (2015b), that the set of equations provided by Marshall et al. (2012) for the prediction of settlement width parameters does not always provide a good fit to data obtained using a concentric RBM model tunnel. It was difficult to isolate a specific reason for the differences, since

the variation of such factors as soil type, sample preparation method, and measurement errors between the different studies inevitably affected results. However, Marshall and Franza (2017) suggested that the different tunnel boundary conditions between the data sets (FM in Franza (2016), Marshall (2009), Zhou et al. (2014) versus displacement control RBM lining in Boonsiri and Takemura (2015b)) was probably the most influential parameter. It is important to have an understanding of the implications of the choice of model tunnel adopted for these types of centrifuge tests, however a thorough evaluation of this has never been conducted. This study aims to address this issue by investigating the effect of the type of centrifuge model (i.e. flexible membrane FM or rigid boundary mechanical RBM) used to simulate 2D tunnelling displacements.

The second section reviewed the tunnelling effect on piles and piled structures. Various researchers studied pile settlement and associated load transfer along the pile during tunnelling using a geotechnical centrifuge. In general, the main factors that could affect the response of the pile during tunnelling are (1) pile installation methods (non-displacement or displacement pile), (2) location of the pile tip relative to the tunnel, (3) amount of load applied to the pile during tunnelling. The piled structure settlement and deformation due to tunnelling, as well as the load transfer between the piles, were reviewed. For centrifuge tests, the physical models of piled structures require some degree of simplification compared to reality. For example, the superstructure (building) was simplified as an equivalent beam/plate, or the piles are rigidly connected to by a pile cap. Theses simplified physical models could over- or under-predict the contribution of superstructure to the global tunnel-pile-structure-interaction (TPSI) problem. As a result, accurately simulating the superstructure is vital for the study of TPSI. This research provides results from tests using coupled centrifuge-numerical modelling (CCNM) (Idinyang et al., 2018), which will be discussed in Chapter 4.3.2. This hybrid test method combines physical and numerical modelling in order to achieve an accurate simulation of the TPSI problem.

The third section reviewed the use of protective structures to reduce ground movements due to tunnelling. In practice, pile walls have been used to protect buildings from tunnelling-induced damage. Bilotta (2008) conducted a series of centrifuge tests to investigate the effectiveness of diaphragm walls to reduce tunnelling-induced ground movement in clay, where the length, location, thickness and roughness of the wall was varied. However, for centrifuge tests, the use of protective walls to protect buildings from tunnelling-induced ground movements are limited. For this research, protective walls were used with different embedded depths to investigate the effectiveness of the protective walls in protecting piled structures from tunnelling-induced damage.

Chapter 3

Review of centrifuge modelling technique

In this chapter , the current technical centrifuge technology and centrifuge modelling technique in relation to model tunnels and piles are discussed. For the centrifuge tests carried out in this research, the Fibre Bragg Grating (FBG) technique was used to measure the axial force of piles and bending moment of model walls, therefore the basic principle of FBG is presented.

3.1 Geotechnical centrifuge technology

Engineering application always involves complex soil behaviour as well as the interaction with structures, protective walls, tunnels and piles. Field measurement and monitoring or so-called site-based research is critical for these cases. However, the number of projects available for site-based research are limited, and the cost associated with them are generally high, and the site conditions are also hard to control. As a result, testing scaled models under a controlled environment, which could replicate the real soil stress condition, is generally accepted by the researchers. Geotechnical centrifuge testing allows a scaled soil model to be tested under an elevated gravity to reproduce the full-scale prototype soil stress condition. Once the model is accelerated in the geotechnical centrifuge, gravity (g) is increased from normal gravity to N times gravity (Ng), and the size of the soil model can be N times smaller than the prototype. For this research, the University of Nottingham Centre for Geomechanics (NCG) 2m radius, 50 g-tonne geotechnical centrifuge described by Ellis et al. (2006) was used.

3.1.1 Scaling concepts

To increase the gravity from normal gravity ($1g$) to N times (Ng), the soil model in the geotechnical centrifuge has to spin to a certain angular velocity (ω), where N can be calculated as:

$$N = \omega^2 R_e / g \tag{3.1}$$

where R_e is the effective centrifuge radius and g =9.81 ms^{-2}. Taylor (1994) summarised the typical parameters considered in centrifuge tests associated with the scaling law used, see Table 3.1.

TABLE 3.1: Centrifuge scaling laws by Taylor (1994)

Parameter	Metric unit	Scaling law (model/prototype)
Gravity	m/s^2	N
Length	m	$1/N$
Area	m^2	$1/N^2$
Volume	m^3	$1/N^3$
Force	N = kg m/s^2	$1/N^2$
Density	kg/m^3	1
Unit weight	N/s^3	N
Stress	Pa=N/m^2	1
Strain	-	1
Bending stiffness, EI	Nm^2	$1/N^4$
Axial stiffness, EA	N	$1/N^2$

During centrifuge spinning, the soil model experiences a non-linear variation of stress profile, which is caused by the variation of the distance between soil depth and the centrifuge rotation axis centre. Taylor (1994) suggested that to minimise the errors, the effective centrifuge radius R_e can be expressed as:

$$R_e = R_t + (h_m/3) \tag{3.2}$$

where R_t is the distance between the soil surface to the centre of the centrifuge rotation axis, and h_m is the height of the soil model. As a result, for the soil with a density of ρ , the model scale vertical soil stress (σ_{vm}) at depth (z) can be calculated as (Taylor, 1994):

$$\sigma_{vm} = \rho\omega^2 z(R_t + z/2) \tag{3.3}$$

The equivalent vertical stress at prototype scale is:

$$\sigma_{vp} = \rho N g z \tag{3.4}$$

3.1.2 Scaling effects

As suggested by Kutter et al. (1994), for centrifuge model tests, it is important to use the same material as in prototype (full scale), as it will keep the same soil properties such as strength and modulus. However, by applying the scaling laws from Table 3.1, the equivalent size of the soil particles in the prototype will be N times bigger than the centrifuge model. As a result, when considering soil and structure interaction problems, the relative size of the model structures to the average particle size of the soil will affect the behaviour of soil in model scale. In order to ensure that the soil behaves in a similar manner close to that of the prototype, Taylor (1994) suggested that a suitable value of relative size between model structures and average soil particle size should be used, which also depends on the structure type.

Kutter et al. (1994) conducted a series of centrifuge tests to investigate the collapse of uniform sand into spherical cavities, which were created by the underground nuclear tests in the prototype scale. These experiments as suggested by Marshall (2009) are significance to the scenario of tunnelling in the sand under centrifuge environment. From the tests, Kutter et al. (1994) indicated that a linear relation between normalised volume (V_{cr}/V_{ci}) (volume loss the crater created V_{cr} divided by the volume loss the cavity V_{ci}) is related to the ratio of diameter of the cavity (D_{ci}) to the average size of the soil particle (D_{50}) under a semi-logarithmic plot. Due to the dilation of sand, the normalised volume loss will be close to 1, and the linear relation for $30 < D_{ci}/D_{50} < 350$ will not be validated with the additional increase in D_{ci}/D_{50} value. Marshall (2009) suggested for analysis of collapse condition, D_{ci}/D_{50} value should be greater than 500, but for study of the pre-collapse condition, the value of D_{ci}/D_{50} can be lower. For the tests conducted in this research, the $D_{ci}/D_{50} = 643$

The effect of cone diameter (B) to the average grain size (D_{50}) was studied by Bolton et al. (1993) using miniature cone penetration test (CPT) probes in centrifuge model on Leighton Buzzard sand. The miniature CPT tests are closely related to the centrifuge pile jacking tests. Bolton et al. (1993) pointed out that cone tests in the sand could produce an unbiased result if the B/D_{50} value is higher then 20, in general. For the tests conducted in this research, the B/D_{50} is 642.

3.1.3 Boundary effect

Bolton et al. (1999) conducted a series of centrifuge cone penetration tests in the sand, to investigate the side boundary effect in a rectangular container. The tests were performed in a 1200 mm × 800 mm rectangular box. The normalised distance S/B (between the side of the wall to the location of the cone S, normalised by the diameter of the cone B) varies from 33 to 2, and the results are shown in Figure 3.1. Based on the results, it is believed that once the S/B value is greater than 10, the side boundary effect should have minimal effect on the cone resistance. For the centrifuge tests conducted in this research, the minimum S/B value is 6.8, hence the results are slightly overpredicted, however conclusions made from this research are mainly based on relative results from one test to another, where the boundary condition is consistent. Hence on relative terms, the outcomes are valid and less affected by boundary effects.

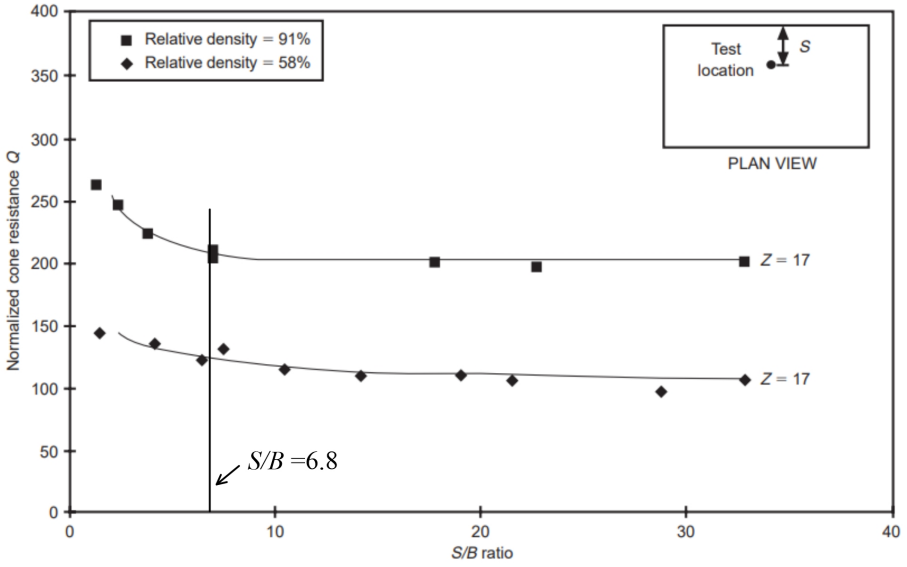


FIGURE 3.1: The effect of side boundary given by Bolton et al. (1999)

3.2 Centrifuge modelling technology

Over the past 20 years, centrifuge modelling techniques have been developed significantly. In this section, centrifuge modelling technique developments related to tunnelling, piles and walls are reviewed. In addition, the basic FBG principle for strain measurement is introduced.

3.2.1 Modelling of tunnel volume loss

The early techniques used to simulate tunnel volume loss in centrifuge tests is by decreasing the internal pressure of a tunnel-shaped airbag (Atkinson et al., 1975). The limitation of the pressurised airbag is that the air is compressible, which makes it difficult to measure the magnitude of the tunnel volume loss. As a result, Loganathan et al. (2000) used silicone oil inside the model tunnel, which can be assumed incompressible within the pressure range applied. The model tunnel used by Loganathan et al. (2000) has an inner core made out of aluminium, a 0.5 mm thick 50 mm diameter membrane is placed outside the aluminium core. To enhance the tunnel stiffness and ensure a uniform tunnel volume loss across the length of the mode tunnel, a 0.5 mm thick PVC spring was used to cover the cylindrical membrane face, and Figure 3.2 shows the model tunnel layout. The tunnel volume loss was controlled by a syringe pump, which was driven by a Maxon 70W DC motor. The DC motor has a built-in digital encoder, which can achieve displacement control. The displacement of the syringe pump was calibrated against the encoder count numbers to ensure consistent tunnel volume loss.

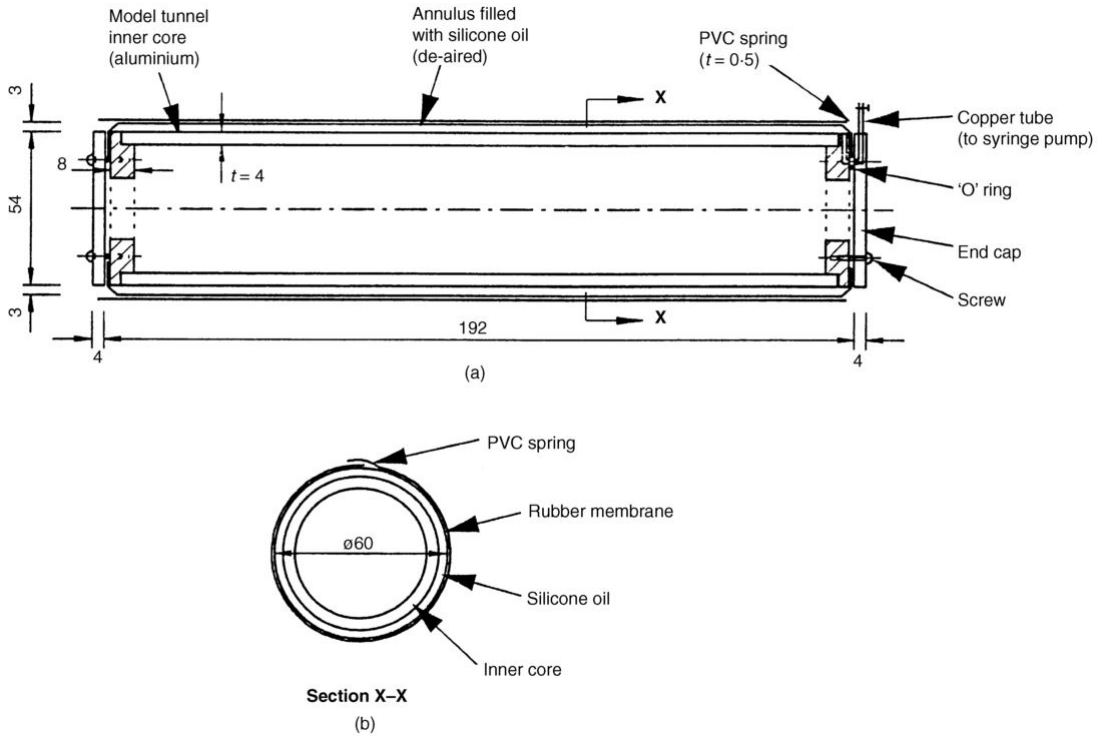


FIGURE 3.2: Details of the model tunnel used by Bolton et al. (1999)

A similar tunnel volume loss model technique was used by Jacobsz (2003), Vorster (2006) and Marshall (2009), but the PVC spring was not used. In order to encourage a more realistic tunnel volume loss shape, the model tunnel used by Marshall (2009) consists of an eccentric shape inner core, where the soil displacements at the tunnel invert are limited. The detailed layout of the model tunnel used by Marshall (2009) is shown

in Figure 3.3. The eccentric shape model tunnel has been used by several researchers (Farrell, 2010, Franza, 2016, Ritter et al., 2017, Williamson, 2014, Zhou, 2015).

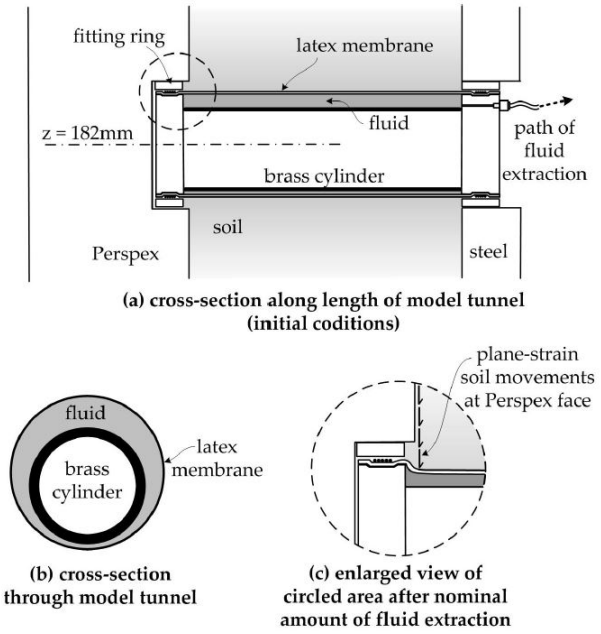


FIGURE 3.3: Details of the model tunnel used by Marshall (2009)

Boonyarak and Ng (2015) developed a so called "donut" tunnel volume loss device, which enables the simulation of tunnel advancement within a centrifuge. Two rubber bags are used to simulate tunnel volume loss and weight losses, which are located outside and inside of the aluminium alloy tube, respectively. Figure 3.4 shows the details of the "donut" for simulating the tunnel volume and weight losses. The outer rubber membrane and the inner rubber bag was filled with heavy fluid ($ZnCl_2$), which has a same density as the sand used in the tests. The tunnel excavation sequence is achieved by gradually draining away the inner and outer heavy fluid in each "donut" subsequently.

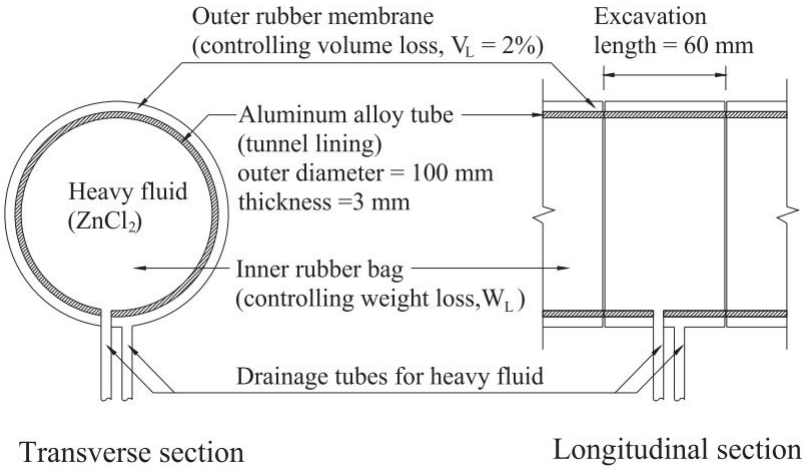


FIGURE 3.4: Details of the model tunnel used by Boonyarak and Ng (2015)

Another option to simulating 2D tunnel volume loss in the transverse plane is the use of a rigid boundary mechanical (RBM) model tunnel. The RBM model tunnel can control the deformed tunnel shape, and the soil displacements around the tunnel lining can be predefined. An RBM model tunnel developed by Katoh et al. (1998) has been used by several researchers to study soil-structure interaction problems (Boonsiri and Takemura, 2015a,b). The RBM model developed by Katoh et al. (1998) consists of a wedge-shaped shaft and six rings. The six rings generated a circular shape and are covered by a steel sleeve and rubber membrane. A screw jack is located at the tunnel centre line, where the wedged shape shaft is connected to allow horizontal movement (inwards and outwards). The screw jack is driven by a speed control motor, where detailed model tunnel configurations are shown in Figure 3.5. The wedge shape shaft has six taper angles, and the six rings are attached to the shaft. When the shaft moves outwards, the six rings will move towards the tunnel centre line uniformly, hence the tunnel volume loss is achieved. This RBM model tunnel imposes concentric uniform displacements around its circumference.

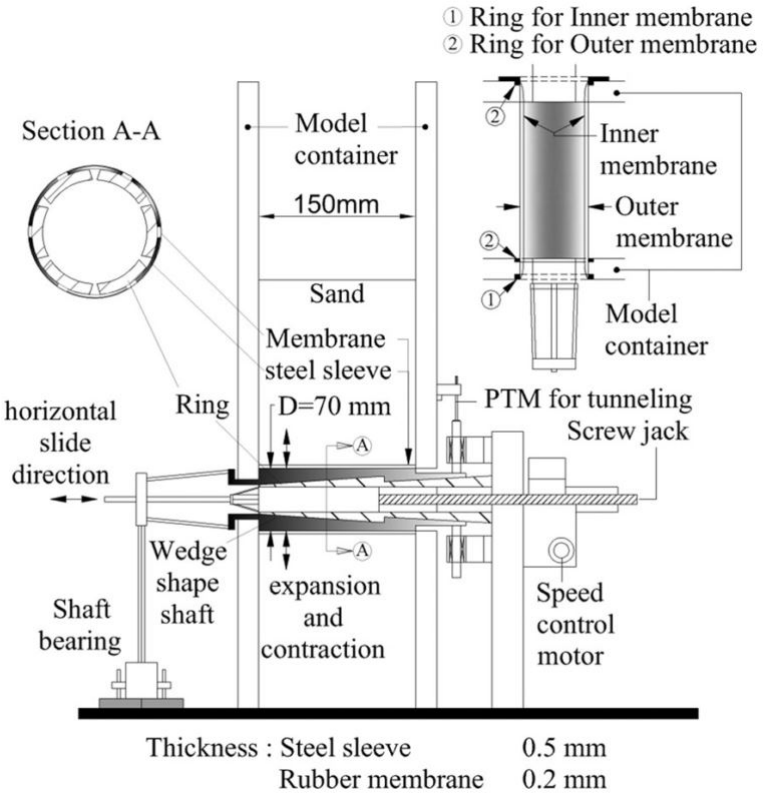


FIGURE 3.5: Details of the model tunnel used by Boonsiri and Takemura (2015b)

3.2.2 Modelling of piles

The model piles used by Loganathan et al. (2000) have an outer diameter of 8 mm and 7.24 mm inner diameter. Strain gauges were placed externally to measure the bending moment and axial force along the pile. The half-bridge strain gauge layout was used to measure the bending moment, where the temperature effect can be compensated, and quarter-bridge was used for axial force measurement. The outer surface of the pile was coated with epoxy, and the final outer diameter of the pile is 9 mm. Figure 3.6 shows the detailed location of the strain gauges in "bending pile" and "axial force pile". The pile did not have the end bearing load measurement, but the axial force measured from the strain gauge located close the pile tip, as suggested by Loganathan et al. (2000), can be considered to have a close approximate to the pile end bearing load.

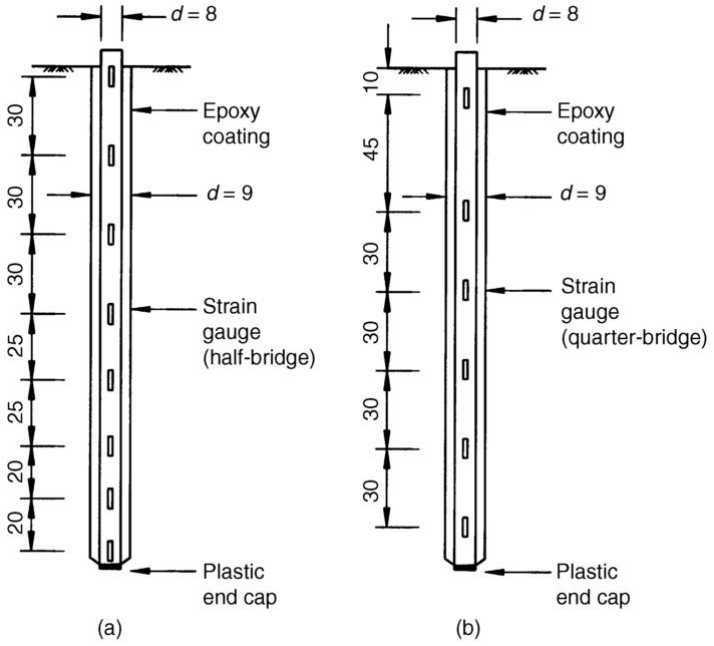


FIGURE 3.6: Model piles used by Loganathan et al. (2000): (a) "bending pile", (b) "axial force pile"

The model piles used by Jacobsz (2003) have a diameter of 12 mm, which were made from aluminium alloy. The wall thickness of the model pile is 0.57 mm, and the pile tip was fitted with a 60° conical shape cap. Axial load cells and radial stress load cells were used to measure the axial force and lateral stress along the pile. The axial load cell was made from a hollow cylinder, which has an internal diameter of 9 mm and 20 mm cover length. The thickness of the wall for strain measurement area was 0.75 mm, and the full bridge strain gauge was placed at the inner surface of the measurable area. The radial stress cell has an "H" structure shape, and the strain gauges were located on both side of the web, which has a thickness of 0.3 mm. The web was orientated vertically during

assembly to avoid the cross-effect caused by pile bending deflection. Figure 3.7 shows the detailed layout of the axial force and radial stress load cell used by Jacobsz (2003).

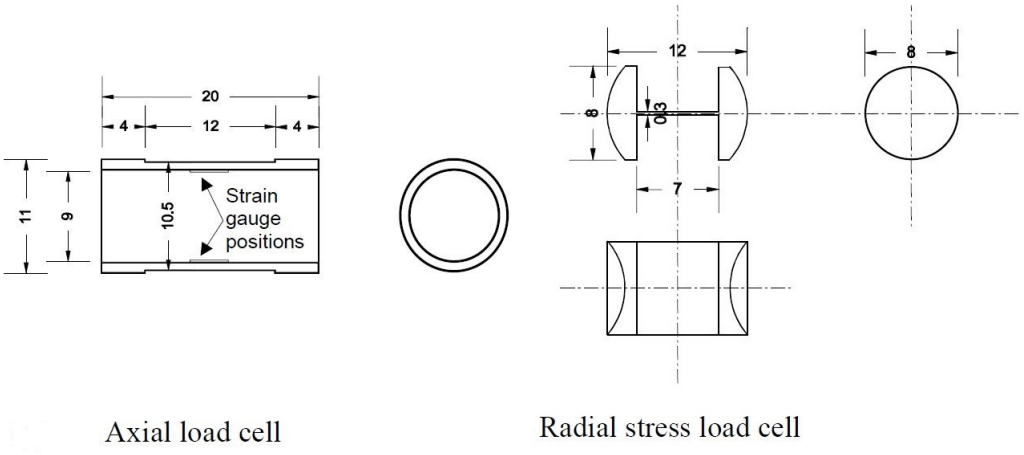


FIGURE 3.7: Axial force and radial stress load cell (Jacobsz, 2003)

The model piles used by Marshall (2009) were made from aluminium alloy, and only half of the pile was represented (split vertically). The piles were placed against the perspex window for PIV analysis. The outer diameter of the pile is 12 mm. Four strain gauges were located at the outer surface of the pile, and the epoxy coating protected the strain gauges. To measure the pile end bearing load, a 45° conical shape cap equipped with a strain gauge was used. Figure 3.8 shows the detail layout of the model pile used by Marshall (2009).

So far, the model piles reviewed were made from aluminium alloy. But some strain gauges may not be capable of measuring the small strain due to tunnelling-induced ground movements. To increase the pile's sensitivity to tunnelling, hollow acrylic piles were used by Boonsiri and Takemura (2015b). The acrylic model piles have a diameter of 10 mm, and the wall thickness is 1 mm. The acrylic material has a large yield strain but is also very flexible. Boonsiri and Takemura (2015b) assumed that the pile deflection due to tunnelling-induced ground movement is under its elastic range. The bending resistance and axial rigidity of the acrylic model pile are less than the conventional aluminium model pile, and Boonsiri and Takemura (2015b) summarised the pile properties in model scale and prototype scale, see Table 3.2.

3.2.3 Principle of FBG sensors

For the centrifuge tests discussed in Chapters 6 and 7, FBG sensors were used to measure the axial force of the pile as well as the bending moment along the protective wall. As indicated by Kersey et al. (1997), that the basic principle of the FBG sensor is to measure

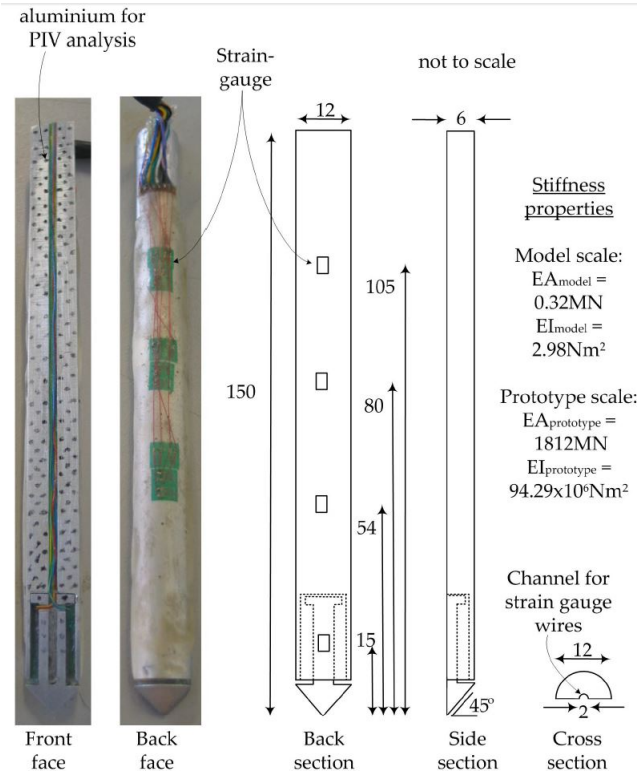


FIGURE 3.8: Model pile used by Marshall (2009)

TABLE 3.2: Pile properties in model scale and prototype scale (Boonsiri and Takemura, 2015b)

Properties	Model	Prototype	Prototype	Prototype
Material	Acrylic pile	Acrylic pile	Concrete pile	Steel pile
Diameter	10 mm	1.0 m	1.0 m	1.05 m
Thickness	1 mm	0.1 m	solid	0.0125 m
Young's Modulus	3.2 GPa	3.2 GPa	20-28 GPa	200 GPa
Bending rigidity	0.93 Nm^2	93 MNm^2	980-1370 MNm^2	1090 MNm^2
Axial rigidity	90 KN	900 MNm^2	16-22$\times 10^3$ MNm^2	8150 MNm^2

the shift in wavelength of the returned "Bragg" due to strain or temperature changes. The Bragg wavelength is defined by Kersey et al. (1997):

$$\lambda_B = 2n\Lambda \tag{3.5}$$

where Λ is the grating pitch and n is the effective index of the core. With a broadband wavelength injected to the fibre, a specific narrow band spectrum is reflected by the grating, and the transmitted light will be missing the spectral component, as illustrated in Figure 3.9.

As suggested by Moyo et al. (2005), the value of n and Λ is affected by the physical

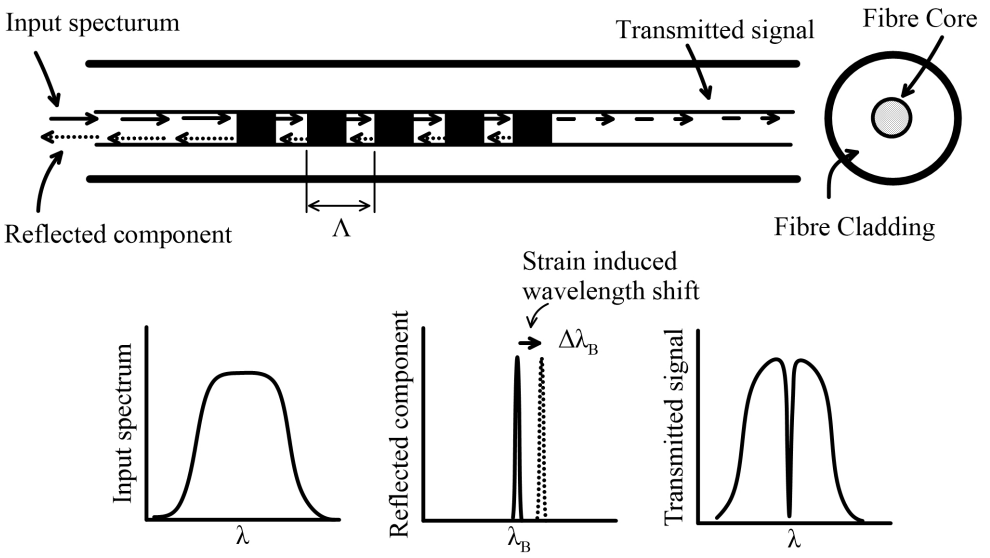


FIGURE 3.9: Basic Bragg grating process based on Kersey et al. (1997)

elongation of the sensor (strain ε), temperature (T) and pressure applied to the sensor (P). The amount of Bragg wavelength shift as given by Kersey et al. (1997) can be calculated as follows:

$$\Delta\lambda_B = K_\varepsilon \varepsilon + K_T \Delta T + K_P P \tag{3.6}$$

where K_ε, K_T and K_P are the coefficients of the wavelength sensitivity to strain (ε), temperature (T) and pressure applied to the sensor (P). Detailed FBG application will be discussed in the next chapter.

3.3 Summary of the chapter

In this chapter, the first section reviewed geotechnical centrifuge technology in relation to scaling concepts, scaling effects and boundary effects. The second section reviewed the centrifuge technique in modelling tunnel volume loss and piles. As discussed previously, the flexible membrane (FM) model tunnel has been widely used in the centrifuge to simulate tunnel volume loss. The displacements around real tunnels have been shown to take an eccentric shape, with greater displacement occurring at the tunnel crown compared to the invert (Loganathan and Poulos, 1998). In order to encourage a more realistic profile of displacement, Marshall (2009) modified the FM model tunnel to create an eccentric shape, where soil displacement at the invert of the tunnel was limited. This eccentric FM model tunnel has been applied in several subsequent centrifuge studies

related to tunnelling (Farrell, 2010, Franza, 2016, Ritter et al., 2017, Williamson, 2014, Zhou, 2015). Rigid boundary mechanical (RBM) model tunnels have also been used to study the soil-structure interaction problems (Boonsiri and Takemura, 2015b). However, the RBM model tunnel developed by Katoh et al. (1998) imposes concentric, uniform displacements around its circumference. For this research, an RBM model tunnel was developed that is able to induce an eccentric profile of ground displacements around the tunnel, predominately near the crown. In addition, the third section reviewed the centrifuge technique in modelling piles, most of the piles were modelled by aluminium tubes, and conventional strain gauges were used to measure the axial force and bending moment profile along the piles. Some of the drawbacks using conventional strain gauges are that: 1) they are often large in size, and could interference the model pile interface, 2) there may be signal interference with each other, 3) lead wires could generate a large bundle of wires, which could have a great influence on the model piles under elevated gravity. For this research, optical fibre Bragg grating (FBG) sensors were used to measure the axial force along the piles; it is believed that this research represents one of the first applications of FBG sensors in a geotechnical centrifuge. As a result, the basic principle of FBG sensors was briefly discussed in this chapter.

Chapter 4

Experimental methods, equipment, and testing configurations

4.1 Introduction

This chapter provides the detailed development of the centrifuge testing facilities for tunnelling, piled structures and protective walls as well as the numerical modelling procedures using hypoplasticity constitutive model. In general, this thesis involves three main centrifuge test packages: (1) greenfield tunnelling in sand, (2) effects of tunnelling on piled structures and (3) the use of protective walls to protect buildings from tunnelling-induced damage.

As a result, this chapter is structured based on the above three packages. For package 1, the use of a newly developed eccentric rigid boundary mechanical (eRBM) model tunnel is presented, and the associated displacements measurement and experimental methods are discussed. Finite element analysis is used in this package to simulate greenfield tunnelling, where the mesh, boundary conditions and constitutive model parameters are discussed. For package 2, the application of the FBG (fibre Bragg grating) sensors in the model piles are presented, and the newly developed pile loading system is introduced. Detailed experimental methods and testing procedures are then provided subsequently. Finally, in package 3, the use of protective walls and the associated testing methods and instrumentation are discussed.

4.2 Greenfield tunnelling in sand

A newly developed eccentric rigid boundary mechanical (eRBM) model tunnel was used with three different tunnel depths (C/D ratio) to investigate the tunnelling-induced soil displacements field. In addition, tested results using flexible membrane (FM) model tunnels from various sources in the literature are compared against the eRBM model tunnel data to study the effect of tunnel boundary (flexible or rigid boundary) on soil displacements shape.

To obtain a better understanding of the relationship between soil movements and tunnel boundary conditions (i.e. displacement or pressure controlled), a series of two-dimensional numerical analyses was performed to simulate eccentric displacement control (EDC), concentric displacement control (CDC), and flexible membrane (FM) model tunnels, all under three different C/D ratios. The ABAQUS (Hibbitt, 2002) finite element (FE) software was used. The hypoplastic constitutive model developed by Gudehus and Mašín (2009), which can describe the non-linear behaviour of the granular materials, was adopted. Results from numerical analyses are compared against centrifuge tests data. In the centrifuge tests, g-level is not constant throughout the depth of the soil; however, in the numerical analyses, it was assumed that g-level is constant.

4.2.1 Experimental programme

Three centrifuge tests were carried out on the University of Nottingham Centre for Geomechanics (NCG) 2 m radius, 50 g-tonne geotechnical centrifuge. All the centrifuge tests reported in this section were tested at a centrifugal acceleration of 80g.

Figure 4.1 shows the centrifuge package for greenfield tunnelling, which includes centrifuge strong box, the soil, newly developed eRBM model tunnel and displacement measurement devices. Table 4.1 summarises key features of the centrifuge tests for greenfield tunnelling.

TABLE 4.1: Summary of the centrifuge tests performed at 80 g for greenfield tunnelling

Test label	Cover depth C (mm)	Diameter of the tunnel D (mm)	Relative density of the soil I_d
GF1	117	90	$\approx 90\%$
GF2	180	90	$\approx 90\%$
GF3	216	90	$\approx 90\%$

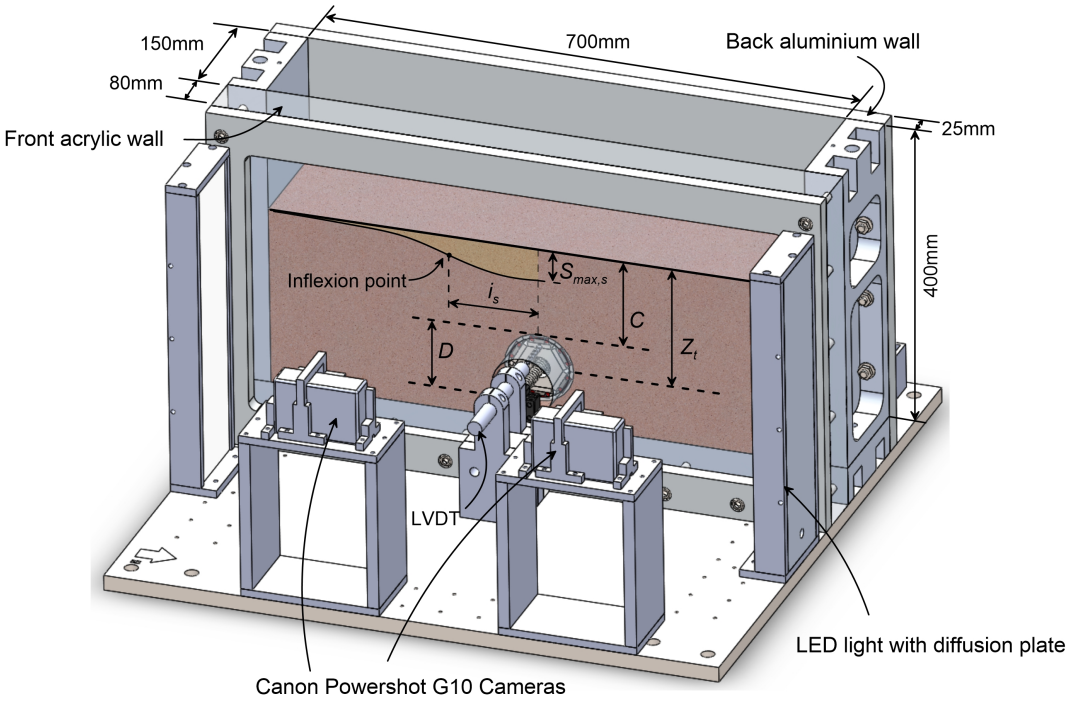


FIGURE 4.1: Strong box for greenfield tunnelling

The model tunnel has a diameter of 90 mm and is located 75 mm above the strong box base, giving a clear distance of 30 mm between the bottom of the tunnel and the strong box base. Zhou et al. (2014) conducted similar centrifuge tests, and suggested that the soil movement below the tunnel invert is minimum, therefore it is believed that 30 mm clear distance between the tunnel invert and the strongbox base can isolate the boundary effect. The centrifuge strong box was designed to allow the measurement of sub-surface soil displacements using an image analysis technique; a transparent front acrylic wall was located at the front of the box. The model strong box has an inner width × height dimensions of 700 mm × 400 mm and is 150 mm wide. The thickness of the acrylic wall and back aluminium wall was calculated to make sure that the average lateral displacement caused by the static lateral earth pressure (K_0=0.5 assumed) under 80g is less than 0.1% of the soil model height as suggested by Taylor (1994).

4.2.2 Simulation of tunnel volume loss

Figure 4.2 illustrates the newly developed eccentric RBM model tunnel. The eccentric tunnel volume loss shape is achieved by controlling six segments that move towards the tunnel centre line at different radial displacements; a maximum displacement of 1.4 mm at the tunnel crown, 0.9 mm at the spring line, and zero displacements at the tunnel invert can be reached. In practice, the use of a tunnel boring machine (TBM) or earth pressure balance machine (EPBM) can achieve a tunnel volume loss around $0.5 - 1\%$,

the model tunnel described in this thesis will cover the volume loss range to a extreme cases with a maximum tunnel volume loss of approximately 3.5%.

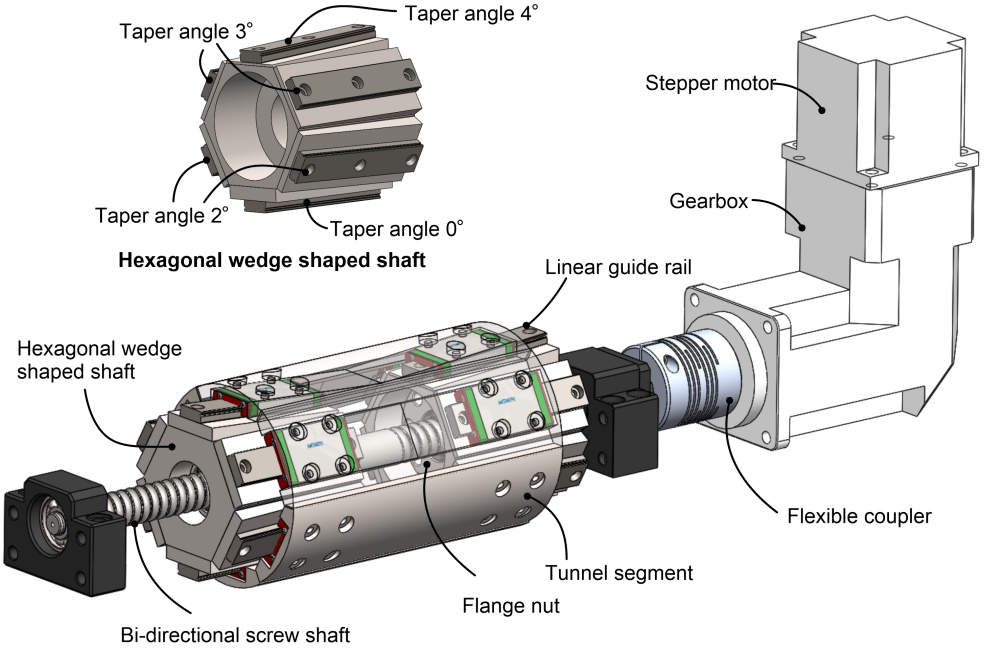


FIGURE 4.2: Eccentric rigid boundary mechanical model tunnel

A single bi-directional screw shaft is placed at the tunnel centre line, fixed by two ball screw supports located on either side (front and back) of the strong box. Two flange nuts are secured on the screw shaft in opposite directions. Each flange nut is connected with a hexagonal wedge-shaped shaft (see Figure 4.3). The hexagonal wedge-shaped shaft consists of six faces with different taper angles, which are varied from 4° at the tunnel crown to 0° at the tunnel invert. Six arch-shaped tunnel segments are connected to the two opposing hexagonal wedge-shaped shafts via two linear guide rails to generate the tunnel circumference. Each segment is equipped with two linear carriages, secured to the opposing wedge-shaped shafts. The linear guide rail with linear carriage enables the relative movement between the six segments and the two shafts along the taper angle. A stepper motor linked with a 10:1 ratio gearbox drives the screw shaft via a flexible coupler, which permits some degree of misalignment between the screw and gearbox shafts. Tunnel volume loss is achieved by rotating the bi-directional screw shaft, causing the two hexagonal wedge-shaped shafts to move apart from each other, and the six segments to move towards the tunnel centre line. Due to the differences in taper angle, the non-uniform tunnel boundary displacement profile is formed.

Figure 4.3 shows the positions of the six tunnel segments before and after tunnel volume loss. Tunnel volume loss is calculated by measuring the radial displacement of each segment, which is related to the horizontal displacement of the wedge-shaped shafts and the taper angle (radial displacement=horizontal displacement $\times$ tan(taper angle)). The

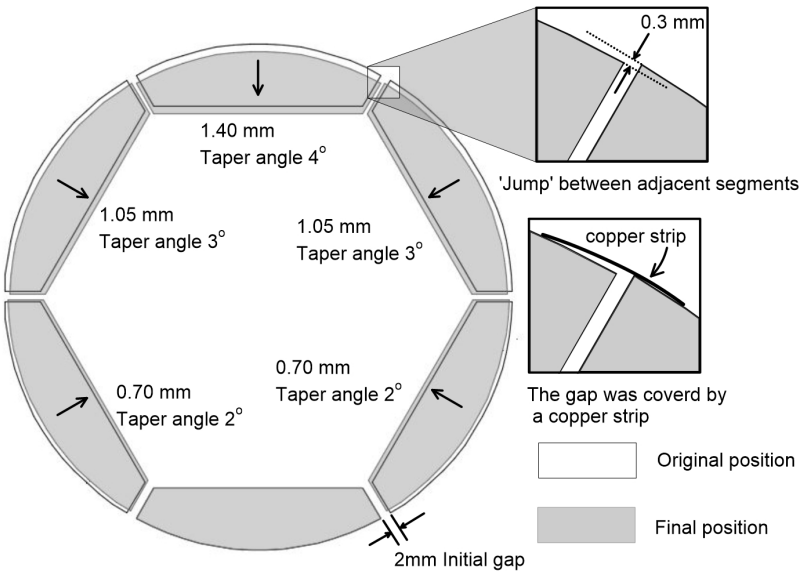


FIGURE 4.3: Eccentric rigid boundary mechanical model tunnel deformed shape

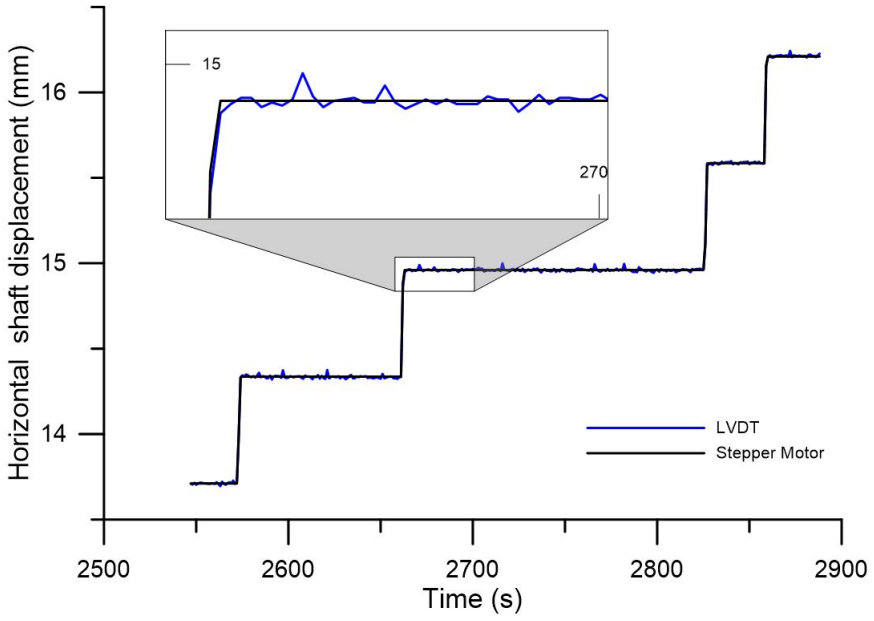


FIGURE 4.4: Cross check the tunnel volume loss measurement

displacement of the wedge-shaped shaft can be estimated from the number of signals sent to the stepper motor (i.e. rotation of screw shaft). During each volume loss stage (equivalent to 0.18% of tunnel volume loss), the screw shaft (with a 1/8 screw pitch) was rotated by 450°, corresponding to 0.625 mm of horizontal displacement of the wedge-shaped shaft. The displacement of the wedge-shaped shaft was further confirmed using a Linear Variable Differential Transformer (LVDT) mounted in front of the strong box (see Figure 4.1). Figure 4.4 shows the LVDT measurement and stepper motor estimation of wedge-shaped shaft horizontal displacement during several volume loss stages. The stepper motor estimation of displacement is shown to be a close match to the LVDT

readings under the tested conditions. The maximum horizontal displacement of the wedge-shaped shafts is around 20 mm.

A gap is created between adjacent segments that make up the tunnel circumference, as illustrated in Figure 4.3, creating a "jump" between segments during tunnel volume loss. The maximum size of the "jump" (at maximum tunnel volume loss) is around 0.3 mm. The gaps are initially 2 mm (before tunnel volume loss) and vary with volume loss at different rates for the various gaps. Copper strips were placed along the gaps in the direction of the tunnel length to create a smooth tunnel surface, as shown in Figure 4.3. The tunnel was then sealed within two latex membranes to protect it from soil intrusion during tests; this also ensured a smooth variation of soil deformation was achieved across the gaps.

4.2.3 Measuring displacements

For the greenfield tunnelling study, the soil displacements were measured via digital image analysis; two Canon Powershot G10 Cameras were placed at the front of the strong box (see Figure 4.1). Images were taken through the front acrylic wall during every tunnel volume loss increments. A remote camera control software (PSRemote©) was used to make sure the images taken from the two cameras were synchronised. GeoPIV-RG (Stanier et al., 2015) was used to process the images taken by the cameras. The basic principle of the GeoPIV-RG can be briefly summarised in the following two steps: (1) calculate the displacement of the seed subset in pixel space, (2) then convert/calibrate the subset pixel space displacement into objective space. As a result, the precision of the geoPIV-RG measurement depends on the stated two steps, which are the accuracy of soil displacement calculated in pixel space ("tracking"), and the accuracy of transferring pixel space soil displacement into objective space ("translation").

For the first step ("tracking"), the accuracy is affected by the subset size, lighting condition and the distance between the camera and the soil. Under the centrifuge environment, the lighting condition and camera distance are fixed; the only factor that could affect the "tracking" accuracy is the size of the subset. To assess the accuracy, two images were taken under the centrifuge environment (same lighting condition and camera distance) with zero soil displacement, and the "tracking" standard error can be calculated by assessing by the displacements data (in both vertical and horizontal directions) calculated by the GeoPIV-RG. In total, 172 subsets were used to calculate the standard error, and Figure 4.5 shows the standard error with subset size in both vertical and horizontal directions. With the increase in subset size, the standard error for "tracking" reduced, suggesting that a larger subset size could perform a better "tracking" results,

but for practical reason, the subset size of 100 pixels was used. A relatively large subset size (140 pixels) could cause low soil displacement field resolution.

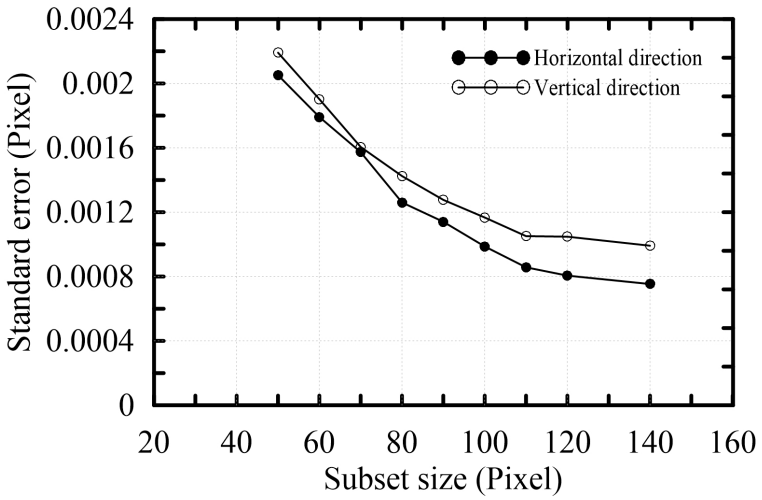


FIGURE 4.5: Standard error for tracking with subset size in pixel space

For the second step, the translation of soil displacements ("tracking" result) from pixel space into objective space was facilitated by the control markers, which were hand painted at the inner face of the front acrylic wall. As a result, the accuracy of the objective space coordinate from each control marker will affect the performance of the soil displacement translation (from pixel space to objective space). Therefore, the photogrammetric calibration process described by Marshall (2009) and Zhou (2015) was used to determine the objective space coordinates of the control markers. The basic idea of this photogrammetric calibration ("calibration") is by using a photogrammetric grid with known objective space coordinates to calculate the object space coordinates for each hand painted control markers. One of the challenges when performing the "calibration" is that the photogrammetric target panel is smaller than the area of the control markers (photogrammetric target panel cannot cover the entire control markers), which means the calibration cannot be processed within a single image. This issue leads to a multiple steps image calibration process, which requires taking multiple images that contain two overlapping control markers in each image and then "stitching" the reference point coordinates together. For every two images contain the same overlapping control markers, the relative coordinate of the reference points in the second image can be related to the position of the control markers in the first image. In these tests, Solidworks was used to "for stitching" the particular reference point coordinates into a single global axis. Figure 4.6 shows the procedure of "stitching" in a schematic diagram. The local objective space coordinates of the control points in every image were replicated into SolidWorks and stored as a "plate", and the stored 'plates' were combined via two overlapping control markers afterwards. Eventually, the combined global coordinate was developed.

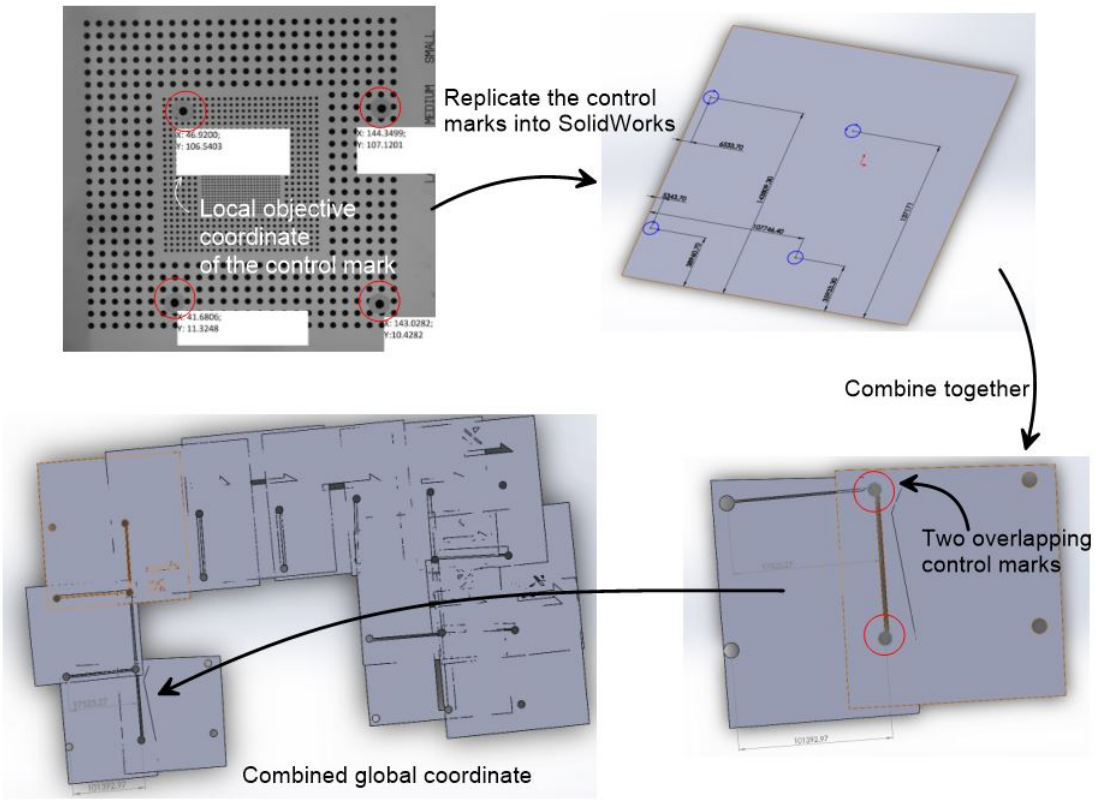


FIGURE 4.6: 'stitch' process using Solidworks

Marshall (2009) pointed out that a small amount of error is introduced in the global coordinate after this "stitching" process. This is due to the two overlapping control markers' relative position calculated based on the two adjacent images are not identical, which leads to an error when "stitching" them together. The error as suggested by Marshall (2009) can be defined using the following equation:

$$\varepsilon = X_{CP_i,image_i} - X_{CP_{i+1},image_{i+1}} \tag{4.1}$$

The error calculated from the Equation 4.1 only considered the horizontal direction. As a result, the error ε can be further modified to consider both directions (vertical and horizontal):

$$\varepsilon = \sqrt{(X_{CP_i,image_i} - X_{CP_{i+1},image_{i+1}})^2 + (Y_{CP_i,image_i} - Y_{CP_{i+1},image_{i+1}})^2} \tag{4.2}$$

Based on Equation 4.2, the maximum error is 0.026 mm, and the average error is 0.012 mm (for the process described above). It is noted that such error ε does not imply the error to translate the soil displacements from pixel space into objective space ('translation'). To reduce the error ε, a larger photogrammetric grid panel can be used,

which means less "stitching" process. In section 4.4.4, an A3 size printed photogrammetric target panel is used to perform photogrammetric grid calibration, and the results will be discussed in Section 4.4.4.

To assess the precision of the geoPIV-RG, two images were taken under centrifuge environment with zero soil displacement. For the analysis, 11844 subset patches were used, and the displacement (in the horizontal and vertical directions) for each patch was calculated. Figure 4.7 shows the histograms of the geoPIV-RG calculated soil displacements in both horizontal and vertical directions. The horizontal displacements data provided a standard division of 4.6 μm, and vertical displacements provided a slightly higher standard division value of 6.4 μm. This level of precision is similar to that reported by Marshall and Mair (2011), who examined GeoPIV (White et al., 2003) precision by analysing seven images taken at elevated gravity when the soil displacement was not expected (small vertical soil settlements are expected due to consolidation).

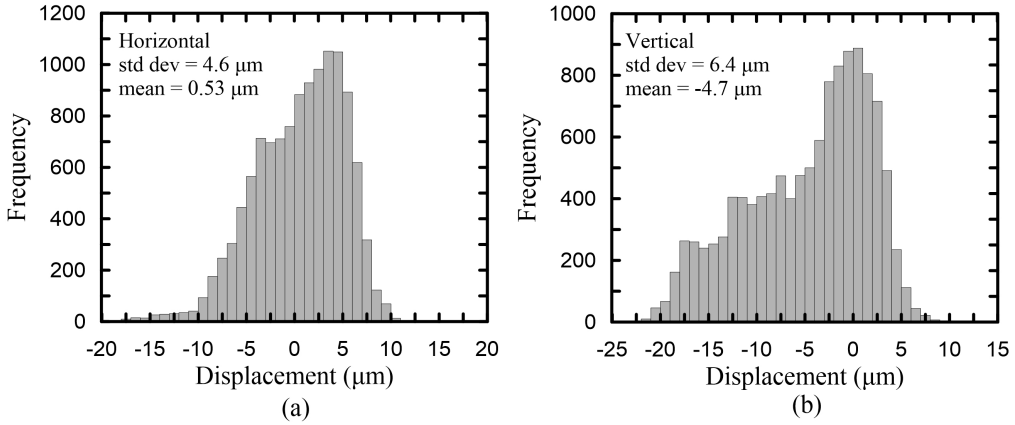


FIGURE 4.7: Histograms of displacement errors on (a) horizontal displacement and (b) vertical displacement

4.2.4 Testing material and model preparations

Fine-Grained silica sand commonly knows as Leighton Buzzard Fraction E sand was used for the tests, which has a typical average diameter of D_{50} of 0.14 mm and specific gravity G_s of 2.65. The sand has a maximum (e_{max}) and minimum (e_{min}) void ratio of 1.01 and 0.61, respectively, a coefficient of uniformity C_u of 1.58, and a critical state friction angle ϕ_c of 33°. The relative density of the sand used for all the tests conducted in this study is $I_d = 90\%$, which is equal to approximately 1603 kg/m^3.

Samples were prepared by using the dry sand pouring technique in order to permit comparision with the work of previous researchers who had used the same method (Vorster 2006; Marshall 2009; Zhou 2015; Franza 2016; Farrell 2010). The tunnel was secured within the strong box prior to sand pouring. To achieve a uniform sample around the

model tunnel, the strong box was placed with the back wall facing downwards, allowing the sand to be poured in the direction of the tunnel longitudinal axis, consistent with the work of the earlier researchers. The sand was prepared according to a methodology calibrated to achieve a relative density (I_d) of 90%. After sand pouring, a thin layer of dyed sand was placed uniformly on the top surface of the sample to increase the contrast and to help the GeoPIV-RG tracking of soil displacements. The front acrylic window was then bolted to the strong box, which was then rotated to its upright position. The gearbox and stepper motor were then assembled, and the LVDT was placed at the front acrylic window to measure the movement of one of the wedge-shaped shafts.

4.2.5 Testing procedures

The centrifuge package was spun to 80 g in stages of 10 g. Three stabilisation cycles were then performed for each tests, whereby the model was spun from 80 g to 10 g and then back up to 80 g. By measuring the displacement at the ground surface during the stabilisation cycles, it was found that for the type of soil used in these tests, three cycles were sufficient to obtain a consistent measurement of surface displacement from 10-80 g. The stabilisation cycles helped the sand to achieve consistency between the tests by reducing localised high-stress zones ("hung-up" particles), thereby achieving a more uniformly stressed soil. After three stabilisation cycles, the tunnel volume loss and image acquisition procedures were started.

4.3 The effects of tunnelling on piled structures

In general, the complex non-linear soil and soil-pile interaction behaviour is modelled within the centrifuge. However, for a structure, traditional simulation requires some degree of simplification. For example, piled structures are modelled by rigidly connected beams, or a constant load was applied to the pile groups to replicate the self-weight of the superstructure. Such an approach could under- or over- estimate the structure stiffness. Therefore, the associated pile responses during tunnel volume loss are not correctly modelled. To overcome these limitations, Idinyang et al. (2018) developed coupled centrifuge-numerical modelling (CCNM) method that the numerical model is used to solve the structural domain, and the complex non-linear soil and soil-pile interaction behaviour is modelled within the centrifuge domain.

In this section, a newly developed CCNM system is presented, and the FBG sensors are applied to measure the axial force along the piles. The subsequent sections introduced the newly developed CCNM system in detail as well as the application of FBG

sensors within the centrifuge to measure model pile axial force. Detailed experimental procedures and testing methods are explained.

4.3.1 Experimental programme

Figure 4.8 shows the layout of the testing geometry and configurations. Four centrifuge tests were conducted, and the key features are listed in Table 4.2 as: (1) pile loading test (Test PL), (2) Constant load pile group test (Test CL), (3) pile group with the consideration of structure stiffness and an ultimate tunnel volume loss of $V_{l,t}$=2.2 % (Test CCNM1), (4) pile group with the consideration of structure stiffness and an ultimate tunnel volume loss of $V_{l,t}$=3.2 % (Test CCNM2, test CCNM1 was stopped early because of mechanical issues with the tunnel, hence repeated by test CCNM2).

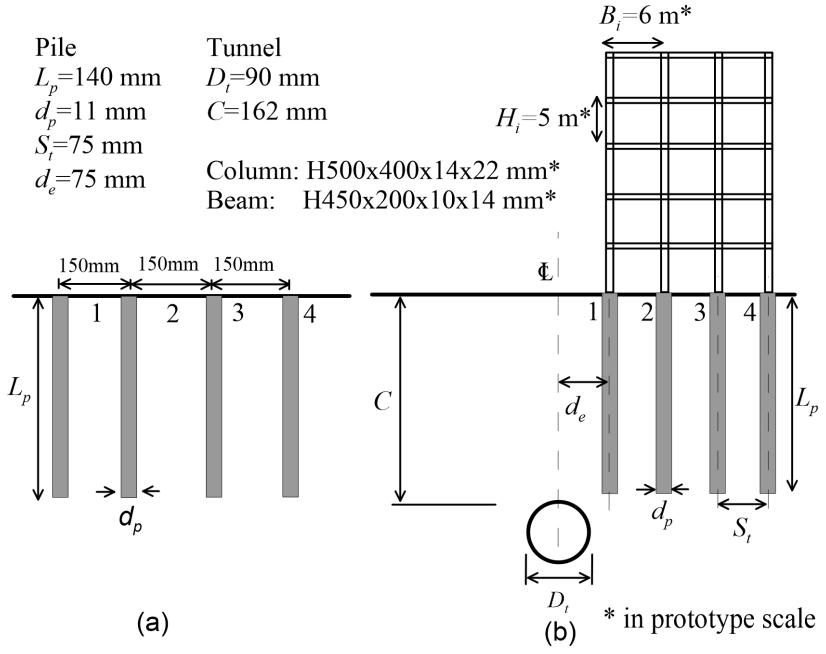


FIGURE 4.8: Test layout in model scale : (a) Pile jacking tests, and (b) tunnelling next to piled frame

4.3.2 Coupled centrifuge-numerical modelling (CCNM)

The CCNM system was originally developed by Franza et al. (2016). The CCNM simulation process for a framed building with a pile foundation is illustrated in Figure 4.9. In general, tunnel, soil and piles are simulated in the geotechnical domain, and the framed building is simulated in the structural domain (numerical model). The real-time interface developed by Idinyang et al. (2018) is used to share the pile load (P_i) and displacement (v_i) between the two domains; the subscripts denote the row of the pile. The CCNM modelling process can be summarised as follows: (1) In the centrifuge, the

TABLE 4.2: Summary of the centrifuge tests performed at 80 g

Test label	Final tunnel volume loss $V_{l,t}$	Structure stiffness †	Note‡
PJ	NA	NA	PJ
CL	3.2%	CL	TPGI
CCNM1	2.2%	F	TPSI
CCNM2	3.2%	F	TPSI

† CL=constant load, F=structure with full stiffness
‡ PJ=Pile jacking, TPGI=tunnel-pile group interaction, TPSI=tunnel-pile-structure interaction

initial pile head load (P_i) for each pile is applied by the actuator, which is determined by the structure's self-weight. One increment of tunnel volume loss $\Delta V_{l,t}$ is achieved using the eRBM model tunnel. (2) The associated ground movements due to tunnel volume loss cause the settlement of the piles (v_i). (3) The pile displacements data (v_i) are sent to the numerical model through the real-time interface. (4) Based on the pile displacements data v_i, the numerical model calculates the modified pile head loads (P_i'). (5) The modified loads P_i' are then fed back into the centrifuge model through the real-time interface, and the pile head loads are adjusted to the modified values using the actuators (discussed in the next section). This process continues to cycle (process 2-5) until a steady state is reached. The steady state can be determined by where the ΔP is less than a certain value ($\Delta P = P_i' - P_i$). To ensure the cycling time is minimum, small increments of tunnel volume loss are used. (6) Once the steady state is reached, tunnel volume loss is increased, and the above process is repeated (process 1-6).

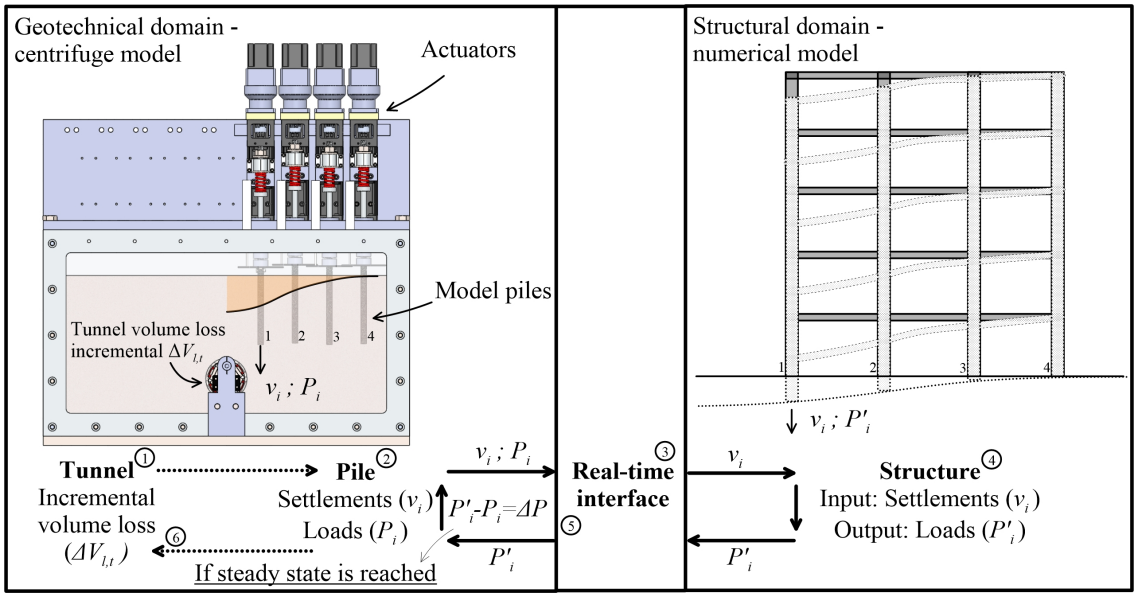


FIGURE 4.9: CCNM simulation process for a framed building with a pile foundation

4.3.3 Pile loading system

The pile loading system is presented in Figure 4.10, which allows individual control of each model pile using linear actuators. The control system was designed under the LabVIEW environment that enables either force or displacement control of the piles. The modular actuator system allows for easy adaptation of specific test configuration. Each model pile is connected to an actuator via a loading shaft with a 5 kN in-line load cell. A die spring (stiffness rate of 219 N/mm) is required between the driving actuator and pile loading shaft to reduce the sensitivity of the load response to movements of the actuator, which was necessary to ensure the control system remains stable (Franza and Marshall, 2018). LVDTs are located at the base of the supporting frame with their armatures resting on a plate fixed to the pile head. The linear actuators have a maximum stroke of 40 mm with a 3 kN axial capacity.

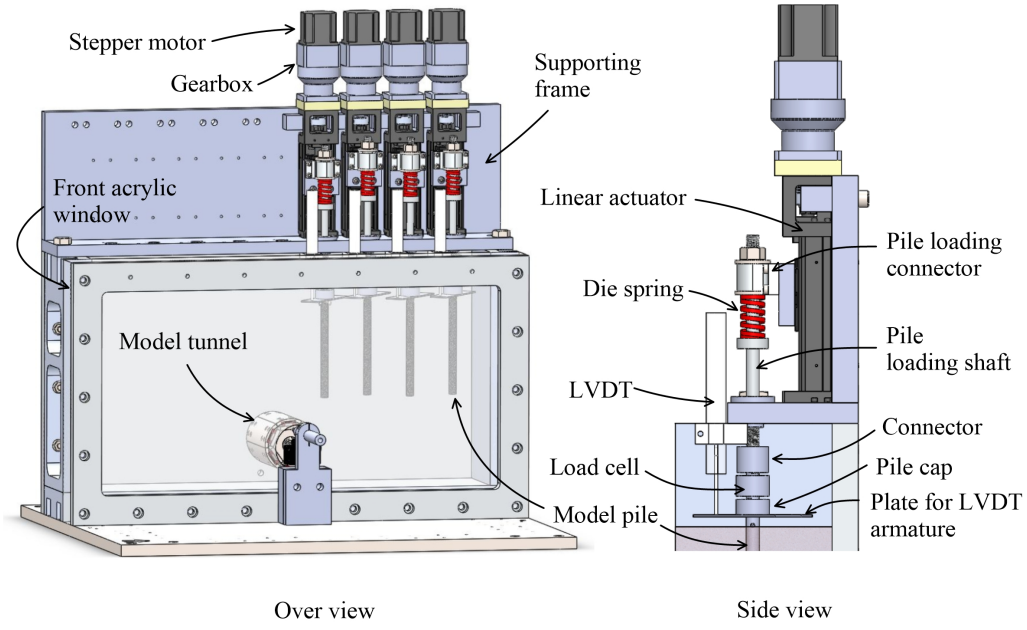


FIGURE 4.10: Pile loading system layout

To evaluate the performance of the pile loading system, a series of load targets were sent to the system to assess the reaction time under centrifuge environment (same model pile and sand density as used for CCNM centrifuge tests). The load control system designed under the LabVIEW environment is based on a Proportional, Integral, Derivative algorithm (PID); to avoid load overshoot, the P value is used only. Figure 4.11 shows the load versus time during load control testing. The target loads were chosen to be similar to the model pile head load during the CCNM centrifuge test. Longer time was required for a greater change in load, for example, 0.6 s was required for a 100 N load change, and 0.05 s was required for a 2 N load change. For tunnelling applications, the

maximum pile head load change in one tunnel volume loss increment ($V_{l,t} \approx 0.1\%$) is around 2.3 N; therefore, the pile loading system reaction time is between 0.05-0.1 s.

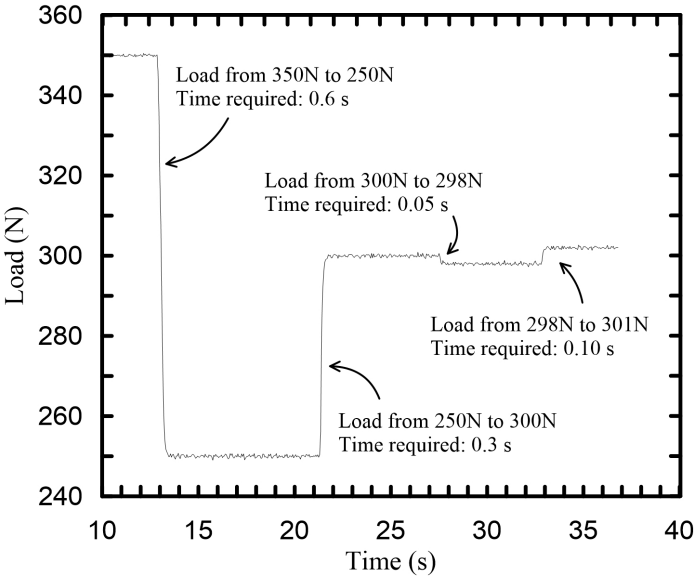


FIGURE 4.11: The load control response time under centrifuge environment

4.3.4 Steel frame structure model

The numerical model for the structure was developed using ABAQUS (Hibbitt, 2002) and simulated a five-storey steel frame building designed for storage and machine plant use, which gives most load to the piles compared with other type of building functions. Building elements such as stairways, façade, and bracings were not considered into the structural stiffness. A linear elastic constitutive model was used for the steel frame with Young's modulus E=2.110^{11} N/m^2 in prototype scale and a Poisson's ratio of μ=0.3. The dimensions of the steel frame building as well as column and beam size, are given in Figure 4.8 (prototype scale). The variable load applied to the building is based on the Eurocode specifications (Gulvanessian et al., 2009) for storage building (7.5 kN/m^2) and the permanent load is 3 kN/m^2, which gives a total load of 2364 kN for the two inner piles and 1630 kN for the two outer piles (prototype scale).

4.3.5 Model piles and instrumentation

The pile modelled in the centrifuge tests is equivalent to a 0.8m diameter concrete pile in prototype scale. An aluminium hollow cylinder was used to model the pile within the centrifuge (model scale). Table 4.3 summarises the pile properties in model and prototype scale. The concrete pile foundation can be briefly categorised into bored piles, that the concrete is cast in the drilled borehole. As a result, for centrifuge tests,

a non-displacement pile is modelled in this study (friction along the pile is not fully mobilised). To increase the interface friction (fully rough interface), sand is bonded to the shaft and tip of the model pile using the same sands as used for centrifuge tests using epoxy and is consistent with the method given by Franza (2016), thus the final pile diameter is 10.5 mm.

TABLE 4.3: Pile properties in model and prototype scale

Properties	Real case	Model	Prototype
Material	Concrete pile	Aluminium	Aluminium
Diameter	0.8 m	10 mm	0.8 m
Thickness	Solid	1 mm	0.08 m
Young's modulus	20-28 GPa	69 GPa	69 GPa
Bending rigidity	0.40-0.56$\times 10^3$ MNm^2	20 Nm^2	820 MNm^2
Axial rigidity	10.0-14.1$\times 10^3$ MN	1952 kN	19.4$\times 10^3$ MN

FBG sensing system

FBG sensors were used within the centrifuge tests to measure the axial force along the aluminium model piles, which is believed to be the first application of this instrumentation in centrifuge testing. The basic principle of FBG sensors was discussed in Section 3.2.3. As noted in Section 3.2.3, the wavelength shift is affected by the physical elongation of the sensor (strain ε), temperature (T) and pressure applied to the sensor (P) (see Equation 3.6). Thus, there is a need to isolate the temperature and pressure effect on the wavelength shift. For temperature isolation, one additional fibre Bragg was used during centrifuge tests, which was not attached to the aluminium model pile, and the wavelength shift for this Bragg was used to compensate the temperature effect. For pressure isolation, as the FBG sensors were located inside the aluminium pile, and during centrifuge tests, no pressure is applied to the surface of the FBG; therefore, the pressure effect to the wavelength shift can be ignored for the tests stated herein.

As stated above, as the effect of temperature and pressure effect on wavelength shift is isolated, the measurement of the wavelength shift can be directly correlated to the elongation of the sensor strain ε, where $\Delta\lambda_B = K_\varepsilon\varepsilon$. In order to measure the physical strain of the aluminium pile, FBG sensors were attached to the internal surface of the aluminium piles. Figure 4.12 illustrates the procedures involved to install the fibre inside the aluminium pile. The flat clamp firstly fixed the aluminium pile. Then the fibre was placed inside the pile, and one end of the fibre (connected to the FBG Interrogator) was surrounded by a mini plastic tube to increase the rigidity of the fibre (prevent damage of the fibre during tests). The UV cured adhesive (Permabond UV620) was used to fixed the location where the fibre is going through the aluminium pile (see Figure 4.12 procedure (1)). The super glue (Loctite Super glue precision) was then used to adhere

a small length of fibre inside the pile as indicated in the procedure (2), see Figure 4.12. Once the super glue was fully curved, the other side of the fibre was clamped to the modified micrometre terminal (procedure (3)). The modified micrometre can move horizontally by rotating the end knob. By moving the modified micrometre outwards, the fibre was "stretched" and fully contacted with the aluminium pile internal surface (procedure (4)). FBG sensors need to fully contact with the aluminium pile to allow the strain measurement from the aluminium pile, and the super glue (Loctite Super glue precision) was applied along the fibre, followed by the UV cured adhesive.

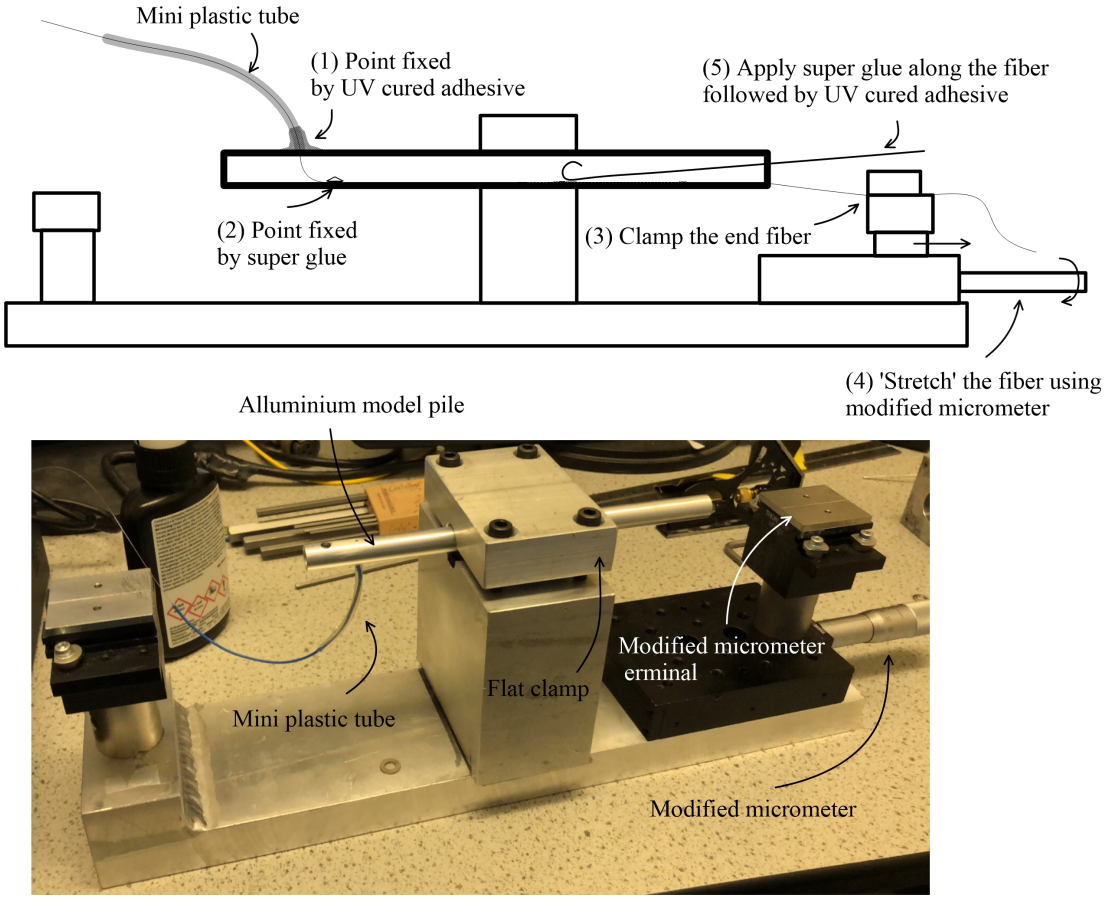


FIGURE 4.12: FBG sensor installation procedure

FBG sensor calibration

The axial force along the pile can be calculated by:

$$\begin{aligned} F &= EA\varepsilon_t \\ \varepsilon_t &\propto \varepsilon \\ \varepsilon &= \Delta\lambda_B / K_\varepsilon \end{aligned} \tag{4.3}$$

where E and A is Young's modulus and cross-sectional area of the aluminium pile, respectively. ε_t is the strain of the aluminium pile. Strain measured from FBG (ε) is not necessarily identical to the aluminium pile strain (ε_t), this is because the aluminium pile strain is transferred from the aluminium pile to the FBG via adhesive. An alternative way is to directly correlate the axial force along the pile with FBG wavelength shift ($\Delta\lambda_B$). Figure 4.13 illustrates the model pile axial force calibration set up. A Global Digital Systems (GDS) load frame was used to apply the axial compression force along the pile. Each model pile contains 6 FBG sensors (3 on each side of the pile), which are denoted B1-B6. A calibrated load cell was fixed at the top loading frame, where a spacer was introduced between the calibrated load cell and pile tip to generate a uniform pressure among the pile tip. The model pile was located at the centre of the loading plate. The 5 kN load cell used to measure the axial force at the pile head during centrifuge tests was fixed to the pile cap, and during FBG sensor calibration, the 5 KN load cell was also calibrated. Below the 5 kN load cell, another spacer was used with a rubber mat underneath to buffer the stiffness of the loading frame.

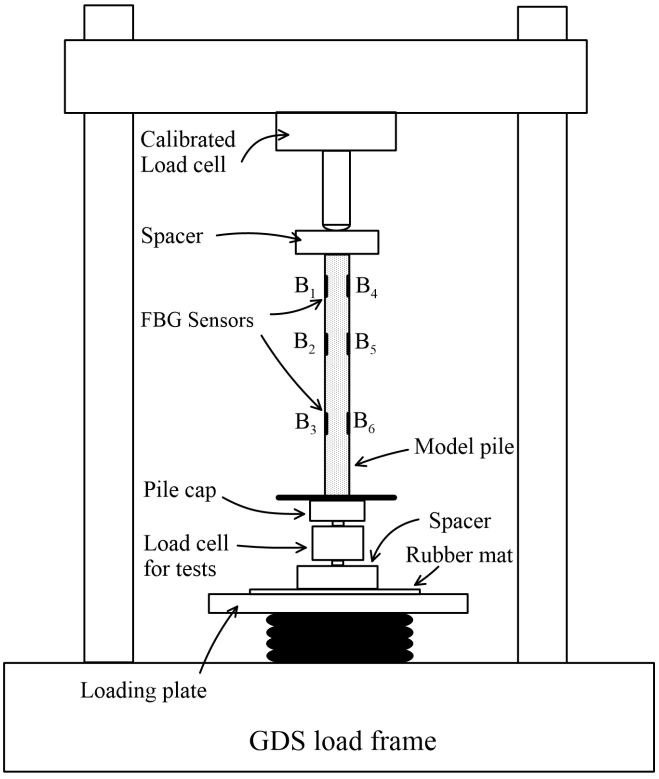


FIGURE 4.13: Model pile axial force calibration

Figure 4.14 (a) demonstrates the loading sequence to calibrate the FBG sensors. Each model pile is calibrated three times, and each calibration consists of twelve loading increments, and the maximum axial load applied to the model pile is 600 N (the maximum pile axial load experienced in centrifuge test is around 400 N). The load for every increment is held for 10s using GDS load control before proceeding to the next increment.

Figure 4.14 (b) shows the model pile 3 axial force with FBG (B_4) wavelength shift during one of the three calibrations. A linear line is fitted to the data, and the slope K_{B_i} is obtained. As a result, the axial force along the pile for a particular FBG sensor (B_i) can be calculated by:

$$F_i = K_{B_i} \Delta\lambda_{B_i} + \lambda_{OS_i} \tag{4.4}$$

where the subscript i is the FBG reference number (see Figure 4.13), and λ_{OS_i} is the wavelength offset. For each FBG sensor (B_i), the value of K_{B_i} is unique, which is the relationship between the axial force and change in the wavelength shift $\Delta\lambda_{B_i}$. For each model pile, three calibrations were conducted, and the average value K_{B_i} for each FBG sensor (B_i) from the three calibrations was used to calculate the axial force during centrifuge tests.

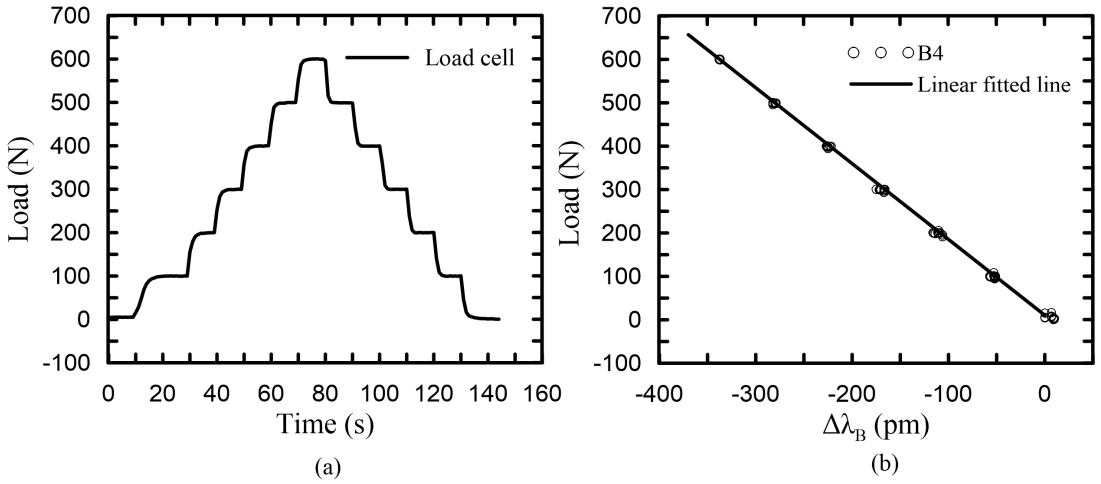


FIGURE 4.14: Model pile axial force calibration: (a) loading sequence; (b) Pile 3 B_4 result

FBG sensor application in centrifuge tests

Four model piles were used to investigate the effect of tunnelling-induced soil displacements on piled structures. FBG sensors were used to measure the axial force along the model pile. The sensors were made from a single mode optical fibre. Each fibre contains three FBGs written by an excimer laser (reflectivity of 90%) with a centre wavelength of 1530, 1535, and 1540 nm or 1545, 1550, 1560 nm. Each pile contains two fibres located on the opposite inner face of the pile. A four-channel commercial FBG interrogator (CASSTK SAI-1122PF) capable of scanning wavelengths of 1525-1565 nm at a frequency of 2 Hz was used to measure the FBG wavelength shifts during the centrifuge tests. The FBG interrogator was mounted in the centrifuge cabinet and was exposed to g-levels of 4-7 g during the tests. For each pile consisting of two fibres, a splitter (coupler) was used, which gives an even split ratio from one input fibre (regardless of input wavelength) to two output fibres; a detailed configuration is shown in Figure 4.15.

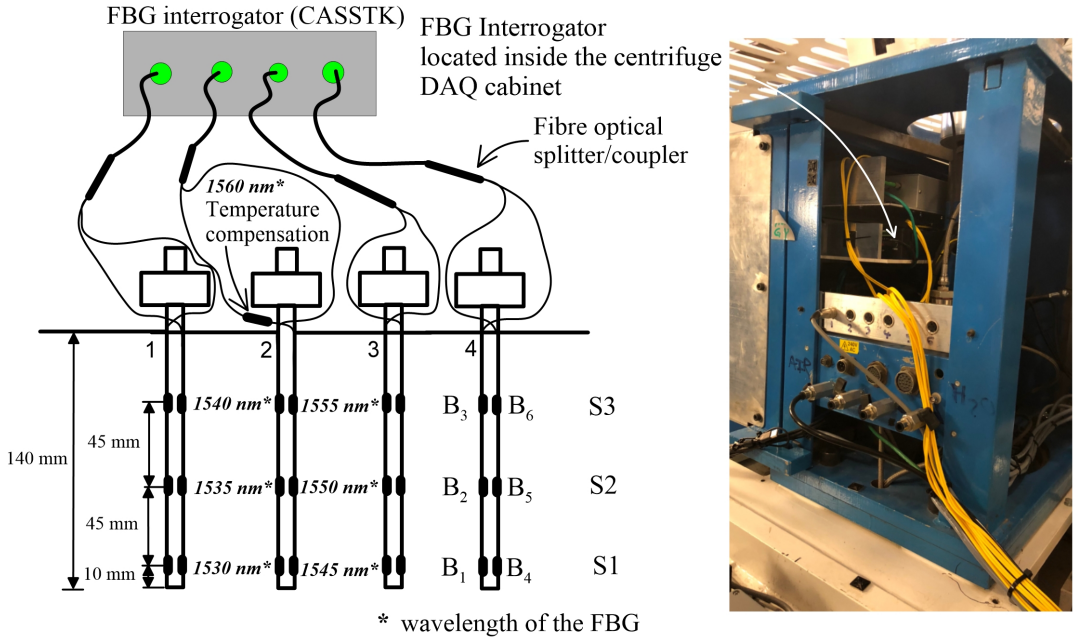
To enable temperature compensation, one additional FBG was located close to the pile head (pile 2 only).

The model pile discussed above contains two fibre cables and each cable was equipped with three FBG sensors. The location of the FBG sensors and the FBG index (B_i) is given in Figure 4.15. The calibration procedure discussed previously was conducted using a uni-axial compression loading frame, where force measured from both sides of the FBG sensors were assumed to be identical. For centrifuge tests involving tunnelling, it is difficult to ensure the force measured on both sides of the pile are identical (bending of the pile), hence the average reading of two FBG sensors located on both sides of the pile (equal depth) was used to calculate the axial force. Therefore, three axial force measurement points can be identified (denoted as S1 to S3, see Figure 4.15). For example, for measurement point S1, the axial force is the averaged force measured by B_1 and B_4.

Preliminary test of FBG sensors within the centrifuge

To verify the performance of the FBG sensors under centrifuge environment, four model piles equipped with FBG sensors were placed inside the centrifuge strong box, with the pile tip resting on a solid wood block. The centrifuge was then spun to the designated speed (80 g), followed by three g-cycles (80 g to 10 g and back up to 80 g). A 5 N constant load was applied to the pile head via the loading system. The weight of the model pile is around 70 grams, at 80 g the total amount of forces at the pile tip was around 57 N (self-weight of the pile combined with a 5 N pile head load). Figure 4.16 shows the testing specification and the expected axial force along the pile due to the self-weight of the pile. As a result, the FBG sensors along the pile are expected to have similar readings to the pile's self-weight. Figure 4.17 shows the FBG sensors' reading after centrifuge acceleration, and the dashed line represents the theoretical self-weight of the pile. The FBG sensors over-predicted the axial force along the pile. As mentioned earlier, the strain measured from the FBG is not necessarily identical to the strain along the aluminium pile. This is because the strain is transmitted through the glue (super glue), and the glue is covered by the UV cured adhesive. It is believed that the UV cured adhesive is over-coated around the FBG sensors' location, and during centrifuge acceleration, the increased self-weight of the UV epoxy could cause the glue to "drag" the FBG sensors downwards (creating a greater compression strain). Therefore the axial force along the pile is over-predicted.

As a result, the over-predicted value can be assumed as the FBG sensor's load offset due to the centrifuge acceleration. For the centrifuge tests carried out in Chapters 5 and 6, to calculate the absolute force for each FBG sensor, the load offset from each FBG sensor was subtracted from the FBG sensor's reading.



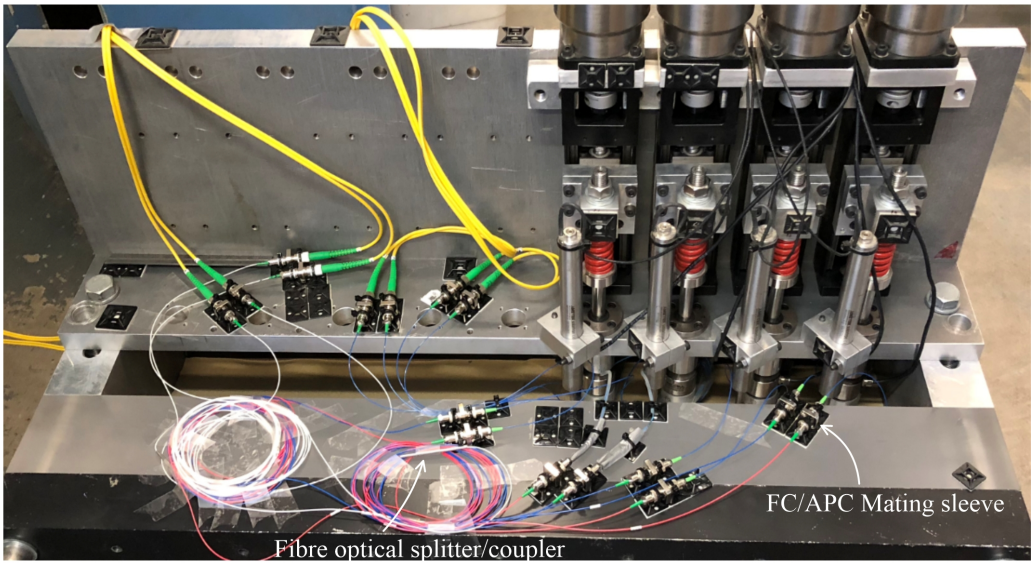


FIGURE 4.15: Centrifuge setup for FBG sensors and interrogator

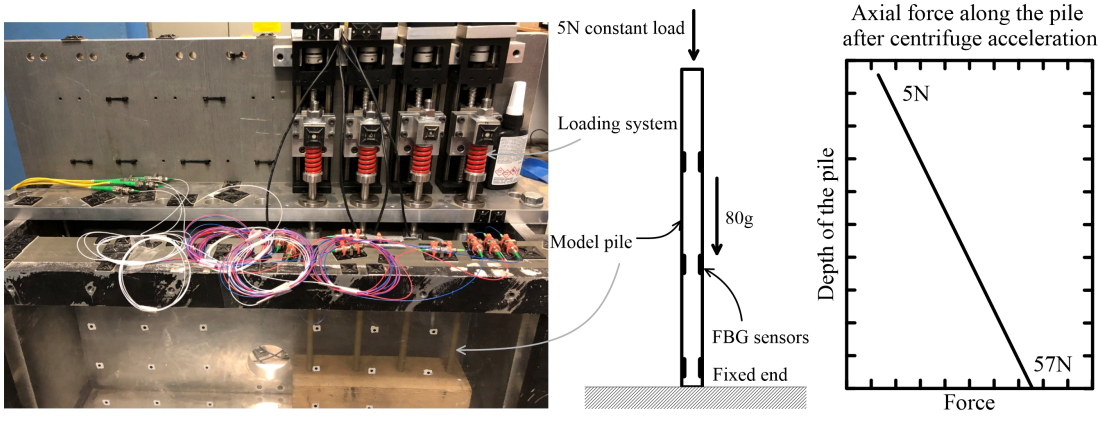


FIGURE 4.16: Verify FBG sensors under centrifuge environment

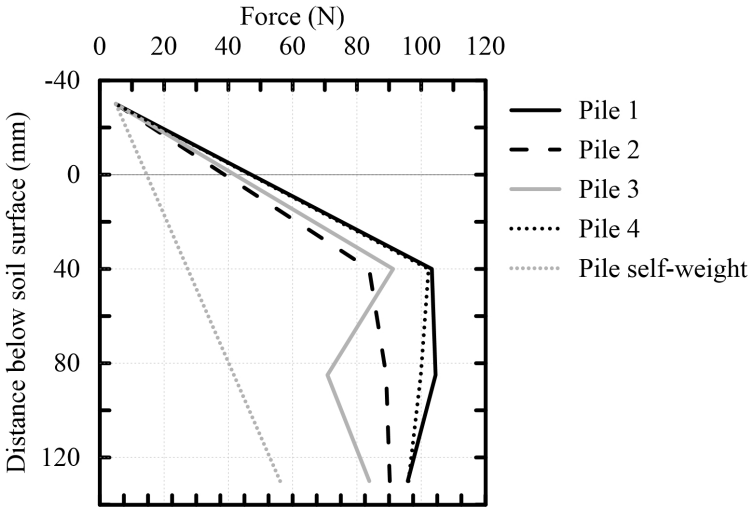


FIGURE 4.17: FBG sensors' reading under centrifuge environment

4.3.6 Testing material and model preparation

Fraction E Leighton Buzzard sand was used for the tests, where detailed specifications have been given in Section 4.2.4. Soil samples were created using the dry sand pouring technique, which is consistent with the procedure described in Section 4.2.4. After sand pouring, the strong box was rotated to its upright position, and the model piles were installed. To replicate non-displacement piles, the piles were pushed into the sand at 1 g, starting with the pile closest to the tunnel and moving outwards. A support frame was used to ensure the pile was pushed vertically, which was temporarily connected to the strong box side wall. Figure 4.18 shows the pile installation procedures. The model pile (contains a load cell and connector) was firstly connected to a steel rod, which was held by a linear motion bearing (ensure vertical displacement). Once the model pile was located to its designated position, the steel rod was then hand pushed downwards to the amendment depth L_p=140 mm. The pile installation procedure is conducted under 1 g; due to the low-stress condition around the soil, hence the disturbance of the soil during pile installation is believed to be minimum, and since the method is consistent between the tests, such effect is considered to be secondary. The steel rod was then disconnected from the pile connector and re-connected to the second pile, and the above procedure was repeated. Once all the piles were installed to the designated position and amendment depth, the support frame was disassembled. The pile loading system was then fixed at the top of the strong box, and the model piles were connected to the linear actuators. The tunnel volume loss control system (gearbox and stepper motor) and LVDTs were then installed.

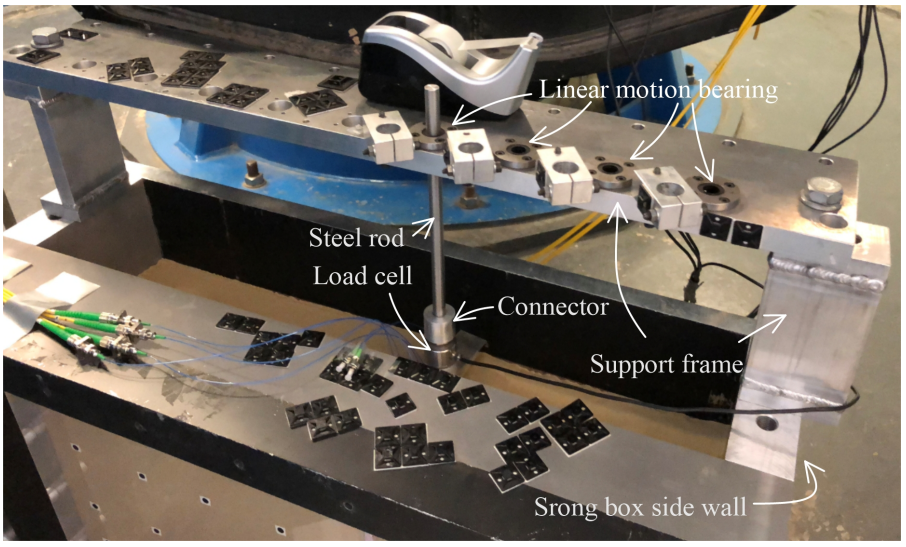


FIGURE 4.18: Model pile installation procedure

4.3.7 Testing procedures

A constant 5 N vertical load (model scale) was maintained at the pile head (load controlled) during centrifuge spin-up to 80 g. This was done to ensure minimum relative displacement occurred between the soil and pile during spin-up (if fixed in place during spin-up, the soil would settle more than the pile). Three stabilisation cycles (going from 80 g to 10 g and back to 80 g) were performed to encourage a uniform stress distribution within the soil body and to improve repeatability between tests. During these cycles the pile load remained at 5 N. The piles were then loaded to the designated working load (255 N for outer piles 1 and 4, and 370 N for inner piles 2 and 3; refer to pile numbering in Figure 4.8) in 50 N stages, starting with pile 1 and moving sequentially to pile 4. For test CL (structure with zero stiffness), these initial pile loads were maintained throughout the volume loss process. For test CCNM1 and 2 (structure with stiffness), the real-time interface was activated, followed by the initiation of ABAQUS (simulating the steel frame structure). This final step gives control of the pile loads in the centrifuge to the ABAQUS program, which takes in measurements of pile displacements from the centrifuge and outputs new pile loads based on the outcomes of the structural numerical simulation; the pile loads were then passed back to the control system, and the load on the piles was adjusted accordingly. The tunnel volume loss ($V_{l,t}$) process was then started, increasing up to $V_{l,t} \approx 2.2\%$ for test CCNM1 and $V_{l,t} \approx 3.2\%$ for test CCNM2 with small increments of approximately 0.1% (the time interval between two small increments is approximately 30s).

4.4 The use of protective structures to protect buildings from tunnelling-induced damage

Tunnelling close to a pile foundation can cause uneven pile settlement, therefore threatening the serviceability of the piled structure. To protect structures from the tunnelling-induced damage, protective structures are used in this study. The purpose of the protective structure is to reduce the tunnelling-induced ground movements and the potential tunnelling-induced superstructure damage.

For all four tests, the eRBM model tunnel was used to simulate tunnel volume loss, the CCNM system described in Section 4.9 was used to simulate the superstructure (identical superstructure as described in Section 4.3.4), and two cameras (Dalsa genie nano-m4020) with 12.4 Megapixel resolution were used to capture the images during each tunnel volume loss. Soil displacement data observed were processed by geoPIV-RG to investigate the ground movement mechanisms. Tests results also include the bending moment measurement along the walls using FBG sensors; the detailed configurations and location of the FBG sensors along the walls are discussed in the following subsections.

4.4.1 Experimental programme

Four centrifuge tests were conducted to analyse the effect of protective walls to the tunnelling-induced damage of piled structures. Figure 4.19 shows the testing layouts. Table 4.4 summarises the testing details. A newly developed strong box was used for the centrifuge tests described in this section. Unlike the previous strong box used for greenfield tunnelling (see, Figure 4.1), the inner height of the strong box was increased, therefore the greenfield tunnelling test was repeated and denote as test GF. Test CCNM3 tested the piled structure with tunnel volume loss, and the protective walls were not used (repeat of test CCNM2). For test CCNM-R-S and CCNM-R-L, two different lengths of protective walls were used, with an embedment depth of 207 mm and 297 mm, respectively. The tests only considered the situation that the protective structures were located 55mm away from the tunnel centre line with a rough surface (to replicate non-displacement secant pile walls).

The newly developed strong box has an inner width × height dimensions of 700 mm × 500 mm and is 150 mm wide. As the height of the box increased, to ensure the lateral soil displacements at the front acrylic window and back aluminium wall under 80 g are less than 0.1% of the soil model height, the thickness of the front acrylic window and back aluminium wall were increased. Figure 4.20 shows the centrifuge strong box used for the centrifuge tests. The model tunnel has an initial diameter of 90 mm, which is located

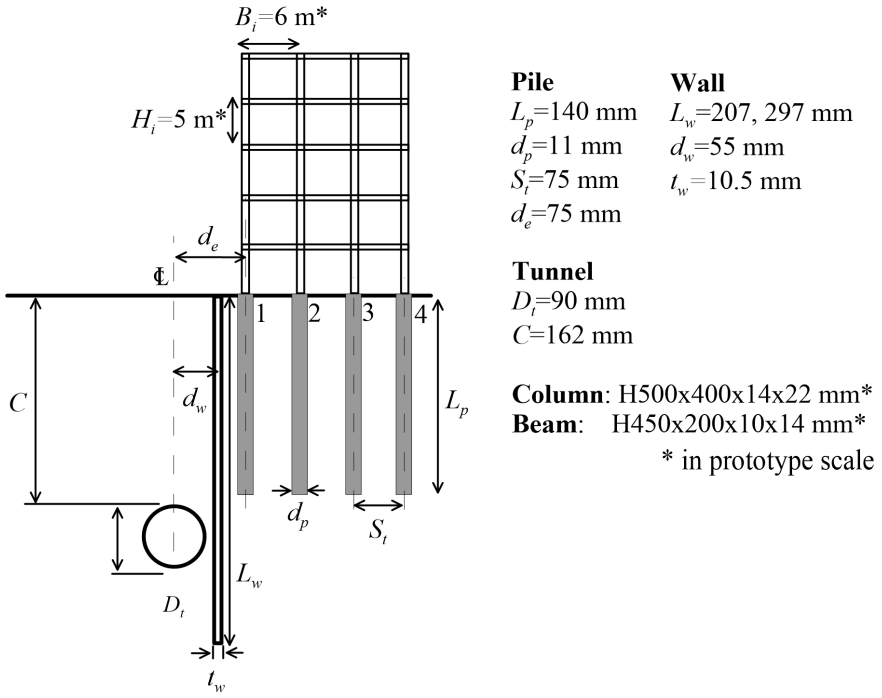


FIGURE 4.19: Testing layout in model scale

TABLE 4.4: Summary of the centrifuge tests performed at 80 g

Test label	Final tunnel volume loss $V_{l,t}$	Structure stiffness †	Length of the wall L_w
GF	2.8 %	GF	NA
CCNM3	2.8 %	F	NA
CCNM-R-S	3.1%	F	207 mm
CCNM-R-L	3.0%	F	297 mm

† F=Structure with full stiffness, GF=Green field

175 mm above the strong box base, and provided a 130 mm clear distance between the bottom of the tunnel and strong box base. The "long" protective wall has an embedded depth of 297 mm and a clear distance of 85mm between the toe of the wall and the strong box base.

4.4.2 Model piles and instrumentation

The model piles used for the tests presented in Chapter 6 are identical to the piles discussed in Section 4.3.5. The properties of the piles are summarised in Table 4.3.

After the centrifuge tests conducted in Chapter 5 (see Table 4.2), four piles were re-calibrated using the method described in Section 4.3.5. Figure 4.21 shows the K_{B_i} values from Each pile based on the initial calibration (first time calibration prior to centrifuge

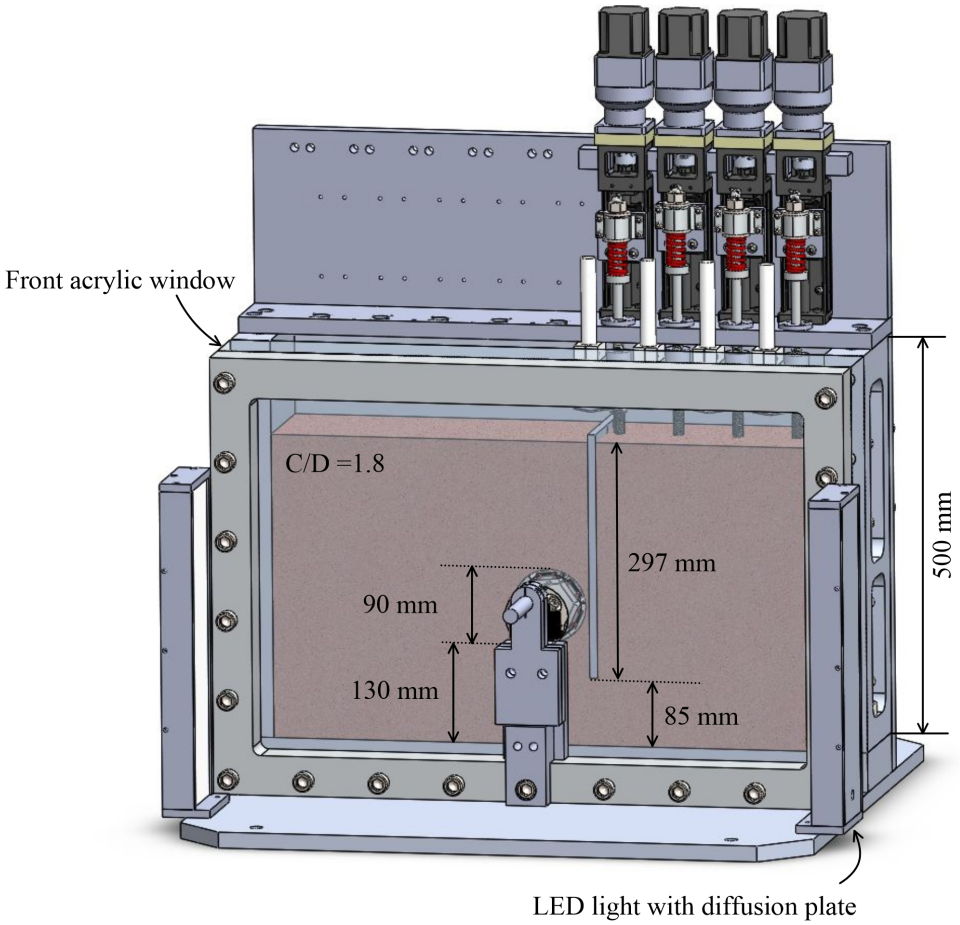


FIGURE 4.20: Strong box for protective wall centrifuge tests

test presented in Chapter 5) and secondary calibration (second time calibration, after centrifuge test presented in Chapter 5). Each pile has 6 FBG sensors, the location and index i for each sensors were shown in Figure 4.15. From Figure 4.21, it can be seen that for Each pile, the K_{B_i} values are not consistent. This is because the K_{B_i} value is highly dependent on the amount of super glue and UV adhesive applied on each FBG sensors (ability of transferring aluminium pile strain ϵ_t into FBG measured strain ϵ). Since the super glue and UV adhesive are coated manually, it is difficult to achieve a uniform coating profile along the fibre. In addition, the value of K_{B_i} changed between the two calibrations. The K_{B_i} values changed most for pile 1 when compared with the other piles. Piles 2 3 and 4 show relatively small changes in K_{B_i} values between the two calibrations, apart from FBG i=1 in pile 4. The fibre end was located extreme close to the pile tip cap, it is believed that the pile cap may physically affect the initial position of the fibre end under a high compression force. Therefore the FBG sensors located closest to the pile end (FBG i=1 and 4) may be affected. Similar changes (increase in K_{B_i} values) can be identified in pile 1 FBG i=1 and 4, which were located closest to the pile tip. Therefore, the axial force at the pile end may not be measured accurately,

but the effect stated above is consistent between the tests.

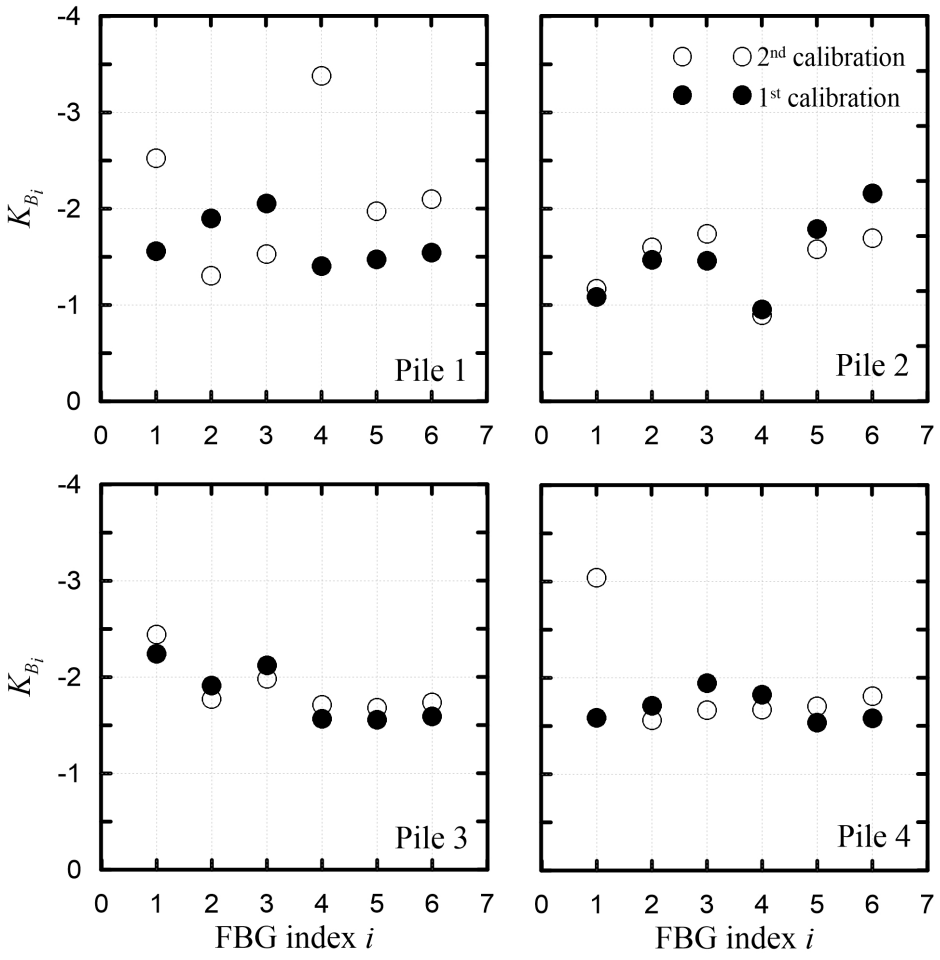


FIGURE 4.21: FBG calibration results

4.4.3 Model walls and instrumentation

A cast-in-situ pile wall has been used in practice to protect buildings from tunnelling-induced damage (Di Mariano et al., 2007, Ledesma and Alonso, 2017). An aluminium plate with a thickness of 10 mm was used within the centrifuge to simulate a 0.8 m diameter concrete pile wall (secant pile wall, regardless the curvature across the wall) in prototype scale. The width of the centrifuge model box as discussed in Section 4.2.2 is 150 mm. The model wall has a width of 148 mm, and two PTFE strips (1 mm thickness) were used on either side of the wall to reduce the interface friction. Fraction E sand was bonded to the front and back side of the wall to increase the friction between the sand and wall interface (same approach as described in Section 4.3.5). The properties of the wall in model and prototype scale are summarised in Table 4.5.

FBG sensing system

As discussed in Section 3.2.3, the wavelength shift of the FBG is affected by the physical

TABLE 4.5: Protective wall properties in model and prototype scale

Properties	Real case	Model	Prototype
Material	Concrete	Aluminium	Aluminium
Thickness	0.8m	10mm	0.8m
Width	11.8m	148mm	11.8m
Young's modulus	20-28 GPa	69 GPa	69 GPa
Bending rigidity	10-14$\times 10^3$MNm^2	851 Nm^2	34.8$\times 10^3$MNm^2

elongation of the sensor (strain ϵ), temperature (T) and pressure applied to the sensor (P). Section 4.3.5 has discussed the temperature compensation procedure. A brass U-channel was used to cover FBG sensors installed on the protective walls, to protect the fibre from soil confining pressure, see Figure 4.22. The FBG fibre installation procedures can be summarised as follows: (1) A 1 mm depth 1.5 mm width slot was machined on the aluminium surface, and (2) FBG fibre is then located in the middle of the slot and was coated by super glue, (3) then the brass U-channel was installed, and the gaps were filled with super glue to ensure the U-channel is permanently fixed inside the slot. The depth of the slot is greater than the diameter of the fibre to ensure enough clearance space between the fibre and the U-channel. As a result, during the centrifuge tests, the soil confining pressure was taken by the brass U-channel. Two fibres located on both sides of the wall were used to measure the bending moment along the depth of the wall. The bending moment measurement positions are located in the middle of the wall and 37.5 mm away from the edge of the wall.

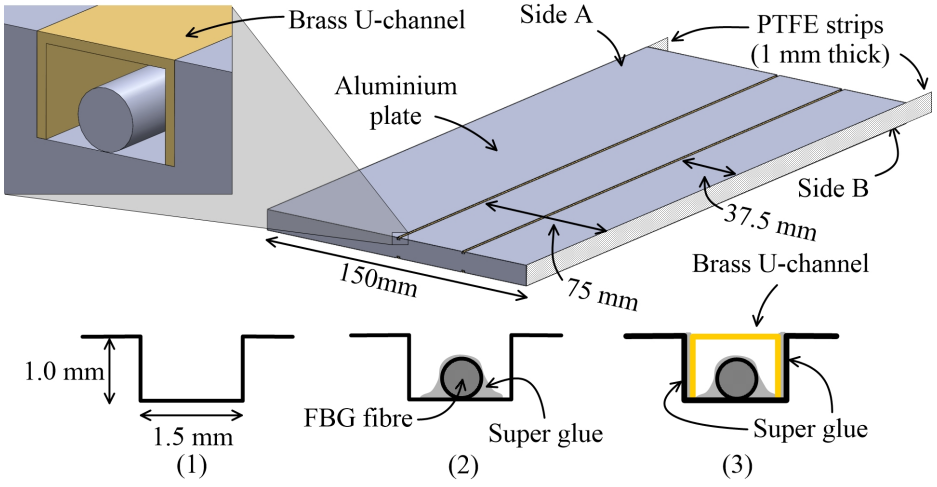


FIGURE 4.22: FBG sensor installation for aluminium plate

FBG sensor calibration

The bending moment of the wall located at each FBG sensors' location can be directly correlated with the FBG wavelength shift ($\Delta\lambda_B$). Figure 4.23 presents the bending

moment calibration procedures. Two aluminium angles were used to support the model wall. The steel rod was placed on the top of the model wall. A rubber strip was placed underneath the rod to ensure the load applied can be evenly distributed across the width of the aluminium wall. Two cable ties were used to transfer the load from the mass hanger to the steel bar. The distance between the two cable ties to the centre line of the aluminium wall is identical; as a result, the force from the two cable ties is equal. Three loading locations were used to conduct the calibration, which is 90, 130 and 180 mm away from the support position (see Figure 4.23). For each loading locations, three loading cycles were conducted, and for each loading cycles, weight was added to the mass hanger by 1 kg increments up to a maximum weight of 13 kg. Once three loading locations were calibrated, the model wall was flipped over with Side B facing upwards, and the calibration procedure described above were repeated.

As stated above, the bending moment at the FBG sensor's location is directly correlated to the FBG wavelength shift ($\Delta\lambda_B$). Five bending moment measurement locations (five FBG sensors along the fibre) were adopted, which were denoted as $P_1 - P_5$. For example, during the calibration process with the wall Side A facing upwards, the FBG sensors located at the Side A was under compression, and the FBG sensors located at the Side B was under extension. Therefore, the change in wavelength ($\Delta\lambda_B P_i$) at the measurement location P_i equals to the sum of the change in wavelength shift from both FBG sensors ($\Delta\lambda_B P_i = |\Delta\lambda_B P_{iA}| + |\Delta\lambda_B P_{iB}|$). Where the subscript i is the FBG sensors locations index ($i = 1 - 5$), and the subscript A or B is the wall side A or B. For sign convention purpose, the change in wavelength shift $\Delta\lambda_B P_i$ is in a negative value when the calibration is conducted with wall Side B facing upwards (see Figure 4.23).

Figure 4.24 shows the change in wavelength $\Delta\lambda_B P_3$ (for position P_3) with bending moment. A linear line can be fitted into the data, and the gradient of the linear line $K_B P_i$ was obtained. Therefore, the bending moment for a particular FBG location (P_i) can be calculated as:

$$M_i = K_B P_i \times \Delta\lambda_B P_i \tag{4.5}$$

Aluminium model wall application in centrifuge tests

Two aluminium model walls were tested, the dimensions of the wall and locations of the FBG sensors are presented in Figure 4.25. As stated above, the length of the wall is 148 mm, and PTFE strips with a thickness of 1 mm were attached on both side of the wall to decrease the interface friction. Two clear plastic strips were attached on the edge of the aluminium model wall in an attempt to prevent the sand particles from getting stuck into the interface. Only half a width of the plastic strip was bonded on the aluminium wall edge, with the other half free to move (see Figure 4.26). The free to move

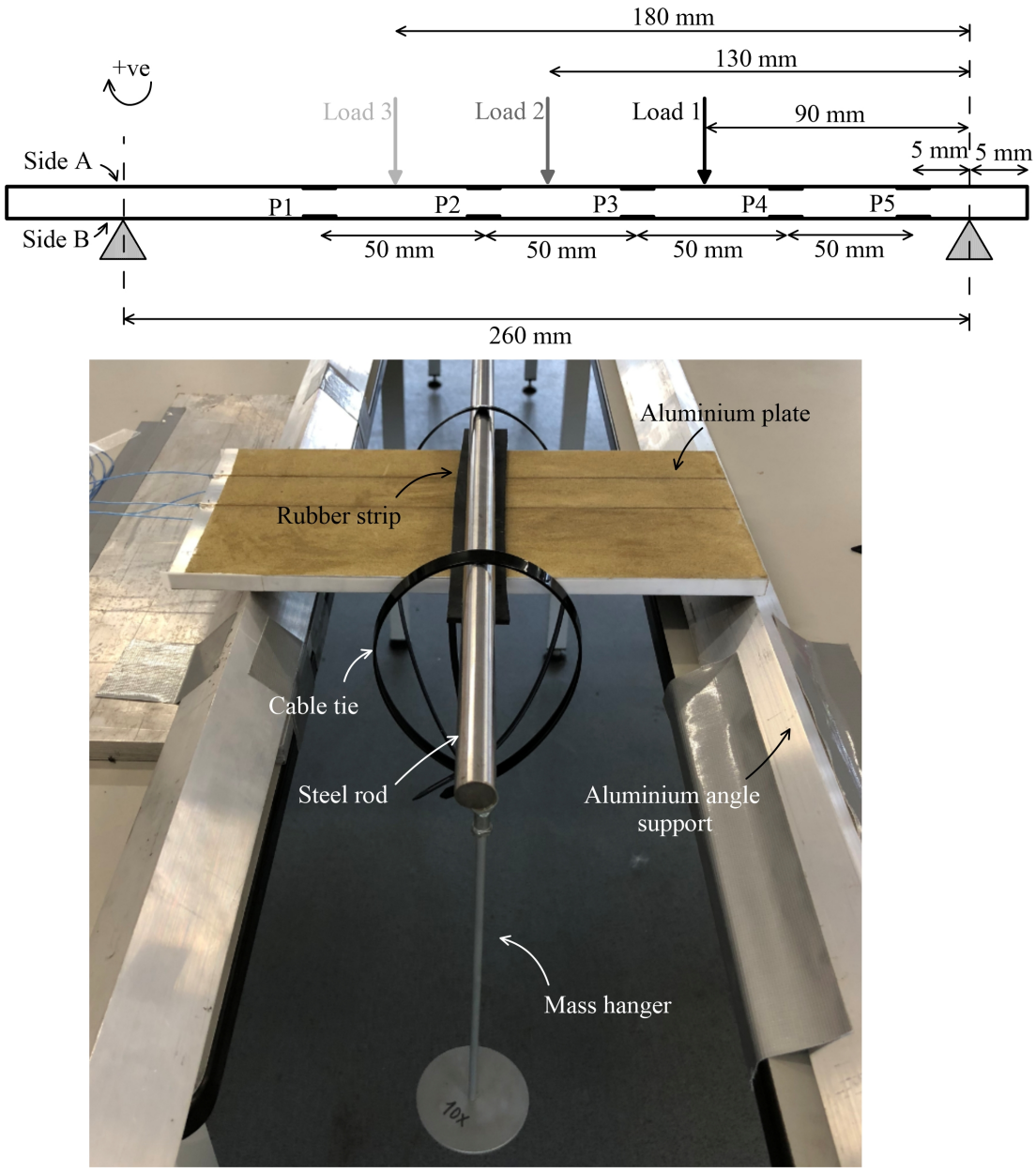


FIGURE 4.23: Bending moment calibration for FBG sensors

plastic strip end is then slightly bent outwards, which should encourage the free end to contact with the acrylic window. Once the free end was fully attached to the acrylic window, the sand pouring process can be started. Due to the use of protective wall, the front acrylic window was faced downwards during sand pouring, which is different from the strong box orientation for tests related to in Chapters 4 and 5 (back aluminium wall facing downwards). Figure 4.26 shows the interface front view after the sand pouring.

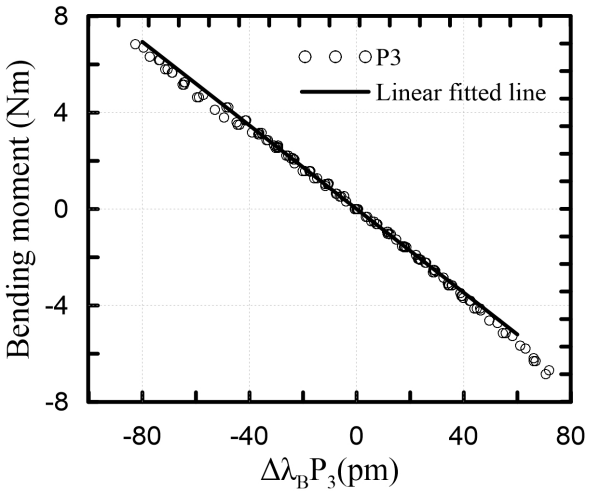


FIGURE 4.24: Change in wavelength $\Delta\lambda_B P_3$ with bending moment

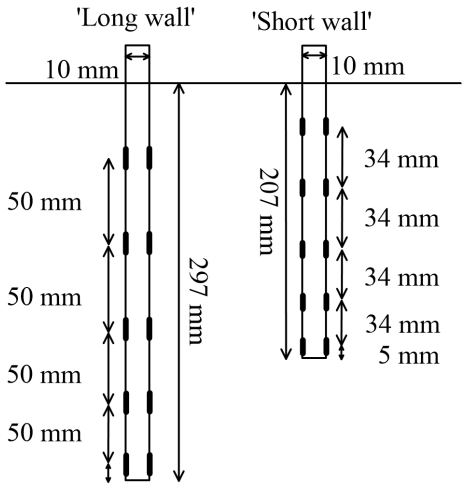


FIGURE 4.25: Locations of the FBG sensors for both model walls

4.4.4 Soil displacements measurement

For the centrifuge tests described in this section, two cameras (Dalsa nano-m4020) were used to track the soil displacements. The cameras used in this section are different from the cameras presented in Section 4.2.3. As a result, the precision of the geoPIV-RG described in Section 4.2.3 needs to be re-assessed. The accuracy of soil displacements calculated in pixel space ("tracking"), and the accuracy of transferring pixel space soil displacement into objective space ("translation") are analysed.

The accuracy of "tracking" using the new cameras is evaluated first. Two images were taken under centrifuge environment (same lighting condition and camera distance) with zero soil displacements, and the standard error of the soil displacements is calculated. Figure 4.27 shows the vertical and horizontal directions standard error with subset size using the new cameras, and the standard errors from the old camera (Canon G10) are

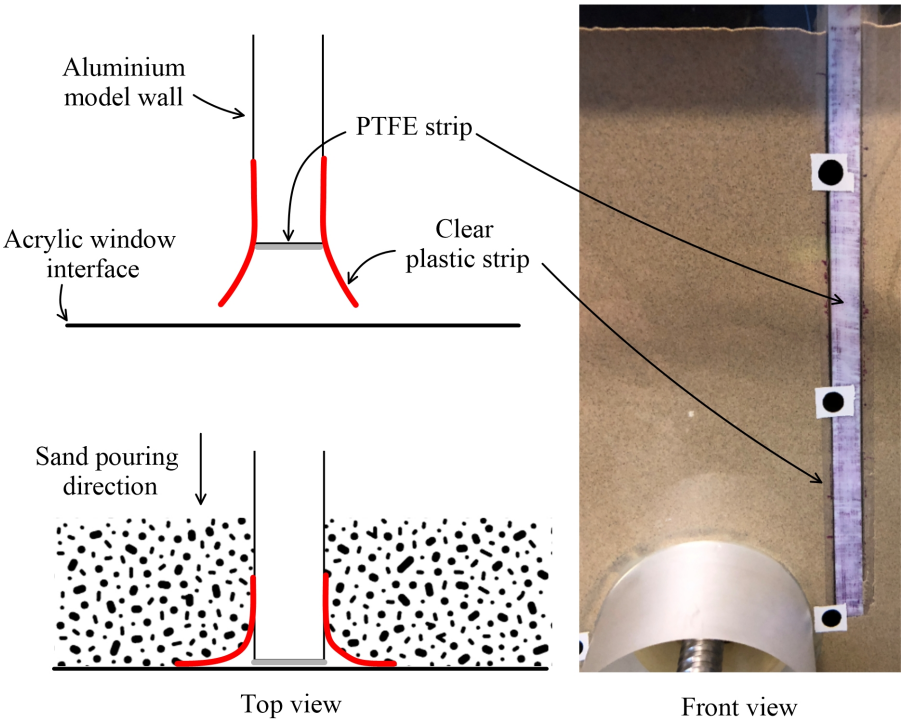


FIGURE 4.26: Interface between the acrylic window and aluminium model wall

also included. In general, the standard error using the new cameras is slightly less than the errors from the old cameras. With the increase in subset size, the value of the standard error in both directions reduced. Thus, the subset size of 80 pixels is used for the analyses in Chapter 6.

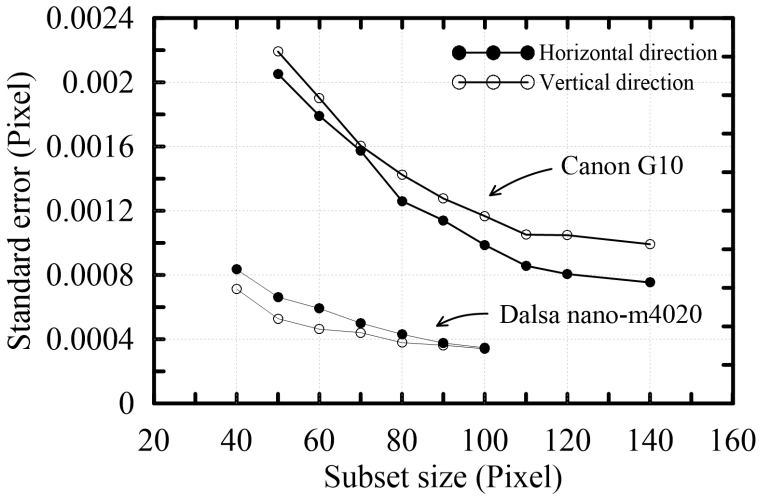


FIGURE 4.27: Standard error for tracking with subset size in pixel space using new camera (Dalsa nano-m4020)

The hand-painted control markers located at the new acrylic window need to be calibrated first. The photogrammetric calibration process discussed in Section 4.2.3 involves

multiple step "stitching", because the the size of the photogrammetric target panel cannot cover the entire control markers. As indicated by Marshall (2009), a small amount of error is introduced when the coordinate of the control markers calculated from each image is "stitched" together (see Section 4.2.3 for detail). To eliminate this error, an A3 size printed target panel was used to perform the calibration. Despite the fact that the precision of the printed targets may be less than the photogrammetric target panel used previously, the error caused by "stitching" can be eliminated. To assess the precision of the geoPIV-RG based on the current camera setup and control maker calibration, two images were taken with zero soil displacements. For the assessment, 53260 subset patches were used, and the displacement of each patch was calculated by tracking the displacement in pixel space, and then translating the pixel space displacement into object space based on the hand-painted control markers' object coordinates, which were calibrated using an A3 size printed target panel. Figure 4.28 shows the histograms of the measured soil displacements in both horizontal and vertical directions. The standard deviation for horizontal displacements is 1.57 μm, and for vertical displacement is 1.77 μm. This level of precision is higher than the previous camera setup (Canon G10, horizontal displacement is 4.6 μm and vertical displacement is 6.4 μm).

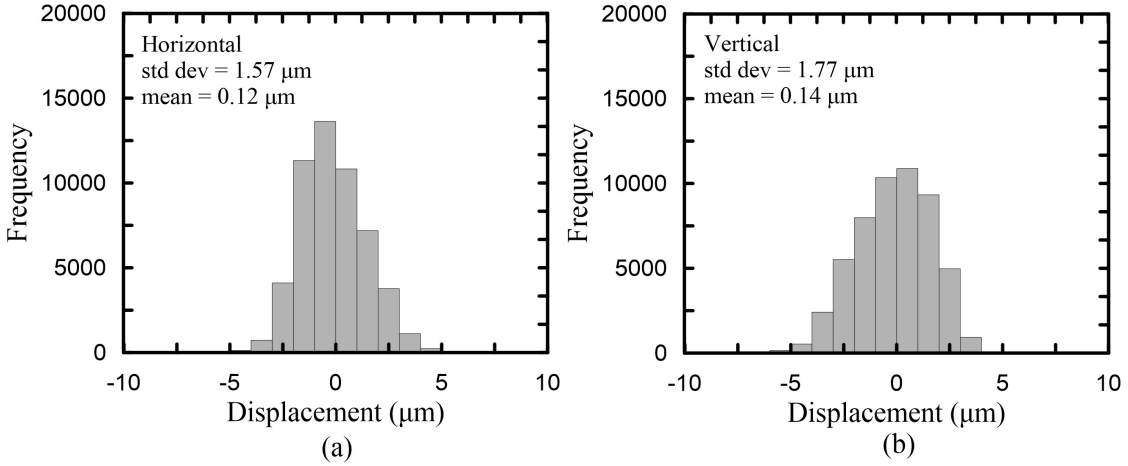


FIGURE 4.28: Histograms of displacement errors on (a) horizontal displacement and (b) vertical displacement using new camera

4.4.5 Model preparation

The strong box was placed with the front window facing downwards, allowing the sand to be poured in the direction of the longitudinal tunnel axis. The tunnel was then secured within the strong box. The aluminium model wall described previously (subsection 4.4.3) was placed on the acrylic window, and the clear plastic strips' free end was fully attached to the acrylic window. Two temporary supports were located inside the strong box to prevent the sand from spreading during sand pouring, and the supports could help the

aluminium model wall remain in an upright position. Prior to sand pouring, a thin layer of dyed sand was placed uniformly on the surface of the acrylic window. The sand was then prepared according to a methodology calibrated to achieve a relative density (I_d) of 90%. After sand pouring, the residual sand located between the two clear plastic strips was removed (see Figure 4.29). The back wall of the strong box was carefully placed on the top of the strong box to make sure that the two clear plastic strips were fully attached to the back wall inner surface. The back wall was then bolted to the strong box, which was rotated to its upright position afterwards.

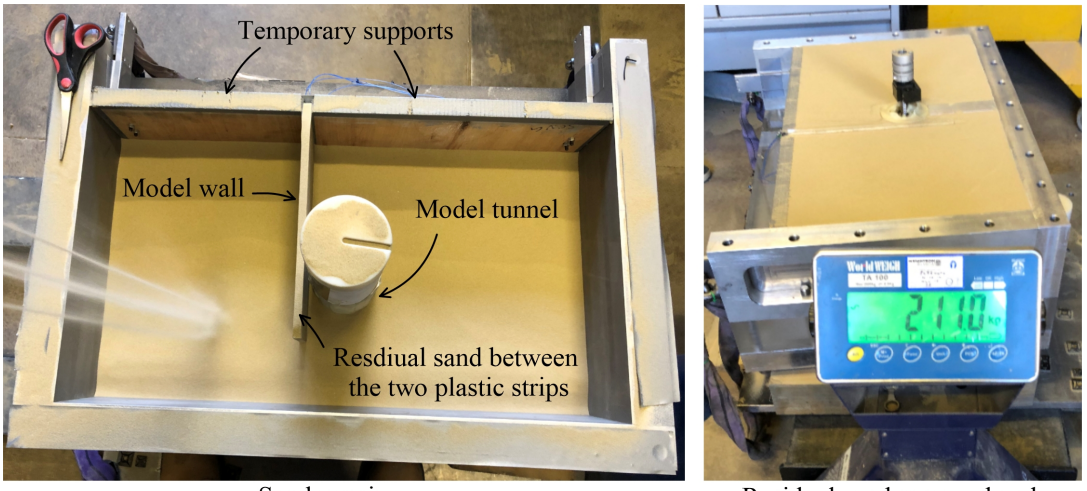


FIGURE 4.29: Sand sample preparation and the location of the model wall

The temporary supports (see Figure 4.29) were disassembled, and the support frame used for model pile installation (described in Section 4.3.6) was fixed to the strong box. The model piles were pushed at 1g into the sand, where detailed model pile installation procedures has been discussed in Section 4.3.6. Once the piles were installed to the designated position and depth, the pile loading system was connected to the model piles, and the FBG fibres were connected to the interrogators, which were located inside the centrifuge data acquisition system (DAS) cabinet. Two interrogators (SmartScan S-SBI-04-F-C, CASSTK SAI-1122PF) were used to measure the axial force along the model piles and the bending moment along the model wall, respectively. Figure 4.30 shows the location of the two interrogators.

4.4.6 Testing procedure

A constant 5N vertical load was maintained at the pile head (load controlled by the loading system) during centrifuge spin-up to 80g. The cameras took images during centrifuge spin-up. Three stabilisation cycles were performed. The piles were then

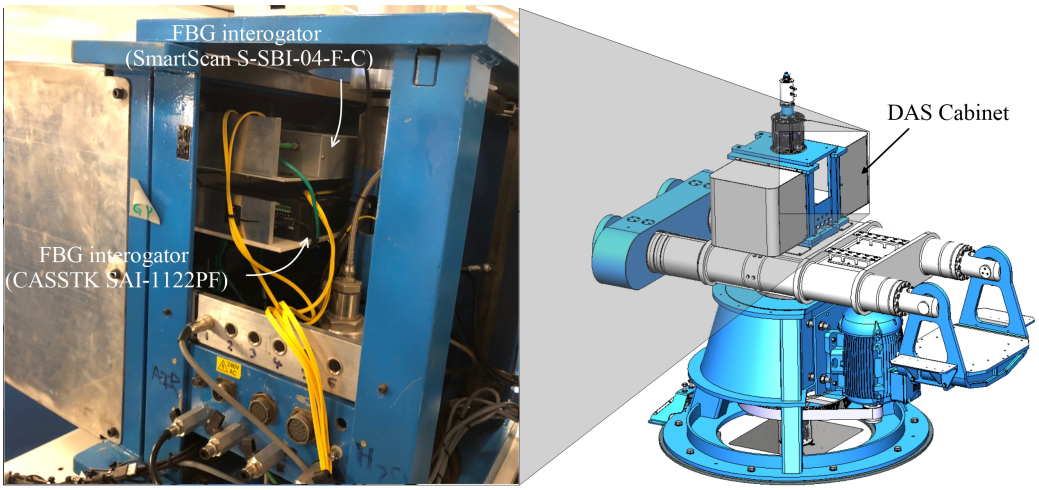


FIGURE 4.30: Locations of the two interrogators

loaded to the designated working load, where detailed loading sequence and magnitudes have been discussed in Section 4.3.7. The real-time interface was then activated, followed by the initiation of the ABAQUS (simulating the steel frame structure). Tunnel volume loss process was then started with a time interval of approximately 30s, and during each increment ($\approx 0.1\%V_{l,t}$) images were taken by the cameras.

4.5 Chapter summary

This chapter summarised the testing layout, testing equipment and experimental methods. In total, three centrifuge testing packages were discussed, which are greenfield tunnelling in sand, the effect of tunnelling on piled structure, and the use of protective structures protective walls to reduce the effect of tunnelling on buildings.

For the first testing package, the newly developed eRBM model tunnel was used to simulate tunnel volume loss. The testing material and model preparation, as well as the testing procedures, were described.

For the second testing package, a modified CCNM system was developed (pile loading system), and the FBG sensors were used to measure the axial force along the model piles. The performance of the pile loading system was evaluated. Detailed FBG sensor applications under centrifuge environment were introduced, including the calibration process and FBG sensor installation methods. The model preparation and testing procedures were then discussed.

For the third testing package, FBG sensors were used to measure the bending moment along the protective walls. The FBG sensor installation and calibration process were presented followed by the model preparation and testing procedures.

This research involves some important novel experimental developments, which are: 1) an eccentric rigid boundary mechanical (eRBM) model tunnel, 2) further improved the current coupling centrifuge numerical modelling (CCNM) technique, 3) development of a modular actuator system with the ability to conduct load/displacement control, 4) integrated fibre Bragg Grating (FBG) sensors within the geotechnical centrifuge to measure the axial force of the model piles as well as the bending moment of the model walls.

Chapter 5

Tunnelling in sandy ground

5.1 Introduction

Tunnel construction in urban areas often occurs close to existing foundation systems or infrastructure, such as pile groups, retaining structures, and pipelines. Understanding the impact of tunnelling-induced ground movements on these critical systems is an important stage during tunnel design or risk assessment processes.

Centrifuge modelling has been used extensively as a tool to study soil movements caused by tunnelling because of its ability to reproduce full-scale soil stress profiles within reduced scale models. Evaluating the effect of tunnelling-induced ground movements on structures is undoubtedly a three-dimensional (3D) problem. Detailed simulation of the 3D interactions between tunnel construction and existing structures can be achieved in a centrifuge (e.g. Ng et al. (2013), Nomoto et al. (1999)), however the most common modelling technique considers displacements in the two-dimensional (2D) plane transverse to the tunnel direction (i.e. the plane-strain condition representing displacements a certain distance behind the excavation face). The modelling of the 2D plane strain scenario in the transverse plane is the focus of this chapter.

One of the early techniques used to simulate the effect of tunnel volume loss in centrifuge tests involved decreasing the internal pressure of a tunnel-shaped airbag (Atkinson et al., 1975, Hagiwara et al., 1999, Potts, 1976). Tunnel volume loss, $V_{l,t}$, is a measure of the ground movement caused by tunnelling and is defined as the ratio between the ground loss at the tunnel periphery and the final tunnel cross-sectional area, expressed as a percentage. A limitation of the pressurised airbag technique is that the compressibility of air makes it difficult to assess the magnitude of tunnel volume loss. This limitation can be eliminated by replacing the air with water or oil (which may be assumed

incompressible within the range of applied pressures). A concentric fluid-filled flexible membrane (FM) model tunnel has been used by several researchers (Jacobsz, 2003, Loganathan et al., 2000, Vorster et al., 2005); the concentric system implies the flexible membrane is sealed onto a shaft located centrally within the membrane. For fluid-filled FM tunnels, the deformed tunnel shape is somewhat unknown. As discussed in Marshall and Franza (2016) and Ritter et al. (2017), the shape of the tunnel lining is controlled by the equilibrium condition between the pressures from the soil and the fluid within the tunnel. Displacements around real tunnels have been shown to take an eccentric shape, with greater displacements occurring at the tunnel crown compared to the base (invert) (Loganathan and Poulos, 1998). In order to encourage a more realistic profile of displacement, Marshall (2009) modified the flexible membrane model tunnel to create an eccentric shape, where soil displacement at the invert of the tunnel was limited. The eccentric model tunnel system has been applied in several subsequent centrifuge studies related to tunnelling (Farrell, 2010, Franza, 2016, Ritter et al., 2017, Williamson, 2014, Zhou, 2015).

Another option for simulating 2D tunnel displacements in the transverse plane is the use of a rigid boundary mechanical (RBM) model tunnel. With RBM model tunnels, the deformed tunnel shape, and by implication the soil displacements around the tunnel, are known. An RBM model tunnel was developed by Katoh et al. (1998) and has been used by several researchers to study soil-structure interaction problems (Boonsiri and Takemura, 2015a,b). This mechanical tunnel imposes concentric, uniform displacements around its circumference. Shahin et al. (2011) presented a tunnelling device with 12 segments that move vertically downwards and converge towards the tunnel centre during the tunnel volume loss process, achieving a fixed tunnel invert during tunnel volume loss, however the device was not used within a centrifuge. In order to better replicate in a centrifuge the real displacements that occur around shallow tunnels (according to Loganathan and Poulos (1998)), Song et al. (2018) developed an RBM model tunnel that is able to induce an eccentric profile of ground displacements around the tunnel, predominately near the crown. 0.69

In this chapter, three centrifuge tests are conducted using a newly developed eccentric rigid boundary mechanical (eRBM) model tunnel with cover to diameter (C/D) ratios of 1.3, 2.0 and 2.4. Figure 5.1 presents the testing layout. Experimental results are used to explore the effect of the different tunnel boundary conditions on resulting ground deformations.

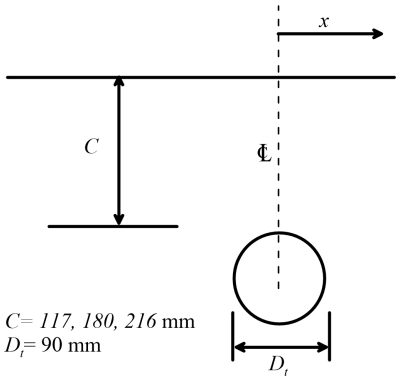


FIGURE 5.1: Test layout in model scale

5.2 Interpretation of measured results

5.2.1 Effect of model tunnel on initial conditions

Before considering tunnel volume loss in detail, it is of interest to investigate the effect of the increased self-weight of the soil in the centrifuge on the soil displacements around the flexible and mechanical model tunnels (i.e. the effect of centrifuge spin-up). For FM model tunnels, the internal tunnel pressure was set to an approximation of the vertical overburden pressure at the tunnel axis depth. The difference in self-weight and lateral earth pressure between the soil and water ($K_0 = 1$ for water; K_0 assumed to be 0.5 for soil) will cause an imbalance of stresses in the region around the model tunnel (also discussed by Ritter et al. (2017)). For the eRBM model tunnel, the tunnel lining was fixed in place (displacement controlled), hence limited displacement is expected for the soil close to the tunnel lining during centrifuge spin-up.

Figure 5.2 shows the centrifuge data for soil movements around the tunnels for the Fraction E sand at a relative density of 90%. Figure 5.2(a) shows that the soil moves downwards in the region above the tunnel crown for both FM and eRBM centrifuge tests.

For the eRBM centrifuge model tunnel, from the horizontal displacement data in Figure 5.2(b), centrifuge model results for the FM model tunnel shows outwards soil movements close to the tunnel springline. This happens because the internal tunnel pressure at the tunnel springline is greater than the horizontal soil pressure, causing the tunnel boundary to push outwards at the springline until an increased passive earth pressure is achieved to balance the internal tunnel pressure.

For the eRBM centrifuge model tunnel, the horizontal displacement for the eRBM did not show a clear mechanism with increase in g-level. Despite the fact that the rigid

boundary was fixed in place initially, the entire mechanical tunnel settled with the increase in g-level due to the increased weight of the tunnel itself.

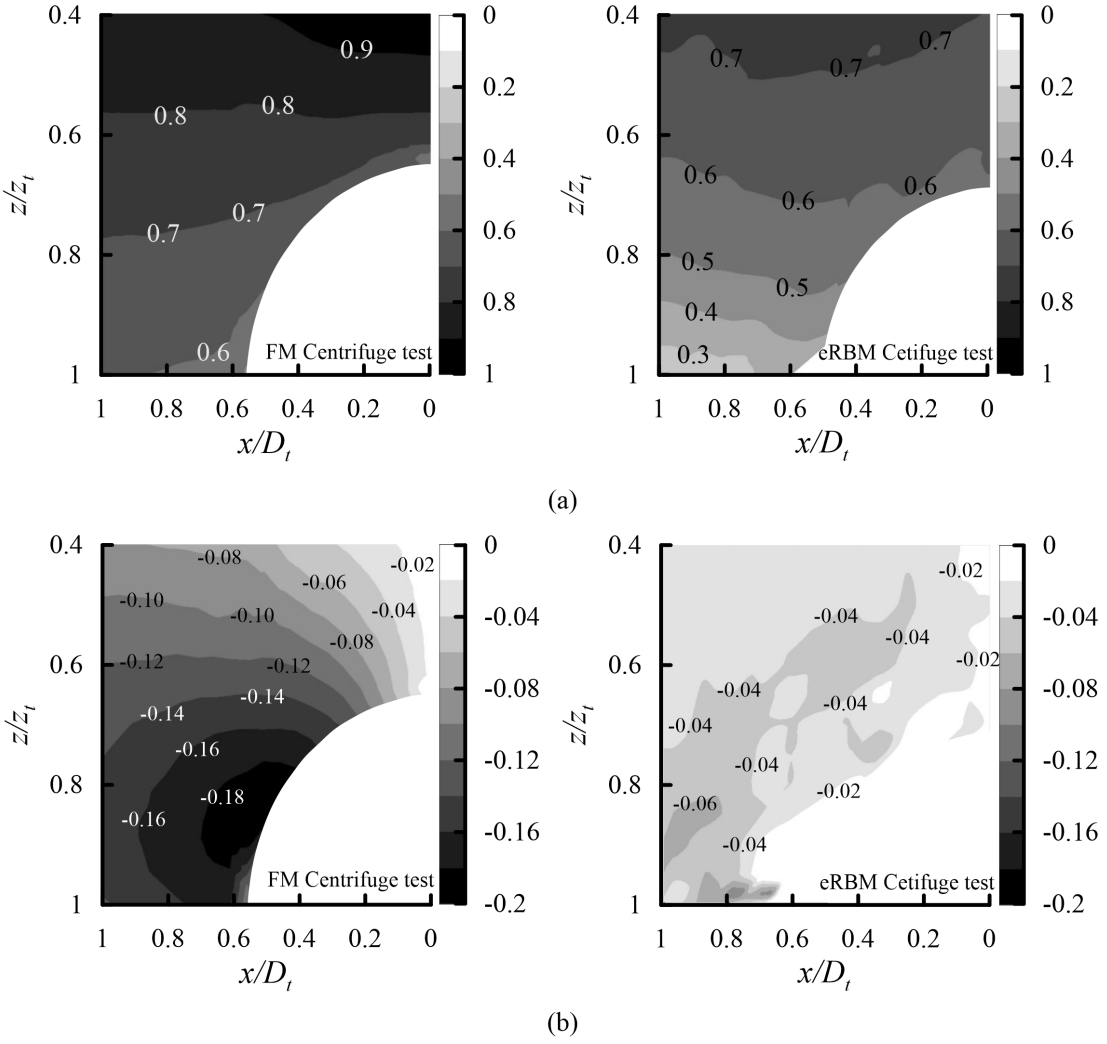


FIGURE 5.2: Soil movements around FM and eRBM model tunnels during centrifuge spin-up: (a) vertical displacements, (b) horizontal displacements

5.2.2 Effect of soil deformation mechanism

For a given tunnel volume loss, the shape and magnitude of soil displacements are affected by the type (displacement/pressure controlled) and displaced shape of the tunnel lining. For eccentric and concentric displacement controlled model tunnels (EDC and CDC, respectively), the displaced tunnel shape is pre-defined, whereas for flexible membrane FM model tunnels, the tunnel boundary shape is free to deform according to the internal/external stresses applied to it. The effect of these differences on resulting ground displacements are considered in this section using centrifuge test data.

Figure 5.3 compares soil displacements from the eccentric rigid boundary mechanical eRBM model tunnel centrifuge test with those from a flexible membrane FM centrifuge test (Franza, 2016) for $C/D = 2$ at a tunnel volume loss of $V_{l,t} = 2\%$. For vertical displacements, the deformation patterns match well between the tests (eRBM and FM); however, the eRBM settlement trough is slightly wider than for the FM model tunnel. For horizontal displacements, the FM model tunnel causes a zone of relatively high magnitude displacements above and slightly to the side of the tunnel crown, as well as a major zone of displacements at the ground surface with a maximum value similar to that near the tunnel. The zone of large horizontal displacements for the eRBM tunnel is located closer to the tunnel springline compared with the FM model tunnel. There is also a large zone of horizontal displacements at the ground surface for the eRBM tunnel, in a similar location but more widespread than that for the FM tunnel; the magnitude of displacements at the ground surface is noted to be less than that at the springline for the eRBM tunnel.

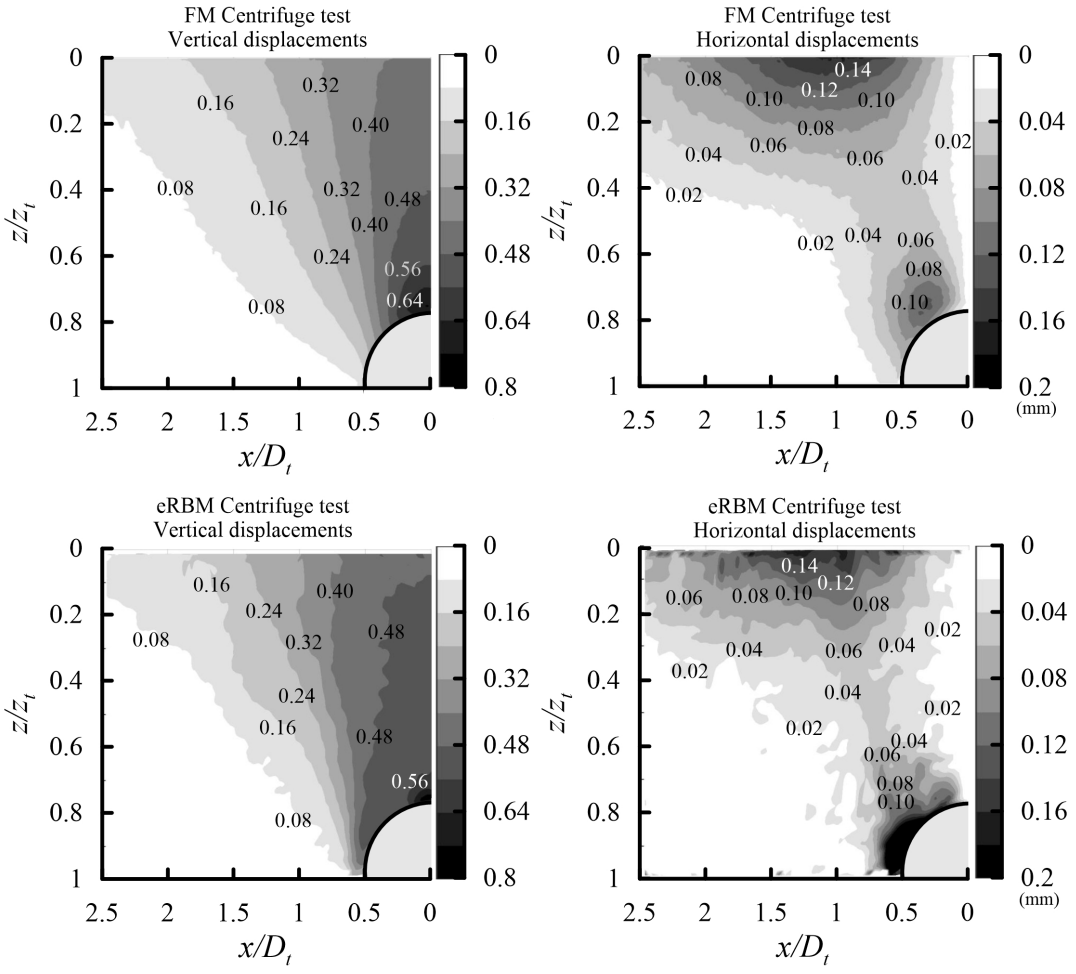


FIGURE 5.3: Centrifuge test results of vertical and horizontal soil displacements for FM and eRBM model tunnels: $C/D = 2$ and $V_{l,t} = 2\%$

5.2.3 Settlement troughs

Figure 5.4 presents the vertical settlement troughs at the surface (z/z_t=0) and subsurface (z/z_t=0.5) for both centrifuge tests (FM and eRBM) at a tunnel volume loss of $V_{l,t} \approx$ 2%. For centrifuge tests (Figure 5.4), settlement troughs provided by Mr. Jingmin Xu (current PhD candidate at NCG) and Marshall (2009) using FM model tunnels are compared against eRBM model tunnel data for C/D = 1.3, 2.0, and 2.4.

In general, for C/D = 2.0 and 2.4, at the given tunnel volume loss of $V_{l,t} \approx$ 2%, the eRBM model tunnel gives a greater maximum settlement at the tunnel centreline than the FM model tunnel. For C/D=1.3, FM and eRBM centrifuge tests show a similar settlement shape and magnitude at the surface. As observed by other researchers (e.g. Franza et al. (2019), Marshall et al. (2012)), the settlement trough shape varies with C/D; a narrower, more chimney-like settlement trough is obtained for C/D = 1.3 than for C/D=2.4. It is believed that such difference in settlement trough shape is mainly due to confining pressure differences with a given z/z_t level (different C/D will result in different confining pressure under a given z/z_t level), for a given tunnel volume loss (shear strain), the soil dilative response is affected by the confining pressure, and this effect will be further discussed later in this chapter (5.2.6).

5.2.4 Change in trough width parameter

The shape of the settlement troughs can be defined by the locations of the inflexion point (i), where $i = K(z_t - z)$, and K is the trough width parameter (Mair et al., 1993). However, the standard use of i and K is not always sufficient to describe the shape of the settlement trough, as identified by Marshall et al. (2012), where different settlement trough curves may have the same value of i. As a result, Marshall et al. (2012) suggested that the shape of the settlement curve could be described by three points related to the Gaussian curve inflexion point (i_g), which is S_{max}, $S_v(i_g) = 0.606\ S_{max}$, and $0.5S_v(i_g) = 0.303\ S_{max}$. The offset of the second and third points ($S_v(i_g)$ and $0.5S_v(i_g)$) are referred to as x^* and x^{**} respectively. These offsets can be defined as $x^* = K^*(z_t - z)$ and $x^{**} = K^{**}(z_t - z)$, where K^* and K^{**} are the trough width parameters.

Figure 5.5 presents data of x^* and x^{**} with soil depth for both centrifuge and finite element analyses at a tunnel volume loss of $V_{l,t} \approx$ 2%. In general, the x^* and x^{**} value decreases with depth. Both centrifuge and finite element analyses show an decrease in values (x^* and x^{**}) with depth, and the values increase with C/D, apart from FM centrifuge tests where C/D=2.4. Marshall (2009) tested the FM model tunnel (C/D =

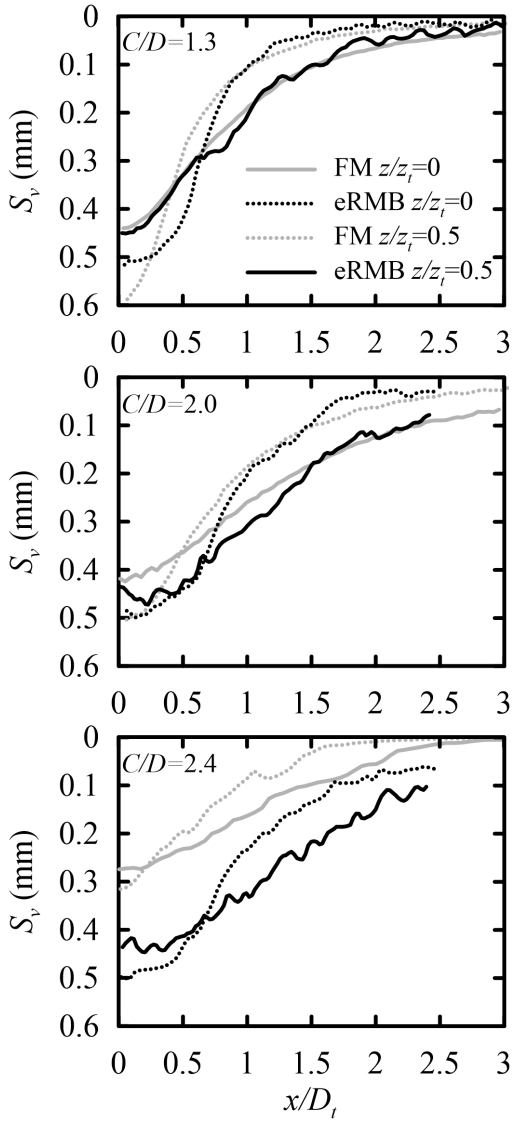


FIGURE 5.4: Settlement trough data at surface and subsurface for $V_{l,t} \approx 2\%$

2.4) using a 62 mm diameter model tunnel, whereas the FM (C/D=1.3 and 2.0) and eRBM model tunnel centrifuge tests here used 90 mm diameter model tunnels. It is believed that a smaller model tunnel will cause a smaller value of x^* and x^{**} at a given tunnel volume loss than using a bigger model tunnel. For example, with a given C/D value, the soil around the tunnel will have lesser confining pressure for the tunnel has a lower z_t depth. With tunnel volume loss (decrease with the tunnel internal water pressure), soil close to the tunnel tends to have greater dilative response. Thus, the horizontal displacement towards the tunnel are expected to be smaller and given a smaller value of x^* and x^{**}. Despite these differences, the value in both centrifuge and finite element analyses show an approximately linear trend with soil depth.

To further study the effect of C/D and tunnel volume loss on settlement trough width parameters (x^* and x^{**}), linear lines were fitted to the results in Figure 5.5, and the

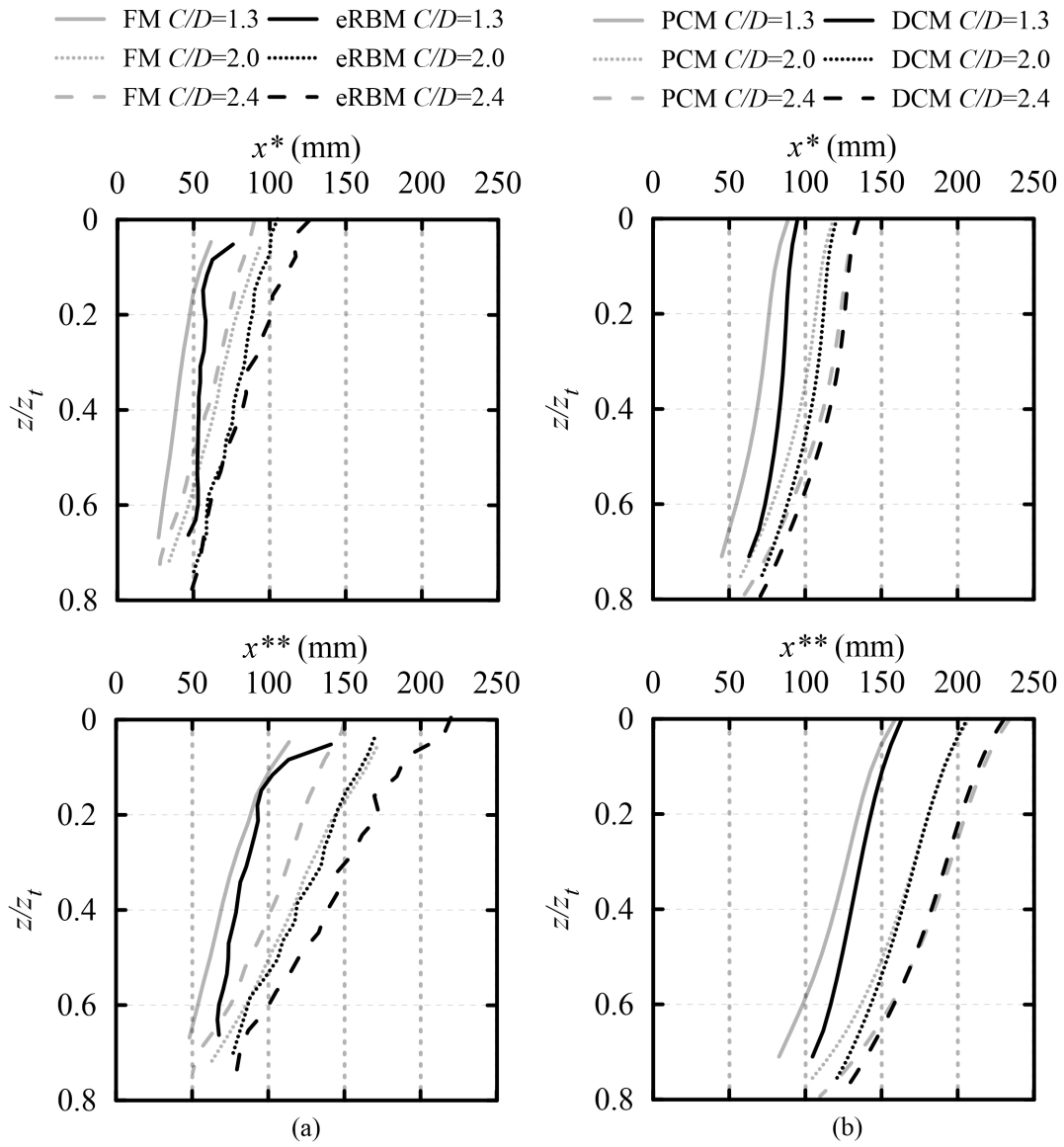


FIGURE 5.5: Variation of x^* and x^{**} with depth at $V_{l,t} \approx 2\%$ for (a) centrifuge test; (b) finite element analysis

slopes of the fitted lines $\partial x^*/\partial z$ and $\partial x^{**}/\partial z$ were calculated. Figure 5.6 (a) shows the values of $\partial x^*/\partial z$ and $\partial x^{**}/\partial z$ with tunnel volume loss. For FM model tunnel, as indicated by Marshall et al. (2012), the variations of $\partial x^*/\partial z$ and $\partial x^{**}/\partial z$ are not significant with tunnel volume loss, and the effect of C/D is not significant. For eRBM model tunnel, however, the values (slopes of the fitted line) tend to increase with tunnel volume loss, and vary with C/D ratio. Figure 5.6 (b) shows the change in trough width parameters at the surface (K_s^* and K_s^{**}) with tunnel volume loss, where $K_s^* = x^*/z_t$ and $K_s^{**} = x^{**}/z_t$. For both FM and eRBM model tunnels, the surface trough width parameters (K_s^* and K_s^{**}) decrease with tunnel volume loss, indicating that the width of the surface settlement trough at lower tunnel volume loss is wider than at higher volume loss, and the settlement trough width increases with C/D ratio.

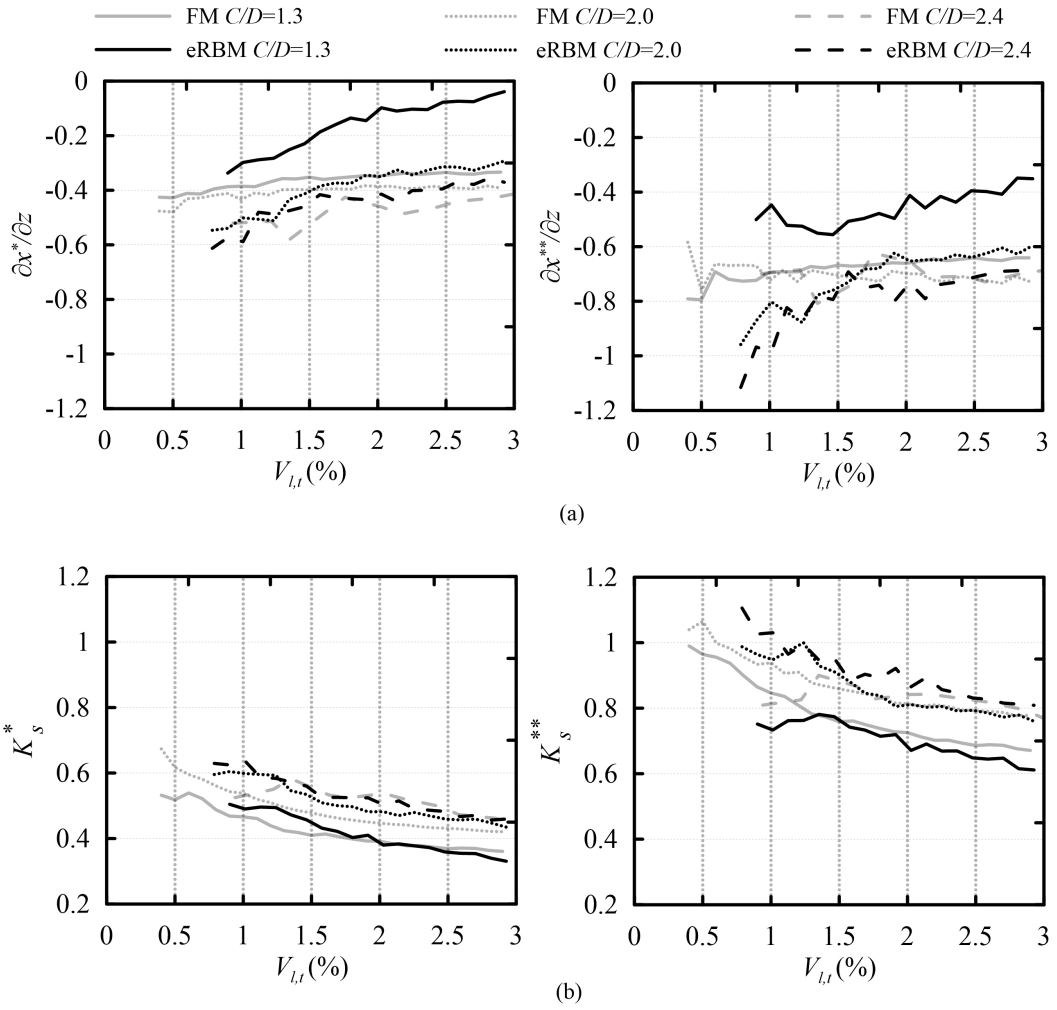


FIGURE 5.6: Centrifuge test fitted curve parameters with volume loss: (a) slope of x^* and x^{**} with depth; (b) surface trough width parameter

Linear lines were fit to the eRBM data presented in Figure 5.6. For $\partial x^*/\partial z$ and $\partial x^{**}/\partial z$ data, the slope of the fitted lines is referred to as $\partial x/\partial z^{*slope}_{V_{l,t}}$ and $\partial x/\partial z^{**slope}_{V_{l,t}}$, respectively. The intercept of the fitted lines at zero tunnel volume loss is denoted by $\partial x^*/\partial z^{int}_{V_{l,t}}$ and $\partial x^{**}/\partial z^{int}_{V_{l,t}}$. Meanwhile, K^*_s and K^{**}_s data can also be fitted with linear lines, and the slope of the lines are defined as $K^{*slope}_{s,V_{l,t}}$ and $K^{**slope}_{s,V_{l,t}}$. The terms $K^{*int}_{s,V_{l,t}}$ and $K^{**int}_{s,V_{l,t}}$ are the interception points for the fitted lines at zero tunnel volume loss. Figure 5.7 plots the features of the linear fitted lines stated above (slope of the line, and the interception point at zero tunnel volume loss).

From Figure 5.7, it can be seen that the relationship between the fitted line features (slope of the lines, and the interception points at zero tunnel volume loss) and C/D ratio is linear. By assessing the fitted line features using a FM model tunnel, Franza (2016) suggested that such fitted line features with C/D ratio may have a non-linear trend at high C/D ratio (transition from shallow to deep tunnels). However, based on

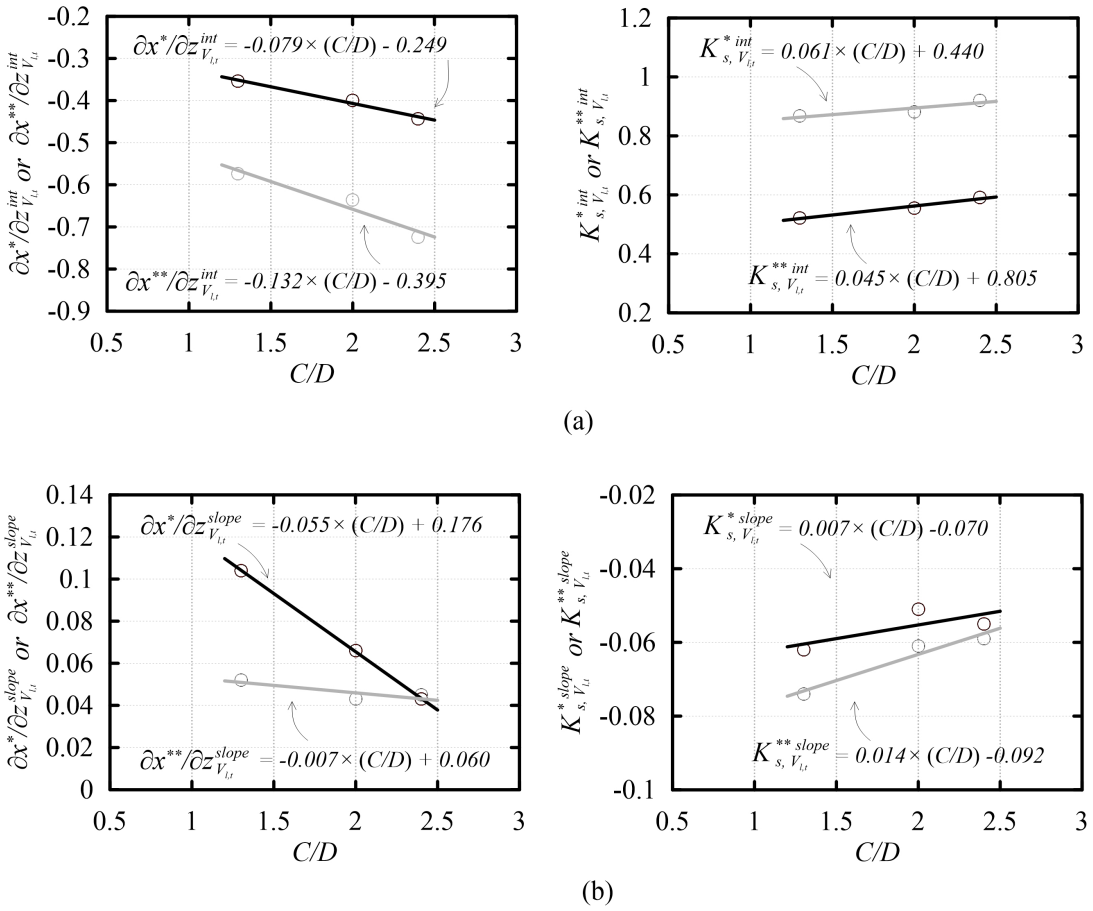


FIGURE 5.7: (a) relationship between intercept of $\partial x^*/\partial z$ or $\partial x^{**}/\partial z$ and $K^*{}_s$ or K^{**} at tunnel volume loss $V_{l,t} = 0\%$ with C/D ratio; (b) slope of the fitted line with C/D ratio

the currently available data using the eRBM model tunnel (C/D=1.3, 2.0 and 2.4), that are generally under a shallow tunnelling scenario, the relationship can be assumed as linear. The equations to calculate the features of the fitted lines in Figure 5.6 are as follows:

$$\begin{aligned}
\partial x^*/\partial z^{int}_{V_{l,t}} &= -0.079 \times (C/D) - 0.249 \\
\partial x^{**}/\partial z^{int}_{V_{l,t}} &= -0.132 \times (C/D) - 0.395 \\
K^{*int}_{s,V_{l,t}} &= 0.061 \times (C/D) + 0.440 \\
K^{**int}_{s,V_{l,t}} &= 0.045 \times (C/D) + 0.805 \\
\partial x/\partial z^{*slope}_{V_{l,t}} &= -0.055 \times (C/D) + 0.176 \\
\partial x/\partial z^{**slope}_{V_{l,t}} &= -0.007 \times (C/D) + 0.060 \\
K^{*slope}_{s,V_{l,t}} &= 0.007 \times (C/D) - 0.070 \\
K^{**slope}_{s,V_{l,t}} &= 0.014 \times (C/D) - 0.092
\end{aligned} \tag{5.1}$$

Thus, based on the equations identified by Marshall et al. (2012), the modified equations to describe the value of settlement trough shape from the centrifuge tests data using the eRBM model tunnel can be expressed as:

$$\begin{aligned} K^* &= \frac{K_s^* + \partial x^*/\partial z(z/z_t)}{1 - z/z_t} \\ K^{**} &= \frac{K_s^{**} + \partial x^{**}/\partial z(z/z_t)}{1 - z/z_t} \\ K_s^* &= K_{s,V_{l,t}}^{*int} + K_{s,V_{l,t}}^{*slope}(V_{l,t}) \\ K_s^{**} &= K_{s,V_{l,t}}^{**int} + K_{s,V_{l,t}}^{**slope}(V_{l,t}) \\ \partial x^*/\partial z &= \partial x^*/\partial z_{V_{l,t}}^{int} + \partial x/\partial z_{V_{l,t}}^{*slope}(V_{l,t}) \\ \partial x^{**}/\partial z &= \partial x^{**}/\partial z_{V_{l,t}}^{int} + \partial x/\partial z_{V_{l,t}}^{**slope}(V_{l,t}) \end{aligned} \tag{5.2}$$

5.2.5 Effect of model tunnel on settlement trough shape characteristics

To further investigate settlement trough shape characteristics, modified Gaussian curves (Vorster et al., 2005) were fitted using the approach of Marshall et al. (2012), who indicated that the conventional Gaussian curve does not always provide a good fit to settlement data for tunnels in sand, which is substantiated by several other studies (Franza and Marshall, 2018, Franza et al., 2019, Marshall et al., 2012, Vorster et al., 2005, Zhou et al., 2014). The goodness of fit (based on the coefficient of determination R^2) of the modified Gaussian curve to vertical displacements was evaluated for the FM and eRBM centrifuge test data. R-Square is defined as the ratio of the sum of squares of the regression (SSR) and the total sum of squares (SST) (R-Square=SSR/SST). Figure 5.8 demonstrates that the modified Gaussian curve provided a very good fit to centrifuge data, but indicates a slight reduction in the goodness of fit to the eRBM centrifuge test data with depth, especially below z/z_t=0.6. Analyses presented next are based on the obtained curve fitting results using the modified Gaussian curve.

Figure 5.9 presents the trough width parameters K^* and K^{**} with soil depth for centrifuge tests at a tunnel volume loss of $V_{l,t} \approx 2.0\%$. The FM model tunnel centrifuge tests give lower trough width parameters than the eRBM model tunnel tests, and the FM K^* values do not increase with depth as quickly as they do for the eRBM model tunnel. With an increase in C/D ratio, the difference in K^* and K^{**} between FM and eRBM model tunnels decreases; at $C/D = 2.4$, the values of K^* and K^{**} are very close for $z/z_t \leq 0.6$.

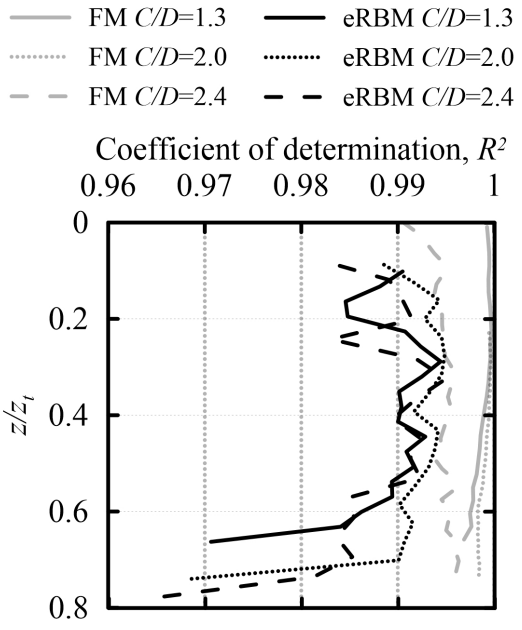


FIGURE 5.8: Goodness of fit of modified Gaussian curves to centrifuge data

5.2.6 Relationship between soil and tunnel volume loss

Figure 5.10 shows the relationship between surface soil volume loss ($V_{l,s,surf}$; calculated as the integration of surface settlement data) and tunnel volume loss ($V_{l,t}$; obtained directly from the displacements or volume changes of the model tunnels) for both FM and eRBM model tunnel centrifuge tests. Note that for an undrained case (zero volumetric strain), $V_{l,s,surf} = V_{l,t}$. As discussed in Marshall et al. (2012) and Franza et al. (2019), for dry sand (or drained soil conditions), soil volume loss will differ from tunnel volume loss due to the dilative/contractive nature of the soil, which depends on the relative density of the soil, magnitude of the shear strain, and the confining pressures during shear. At a given soil depth (z/z_t), if the value of $V_{l,s,surf}$ is lower than $V_{l,t}$, the soil below that level has undergone an overall dilative response. For the FM model tunnel with $C/D = 1.3$, $V_{l,s,surf}$ is always less than $V_{l,t}$, indicating that the soil below the surface experienced a dilative response, whereas for $C/D = 2.0$ and 2.4, the value of $V_{l,s,surf}$ is greater than $V_{l,t}$ for tunnel volume losses lower than $V_{l,t} \approx 1.8\%$ and 2.3%, respectively. This indicated a contractive soil behaviour under the surface level. These trends are consistent with the expected effect of C/D, where the soil above shallower tunnels is more dilative because the soil is under lower levels of confining stress. The trends of the data for the eRBM model tunnel follow those of the FM model tunnel, however the eRBM values of $V_{l,s,surf}$ are consistently lower than the FM values, indicating more dilative conditions in the eRBM tests. This suggests that the magnitude of shear strains around the tunnel circumference in the eRBM model tunnel tests were greater than in

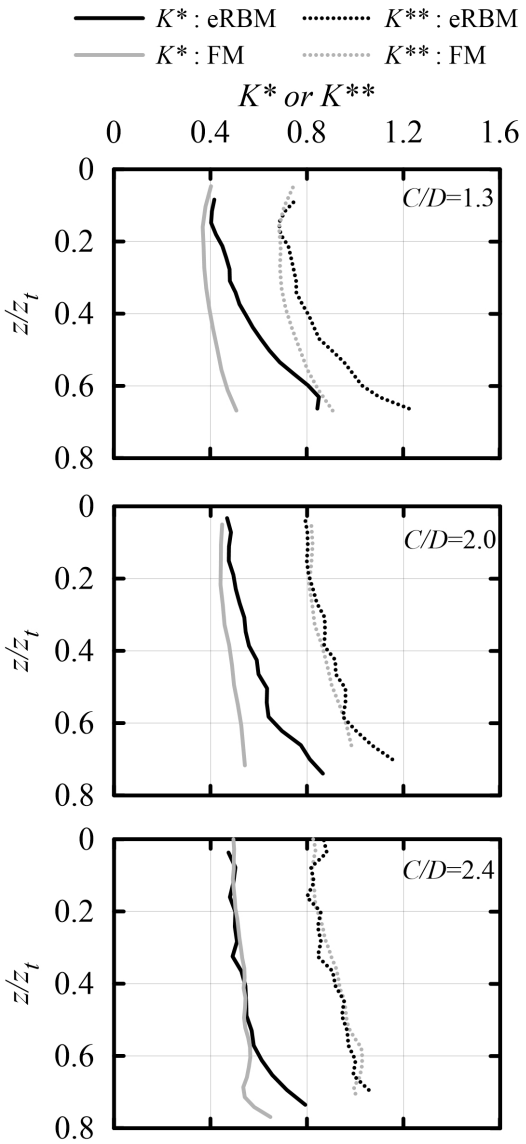


FIGURE 5.9: K^* and K^{**} with depth for centrifuge tests at $V_{l,t} \approx 2.0\%$

the FM model tunnel tests. The magnitude of shear strain around the tunnel boundary is discussed next.

The accumulated soil response indicated by $V_{l,s}$ averages out localised volumetric response within the depth of the soil; the soil may experience localised contraction at a certain depth yet $V_{l,s}$ could still indicate an overall dilative response. To investigate this feature, Figure 5.11 plots soil volume loss ($V_{l,s}$) with depth at a tunnel volume loss of $V_{l,t} \approx 2.0\%$ for both centrifuge tests (FM and eRBM model tunnels). The vertical dashed lines indicate a constant-volume condition (undrained condition). From Figure 5.11, $V_{l,s}$ values are always less than $V_{l,t} \approx 2.0\%$, apart from the FM $C/D = 2.4$ test, where the cumulative soil response close to the surface ($z/z_t < 0.1$) gives a soil volume loss slightly greater than 2.0%. The value of $V_{l,s}$ for the centrifuge tests reduces

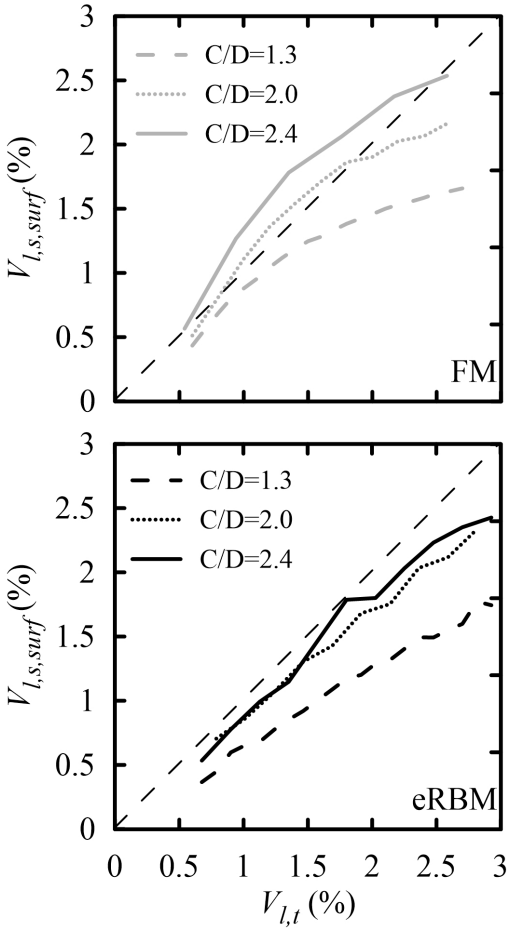


FIGURE 5.10: Variation of surface soil volume loss with tunnel volume loss for both FM and eRBM model tunnels

approximately linearly with depth (z/z_t) and shows a maximum value at the soil surface and a minimum value close to the tunnel crown. The soil volume loss at a given depth also differs with C/D ratio, where a greater C/D gives a higher soil volume loss. For centrifuge tests with $C/D = 1.3$ (both FM and eRBM), the soil close to the tunnel crown ($z/zt \approx 0.7$) shows a value of $V_{l,s}$ less than $V_{l,t}$ by almost 50%. These data indicate that the soil experienced considerable localised dilation below $z/zt \approx 0.7$. In addition, with a decrease in z/z_t (further away from the tunnel), the value of $V_{l,s}$ tends to increase, suggesting that the soil above $z/z_t = 0.7$ underwent overall contraction.

For greater tunnel depths (greater mean effective stress), the soil will tend to have a greater contractive response (less dilative). The rate of change of contractive response with depth can be indicated by the slope of $V_{l,s}$ with depth. The slope for $C/D = 1.3$ for both centrifuge model tunnels (FM and eRBM) is less than for $C/D = 2.0$ and 2.4, indicating that for a given shear strain, the soil in $C/D = 1.3$ tests is less contractive than the soil in the tests with greater tunnel depths ($C/D = 2.0$ and 2.4).

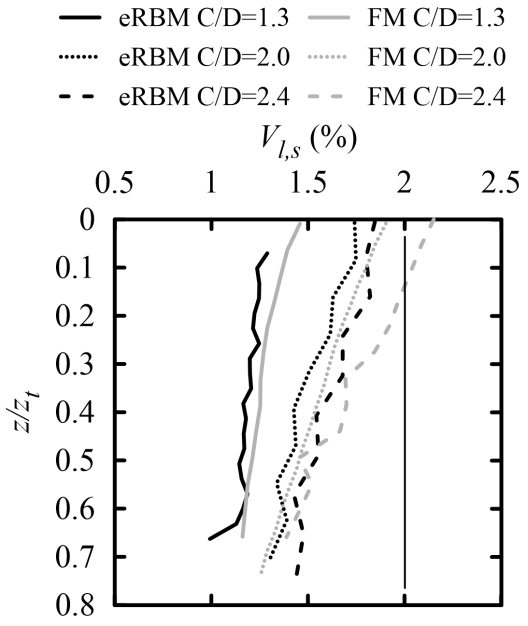


FIGURE 5.11: Variation of $V_{l,s}$ with depth at $V_{l,t} \approx 2.0\%$

To summarise from Figure 5.11, soil experienced strong localised dilation below $z/zt \approx 0.7$ (close to the tunnel boundary), the soil above the $z/zt \approx 0.7$ level underwent contractive response, and the rate in change of contractive response with soil depth under a given tunnel volume loss ($V_{l,t} \approx 2.0\%$) is affected by the C/D value.

Figure 5.12 shows the spatial distribution of volumetric and shear strains from the eRBM and FM centrifuge tests for $C/D = 2.0$ at a tunnel volume loss of $V_{l,t} = 2.0\%$. Both model tunnels indicate concentrated zones of shear and negative volumetric (dilation is negative) strain close to the tunnel boundary; near the crown/shoulder for the FM test and closer to the tunnel springline for the eRBM test. The magnitudes of the shear and volumetric strains for the eRBM test are considerably larger than for the FM test, confirming the conclusions made earlier (i.e. eRBM values of $V_{l,s,surf}$ are consistently lower than the FM values, indicating more dilative conditions in the eRBM test). In Figure 5.12, the highlighted regions of dilating soil are very localised around the tunnel; the majority of the soil is contractive, which explains the trends in Figure 5.11a (i.e. an increase in soil volume loss with a decrease in depth, suggesting contractive soil behaviour above $z/z_t \approx 0.7$).

Figure 5.13 summarises the key features from the shear and volumetric strain distributions of the centrifuge tests. For a given tunnel volume loss, the eRBM model tunnel causes higher magnitude shear strains than the FM model tunnel, resulting in a more dilative volumetric response in the eRBM test than the FM test. The zone of dilating soil for the FM model tunnel is located above the tunnel crown, whereas for the eRBM model tunnel, the zone is located above the tunnel springline. The soil located outside

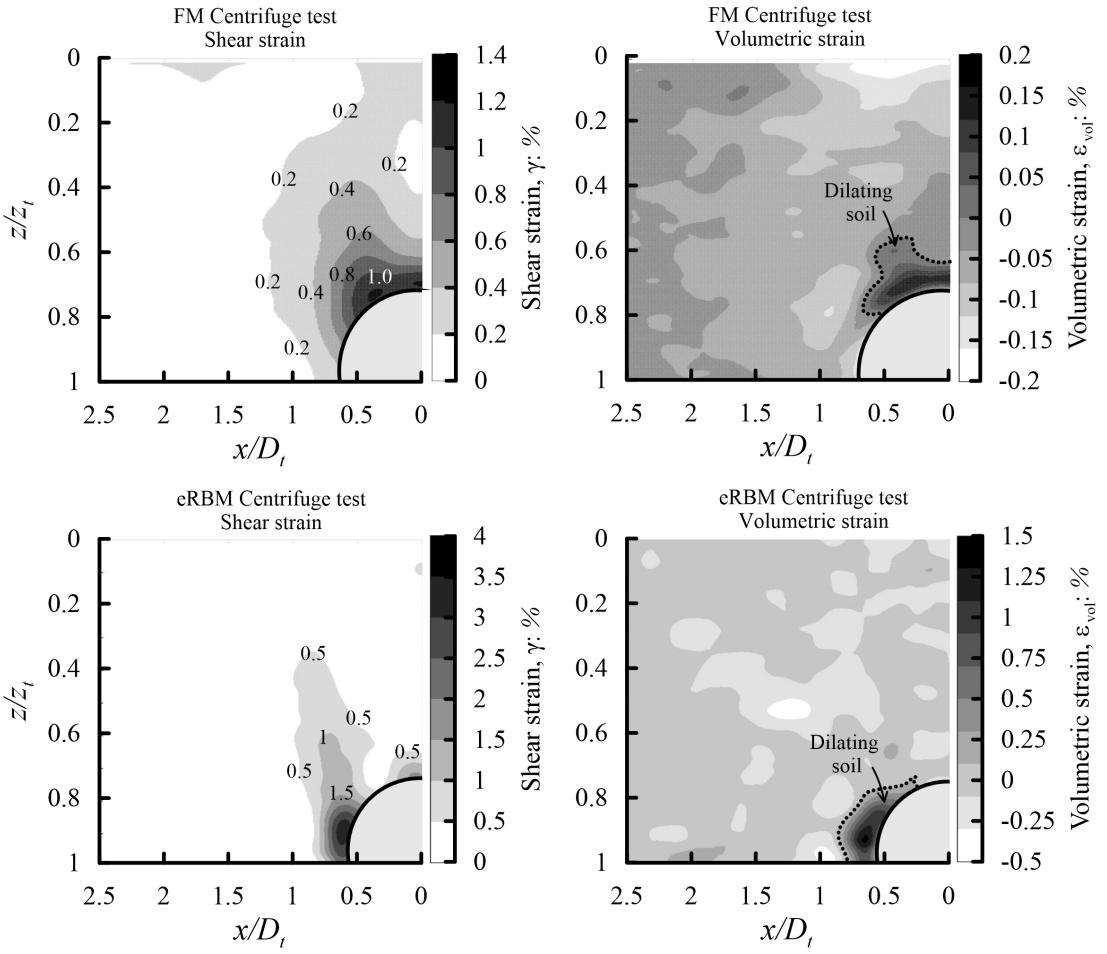


FIGURE 5.12: Contours of shear and volumetric strain for centrifuge test $C/D = 2.0$ at $V_{l,t} = 2.0\%$

the dilative area undergoes contractive soil behaviour, hence soil volume loss increases as depth decreases.

5.3 Conclusions

This chapter presented the results of three centrifuge tests using the eRBM model tunnel, along with data from FM model tunnel tests from various sources. Finite element analyses were also conducted, which simulated two different tunnel volume loss techniques: pressure controlled (replicating FM model tunnel) and displacement controlled (replicating the eRBM model tunnel). Based on the results obtained above, the following conclusions can be made:

- The newly developed eccentric rigid boundary mechanical model tunnel allows replication of non-uniform radial displacements around the tunnel boundary, with

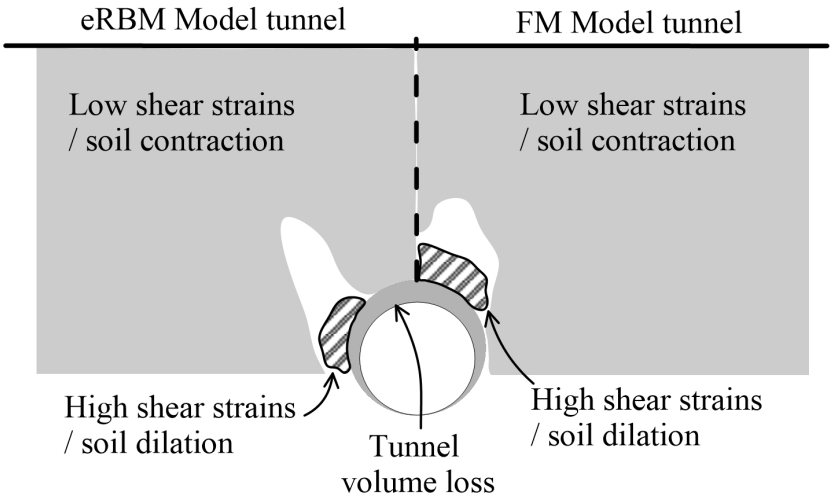


FIGURE 5.13: Illustration of soil strains due to tunnel volume loss based on the observations in Figure 5.12

maximum displacements at the tunnel crown and zero displacements at the tunnel invert.

- For centrifuge tests, during the g-level increase, the internal tunnel pressure for FM tunnels at the springline is higher than the horizontal soil pressure, which can cause the flexible membrane boundary to push outwards and increase the horizontal stress in the soil around the tunnel springline. The overall shape of the eRBM model tunnel does not change as significantly as the FM model tunnel during centrifuge spin-up.

- At a given tunnel volume loss, the eRBM model tunnel showed a similar magnitude and shape in vertical settlement to the FM model tunnel. However, for horizontal displacements, the eRBM model tunnel gives greater magnitudes than the FM model tunnel and generated a zone of major horizontal displacements located close to the tunnel springline.

- A set of the equations was developed based on eRBM model tunnel centrifuge tests to predict the settlement trough width parameters K^* *and* K^{**}. The centrifuge results showed that the eRBM model tunnel always provided a wider settlement trough than the FM model tunnel.

- The surface soil volume loss $V_{l,s}$ for the eRBM model tunnel was generally smaller than the tunnel volume loss $V_{l,t}$, suggesting that the soil below the surface has an accumulated dilative soil response. The soil volume loss close to the tunnel crown was smaller than the tunnel volume loss for all centrifuge tests, indicating that the soil close to the tunnel crown was undergoing dilation. For soil above the tunnel

crown, an increase in soil volume loss with a decrease in soil depth was observed. This increase in soil volume loss indicates an overall soil contractive behaviour above a depth of z/z_t=0.7, but based on the volumetric strain distribution identified by Franza et al. (2017) and Marshall et al. (2012), localised soil dilation is expected for the soil close to the tunnel centreline.

Chapter 6

The effect of tunnelling on piled structures

6.1 Introduction

Underground tunnels in urban areas are increasingly excavated close to and underneath existing infrastructures. The study of tunnelling-induced ground movements on infrastructures has received particular attention by researchers around the world using numerical analysis, analytical solutions and centrifuge modelling (e.g. Burland et al. (2001), Mair (2008), Marshall et al. (2010), Marshall and Mair (2011), Potts and Addenbrooke (1997), Poulos (2006), Standing and Potts (2008)). By successfully applying advanced constitutive soil models, several authors have investigated the effect of tunnelling on piled foundations using numerical approaches (e.g. Hong et al. (2015), Lee (2012), Ng et al. (2015)). The complex non-linear soil behaviour and soil-structure interactions predicted through numerical simulations should be validated via laboratory and/or field data. Centrifuge modelling has been widely accepted as a tool to investigate the complex tunnel-pile-structure interaction (TPSI) problem (e.g. Franza and Marshall (2017), Jacobsz et al. (2004), Lee and Chiang (2007), Loganathan et al. (2000), Marshall and Mair (2011), Ng et al. (2014)). This chapter will present new centrifuge test data related to tunnel-pile and tunnel-pile-structure interaction. These data may prove useful for the verification of others' numerical and analytical outcomes.

Physical models of piled structures require some degree of simplification compared to reality. For example, a superstructure (building) can be simplified as constant load piles with an equivalent beam/plate (i.e. piles are rigidly connected to a plate). Simplified physical models could over- or under-predict the contribution of superstructure to the global TPSI problem. For society and public safety, it is essential to understand and

evaluate the potential damage of a superstructure caused by tunnelling-induced ground movements. Furthermore, it is beneficial to improve the accuracy of superstructure simulation within geotechnical centrifuge tests.

In this chapter, the global TPSI problem is investigated using the novel CCNM (coupled numerical-centrifuge method) approach (Franza et al., 2019), which was discussed in Chapter 4.3.7. Tunnel volume loss is simulated using the eRBM (eccentric rigid boundary mechanical) model tunnel. The outcomes from four centrifuge tests are presented in this chapter: (1)"greenfield" (only soil and isolated piles are considered) pile jacking test (Test PJ), (2) TPSI test with constant load pile group (Test CL), (3) TPSI test with pile group test that considered structure stiffness (CCNM) and tunnel volume loss up to $V_{l,t}$=2.2% (Test CCNM1), (4) repeat of test CCNM1 with tunnel volume loss up to $V_{l,t}$=3.2% (Test CCNM2). The detailed testing plan and experimental programmes were described in Chapter 4.3.1.

This chapter is structured as follows. The first section of the chapter presents the pile jacking results and illustrates the pile axial load capacity. Two different structure stiffnesses are investigated, which are fully flexible (constant load on each pile) and full structure stiffness (structure stiffness simulated using a numerical model within the CCNM application). The results of pile settlement and load transfer between the piles due to tunnelling-induced ground movements are discussed. Then, the axial force along the pile during tunnel volume loss measured by FBG (fibre Bragg grating) sensors are presented. Finally, after tunnel volume loss, the piles are further jacked into the soil, and the post-tunnelling pile capacity is determined and compared with the outcomes from "greenfield" pile jacking (Test PJ). All results are reported in model scale unless otherwise stated, and centrifuge tests described in this chapter were tested under 80 g.

6.2 Interpretation of measured results

6.2.1 Axial force along the pile after centrifuge acceleration

A constant 5 N vertical load was applied to the pile head (load controlled) during centrifuge spin-up (acceleration to 80 g). This was done to ensure minimum relative displacement occurred between the soil and pile during spin-up (if the pile is fixed in place during spin-up, the soil will settle more than the pile). Three stabilisation cycles (going from 80 g to 10 g and back to 80 g) were performed to encourage a uniform stress distribution within the soil body and to improve repeatability between the centrifuge tests.

Figure 6.1 shows the axial force along the pile after centrifuge acceleration for all four centrifuge tests; the dotted grey line represents the theoretical self-weight of the pile after centrifuge acceleration; the surface is at a y-axis value of 0 mm. All piles show an increase in axial force with centrifuge acceleration, and that axial force along the pile gradually increased with depth. It is believed that such an increase in axial force along the pile is caused by (a) the increased self-weight of the pile and (b) the shear force around the soil-pile interface. The data indicates that the soil located close to the upper portion of the pile tends to settle more than the pile, causing a downwards "drag" force along the pile. As a result, the axial force of the pile increased with depth along the upper portion of the pile (0-80 mm below the soil surface). To further investigate the axial force distribution along the pile after centrifuge acceleration, it is necessary to compare soil settlements with depth against pile settlement; this is presented in section 7.2.1.

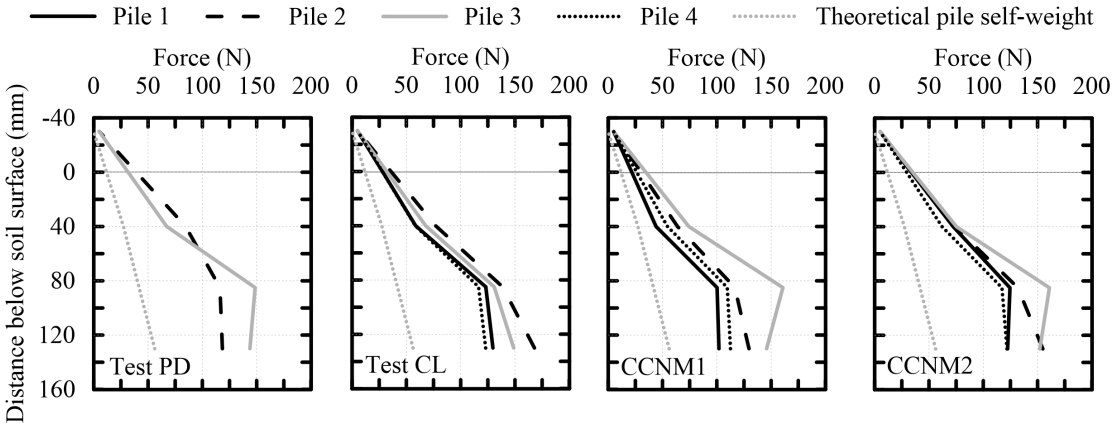


FIGURE 6.1: Axial force along the pile after centrifuge acceleration

6.2.2 Determination of pile axial load capacity

The pile axial load capacity was determined by in-flight pile jacking tests. All four piles (Test PJ) were jacked in the order of pile number: 2-4-3-1 (model tunnel was not included, refer to Figure 4.8 for pile numbering). Displacement control was used to perform pile jacking, with an actuator displacement rate of 0.1 mm/s. Note that this is the speed of the actuator; the rate of pile displacement varies somewhat during jacking due to the effect of the die spring. Figure 6.2 presents the load versus pile settlement (S_p) normalised by the pile diameter (d_p) for all four piles. Piles 1 and 2 provided relatively consistent results, but the curves are different between piles 3 and 4, which indicate a stiffer pile jacking response than piles 1 and 2. This occurred because piles 3 and 4 were "new" piles, which had not previously been jacked within centrifuge tests. As a result, the surface roughness of piles 3 and 4 was greater than piles 1 and 2. It can be assumed that the repeated use of the model piles will cause pile shaft roughness

degradation; Jacobsz (2003) reported a similar issue that surface roughness of the pile reduced with repeated usage. The effect of pile roughness on pile loading tests will be further discussed in Section 6.2.3.

For a conservative estimation of pile axial load capacity, the results from pile 2 are considered. The assumption was made that the ultimate load capacity of a non-displacement pile is defined at the point when the pile shaft resistance is fully mobilised. The accumulated shaft resistance (as a force) along the pile 2 is shown in Figure 6.3, which demonstrates that shaft resistance was fully mobilised at S_p/d_p of about 8% (this was sufficiently consistent and conservative for all piles). This magnitude of settlement corresponds closely to the point where the rate of pile settlement versus head load increased (see Figure 6.2). At S_p/d_p=8 %, pile 2 capacity was 893 N (see Figure 6.2), which is a conservative value for all piles. Considering the total load applied to piles during the tunnel-pile interaction tests (255/370 N for outer/inner piles at model scale), this gives a factor of safety of 3.5 and 2.4 for outer and inner piles, respectively.

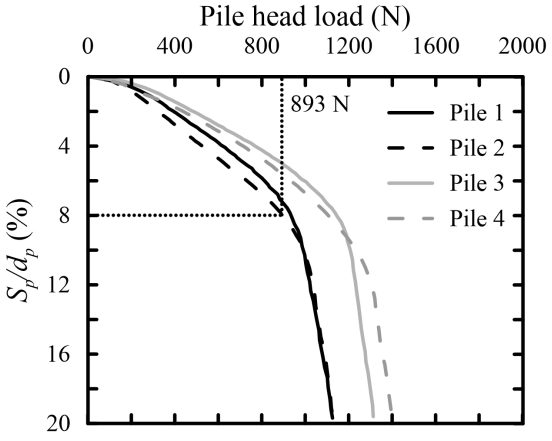


FIGURE 6.2: Load settlement curve for pile jacking test

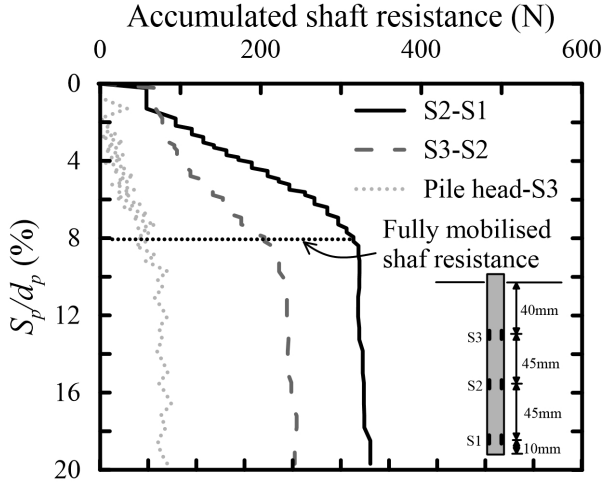


FIGURE 6.3: Shaft resistance during pile jacking test: pile 2

To further investigate the pile jacking response (pile jacking stiffness) with the increase in pile head load, the global pile stiffness versus pile head load is presented in Figure 6.4. The global secant stiffness of the pile is determined as the change in pile head load (ΔQ_t) from the initial pile head load prior to pile driving, divided by the pile head settlement (S_p). The initial stiffness for all piles is between 4000-6000 N/mm; with further increase in pile head load, the pile stiffness decreased. The trend of global stiffness degradation in pile head load is non-linear, and can generally be categorised into three stages (see Figure 6.4):

1. **Global stiffness degradation stage (GSDS) 1**: rapid degradation at the start of pile jacking, this stage typically has a decrease in stiffness of around 3000 N/mm with an increase in pile head load of about 200 N.

2. **GSDS 2**: progressive stiffness degradation with further increase in pile head load, a typical decrease in stiffness of about 1000 N/mm with an increase in pile head load of around 600 N.

3. **GSDS 3**: rapid decrease in pile stiffness, in which the pile head load can be assumed to be close to the axial load capacity of the pile.

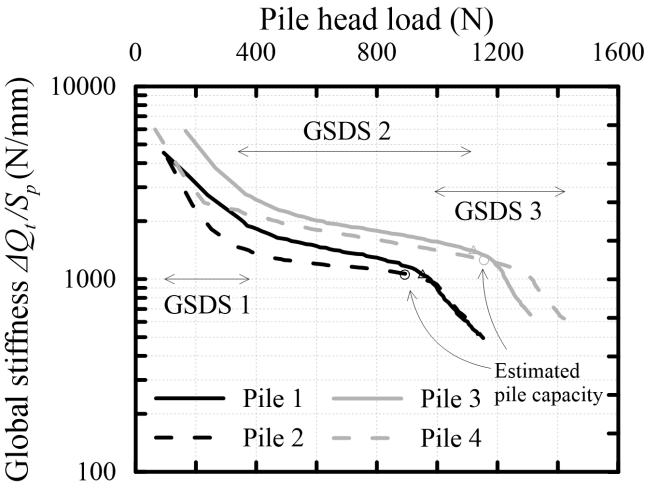


FIGURE 6.4: Global pile stiffness versus pile head load for test pile jacking

6.2.3 Pile loading

After centrifuge acceleration (including three stabilisation cycles), the piles were loaded to the designated working load (255 N for outer piles 1 and 4, and 370 N for inner piles 2 and 3; refer to pile numbering in Figure 4.8) in 50 N stages, starting with pile 1 and moving sequentially to pile 4. Figure 6.5 shows the axial force distribution along the pile before and after pile loading. With the increase in pile head load, all piles show an

increase in axial force along the pile. After pile loading, the axial force at the upper portion of the pile (0-40 mm below the soil surface) presents a similar value to the pile head load, suggesting that the shaft friction along the upper portion of the pile is minimal. The axial force decreases with depth along the middle and lower portions of the pile, indicating that the shaft friction at the lower portion of the pile is mobilised. Thus, the amount of increase in axial force close to the pile tip is generally less than the pile head load applied (pile head load was taken by the shaft friction along the middle and lower portion of the pile).

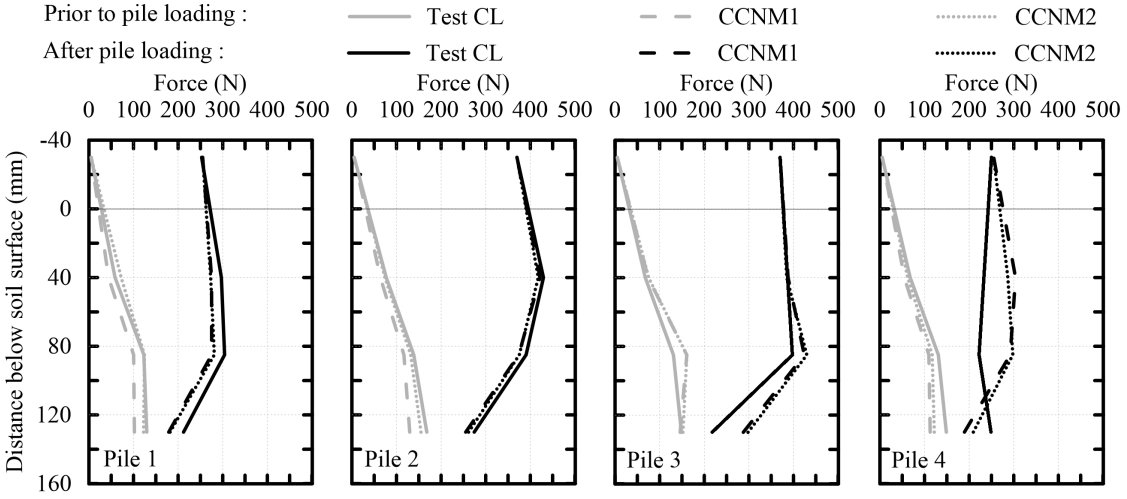


FIGURE 6.5: Axial force along the pile before and after pile loading

Figure 6.6 shows the pile head load against normalised pile settlement during pile loading for Test CL, CCNM1 and CCNM2. In section 6.2.2, the pile jacking results suggested that the pile shaft roughness degradation could affect the pile jacking behaviour. However, the pile loading results in Figure 6.6 show good repeatability between the tests; hence, it can be suggested that the repeated use of the model piles within the centrifuge tests (Test CL, CCNM1 and CCNM2) did not have a significant effect on the pile loading results. It is believed that the effect of pile shaft roughness degradation on pile loading response also depends on the level of force applied to the pile. The amount of pile head load applied in pile loading tests (255/370 N for outer/inner piles) is much smaller than the force during pile jacking test (in Test PJ, the ultimate axial load was 893 N, see section 6.2.2). Therefore, it can be concluded that the effect of pile shaft roughness degradation on pile loading response was not significant.

Pile loading will cause disturbance to the adjacent pile, and consequently affect its pile loading response. Figure 6.7 shows the load versus pile settlement data for piles 2 and 3 during the pile loading stage for all three centrifuge tests. Pile 2 was loaded prior to pile 3 in all three tests; at a given pile settlement, pile 3 shows a greater pile head load than pile 2. To further investigate the effect of pile loading on adjacent piles, Figure 6.8

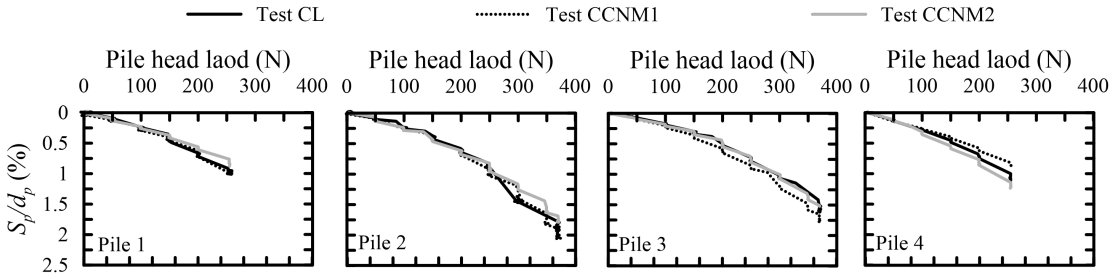


FIGURE 6.6: Load settlement curve for piles during pile loading

(a) shows pile 3 settlement during pile 2 loading, and (b) shows the changes in axial force along pile 3 after pile 2 loading for centrifuge tests CCNM1 and CCNM2. After pile 2 loading, the axial force close to pile 3 tip increased by 2.8 N and 3.9 N in tests CCNM1 and CCNM2, respectively. In addition, after pile 2 loading, pile 3 settled by about S_p/d_p=0.14 % in both tests. This outcome suggests that for the experimental setup used in these tests, loading of a pile causes the adjacent piles to settle by about 10% of the amount of the loaded pile and the amount of increase in axial force close to the tip of the adjacent pile is not significant.

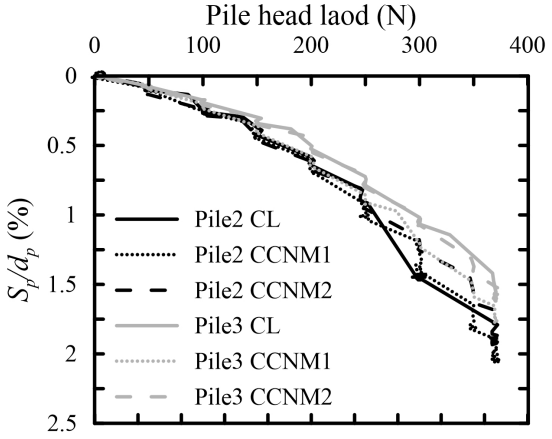


FIGURE 6.7: Load settlement curve for piles 2 and 3 during pile loading

6.2.4 Effect of structure stiffness on pile settlement due to tunnel volume loss

The results from three centrifuge tests (CL, CCNM1 and CCNM2) are used to investigate the effect of structure stiffness on pile settlements caused by tunnelling-induced soil movements. To isolate the effect of structure stiffness on pile settlements, a constant pile head load (load controlled) centrifuge test was first conducted (Test CL), which is equivalent to a zero stiffness structure. This was followed by two centrifuge tests (CCNM1 and CCNM2); the only difference between tests CCNM1 and CCNM2 was

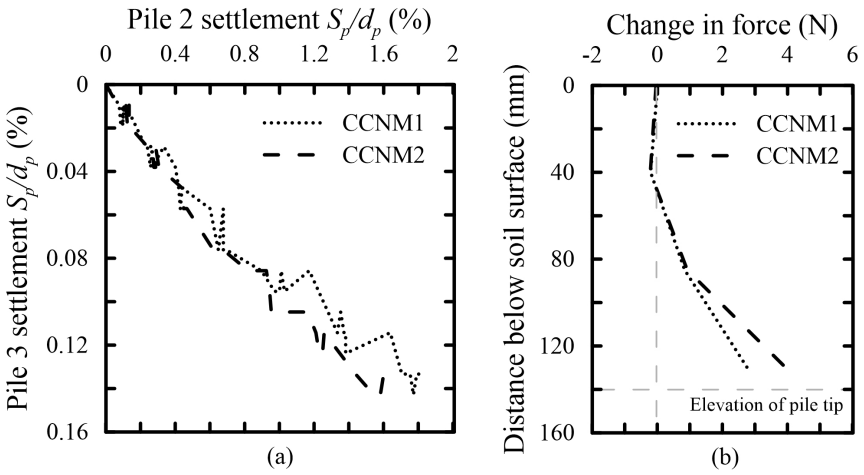


FIGURE 6.8: (a) Pile 3 settlement during pile 2 installation (b) Change in axial force along the pile 3 after pile 2 installation

the maximum tunnel volume loss reached was $V_{l,t}$=2.2 % and 3.2%, respectively. The purpose of having two different values of $V_{l,t}$ was to evaluate the effect of tunnel volume loss on post-tunnelling pile jacking response (discussed later).

Figure 6.9 presents the pile head settlement with tunnelling for all three centrifuge tests, as well as the greenfield tunnelling surface and subsurface (at pile tip depth) soil displacements at the location of each pile (note that the scales vary in each plot). The greenfield tunnelling test (Test GF) layout and testing configurations were discussed in Chapter 4.4.1. In general, pile 1 shows greater settlement with tunnel volume loss than all other piles. For pile 1, the difference in the settlement between Test CL and CCNM1 / CCNM2 is not significant. Compared with the greenfield settlement, pile 1 shows a greater settlement with tunnelling than the surface and subsurface soil settlement. For pile 2, pile head settlement in test CCNM2 became greater than test CL with the increase in tunnel volume loss, and for CCNM1 the pile 2 settlement shows a close match to test CL. In addition, the pile 2 settlements for all three centrifuge tests are less than the greenfield surface settlement and higher than the subsurface settlement (at pile tip depth). For pile 3, the settlement in test CCNM1 and CCNM2 is slightly greater than in test CL, the settlement of the pile is close to the subsurface greenfield soil settlement, and with tunnel volume loss, the pile settlements are less than the greenfield surface soil settlement. For pile 4, the difference in pile settlement between the tests is not significant; the greenfield soil displacements are not available at the location of pile 4 because pile 4 is located close to the strong box boundary and outside the camera field of view. Based on the results from pile 3, it is believed that the pile 4 settlement is close to the greenfield subsurface soil settlement.

Based on the results from CCNM1 and CCNM2, the pile head settlement (S_p) is a combination of settlement caused by (1) the tunnel volume loss ($S_{p,t}$) and (2) the effect

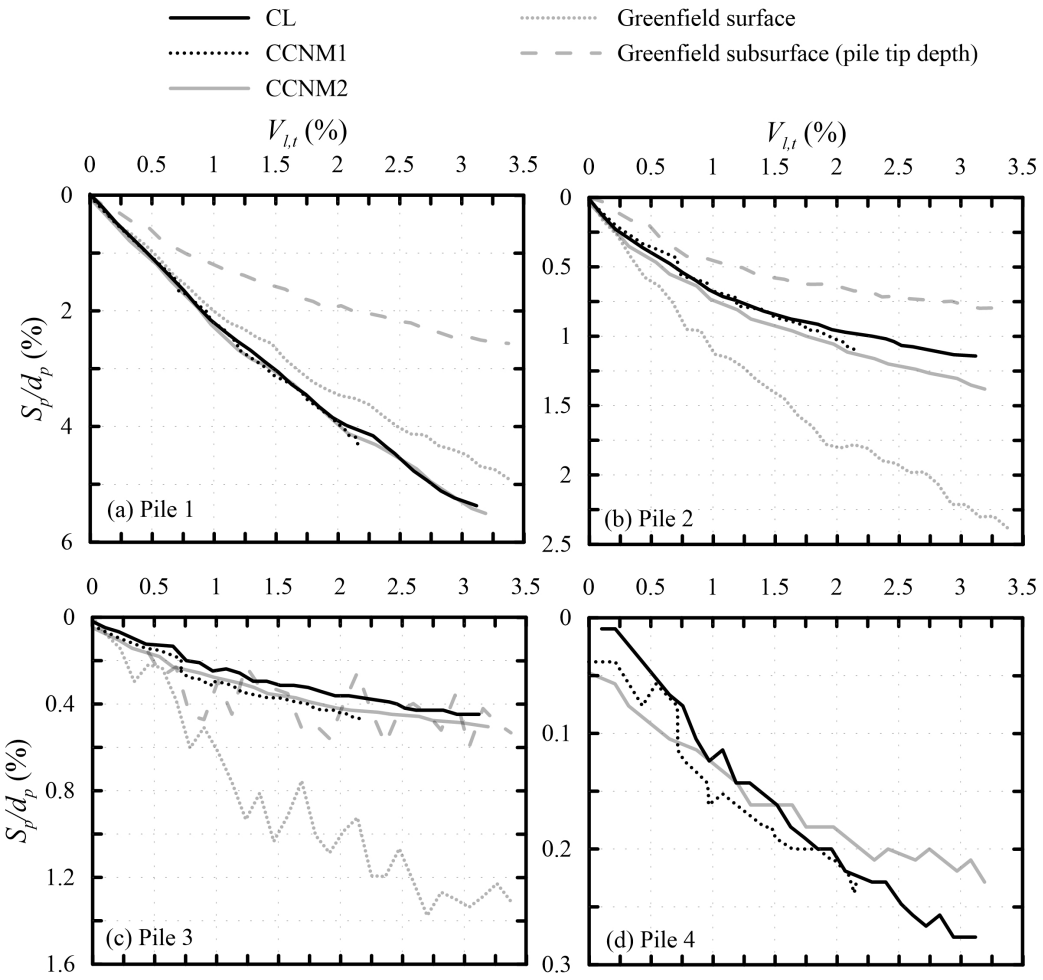


FIGURE 6.9: Pile settlement with tunnel volume loss: (a) pile 1, (b) pile 2, (c) pile 3, (d) pile 4

of structure stiffness ($S_{p,s}$). It is possible to find a correlation between tunnel volume loss and pile settlement due to the effect of structure stiffness only (isolate the structure stiffness effect). For test CL, as the pile head load remains unchanged, the pile head settlement ($S_{p,t}$) is only caused by the tunnelling-induced ground movement. Thus, the pile settlement due to the structure stiffness ($S_{p,s}$) can be isolated:

$$S_{p,s} = S_p - S_{p,t} \tag{6.1}$$

Figure 6.10 shows tunnel volume loss versus the pile settlement caused by structure stiffness ($S_{p,s}$) normalised by the pile head settlement (S_p). For pile 1 (closest to the tunnel), the contribution of structure stiffness to the overall pile settlement is minimal. For pile 2, with an increase in tunnel volume loss, the amount of pile settlement due to structure stiffness in relation to overall pile settlement increased. At a tunnel volume loss of 3.2 %, 14 % of the pile 2 settlement was due to the contribution of structure

stiffness. Pile 3 settlement is not significantly affected by structure stiffness. For pile 4, a decrease in pile settlement is observed with tunnel volume loss due to the effect of structure stiffness; however, the overall magnitude of pile 4 settlement was very small.

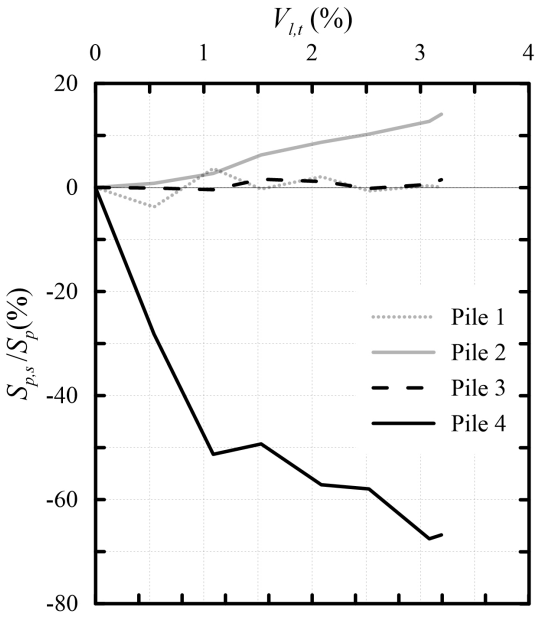


FIGURE 6.10: Contribution of structure stiffness to pile settlement

6.2.5 Effect of structure stiffness on pile head load distribution with tunnel volume loss

Figure 6.11 shows the pile head load versus tunnel volume loss for centrifuge tests CL, CCNM1 and CCNM2. For test CL, the pile head load remains unchanged with the increase in tunnel volume loss. For CCNM1 and CCNM2, a variation of pile head loads was observed with tunnel volume loss. Tests CCNM1 and CCNM2 show good consistency in pile head load variation with tunnel volume loss, which confirms the repeatability of the centrifuge tests using the hybrid testing technique. For pile 1, with an increase in tunnel volume loss, tests CCNM1 and CCNM2 show a decrease in pile head load. In test CCNM2, at a tunnel volume loss of 3.2 %, pile 1 head load decreased by about 45 N (a decrease of about 18%). The decreased pile head load from pile 1 will transfer to the other piles; most of the load from pile 1 was apparently transferred to the adjacent pile 2 where at a tunnel volume loss of 3.2 %, pile 2 head load increased by 63 N (an increase of about 17%). The increase in pile 2 head load in tests CCNM1 and CCNM2 caused a greater pile head settlement compared with the pile in test CL, as shown in section 6.2.4. A very small increase in pile head load with tunnel volume loss is observed for pile 3 in tests CCNM1 and CCNM2. In test CCNM2, at a tunnel volume loss of 3.2 %, the pile 3 head load increased by 11 N (an increase of about 3%),

this increase in pile head load did not cause a significant increase in pile settlement when compared with the pile in test CL (see Figure 6.9). For pile 4, at a tunnel volume loss of 3.2 %, pile head load decreased by about 28 N (a decrease of about 11%). As discussed in section 6.2.4, the effect of structural stiffness reduced pile 4 settlement, which was due to the reduction in pile 4 head load.

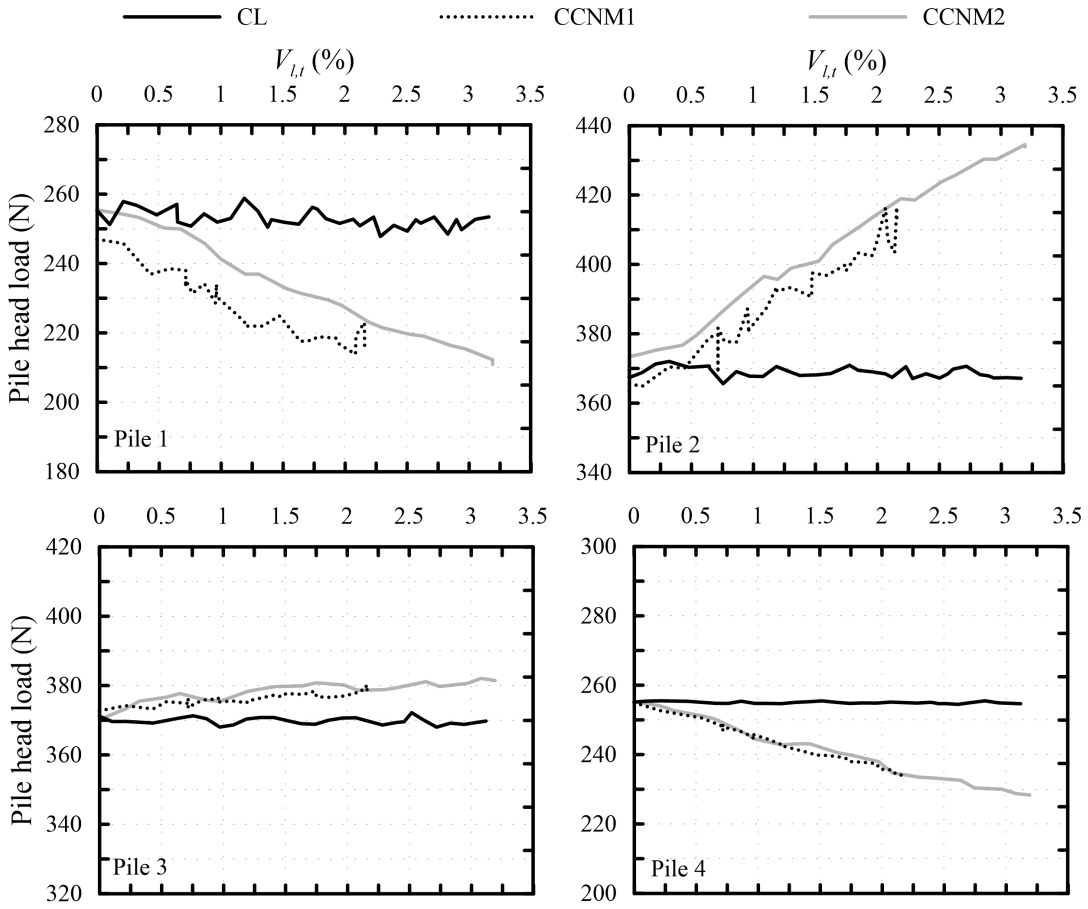


FIGURE 6.11: Pile head load with tunnel volume loss: (a) pile 1, (b) pile 2, (c) pile 3, (d) pile 4

It is also possible to quantify the isolated pile settlement caused by the structure stiffness ($S_{p,s}$; see Equation 6.1) against the change in pile head load (difference in pile head load due to structure stiffness). Figure 6.12 shows the change in pile head load versus pile settlement caused by the structure stiffness ($S_{p,s}$) normalised by pile diameter (d_p). For pile 2, the pile settles with an increase in pile head load. For pile 3, the increases in head load and settlement are not significant. Pile 4 head load decreased during tunnel volume loss, and the pile head settlement caused by structure stiffness follows a line with a similar slope as for pile 2, but in the opposite direction (pile 4 moves upwards with tunnelling). For pile 1, no obvious correlation can be established between $S_{p,s}$ and change in pile head load. It follows that, as pile 1 is located closest to the tunnel, the variation of the pile head load has a limited effect on pile settlement, and the tunnelling-induced ground

movement dominates the pile settlement. As discussed in Section 6.2.4, the amount of pile settlement due to the effect of structure stiffness is minimal for pile 1. For the other three piles, as the piles are further away from the tunnel, the structure stiffness (the variation of pile head load) has the dominant influence on pile head settlement ($S_{p,s}$) with tunnelling.

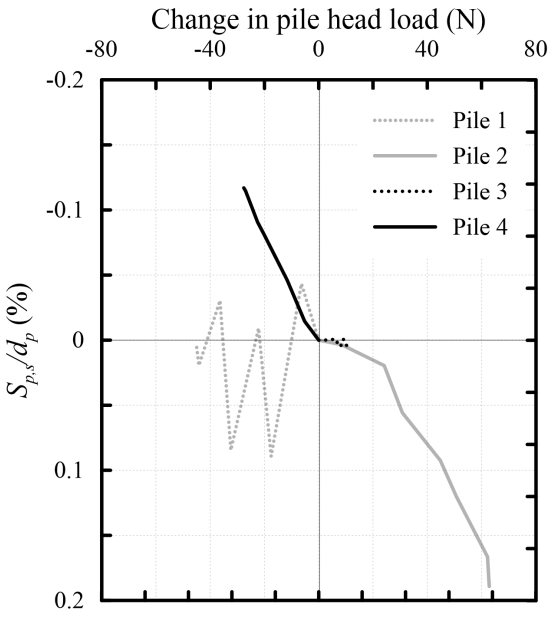


FIGURE 6.12: The pile settlement due to change in pile head load during tunnel volume loss for test CCNM2

6.2.6 Axial force redistribution along piles and change in mobilised pile shaft friction during tunnelling

The axial load distribution along the piles for centrifuge tests CL, CCNM1 and CCNM2 are presented in the upper, middle and lower plots of Figure 6.13, respectively. The load applied to the pile head (Q_t) is carried by a combination of (1) shaft resistance force (Q_s) and (2) end-bearing force (Q_b). FBG sensors were used to measure the axial force along the piles; measurement techniques and calibration procedures were given in Section 4.3.5. The pile end-bearing force was not directly measured but approximated using the closest FBG measurement point to the pile tip, which was located 10mm above the tip. Lee and Chiang (2007) suggested that the end-bearing force can be determined by extrapolating the load measurement locations above the pile tip (see Figure 6.13 (a)). As a result, the two load measurement points S1 and S2 (refer to Figure 4.15 for measurement point numbering) were used to estimate the end-bearing force.

The axial force along the piles is mainly affected by two mechanisms: (1) change in pile head load due to structure stiffness, (2) the effect of tunnelling-induced ground

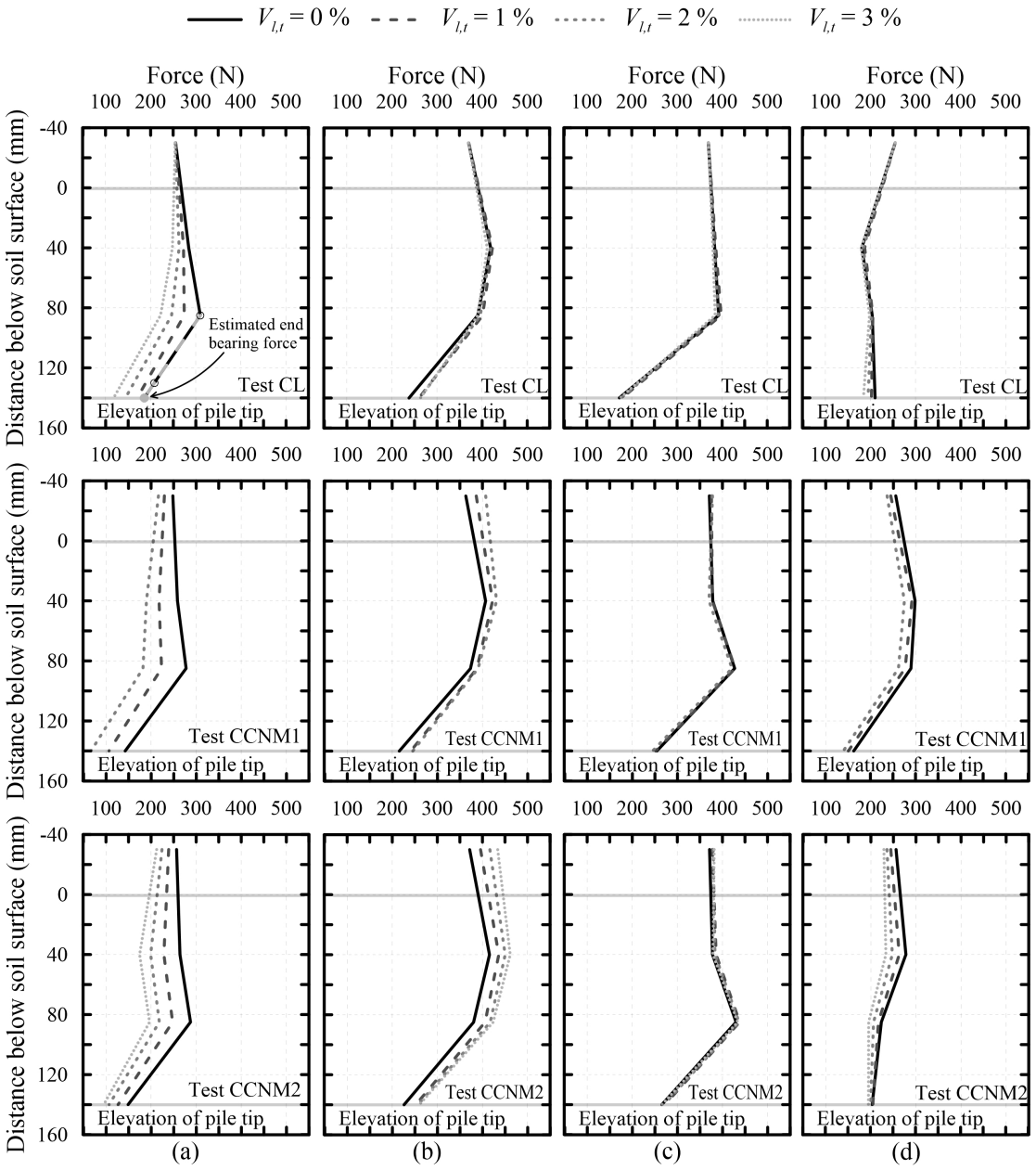


FIGURE 6.13: Pile axial load at $V_{l,t} = 1,\ 2,$ and 3% : (a) pile 1, (b) pile 2, (c) pile3, (d) pile 4

movements; there are also pile-pile interactions, but this research focused on the above two mechanisms. In test CL, pile 1 head load remains unchanged, and the amount of decrease in axial force along the upper portion of the pile is not as significant as the lower portion. For pile 1 in tests CCNM1 and CCNM2, the pile head load decreased with tunnel volume loss, and the axial force along the upper portion of the pile decreased accordingly. The change in axial force close to the pile tip is similar to test CL. Based on the above results, it can be suggested that for pile 1 (located closest to the tunnel), the axial force along the upper portion of the pile (0-80 mm below the soil surface) is mainly affected by the change in pile head load (mechanism 1), and the axial force along

the lower portion of pile 1 (80-140 mm below the soil surface) is mainly affected by the tunnelling-induced ground movements (mechanism 2).

For pile 2 in test CL, a small increase in end bearing force is observed at a tunnel volume loss of $V_{l,t}$=1 %. Referring back to Figure 6.9, with an increase in tunnel volume loss, pile 2 settlement is greater than the greenfield soil settlements located at the pile tip but smaller than soil settlements located close to the soil surface. Therefore, the pile is being "dragged down" by the soil at the upper portion of the pile, and the axial force close to the pile tip increased accordingly (mechanism 2). For pile 2 in tests CCNM1 and CCNM2, with tunnelling, pile 2 head load increased; hence the axial force along the upper portion of the pile increased (mechanism 1). The amount of increase in axial force close to the pile tip is similar to test CL (mechanism 2).

For pile 3 in test CL, the change in axial force is minimal, and referring back to Figure 6.9, the amount of pile 3 settlement with tunnelling is similar to the greenfield soil settlements at pile tip depth. In addition, the soil settlements at the surface are higher than the pile 3 settlement; however, the overall amount of soil settlements are not significant; hence the increase in axial force due to the soil friction is minimal. Similar to test CL, pile 3 in tests CCNM1 and CCNM2 has a minimal change in axial force with tunnelling, and the increase in pile head load is minimal (see Figure 6.11). As a result, for pile 3, the effect of mechanisms 1 and 2 are insignificant.

For pile 4 in test CL, the change in axial force along the pile due to mechanism 2 (tunnelling-induced ground movement) is small. For pile 4 in test tests CCNM1 and CCNM2, pile head load decreased due to the effect of structure stiffness, and consequently, the axial force along the pile decreased (mechanism 1).

The change in unit shaft resistance along the depth of a pile with tunnel volume loss ($\Delta f_{vl}(z)$) can be calculated from the variation of axial force measured along the pile:

$$\Delta f_{vl}(z) = \frac{\Delta Q_s^f(z) - \Delta Q_s^i(z)}{\Delta z} \left(\frac{\mathrm{N}}{\mathrm{mm}}\right) \tag{6.2}$$

where superscripts f and i relate to force after and before tunnel volume loss, respectively; and Δz is the distance between the two measurement points (see Figure 4.16 for the location of the measurement points). For example, if the shaft resistance along a given depth of the pile is increased, then $\Delta f_{vl}(z)$ is positive. In addition, the increase in shaft resistance could be caused by upwards shaft resistance, or an increase in downwards shaft resistance, for the case involves tunnelling-induced ground movement, the assessment of pile and soil settlements (referring back to Figure 6.9) could indicate the

direction of the increase in pile shaft resistance. Figure 6.14 shows the changes in unit shaft resistance ($\Delta f_{vl}(z)$) at various tunnel volume losses.

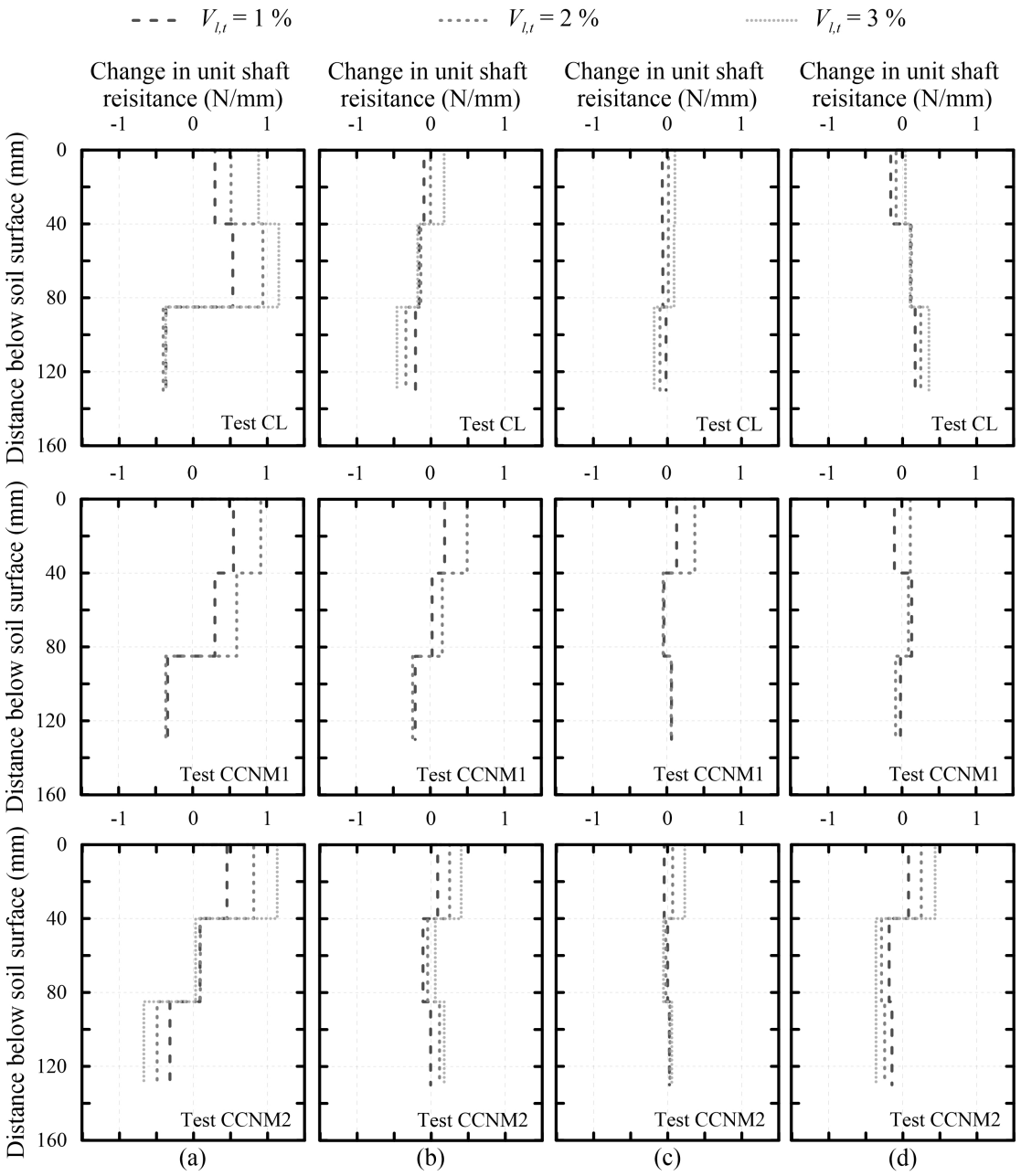


FIGURE 6.14: Change in unit shaft resistance at $V_{l,t} = 1,\ 2, \text{and } 3\%$: (a) pile 1, (b) pile 2, (c) pile3, (d) pile 4

For pile 1 in test CL (with constant pile head load), the pile settles with tunnel volume loss, and the end bearing force reduces. Referring back to Figure 6.9, the pile 1 settlement in test CL is higher than the soil settlements close to the depth of pile tip, and it shows a similar increase in the settlement with tunnelling to the greenfield soil surface. As a result, the pile is being "pushed down", and to maintain the pile head load applied, additional shaft resistance along the upper and middle portions of the pile (0-85 mm

below the soil surface level) is increased (increase in upwards shaft friction). The lower portion of pile 1 maintained a negative shaft resistance with tunnelling in tests CL, and this is caused by the tunnelling-induced soil movements close to the pile tip (loss of end bearing force). For pile 1 in tests CCNM1 and CCNM2, pile end bearing load is decreased, and the piles show similar settlement with tunnelling to pile 1 in test CL, therefore, the increase in unit shaft resistance along the upper portion of the pile (0-40 mm below the surface) is caused by the upwards shaft friction (soil tends to resist the downward movement of the pile). In addition, with tunnelling, the unit shaft resistance at the lower portion of the pile reduced (85-130 mm below the surface).

For pile 2 in test CL, the magnitude of change in unit shaft resistance with depth is not as significant as pile 1. The unit shaft resistance increased at the upper portion of the pile, whereas the resistance decreased around the pile tip. Referring back to Figure 6.9, pile 2 settlement in test CL is greater than greenfield soil subsurface settlements and lower than surface soil settlements. From the settlements data, it is believed that the soil at the upper portion of the pile tends to "drag down" the pile, and causes the increase in downwards shaft resistance. The soil close to the pile tip tends to resist pile settlement, but the upwards shaft resistance decreased due to tunnelling-induced soil movements. In general, the overall change in unit shaft resistance of pile 2 is minimal. For pile 2 in tests CCNM1 and CCNM2, pile head load increased with tunnelling due to the effect of the structure stiffness; consequently, the end bearing force is increased (see Figure 6.13). The change in unit shaft resistance is positive at the upper portion of the pile, due to the increase in upwards shaft friction. In general, the overall change in unit shaft resistance is not significant. It is believed that the pile base takes the majority of the increased load from the pile head.

For pile 3 in tests CCNM1 and CCNM2, the variation of pile head load due to the effect of structure stiffness is not significant, and consequently, the changes in unit shaft friction along the pile are small, which also applies to the result for pile 3 in test CL.

For pile 4, a reduction in pile head load is observed for tests CCNM1 and CCNM2 (see Figure 6.13), hence a reduction in unit shaft resistance along the depth of the pile is expected. The unit shaft resistance at middle and lower portions of the pile show a negative value in test CCNM2, and the upper portion of the pile unit shaft friction increases with tunnel volume loss. In test CCNM1, the change in unit shaft resistance is minimal. For pile 4 in test CL (constant pile head load), a small reduction in pile end bearing force is observed from Figure 6.13, and the magnitude of change in unit shaft friction is small. An increase of unit shaft friction at the middle and lower portions of the pile is identified, but the overall change in shaft friction is not apparent. Piles 1 and 4 in test CL have the same pile head load (constant pile head load). For pile

1, which is located closest to the tunnel, with an increase in tunnel volume loss, the unit shaft resistance at the lower portion of the pile reduced, whereas for pile 4 (located furthest away from the tunnel) the magnitude of change in shaft friction is minimal. These data illustrate that for piles located far from the tunnel, the shaft friction at the lower portion of the pile is less affected by tunnelling-induced ground movement than piles located close to the tunnel.

6.2.7 Determination of post-tunnelling pile axial capacity

tunnelling-induced ground movements can affect the soil stress profile around the pile. As a result, the axial capacity of the pile after tunnel volume loss may be reduced. To further understand the effect of tunnelling on pile capacity, post-tunnelling pile jacking tests were conducted. The ultimate tunnel volume loss was $V_{l,t}$=3.2 % for tests CL and CCNM2, whereas for CCNM1 it was $V_{l,t}$=2.2 %. The pile jacking method discussed in section 6.2.2 was adopted for these tests, and the displacement control method was applied with a jacking rate of 0.1 mm/s. The pile jacking sequence follows the pile number: 1-2-3-4. Figure 6.15 shows the pile 2 settlement and head load change during pile 1 jacking. When pile 1 is being jacked into the soil, the actuators connected to the remaining piles (2, 3 and 4) were deactivated, which restricted the movement of the piles. In addition, pile 1 jacking causes soil movements downwards, despite the settlement of piles 2, 3 and 4 was restricted, the piles were connected to the actuators via a dye spring (see Figure 4.10), which could "release" the piles to follow with the settlements of the soil. From Figure 6.15, it can be seen that pile 2 settles during pile 1 jacking, and the maximum settlement for pile 2 is around 3.4% of the settlement of the jacked pile (pile 1), and the pile 2 head load remains unchanged with pile 1 jacking. After pile 1 jacking, the actuator connected to pile 1 deactivated, and pile 2 jacking started. Figure 6.16 shows the load-displacement curves for all piles in the three centrifuge tests, as well as the "greenfield" pile jacking in test PJ (pile 2). During pile jacking, the gradient of the load-settlement curve indicates the pile jacking stiffness, and Figure 6.17 shows the post-tunnelling pile jacking stiffness for all three centrifuge tests, as well as the "greenfield" pile jacking result (pile 2) in test PJ.

For pile 1 in tests CL and CCNM2, the load-displacement curve shape is similar, despite the fact that the initial pile head load is different. The pile jacking stiffness for pile 1 in test CCNM1 is less than other tests (CL, CCNM2 and PJ), and in general, "greenfield" pile jacking shows least jacking stiffness. For pile 2, the load-settlement curve shape from all tests is similar, apart from test CCNM1. The pile jacking stiffness curve also indicated similar shape in tests CL and CCNM2. For tests CCNM1, pile 2 initial stiffness is similar to pile 2 in the other tests (tests CL and CCNM2), but when the pile head load

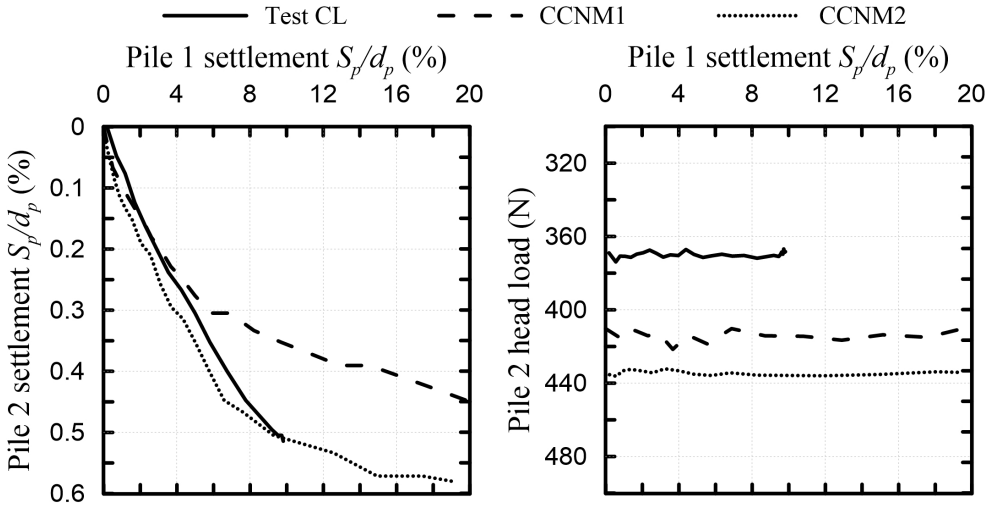


FIGURE 6.15: Pile 2 settlement and head load change with pile 1 jacking

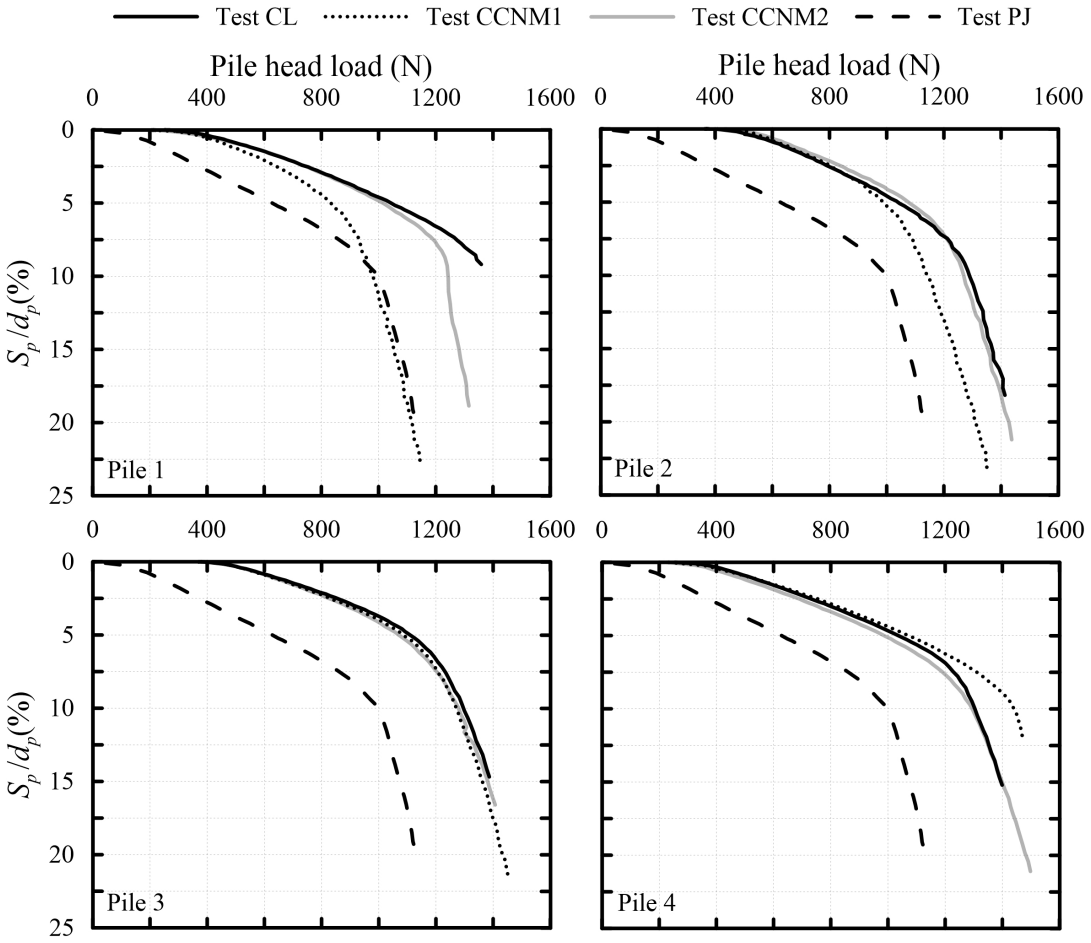


FIGURE 6.16: Load-displacement curves for all the tests

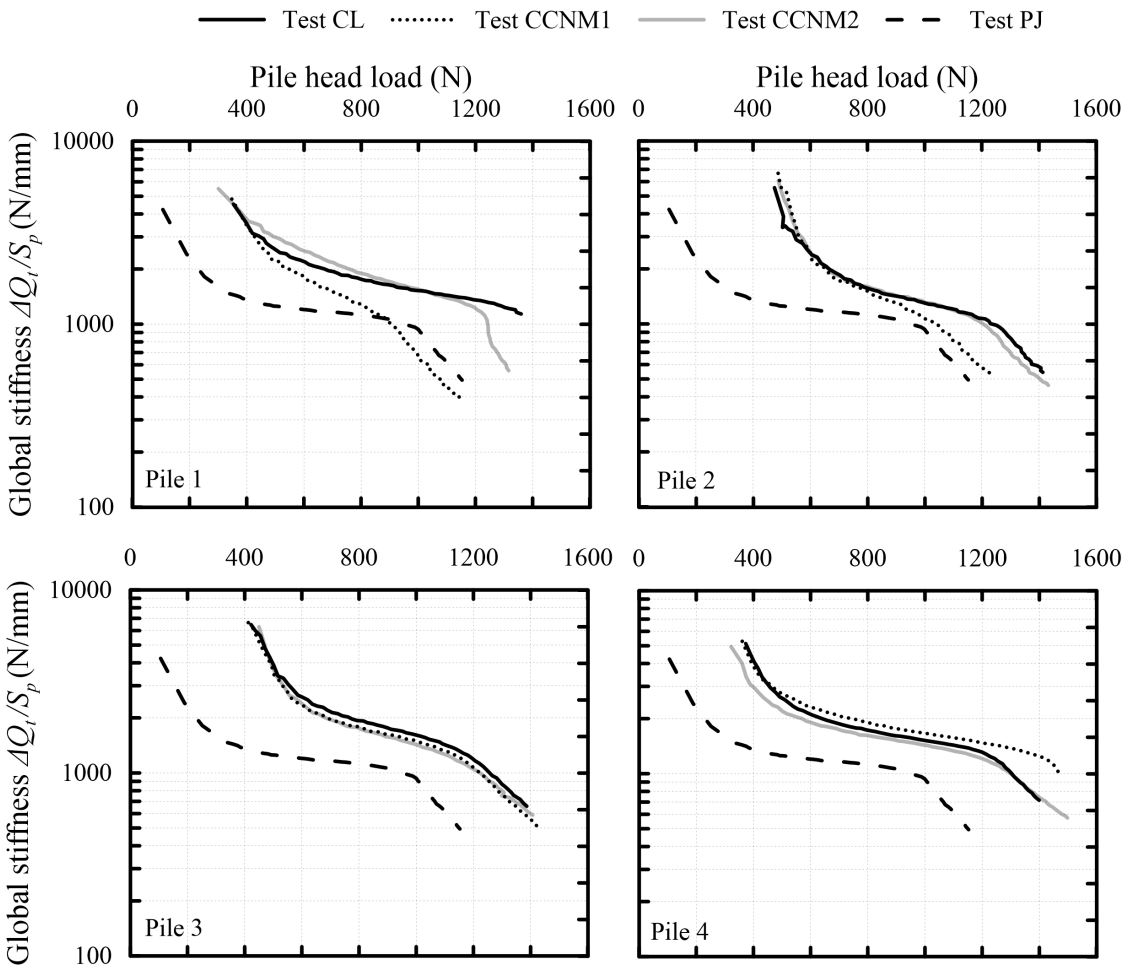


FIGURE 6.17: Post-tunnelling pile global stiffness with pile head load

exceeds 800N, the pile 2 stiffness decreased more rapidly than other two tests. For pile 3, the pile jacking stiffness in tests CL, CCNM1 and CCNM2 is greater than "greenfield" test PJ, and load-displacement curve shape in tests CL, CCNM1 and CCNM2 is similar. For pile 4, the initial pile jacking stiffness is similar in all three tests (CL, CCNM1 and CCNM2), but with a further increase in pile head load, the pile in test CCNM1 shows a stiffer response than the pile in other tests CL and CCNM2.

During pile jacking, the pile head load is taken by the end bearing force and shaft resistance. An assumption was made that the ultimate load capacity is defined when the shaft resistance along the pile is fully mobilised. Figure 6.18 presents shaft resistance versus pile settlement in all centrifuge tests. A comparison is made to the "greenfield" pile jacking test (PJ), using pile 2.

For test PJ (black dashed line in Figure 6.18), the shaft resistance increases with pile settlement, and the pile reaches the maximum shaft resistance at $S_p/d_p \approx 8$ %. For pile 1 in test CCNM1, shaft resistance reaches a maximum value at $S_p/d_p \approx 5$ %, which is

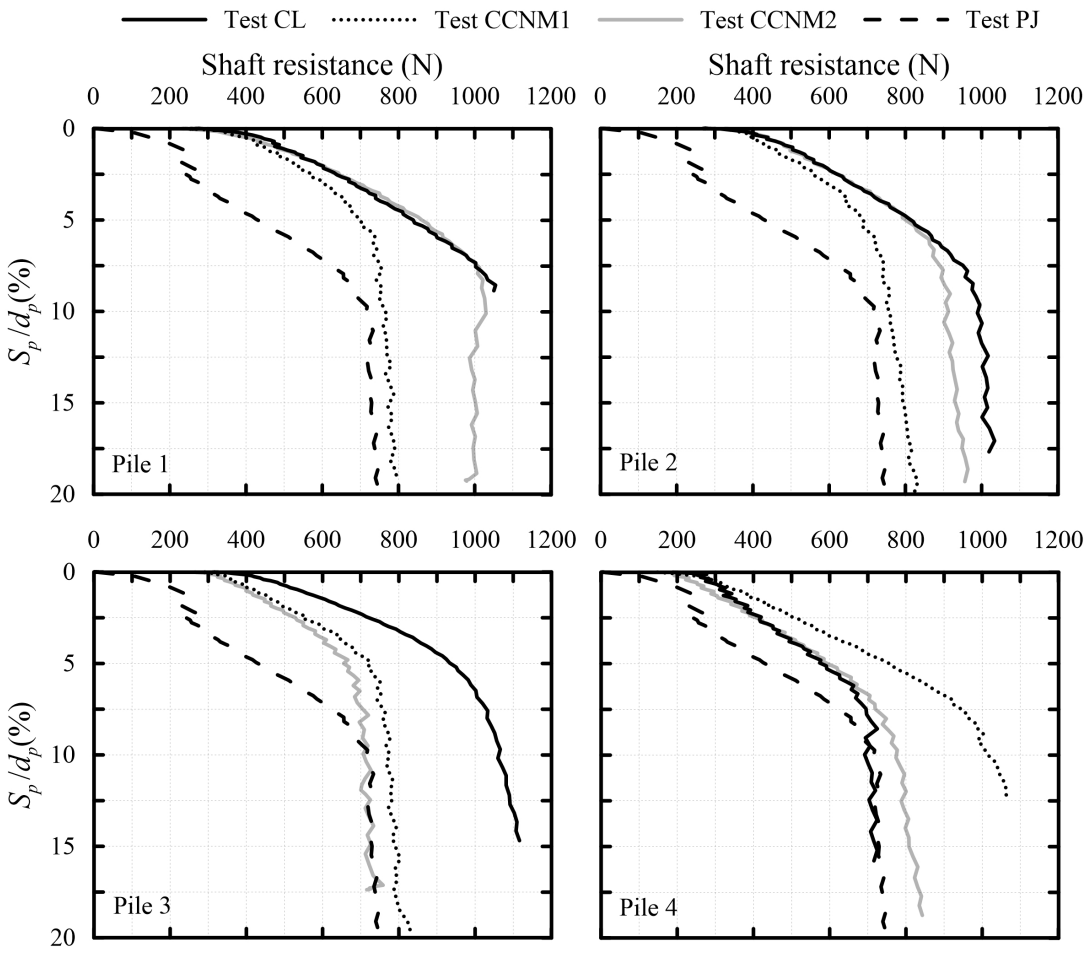


FIGURE 6.18: shaft resistance of piles in all the tests

less than the settlement required for test PJ. For pile 1 in test CCNM2, displacement required to fully mobiles shaft resistance is $S_p/d_p \approx 7$ %. For test CL, the pile 1 jacking terminated at $S_p/d_p \approx 7$ % (this is due to the amount of load required to further jack the pile is about to exceed the load capacity of the actuator), and the ultimate shaft resistance is assumed to be fully mobilised at $S_p/d_p \approx 7$ %. For pile 2 in tests CL and CCNM2, the displacement required to fully mobilise shaft resistance is $S_p/d_p \approx 7$ %, and for test CCNM1 it is $S_p/d_p \approx 5$ %. For pile 3 in tests CL, CCNM1 and CCNM2, the pile shaft resistance fully mobilised at $S_p/d_p \approx 5$ %, and for pile 4 shaft resistance fully mobilised at $S_p/d_p \approx 7$ %. In general, the amount of pile settlement to fully mobilise shaft friction in tests CL, CCNM1 and CCNM2 is less than test PJ, suggesting that tunnelling-induced ground movements affect the development of shaft resistance with pile settlement.

Referring back to Figure 6.14 (a), a decrease in unit shaft resistance is identified at the lower portion of pile 1 in tests CCNM1 and CCNM2. As discussed in section 6.2.6, the pile 1 head settlement is greater than the subsurface soil settlements at a depth of the

pile tip, therefore the soil at the lower portion of the pile tends to resist the settlement of the pile, but due to the tunnelling-induced soil movements, the amount of upwards shaft friction decreased with tunnelling. In test CCNM2, the amount of decrease in shaft resistance at the lower portion of the pile is greater than the decrease in CCNM1, as the ultimate tunnel volume loss in test CCNM2 is greater than CCNM1. During pile jacking, the shaft friction is re-mobilised, and more pile settlement is required for the case where more reduction in shaft resistance has been taken place during tunnelling (case in test CCNM2). Figure 6.18 shows that for pile 1, the amount of pile settlement required to re-mobilise the shaft friction is $S_p/d_p \approx 7$ % for test CCNM2 and $S_p/d_p \approx 5$ % for test CCNM1.

Based on the above results, the post-tunnelling axial capacity of the piles in all three tests (CL, CCNM1 and CCNM2) can be defined, see Figure 6.19. For piles in tests CCNM1 and CCNM2, the axial capacity varies with the distance from the tunnel (x/D_t), and no apparent correlation can be identified. In general, the post-tunnelling pile axial capacity is affected by (1) the pile position with respect to the tunnel, (2) the tunnel volume loss prior to pile jacking, (3) pile jacking of adjacent piles (pile-pile interaction), and (4) the initial pile head load prior to pile jacking. Further discussion in post-tunnelling axial capacity will be given in Chapter 6.

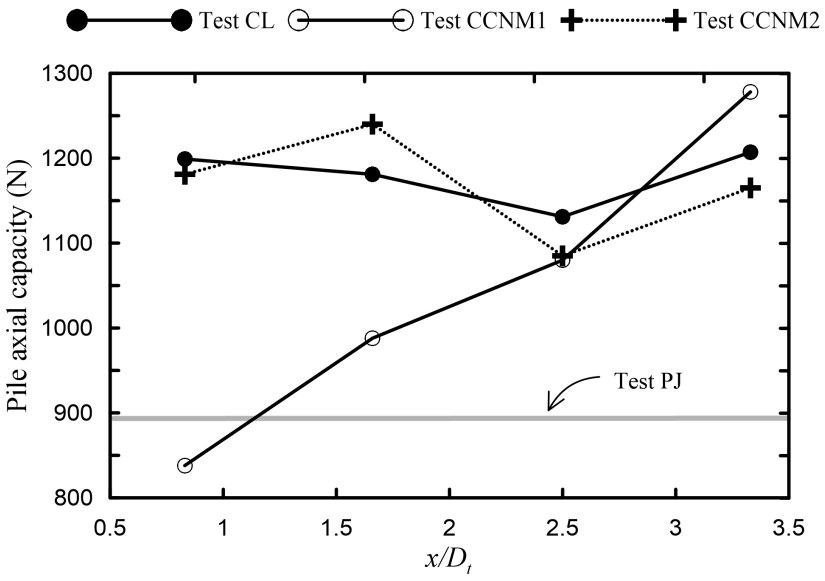


FIGURE 6.19: Post-tunnelling pile axial capacity

6.3 Summary and conclusions

Four centrifuge tests were conducted under 80g. Test PJ is the "greenfield" pile jacking test, where piles were driven into the ground at a constant speed, and the pile axial load

capacity was determined. Tests CL, CCNM1 and CCNM2 involve the study of tunnel-pile-structure interaction (TPSI) problem. For test CL, the structure has zero stiffness (constant load applied to piles during tunnelling). For tests CCNM1 and CCNM2, a five-storey steel frame structure was simulated. FBG sensors were used to measure the axial force along the model piles. The effect of tunnelling-induced soil movements on pile settlement and load transfer were analysed. Post-tunnelling pile jacking tests were carried out to investigate the pile jacking response, and the results were compared with the outcomes from pile 2 in test PJ (pile jacking without a tunnel).

For the "greenfield" pile jacking test (test PJ), four model piles were driven into the ground. Based on the axial force measured along the depth of the piles, the development of shaft resistance with pile settlement indicated that the pile shaft resistance was fully mobilised at a pile settlement of $S_p/d_p \approx 8$ %. For a conservative estimation, the ultimate axial load-bearing capacity of the piles was defined at the point where the pile shaft resistance was fully mobilised.

For pile loading to account for structural weight, all four piles were loaded to their designated load in increments of 50 N. The piles in all three centrifuge tests showed a similar loading response. The loading of a given pile affected adjacent piles (pile-pile interaction), where the axial force at the lower portion of adjacent piles increased and the piles settled by ≈ 10 % of the amount of the loaded pile.

For the CCNM centrifuge tests (CCNM1 and CCNM2), the settlement of the piles during tunnelling was affected by the tunnelling-induced ground movements and changes in pile head load (caused by structure stiffness). In addition, the axial force along the depth of piles was affected by the changes in pile head load and tunnelling-induced ground movements. For piles located close to the tunnel (piles 1 and 2), the axial force along the lower portion of the pile reduced with tunnelling. For the piles located further away from the tunnel (piles 3 and 4), the axial force along the depth of the pile was less affected by the tunnelling.

Based on the load-settlement curves from post-tunnelling pile jacking tests, all piles showed a similar load-settlement shape, despite the difference in initial pile head load. For piles 3 and 4, which were located further away from the tunnel, the initial pile jacking stiffness was higher than the "greenfield" test PJ. The amount of settlement required to fully mobilise the pile shaft resistance in tests CL, CCNM1 and CCNM2 was less than the settlement required for the "greenfield" pile.

Chapter 7

The use of protective walls to reduce buildings from tunnelling-induced damage

7.1 Introduction

Tunnel excavation in urban areas causes ground movements which could damage existing nearby piled structures. The tunnelling-induced ground movements, as highlighted by Mair and Taylor (1997) (see Figure 2.1) are mainly due to (1) soil stress-relief at the tunnel excavation face, (2) overcutting from the tunnel excavation face, and (3) the development of ground stress close to the tunnel lining (long-term effect due to consolidation). Tunnel-pile-structure interaction (TPSI) problems have drawn considerable attention from researchers (Franza et al., 2019, Hong et al., 2015, Jacobsz, 2003, Lee, 2012, Loganathan et al., 2000, Mair and Taylor, 1997, Standing and Potts, 2008). In general, the construction of a tunnel close (adjacent) to a piled structure will have the potential to cause uneven pile settlement, therefore threaten the serviceability of the structure. To protect structures from tunnelling-induced damage, several remedial measures have been adopted in practice: (1) compensation grouting, (2) structure jacking and (3) the use of a protective structures or curtain walls. The purpose of the remedial measures are to reduce the uneven structure settlements caused by tunnelling. There are several examples of the application of protective structures applied as a barrier between a tunnel and an adjacent piled foundation (Di Mariano et al., 2007, Ledesma and Alonso, 2017), however there are very few experimental studies which have considered this problem. Bilotta (2008) conducted centrifuge tests to investigate the effect of a diaphragm wall on soil movements caused by tunnel volume loss in over-consolidated clay;

the study did not explicitly include a structure or foundation system. To the authors' knowledge, no centrifuge modelling studies have yet been conducted which include all the interacting components; i.e. tunnel, protective structure, foundations, and structure. In order to achieve more sustainable cities and enable more efficient and cost-effective protective measures to be developed, it is necessary to improve our understanding of these complex interaction problems. Owing to the advantages of centrifuge tests (it allows the previous inaccessible data such as axial force along the pile, as well as the ground deformation shape to be assessed). The geotechnical centrifuge is used as a platform to investigate the problem stated above.

In this chapter, results from four centrifuge tests are presented, to study the performance of protective walls in protecting structures from tunnelling-induced damage. All tests were conducted at 80 g using dry silica sand. The test layout was discussed in Chapter 4.4.1, and Table 4.4 summarised the test details. Unlike the tests conducted in Chapters 4 and 5, a newly designed centrifuge strong box was used (see Figure 4.20). The strong box inner height was increased from 400 mm to 700 mm, and the eRBM model tunnel was located 175 mm above the strong box base, which provided 130 mm of clear distance between the bottom of the tunnel and strong box base. Test GF is a greenfield tunnelling test where the piled structure and protective wall were not included. Test CCNM3 repeated Test CCNM2 (presented in Chapter 5), and the same structure was modelled using the newly developed CCNM (coupled centrifuge-numerical model) method. Two protective wall tests are presented: CCNM-R-S (where the R denotes a protective wall, and S denotes a short wall), and CCNM-R-L (where the L denotes a long wall). The short and long protective walls were 207 mm and 297 mm, respectively. The long protective wall (297 mm embedded depth) has a clear distance of 85 mm between the toe of the wall and strong box base. In both tests the protective walls were located 55 mm away from the tunnel centreline and the wall interface was rough. For all four centrifuge tests (GF, CCNM3, CCNM-R-S and CCNM-R-L), the eRBM model tunnel was used (as discussed in Chapter 4). Two Dalsa nano-m4020 cameras were adopted to "track" the soil displacements; the precision of the "tracking" was discussed in Section 4.4.4. Figure 7.1 shows the location of the protective wall, piles and the field of view for geoPIV-RG. The test results presented in this chapter also include bending moments along the depth of the protective walls measured by fibre Bragg grating (FBG) sensors; detailed configurations and bending moment calibration procedures were discussed in Section 4.4.3.

This chapter is structured as follows. The axial force along the piles after centrifuge acceleration are discussed first (follows the discussion in Section 6.2.1). The piles were then loaded to their designated load. The pile-pile interaction and the effect of pile loading on a protective wall are then discussed. Results from geoPIV_RG are used to investigate

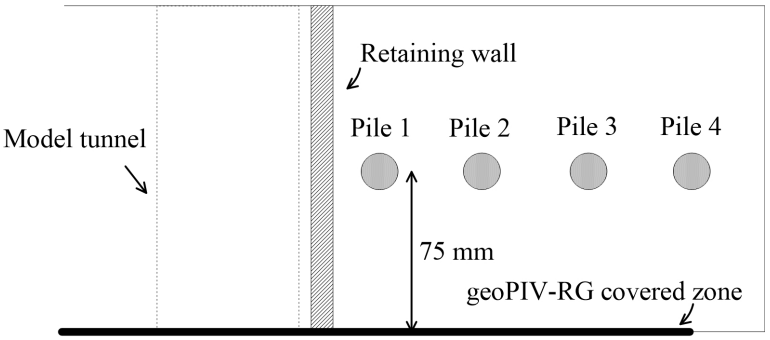


FIGURE 7.1: Location of the protective wall, piles and the field of view for geoPIV-RG

the effect of protective walls on tunnelling-induced ground movements (greenfield soil displacements are compared against the results from tests CCNM3, CCNM-R-S and CCNM-R-L). The geoPIV_RG "tracked" protective wall movements with tunnel volume loss, and the effect of tunnelling on the protective wall deformations and associated bending moment along the depth of the walls are discussed. Data from pile head settlements, pile head loads and axial forces along the piles are analysed and presented to investigate the effect of a protective wall on piled structure response to tunnelling. Post-tunnelling pile jacking results are discussed, and the axial load capacity of the piles is identified. Finally, Section 7.3 summarises the main observations and findings from the tests.

7.2 Interpretation of measured results

7.2.1 Axial force along the piles and pile settlement after centrifuge acceleration

Figure 7.2 shows the axial force along the piles after centrifuge acceleration for all three centrifuge tests. The weight of every pile is around 70 grams; at 80 g the pile weight is 55 N. The grey dotted line in Figure 7.2 shows the theoretical axial force along the pile due to self-weight of the pile. From Figure 7.2, FBG sensors show that the axial force along the pile is higher than the self-weight of the pile, which indicates that a compression force is generated at the soil-pile interface. For most of the piles (apart from pile 2 and 3 in test CCNM3), the compression force shows a maximum value close to the tip of the pile. It is believed that these compression forces were caused by the uneven settlement between the soil and the pile.

To understand the mechanism of the compression force along the pile, it is necessary to investigate the settlement of the pile with respect to the surrounding soil. During centrifuge acceleration, pile settlement was measured by the LVDTs; GeoPIV-RG was

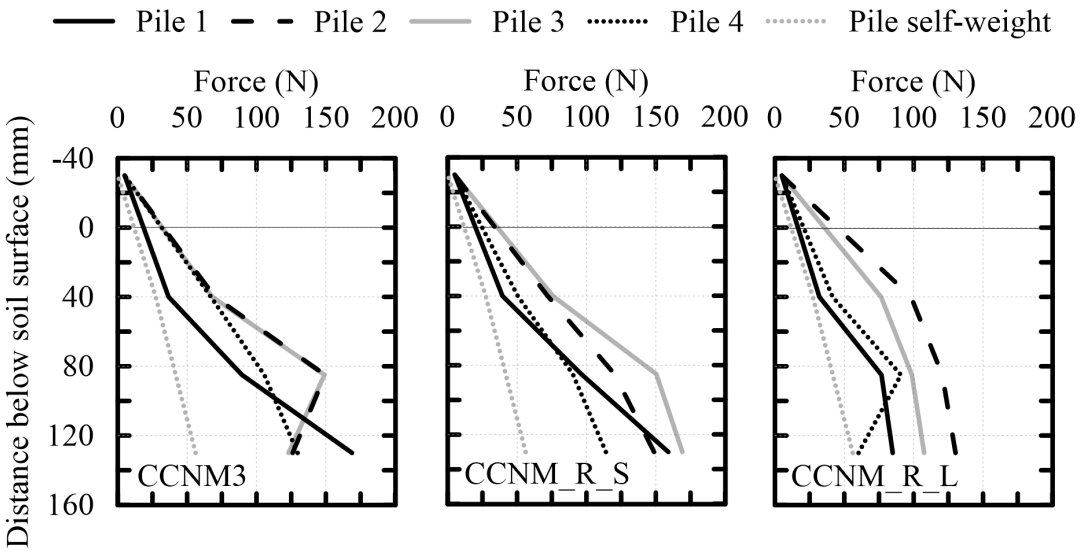


FIGURE 7.2: Axial force along the pile after centrifuge acceleration

used to measure the soil settlements (at the acrylic window, 75 mm away from the pile, see Figure 7.1). Figure 7.3 shows the pile and soil settlements after centrifuge acceleration for all three tests. Piles are assumed to be rigid, with a uniform settlement along their length. All piles show greater settlements than the surrounding soil at the lower portion of the piles, and less settlement than the soil at the upper portion of the piles.

Figure 7.4 illustrates the typical movement of soil along the depth of a pile with respect to the settlement of the pile after centrifuge acceleration. As the relative displacement of the soil on both ends of the pile (top and bottom) tends to move towards the centre of the pile, friction along the pile will mobilise from both directions, and cause the pile to go into compression; therefore, the axial force along the pile increased (see Figure 7.2).

As discussed in Section 4.4.1, the newly developed strong box was used for the centrifuge tests present in this chapter. The newly developed strong box has a greater inner height compared to the one used for test CCNM2 (an increase from 400 mm to 500 mm); as a result, the depth of the soil was increased. Figure 7.5 shows the pile head settlements after centrifuge acceleration (three g-cycles) for all the tests using the "old" strong box (black dots) and the "new" strong box (grey dots). After centrifuge acceleration, in general, piles show less settlement in old strong box than the "new" strong box. The pile settlement is affected by the soil settlements, as the amount of soil underneath the pile in the "new" strong box is greater than the soil in the "old" strong box; therefore, the total amount of soil settlements due to the increase in effective vertical stress (increase in g-level) is greater for the soil in the "new" strong box. Assumption was made that the soil underneath the piles in the "old" strong box has a greater overall stiffness than

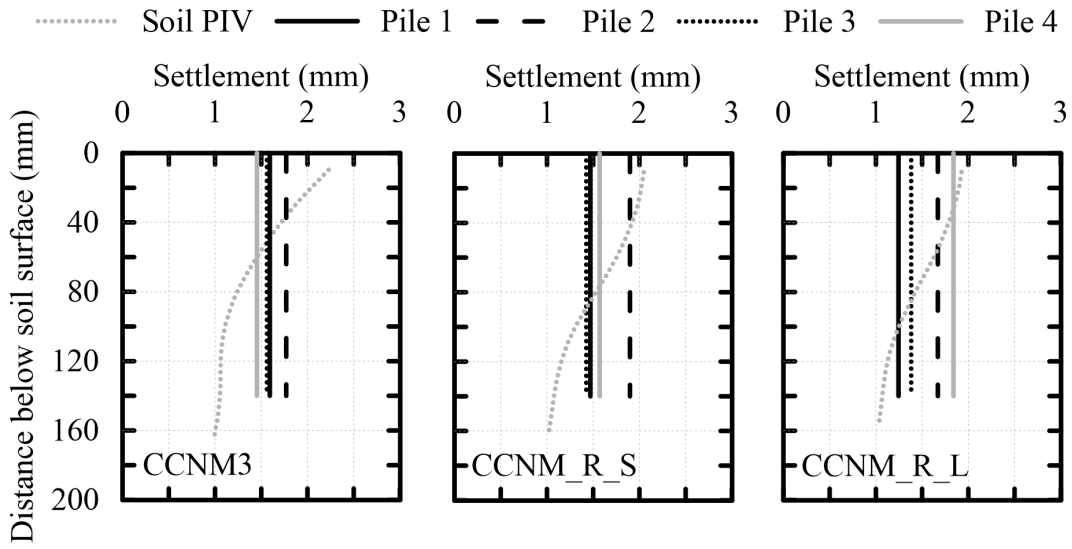


FIGURE 7.3: Vertical settlement of the soil and piles after centrifuge acceleration

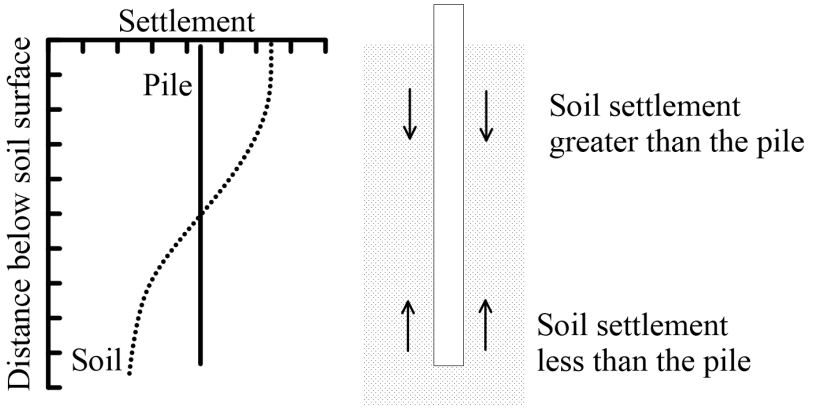


FIGURE 7.4: Illustration of the pile and soil settlements after centrifuge acceleration

the soil in the "new" strong box due to the proximity of the rigid base of the box. As a result, the associated pile settlements are affected, which will be discussed later in this chapter.

7.2.2 Pile loading

The pile loading procedures discussed in Section 6.2.3 were adopted, and Figure 7.6 shows the axial force distribution before (grey line) and after the pile loading (black line). For tests CCNM-R-S and CCNM-R-L, protective walls were located adjacent to the piles; for test CCNM3, protective walls were not used. Despite the difference in testing configurations (with or without protective wall), all four piles in all three centrifuge tests generally show a greater amount of increase in axial force along the upper and middle portions of the pile than the lower portion. This response indicates that, with pile loading, the shaft resistance at the lower portion of the pile is mobilised, and

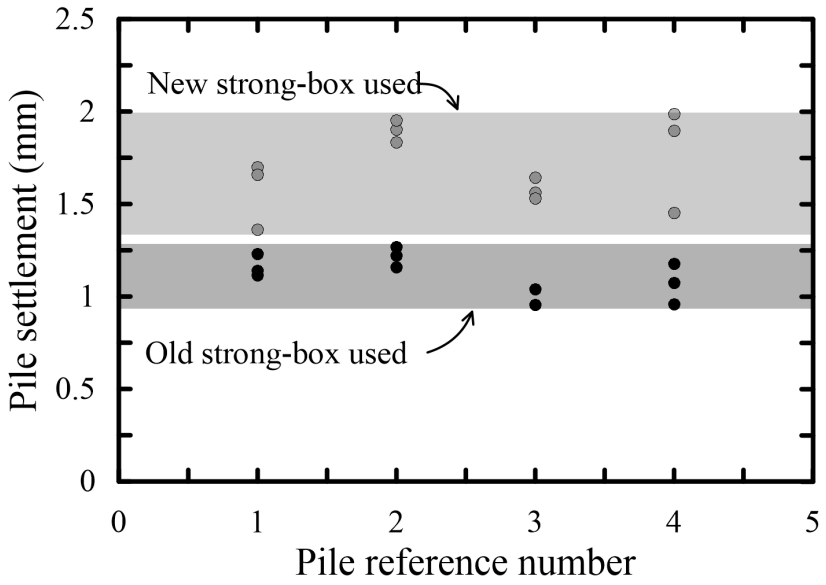


FIGURE 7.5: Pile head settlement after centrifuge acceleration

shaft resistance at the upper and middle portions of the pile is not changed significantly (consistent with the results discussed in Chapter 6.2.3).

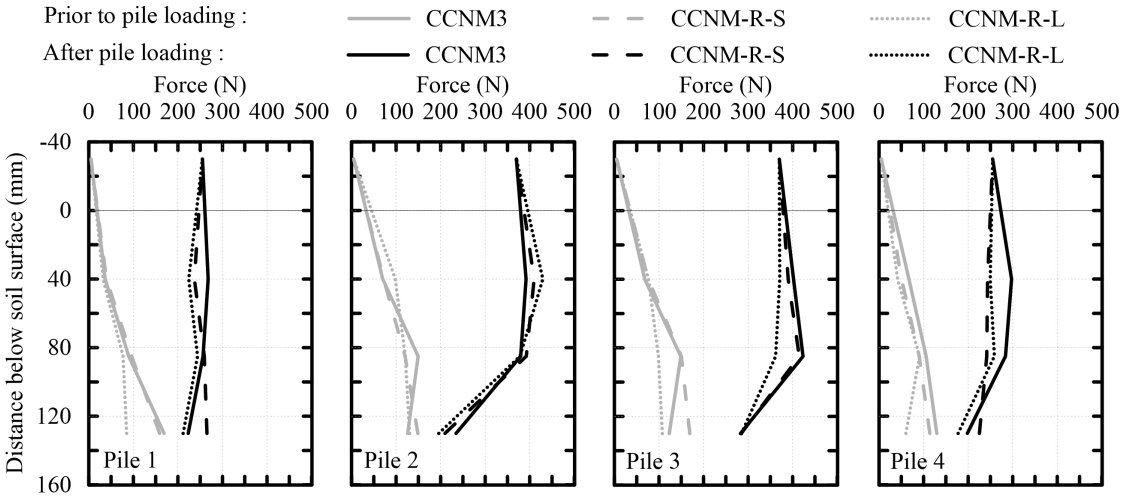


FIGURE 7.6: Axial force distribution before and after pile loading

Figure 7.7 shows the load-settlement curve for all piles during pile loading. For pile 1 in tests CCNM-R-S and CCNM-R-L, the piles show a less stiff loading response to the pile in test CCNM3, suggesting that protective wall affects the pile loading response. For pile 2, the loading response in test CCNM-R-L is less stiff than in test CCNM-R-S, followed by test CCNM3. Pile 3 in tests CCNM3, CCNM-R-S and CCNM-R-L shows similar loading stiffness. Pile 4 in all three tests shows different pile loading response. The reason for these differences is not well understand. It could be caused by variations during model preparation stages, during the sand pouring stage, however, the average sand density showed good consistency between the tests.

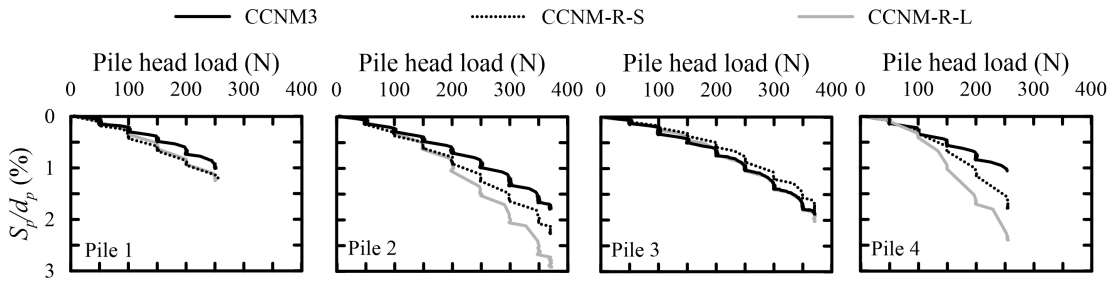


FIGURE 7.7: Pile head settlement during pile loading

To further investigate the "unusual" pile loading behaviour of pile 4, Figure 7.8 shows the pile head settlement and change in axial force along pile 4 during the loading of the adjacent pile (Pile 3) in all three tests (CCNM3, CCNM-R-S and CCNM-R-L). During pile 3 loading, pile 4 head load remained unchanged. In Figure 7.8 (a), the settlement of pile 4 during pile 3 loading shows a consistent response in all three centrifuge tests, but in Figure 7.8 (b), the change in axial force along the pile is different. For test CCNM3 in particular, a small amount of increase in axial force at the lower portion of the pile is observed, which is similar to the observation for tests CCNM1 and CCNM2 (in Chapter 5, see Figure 6.8). For test CCNM-R-L, a reduction in axial force is observed at the upper portion of the pile, and axial force at the lower portion remains unchanged. Test CCNM-R-S shows a reduction in axial force at the upper portion of the pile, but an increase in axial force at a lower portion. It is believed that these differences in axial force distribution along the pile between the tests are mainly caused by the localised inconsistent sand pouring, which would affect the pile load-settlement response.

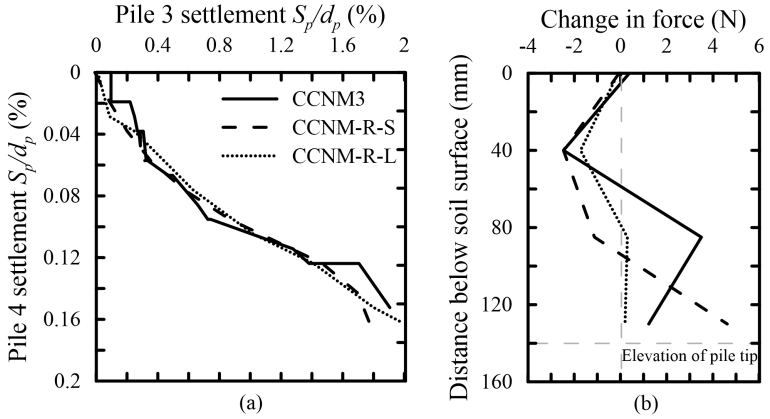


FIGURE 7.8: (a) Pile head settlement and (b) change in axial force for pile 4 during pile 3 loading

The effect of pile loading on the protective wall was analysed by measuring the bending moment along the wall using FBG sensors. Figure 7.9 shows the bending moment profile of the walls in both tests (CCNM-R-S and CCNM-R-L) after pile loading. The bending moment of the wall close to the depth of the pile tip increased in both tests. It is believed

that the pile loading causes the soil close to the pile tip to move laterally towards the wall, hence applying additional horizontal pressure to the wall. The geoPIV-RG data observed from the front acrylic window did not indicate the soil movements towards the wall close to the pile tip after pile 1 loading, this is because the soil displacement is not plane strain; where the soil movements close to the pile tip (located in the middle of the strong box) do not necessary equal the soil movements located behind the front acrylic window (see Figure 7.1).

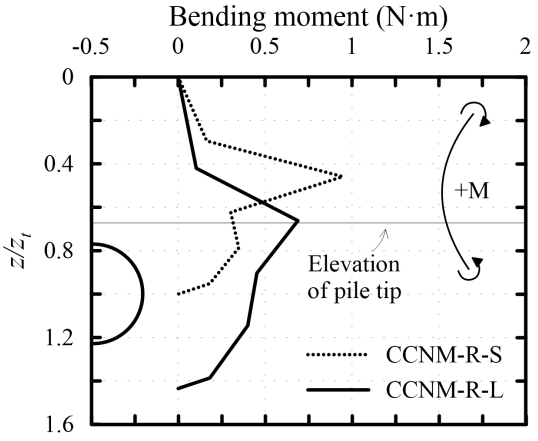


FIGURE 7.9: Bending moment along the protective wall after pile loading

This phenomenon does not apply in practice. During pile loading (construction of the upper superstructure), protective wall does not exist. For the centrifuge tests discussed in this section, the model protective wall is placed in the designated location prior to sand pouring. During centrifuge pile loading, the wall can acts as a "protective wall" to prevent the soil movements caused by pile loading (especially for pile 1). As a result, the soil close to the pile tip after pile loading may experience greater stress than the case without protective wall. In practice, Ledesma and Alonso (2017) reported the use of bored piles to act as a protective wall to protect sensitive constructions from tunnelling. The construction of the bored pile involves excavation of soil along the depth of the wall, which could cause stress release to the surrounded soil. Such stress release process is not simulated correctly within the centrifuge tests, hence the stiffness of the soil close to the protective wall is higher in the centrifuge tests than in reality. These differences will affect global TPSI (tunnel pile structure interaction) behaviour. However, the effects are unknown and not the focus of this research.

7.2.3 The effect of protective walls on tunnelling-induced ground movements

Figure 7.10 shows the ground surface vertical and horizontal displacements for tests GF, CCNM3, CCNM-R-S and CCNM-R-L at a tunnel volume loss of $V_{l,t}$=1, 2 and 2.8 %. For

test GF, the piled structure and protective wall are not considered. For test CCNM3, the ground movements due to tunnelling are affected by the loaded piles (piled structure), and for tests CCNM-R-S and CCNM-R-L, the ground movements are affected by the protective structures and loaded piles. All the CCNM tests include pile load redistribution due to the existence of a framed building, with full details provided in Section 4.3.2.

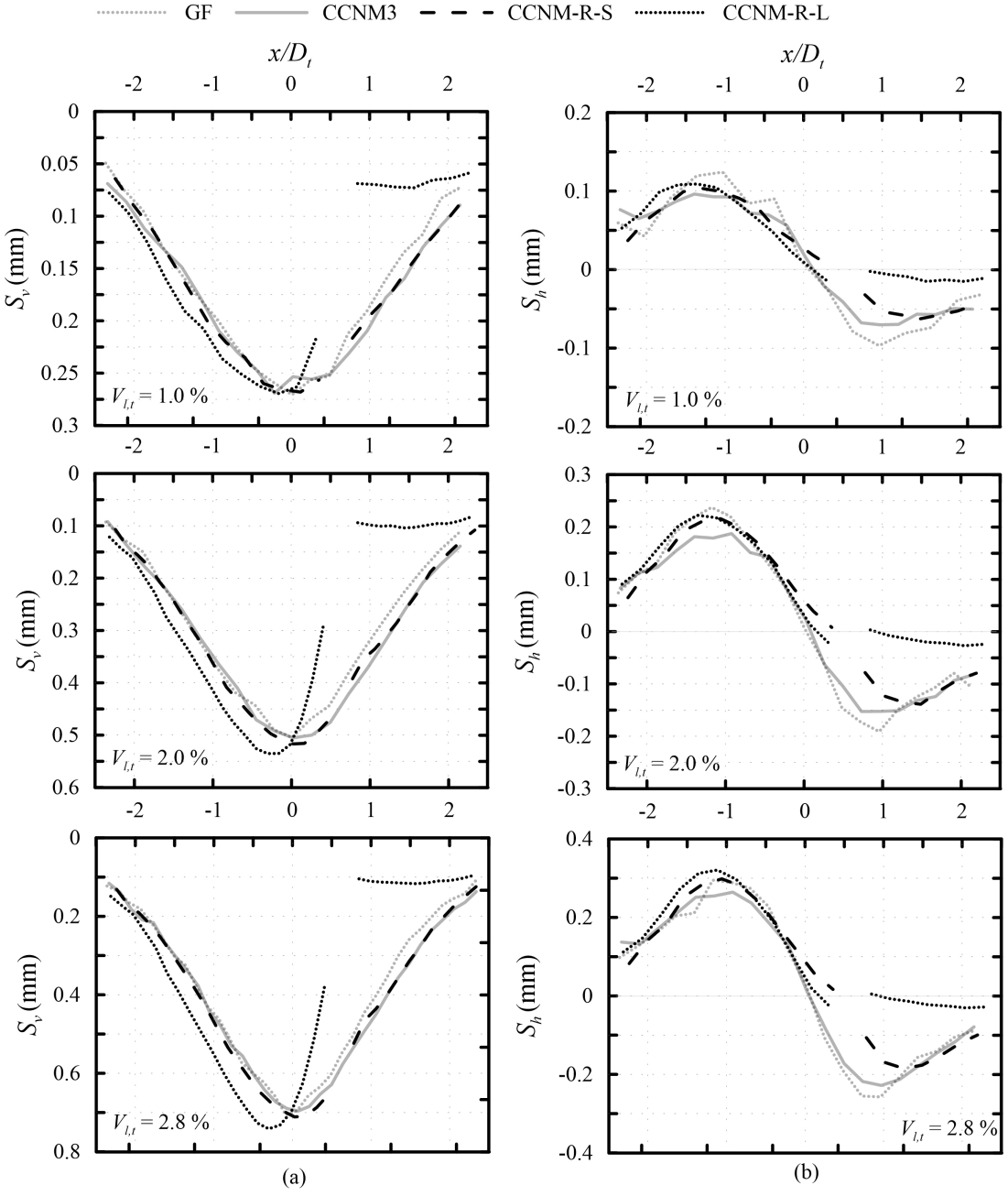


FIGURE 7.10: Measured surface displacement: (a) vertical settlement, (b) horizontal displacement (positive value is moving downwards or towards right)

In general, the vertical and horizontal displacements increase with tunnel volume loss for all three tests. It is worth to notice that the vertical and horizontal displacements

discussed in this section are not measured under plane strain condition due to the existence of the piles. For test CCNM3, the ground surface settlements at the right side of the tunnel (where the piled structure was located) are slightly greater than the settlements given in test GF at the same location under the same tunnel volume loss (effect of loaded piles). Test GF provides slightly greater horizontal displacements towards the tunnel than test CCNM3 for the soil located around 0.5-1.0 x/D_t. For test CCNM3, the horizontal movement of the piles was limited by the support frame located at the top of the strong-box, hence piles prevent the nearby soil horizontal displacements. For this research, the horizontal displacement and bending moment actuation (pile rotation) of the pile is not considered, as the vertical load is believed to be the dominating factor and the primary focus of this research (Franza et al., 2017).

For test CCNM-R-S, the soil on the retained side of the wall (x/D_t >0.7) shows a broadly similar magnitude of vertical settlement to the soil in test CCNM3, suggesting that the length of the wall in test CCNM-R-S was not sufficient to reduce tunnelling-induced surface soil settlement at the location of the building. In test CCNM-R-S, the surface soil horizontal displacements close to the wall (x/D_t between 0 and 1) shows less displacement towards the tunnel than the soil in test CCNM3. As a result, it can be summarised that for test CCNM-R-S, the wall did not significantly reduce tunnelling-induced surface soil displacement in the vertical direction at the location of the building, but for horizontal movements, the wall provided a limited degree of protection.

For the vertical settlement in test CCNM-R-L, the amount of settlement behind the wall (x/D_t >0.7) is minimal. For a given tunnel volume loss, surface soil settlements located "in front" of the wall (x/D_t <0) are greater than the soil in the greenfield condition (Test GF). Lesser horizontal soil displacements towards the tunnel were observed in test CCNM-R-L than CCNM-R-S. The longer wall in test CCNM-R-L had a more significant effect than the shorter wall in test CCNM-R-S, providing a greater level of reduction of surface soil displacements (vertical and horizontal). To quantify the reduction in soil displacements associated with pile settlement due to the use of protective walls, efficiency parameter is used, and this efficiency is discussed in Section 7.2.5.

Figure 7.11 presents the vertical soil displacement contours for all four centrifuge tests at a volume loss of $V_{l,t}$=2.0 %. For the greenfield test (Test GF), a concentrated zone of the major vertical settlements was observed above the tunnel crown. Test CCNM3 shows a similar settlements shape, despite the fact that the piled structure is located at the right-hand side of the tunnel (which causes greater surface settlements, and the geoPIV-RG data is not measured along plane of piles, see Figure 7.1). For test CCNM-R-L ("long" protective wall), the soil located on the retained side of the wall ($x/D_t > 0.7$) shows less settlement than the soil at equivalent distance on the opposite side ($x/D_t < -0.7$).

For test CCNM-R-S, the soil behind the wall does not show a as significant reduction in soil settlements as CCNM-R-L. For both protective wall tests, the chimney-like soil settlement mechanism above the tunnel crown tends to "tilt" towards left.

Figure 7.12 shows the horizontal soil displacement contours for all four centrifuge tests at a volume loss of $V_{l,t}$=2.0 %. The the greenfield test (Test GF) presents a symmetric shape in the displacement field, and the major zones of horizontal displacements are located slightly above both sides of the tunnel springline (agreeing with observations from Chapter 4). The major horizontal displacement zones propagate towards the soil surface with an inclined angle and generate zones of large horizontal displacements at the surface. The horizontal displacements along the tunnel centre line show very minimal displacement and generate a boundary line that distinguishes the soil displacements directions (moving towards the left or right). For test CCNM3, as discussed previously, the piles located at the right side of the tunnel tend to reduce tunnelling-induced horizontal soil movements in the region around the piles. As a result, the boundary line (distinguishing the soil displacement directions) is tilted slightly towards the right. For tests CCNM-R-S and CCNM-R-L, in general, the horizontal soil displacements behind the wall are less than the soil displacements in test CCNM3. For test CCNM-R-S, the major zone of horizontal displacement was located close to the tunnel springline (identified from test GF), which will encourage the toe of the protective wall to move towards the left. For test CCNM-R-L, the toe of the wall was located below the tunnel invert. Data from Zhou (2015) (greenfield tunnelling) showed that the soil around the bottom half of the tunnel undergoes very little to no displacements. Therefore, the soil displacements around the toe of the protective wall are expected to be very small. However, a zone with concentrated horizontal displacement is observed at the retained side of the wall at a depth between z/z_t= 0.4-1.2. Such concentrated displacements were caused by the deformation of the wall around the depth of the tunnel spring line and will be discussed in Section 7.2.4.

7.2.4 Protective wall response to tunnelling

The displacement of the protective wall with tunnel volume loss was measured by the cameras located at the front of the model box. One side of the protective wall facing towards the cameras was painted with random black lines to increase the "tracking" texture (colour contrast), and clear plastic strips were used to prevent sand intruding into the gaps between the side of the wall and the front acrylic window (as discussed in Section 4.4.3). Figure 7.13 shows the horizontal displacement (S_h) and bending moment along the walls for both tests as it varies with tunnel volume loss.

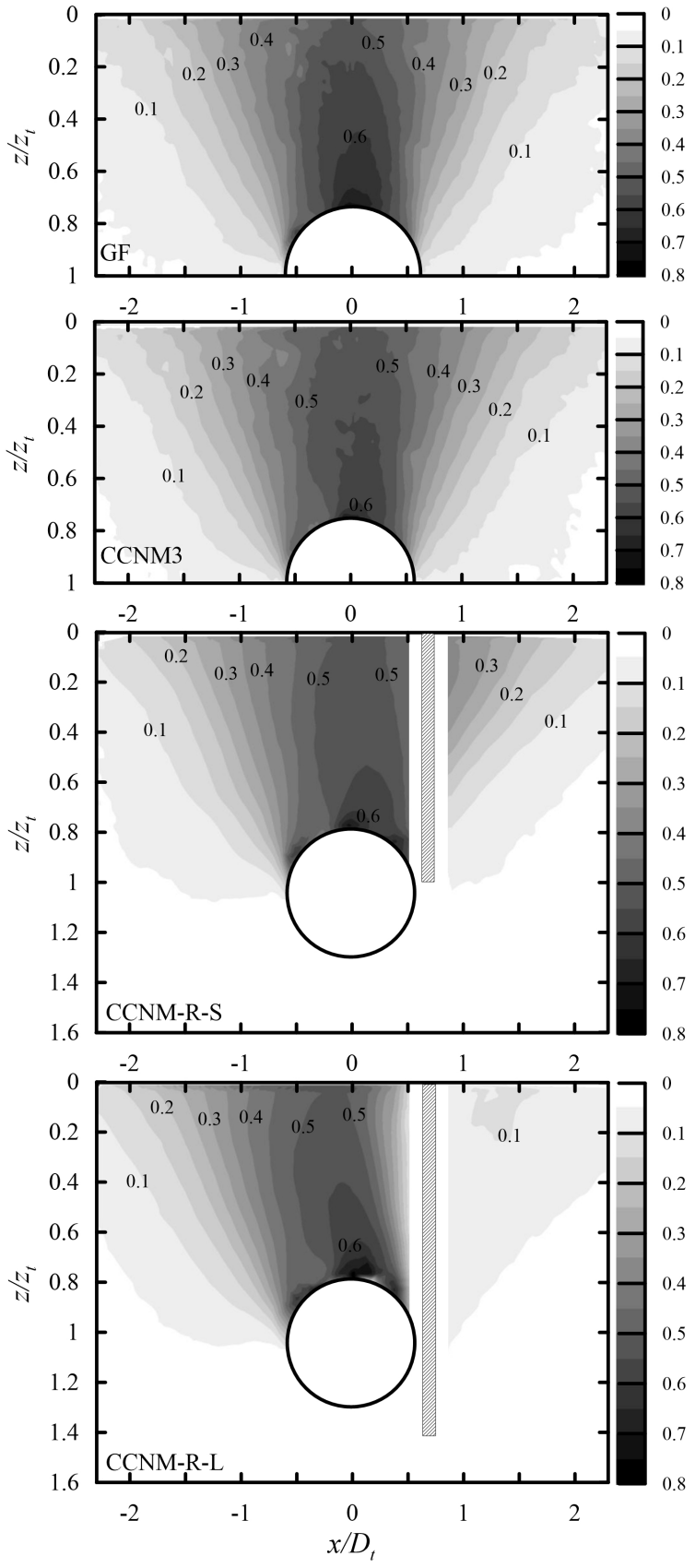


FIGURE 7.11: Contours of vertical settlement (mm) at $V_{l,t}$=2.0 % for all tests (soil moving downwards is positive)

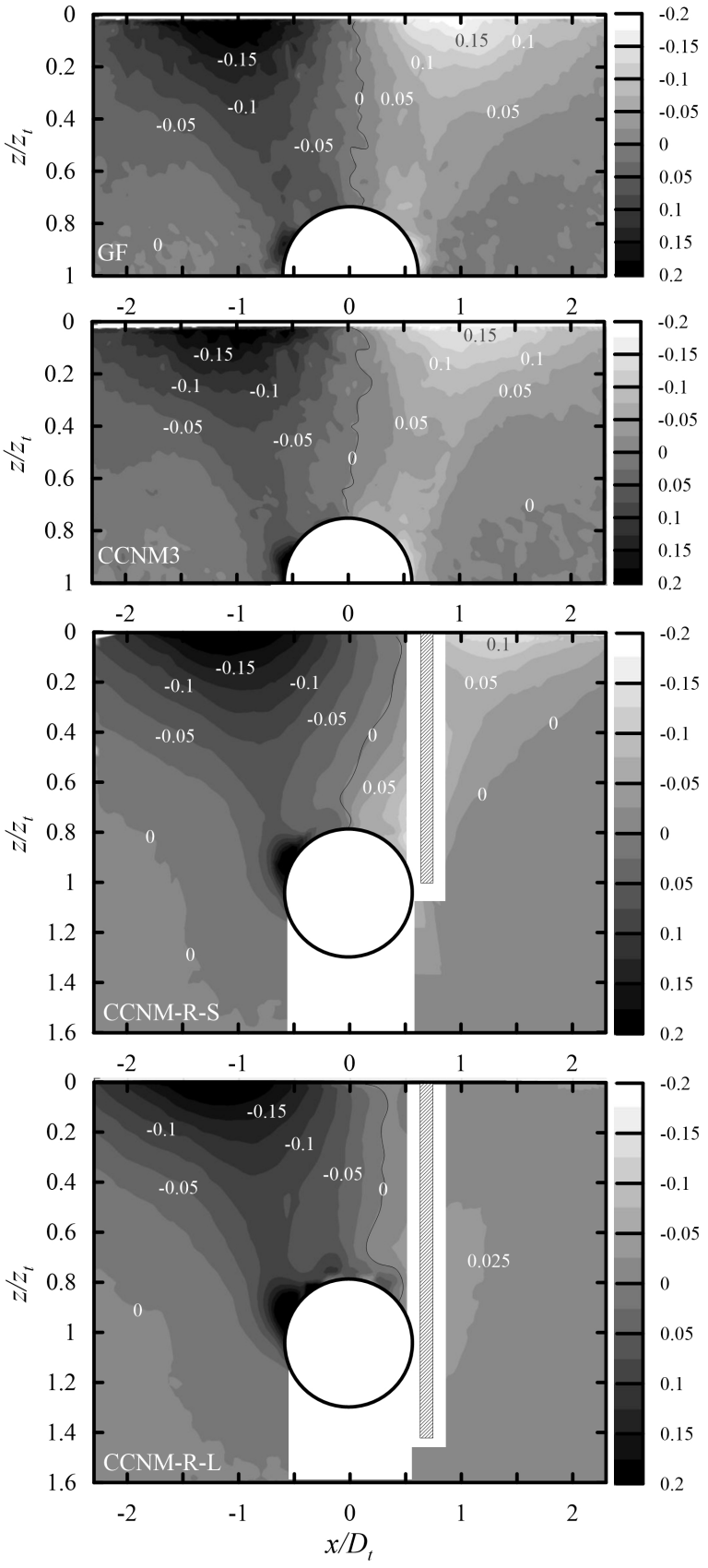


FIGURE 7.12: Contours of horizontal movement (mm) at $V_{l,t}$=2.0 % for all tests (soil moving to the right is positive)

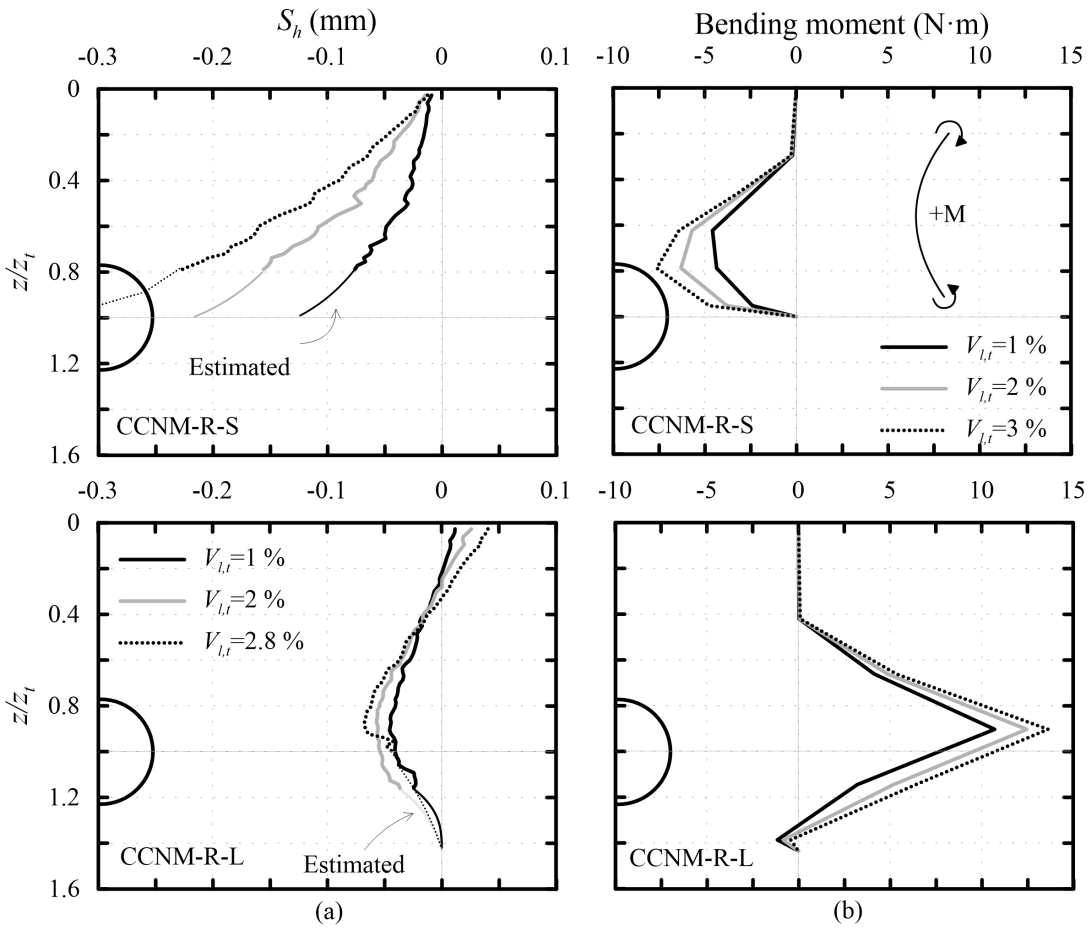


FIGURE 7.13: Horizontal displacement and bending moment along the wall with tunnel volume loss: (a) horizontal displacement, (b) bending moment

Despite the efforts adopted to prevent sand intrusion into the gaps between the side of the walls and the front acrylic window, some sand particles were observed at the toe of the wall in both tests, and the geoPIV-RG displacement data close to the toe of the wall was not used (sand intrusion makes the displacement data not reliable). Therefore, the displacement was estimated based on the deformation shape of the wall (upper and middle portions of the walls).

The deformed shape of the "short" and "long" protective walls is very different. For test CCNM-R-S, the toe of the wall was located at a depth of tunnel springline (z/z_t= 1). With tunnel volume loss, the major zone of horizontal displacements towards the tunnel identified in Figure 7.12 was located above the tunnel spring line (z/z_t= 0.8), and the tunnelling-induced soil movements tended to move the toe of the wall towards the tunnel. The displacement at the upper portion of the wall (close to the soil surface) is minimal. A maximum negative bending moment is observed at a depth of z/z_t= 0.8 in Figure 7.13 (b). Referring back to the horizontal displacement plot (Figure 7.13 (a)), the displacement below z/z_t=0.8 was not recorded (sand intruded into the interface), the

assumed wall displacement towards the tunnel is consistent with the bending moment profile. For test CCNM-R-L, the toe of the wall is located below the tunnel, where the surrounding soil experiences limited movement during tunnelling. With an increase in tunnel volume loss, the middle portion of the wall (above to the tunnel spring line at z/z_t=0.8-1.0) shows the most horizontal displacement towards the tunnel, whereas the upper portion of the wall moved towards the right (clockwise rotation). The fixity of the wall beneath the tunnel level causes clockwise wall rotation at a depth of $z/z_t \approx 0.4$; the soil located near the upper portion of the wall provides little resistance (low horizontal confining stress) and can not prevent the wall from rotating. The bending moment profile for test CCNM-R-L shows a minimum value at the upper portion of the wall (z/z_t= 0-0.4), whereas a maximum positive bending moment is located at the middle portion of the wall near the level of the tunnel (z/z_t= 0.8-1.0). Also, a small amount of negative moment is located at the very bottom of the wall. As a result, estimated wall displacement close to the toe of the wall is believed to be close to zero.

To summarise, the displaced shape of the protective wall highly depends on the length of the wall with respect to the depth of the tunnel. For CCNM-R-S, the tunnelling-induced ground movements caused the toe of the wall to move towards the tunnel, with maximum negative bending moment located at a depth of z/z_t= 0.8. For CCNM-R-L, the toe of the wall was located below the tunnel, and experienced limited displacement. With an increase in tunnel volume loss, soil movements towards the tunnel occurred at a depth of z/z_t= 0.8, resulting in a clockwise rotation motion at the upper part of the wall.

7.2.5 The effect of protective walls on pile settlement and pile head load distribution with tunnelling

Figure 7.14 shows the pile head settlement with tunnel volume loss for all three centrifuge tests (CCNM3, CCNM-R-S and CCNM-R-L), as well as the results for test CCNM2 (using the "old" strong box). In test CCNM-R-L, the settlement of pile 1 is significantly less than the settlement in the other tests (CCNM2, CCNM3 and CCNM-R-S). This is due to the use of the "long" protective wall which reduces tunnelling-induced soil movements on the retained side of the wall (as discussed in Section 7.2.3). For pile 1 in test CCNM3, as the protective wall was not used, the pile shows the greatest settlement with tunnelling. The magnitude of pile 1 settlement with tunnelling in tests CCNM2 and CCNM-R-S is similar. For pile 2, test CCNM-R-L shows the least pile settlement, followed by tests CCNM-R-S and CCNM3. For pile 2 in test CCNM2, the amount of pile settlement with tunnelling is less than test CCNM3 due to the use of "old" strong box (which will be discussed later). For pile 3, the amount of pile settlement with tunnelling

is generally less than pile 1 and pile 2 in all four centrifuge tests. With tunnelling, test CCNM-R-L provided the least pile settlement, and the pile 3 settlement in test CCNM-R-S and CCNM3 show similar magnitude, whereas pile 3 in test CCNM2 presents the lowest settlement with tunnelling. For pile 4, as the location of the pile is furthest away from the tunnel and protective wall, the effect of the protective wall on pile head settlement is minimal, and all tests present a similar settlement with tunnelling result for tests CCNM3, CCNM-R-S and CCNM-R-L. For pile 4 in test CCNM2, settlement observed is less than the other tests (which all used the "new" strong box).

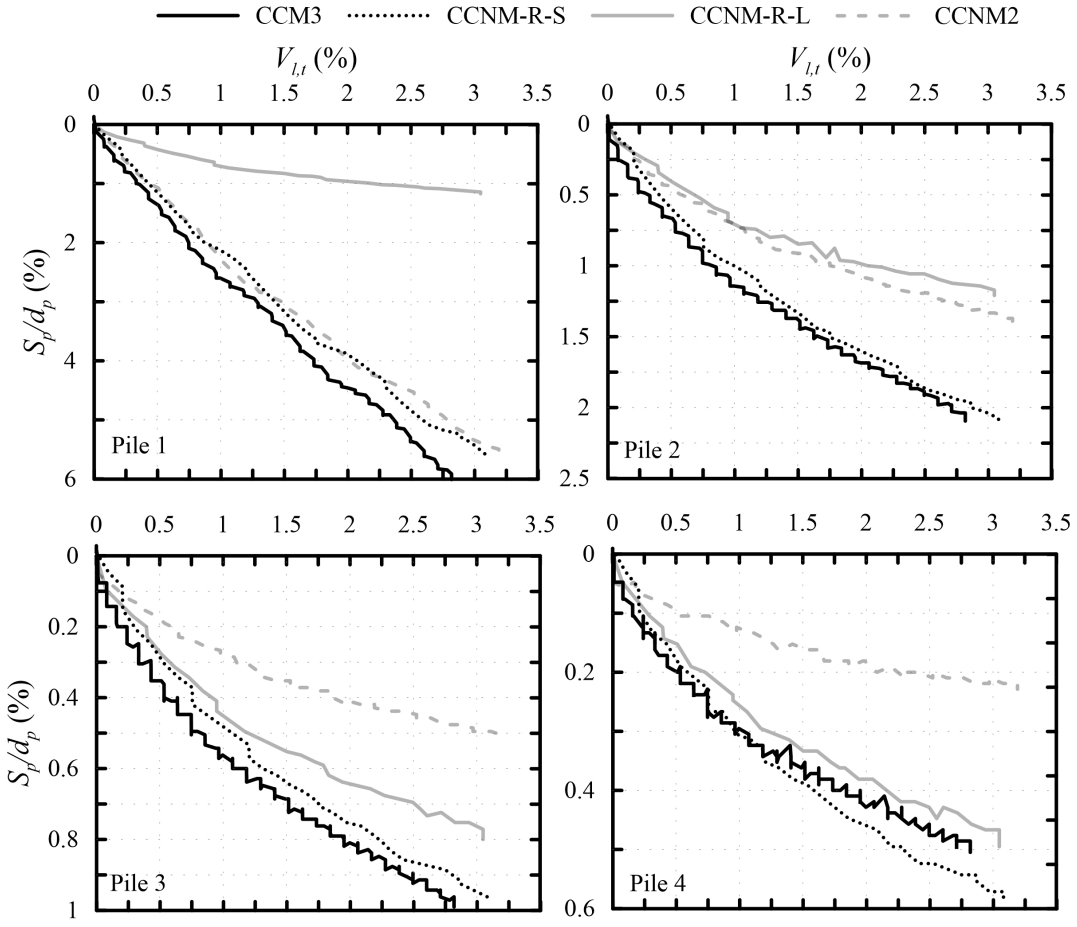


FIGURE 7.14: Pile head settlement with tunnel volume loss

The above data indicate that under a given tunnel volume loss, pile settlement in test CCNM2 is less than test CCNM3. As discussed previously (Section 7.2.1), test CCNM3 repeated test CCNM2 using the newly developed strong box, which has a greater soil depth below the pile tip. The difference in model container has a clear effect on the resulting soil and pile displacements during tunnelling. The difference in pile settlement ($\Delta S_p/d_p$, where $\Delta S_p = S_{CCNM3} - S_{CCNM2}$) between the two tests is presented in Figure 7.15. The difference in pile settlement is affected by tunnel volume loss and the location of the pile (x/D_t). For a tunnel volume loss $V_{l,t}$=1 or 2 %, the difference in

pile settlement decreases with x/D_t for piles 2, 3 and 4; pile 1 shows less difference than pile 2. With further increase in tunnel volume loss ($V_{l,t}$=2.8 %), the difference in pile 1 settlement is greater than pile 2, 3 and 4. The degree of difference in pile settlement between the two tests (CCNM2 and CCNM3) is proportion to tunnel volume loss for each pile, and the difference is decreased with the pile further away from the tunnel. Such a difference in pile settlement is mainly affected by the amount of soil below the pile tip. For the "old" strong box the soil underneath the pile has greater overall stiffness than the soil in the "new" strong box, and during tunnel volume loss (the stress releases process) piles are expected to settle more in the '1less stiff" soil (soil within the "new" strong box).

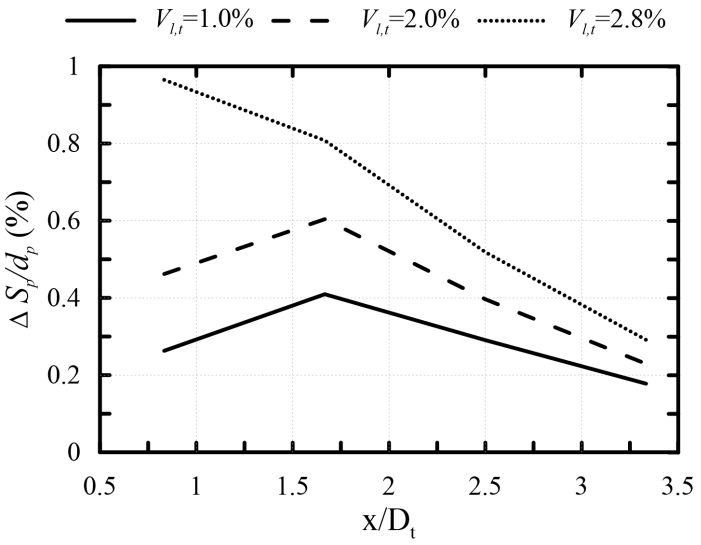


FIGURE 7.15: The difference in pile settlement with tunnelling between tests CCNM2 and CCNM3

Tests GF, CCNM3, CCNM-R-S and CCNM-R-L are conducted in the "new" strong box, which has same soil depth and test conditions, and the relative results are valid. From the above discussion, it can be summarised that the use of protective walls can reduce tunnelling-induced pile settlement. It is possible to quantify the efficiency of the protective walls in terms of pile settlement. The maximum efficiency of a protective wall is assumed that the tunnelling-induced pile settlement is fully prevented (zero pile displacement), whereas the other extreme case is that the protective structure has zero protection to pile settlement (wall does not exist). Centrifuge tests CCNM-R-S and CCNM-R-L should fall into these two extreme cases. As a result, the efficiency of the protective structure for every pile can be defined as:

$$\eta^{rs}_{V_{l,t}} = \frac{S_{V_{l,t}} - S^{rs}_{V_{l,t}}}{S^{s}_{V_{l,t}}} \times 100\% \tag{7.1}$$

where S is the pile settlement, the subscript $V_{l,t}$ indicated the tunnel volume loss, and the superscripts rs referred to the case that protective wall is considered and the case without the use of protective wall is referred to as $S_{V_{l,t}}$. Figure 7.16 shows the efficiency parameter $\eta^{rs}_{V_{l,t}}$ for all four piles with tunnel volume loss in both tests (CCNM-R-S and CCNM-R-L). The efficiency parameter varies with tunnel volume loss and pile location. For test CCNM-R-S ("short" protective wall), with increase in tunnel volume loss ($V_{l,t}$=0-1.5 %), the efficiency parameter for all four piles decreased, and with further increase in tunnel volume loss ($V_{l,t} > 1.5$ %), the parameter increased slightly. The pile located closet to the tunnel (Pile 1) shows the highest efficiency value, followed by piles 2, 3 and 4. For test CCNM-R-L, Pile 1 shows an increase in efficiency parameter with tunnel volume loss; for pile 2 and 3, the efficiency varies with tunnel volume loss (similar to CCNM-R-S). For pile 4, the efficiency initially decreases with tunnel volume loss and tends to flatten out when $V_{l,t} > 1.5$ %.

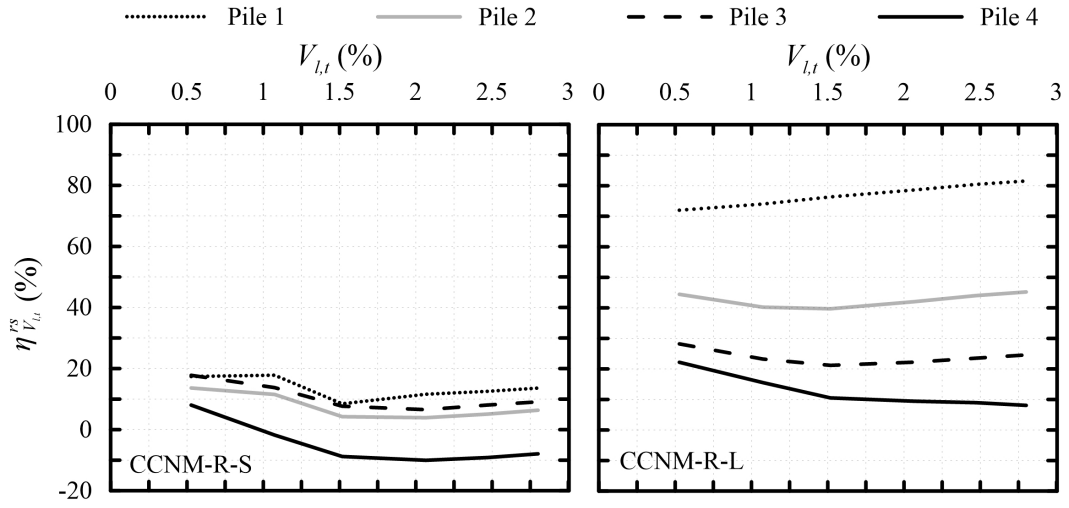


FIGURE 7.16: Efficiency parameter $\eta^{rs}_{V_{l,t}}$ with tunnel volume loss

In general, the variation of efficiency parameter for all four piles is not very sensitive to tunnel volume loss, but is more significantly affected by the location of the pile. As a result, the average efficiency parameter $\overline{\eta^{rs}}$ (regardless of tunnel volume loss) for all four piles is plotted against the relative position of the pile to the tunnel (x/Dt) in Figure 7.17. In test CCNM-R-L, the average efficiency parameter decreases with an increases in x/Dt and shows higher value of efficiency than test CCNM-R-S.

Figure 7.18 shows the pile head load with tunnelling for all tests (CCNM3, CCNM-R-S and CCNM-R-L), as well as the results from test CCNM2 (using the "old" strong box). The effect of the superstructure on pile head load was discussed in Section 6.2.5 (based on the results from tests CCNM1 and CCNM2). In general, for test CCNM3 (repeat of test CCNM2), pile 1 head load decreased with tunnel volume loss, and the decreased load from pile 1 tends to transfer to the adjacent piles, which causes an increase in pile

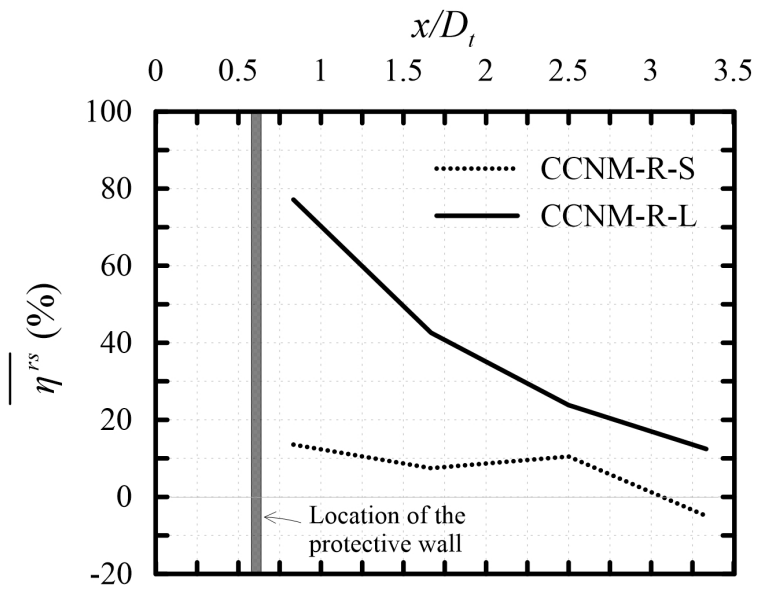


FIGURE 7.17: Average efficiency parameter $\overline{\eta^{rs}}$ with respect to pile location

2 head load and a very little increase in pile 3 head load. Meanwhile, due to the stiffness of the superstructure pile 4 head load decreased with tunnelling, hence part of the pile 4 head load was also transferred to piles 2 and 3.

Test CCNM-R-S shows similar load transfer among the piles to test CCNM3. At $V_{l,t}$=2.8 %, pile 1 head load in test CCNM-R-S decreased by 32 N, which is less than CCNM3 (pile 1 head load decreased by 40 N). For pile 2, at $V_{l,t}$=2.8 %, pile head load increased by 42 N in test CCNM-R-S and 56 N in CCNM3. Pile 3 head load increased by 12 N and 11 N in tests CCNM-R-S and CCNM3, respectively. For pile 4, a decrease in pile head load of about 22 N and 25 N WAS observed for tests CCNM-R-S and CCNM3 at $V_{l,t}$=2.8 %. The above results indicate that the use of the "short" protective wall (CCNM-R-S) reduces the load transfer between the piles, but the pile head settlement with tunnelling is similar to test CCNM3 (see Figure 7.14).

For Test CCNM-R-L ("long" protective wall), where the toe of the wall was located below the tunnel invert, at $V_{l,t}$=2.8 %, pile 1 head load increased slightly by about 5 N, and the adjacent pile 2 head load decreased by about 8 N. In the same time, pile 3 head load increased by about 3 N and pile 4 head load remained unchanged. As a result, the use of the "long" protective wall significantly reduced the amount of load transferred between the piles during tunnel volume loss.

In addition, Figure 7.18 presents the pile head load with tunnelling for test CCNM2 (using the "old" strong box). In Figure 7.14, the pile settlement data shows that for a given tunnel volume loss, settlement of the piles in test CCNM2 is less than test CCNM3, and the difference in pile settlement between the two tests increases with tunnel volume

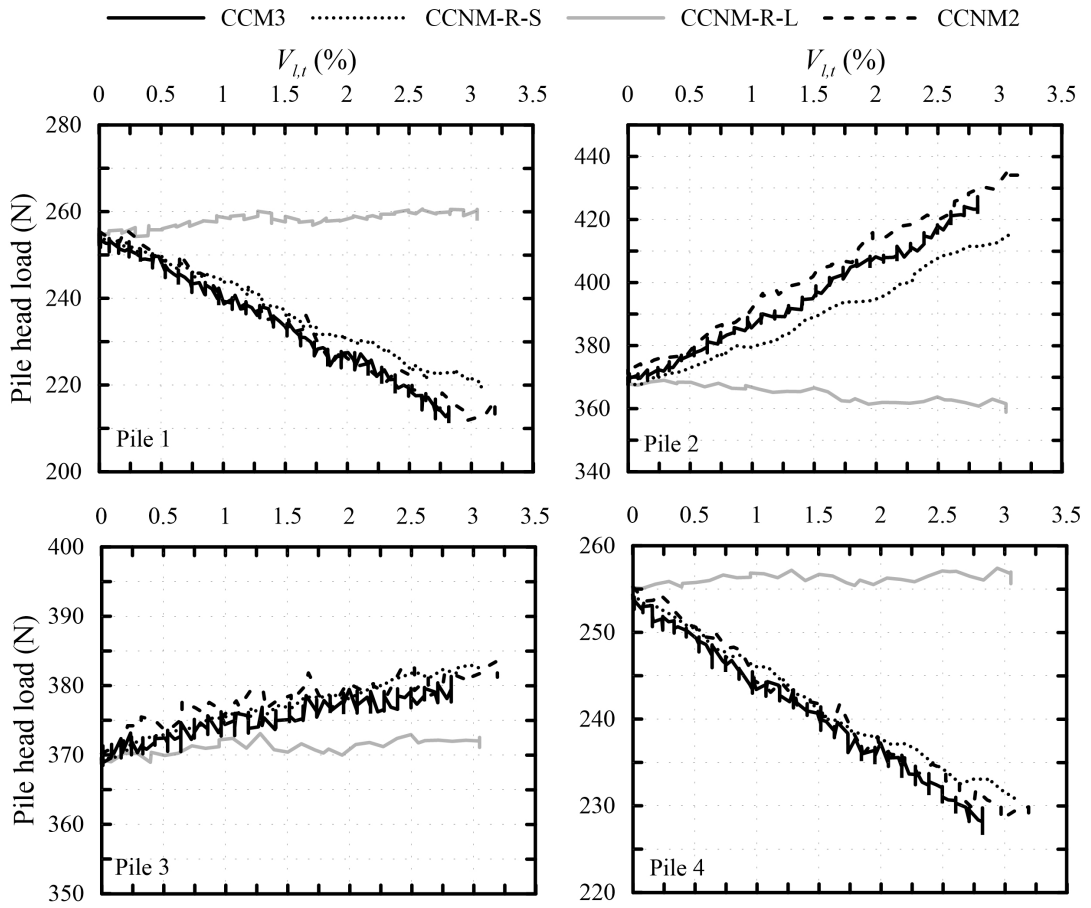


FIGURE 7.18: Pile head load with tunnel volume loss

loss. In test CCNM2, the pile 2 head load increased more significantly with tunnelling than in test CCNM3. Piles 1, 3 and 4 in test CCNM2 show similar load change with tunnelling as in test CCNM3, and the difference in pile head load is minimal. Tests CCNM2 and CCNM3 have the same structure layout (same structure stiffness), and the pile head load was governed by the deformation of the structure (relative displacement between the piles). The difference in structure deformation shape between the two tests will be discussed in the next section.

7.2.6 Settlement and deformation of structures

Figure 7.19 shows the settlement of the modelled structure in the following five centrifuge tests at a tunnel volume loss of $V_{l,t}$=2.8 %: CL (zero structure stiffness; using the "old" strong box), CCNM2 (using the "old" strong box), CCNM3 (using the "new" strong box), CCNM-R-S ("short" protective wall; using the 'new' strong box) and CCNM-R-L ("long" protective wall; using the "new" strong box). The magnitude of structure settlement between tests CL and CCNM2 is similar, suggesting structure stiffness has a

limited effect on tunnelling-induced structure settlement. For test CCNM3, in general, the structure settlement is greater than test CCNM2; this is because the height of the strong box used in these two tests was different (as discussed in Section 7.2.5). The use of the protective wall can prevent the pile head settlement due to tunnelling-induced ground movements; test CCNM-R-S shows less structure settlement than CCNM3, and CCNM-R-L shows a significant reduction in structure settlement compared to other tests.

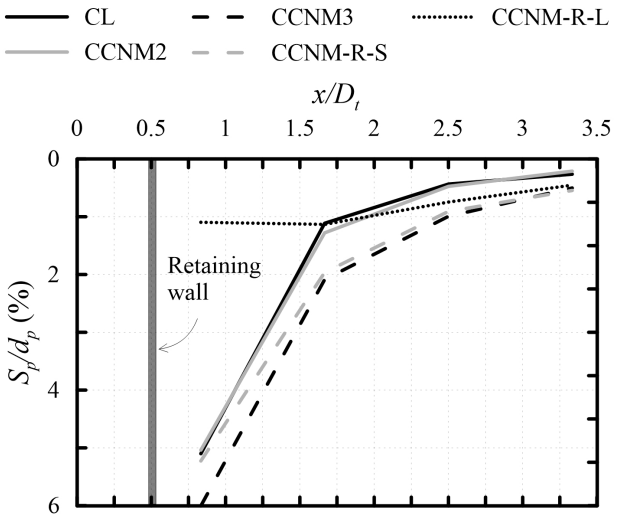


FIGURE 7.19: Structure settlement at $V_{l,t} = 2.8\%$

To quantify the deformation of a structure, Son and Cording (2005) developed a set of equations to calculate the angular distortion (β), see Figure 7.20:

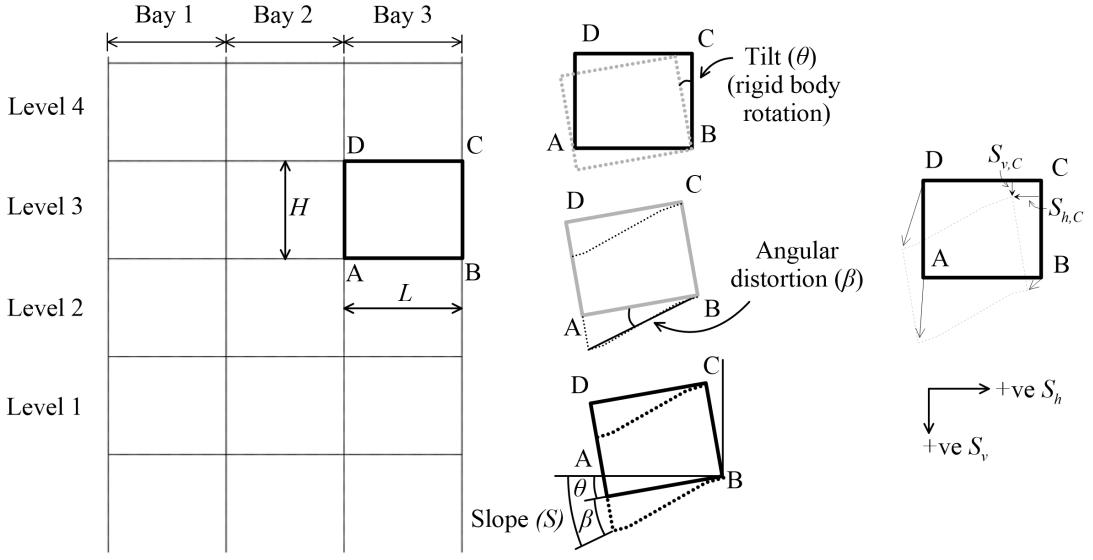


FIGURE 7.20: Illustrate of the structure layout and angular distortion calculation

$$\begin{aligned} \text{Angular distortion}(\beta) &= \text{Slope}(S) - \text{Tilt}(\theta) \\ \text{Slope}(S) &= \frac{S_{v,A} - S_{v,B}}{L} \\ \text{Tilt}(\theta) &= \frac{(S_{h,A} - S_{h,D}) + (S_{h,B} - S_{h,C})}{2H} \end{aligned} \tag{7.2}$$

For each frame, as the highlighted frame in Figure 7.20 for example, a angular distortion value (β) can be calculated based on the displacement of the four structure joints (A, B, C and D), where the L is the length of the structure bay, and H is the height of the structure storey, and S_v and S_h is the vertical and horizontal displacement of a structure joint, respectively.

Figure 7.21 shows the angular distortion (β) of the frames in each bay at a tunnel volume loss of $V_{l,t} = 2.8\%$. For the frames in Bay 1, with the increase in structure level, the angular distortion (β) decreased, suggesting the amount of structure distortion reduced at the upper level, and test CCNM2 and CCNM3 shows similar angular distortion (β) value with increase in structure level, and CCNM-R-S shows the least value then other two tests (CCNM2 and CCNM3). The angular distortion for the frames in test CCNM-R-L is not presented in Figure 7.21, because the value is minimal, and changes very little with structure level; a factor that will be discussed next. For Bay 2 and 3, the value of angular distortion for the frames are in negative value, suggesting the different distortion direction compared with the frames in Bay 1, and with the increase in structure level, the angular distortion decreased, which is similar to the observation in Bay 1.

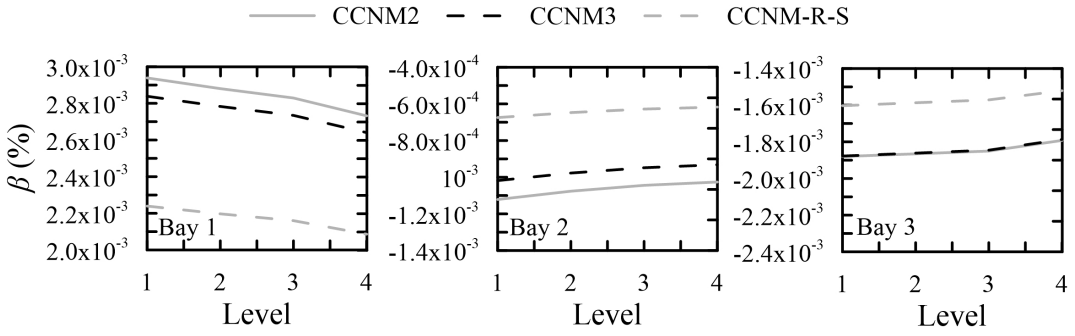


FIGURE 7.21: Angular distortion of the frames in 3 bays at a tunnel volume loss of $V_{l,t} = 2.8\%$

Based on the above data, it can be suggested that for the structure, the most significant angular distortion undergoes at the lowest structure level (level 1) with tunnel volume loss, and Figure 7.22 shows the angular distortion of the frame at level 1 with tunnelling for tests CCNM2, CCNM3, CCNM-R-S and CCNM-R-L. For Bay 1 level 1 frame, with tunnelling, the value of angular distortion increased in tests CCNM2,

CCNM3 and CCNM-R-S. Test CNM2 and CCNM3 shows similar angular distortion value with tunnelling, referring back to Figure 7.19, despite the fact that test CCNM2 has greater pile settlement than CCNM3 (due to the use of different strong box, depth of the soil below the pile tip is different), the general structure frame distortion is similar in tests CCNM2 and CCNM3. The distortion of the frames governs the pile head load, and referring back to Figure 7.18, the difference in pile head load between the two tests is minimal. With the use of "short" protective wall, test CCNM-R-S shows a slightly lower value of angular distortion with tunnelling than test CCNM3. For test CCNM-R-L (use "long" protective wall), the angular distortion is minimum with tunnel volume loss in Bay 1, and the value is negative, suggesting the direction of the angular distortion for Bay 1 in test CCNM-R-L is different to the other tests.

For Bays 2 and 3, negative angular distortion values are observed for tests CCNM2, CCNM3 and CCNM-R-S. With the increase in tunnel volume loss, tests CCNM2 and CCNM3 show a similar increase in angular distortion value (absolute value), and CCNM-R-S shows less increase than tests CCNM2 and CCNM3. For test CCNM-R-L, the angular distortion value increases slightly with tunnelling, but the value is insignificant.

Based on the above results, the use of protective wall had some ability to protect the structure from distortion caused by tunnelling-induced soil movements. The degree of angular distortion decrease with structure level, where the most significant frame distortion is located at the lowest structure level, and for each bay, the degree of distortion decreased for the Bay located further away from the tunnel.

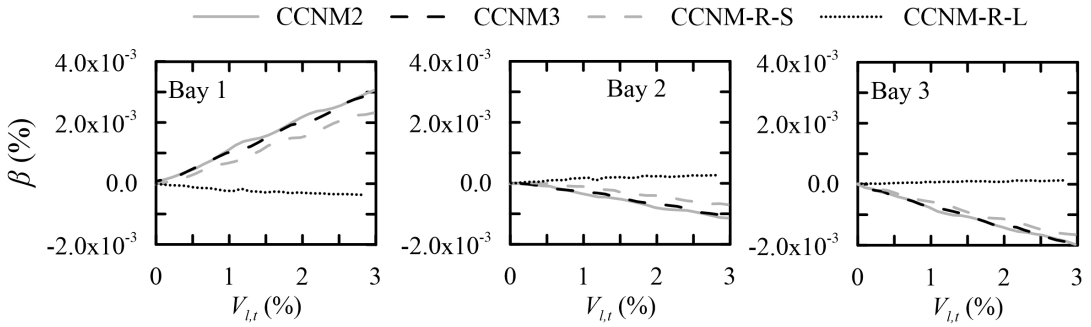


FIGURE 7.22: Angular distortion of the frame at level 1 with tunnelling

7.2.7 The effect of protective walls on the axial force distribution along the piles and change in pile shaft resistance with tunnelling

Figure 7.23 presents the axial force along the piles with tunnelling for tests CCNM3, CCNM-R-S and CCNM-R-L. As discussed in Section 6.2.6, the axial force along the pile is mainly affected by two mechanisms: (1) change in pile head load due to structure

stiffness, and (2) the effect of tunnelling-induced ground movements (pile-pile interaction is not considered in this study).

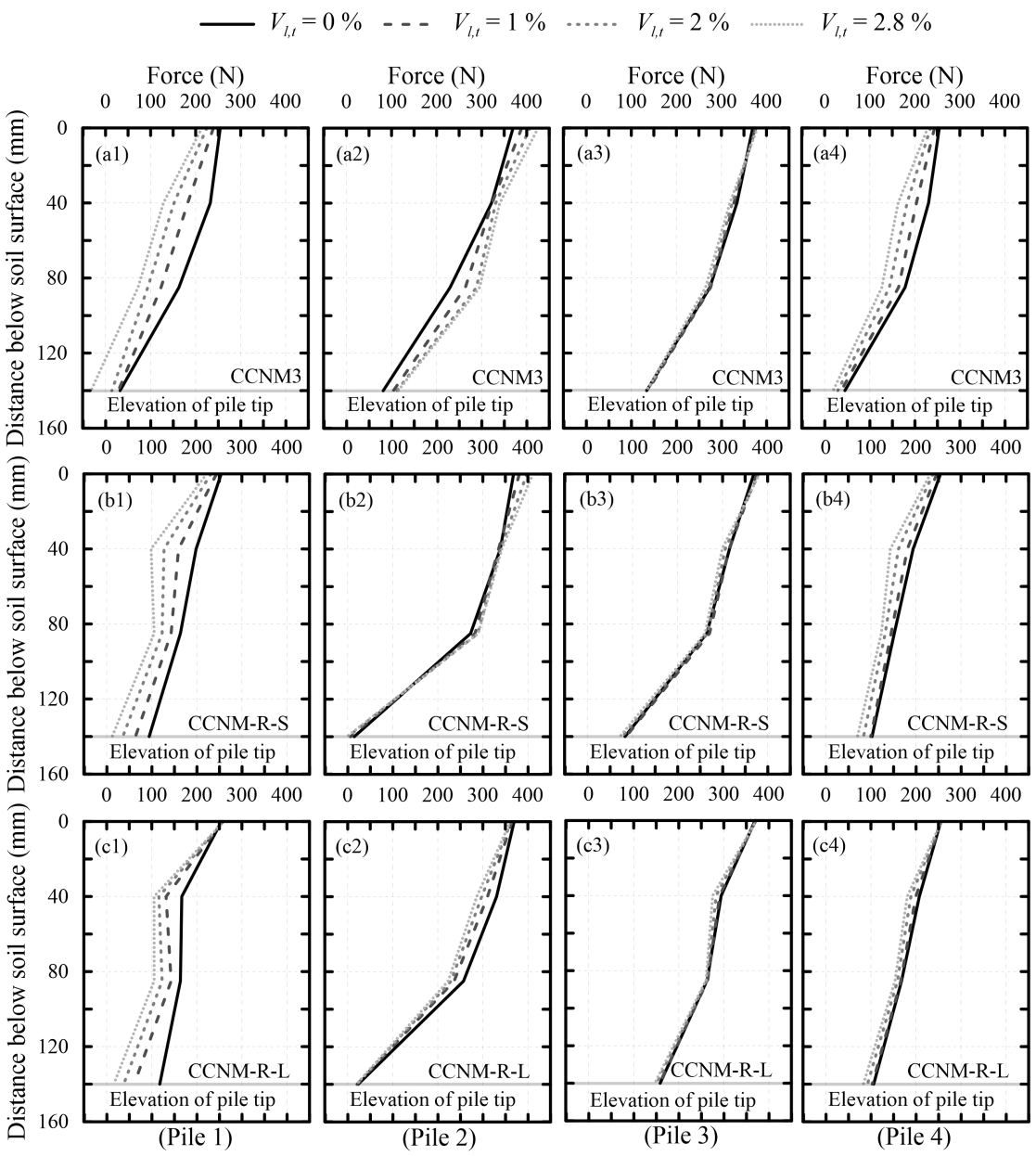


FIGURE 7.23: Pile axial load at $V_{l,t} = 0,\ 1,\ 2,$ and 2.8 % : (a) CCNM3 1, (b) CCNM-R-S, (c) CCNM-R-L

For pile 1 in test CCNM3, pile head load decreased with tunnelling due to the effect of structure stiffness, and the axial force along the upper portion of the pile decreased (mechanism 1). In addition, the axial force close to the pile tip reduced; as discussed in Section 6.2.6, the axial force along the lower portion of the pile is mainly affected by the tunnelling-induced ground movements (mechanism 2). For pile 1 in test CCNM-R-S, pile 1 head load decreased with tunnelling, as well as the force close to the pile tip; the change in axial force close to the pile tip is similar in magnitude to test CCNM3. For pile

1 in test CCNM-R-L, the pile head load remains unchanged, and the axial force at the lower portion of the pile decreased (similar to pile 1 in tests CCNM3 and CCNM-R-S). These results suggest that, despite the use of protective walls, for pile 1, the axial force along the lower portion of the pile decreases with tunnelling (loss of pile end bearing load), and is mainly affected by the tunnelling-induced ground movements (mechanism 2). Referring back to Figure 7.12, despite the use of protective walls, both tests CCNM-R-S and CCNM-R-L show horizontal displacement towards the tunnel along the lower portion of the pile z/z_t=0.8 (where the pile 1 is located). The decrease in pile 1 axial force at the pile tip (loss of pile end bearing load) is clearly affected by the tunnelling-induced horizontal soil movements (applies to tests CCNM3, CCNM-R-S and CCNM-R-L).

For pile 2 in test CCNM3, pile head load increased with tunnelling, and the axial force along the depth of the pile increased accordingly; the amount of increase in end bearing force with tunnelling is less than the pile head load. For pile 2 in test CCNM-R-S, pile head load increased with tunnelling, the axial force along the upper portion of the pile increased, and the axial force along the lower portion of the pile remain unchanged, suggesting the increased force was taken by the shaft friction at the middle and upper portions of the pile. Based on the above data, it can be suggested that for pile 2 in CCNM3, the increased pile head load was mainly taken by the end bearing force, whereas for pile 2 in CCNM-R-S, the increased pile head load was mainly taken by shaft friction at the middle and upper portions of the pile. As a result, the tunnelling-induced ground movements (mechanism 2) have a limited effect on pile 2 in test CCNM-R-S (prevented by the protective wall). For pile 2 in test CCNM-R-L, the pile head load and end bearing force have minimum change with tunnelling, and the axial force at the middle and upper portions of the pile reduced, suggesting some degree of load transfer at the middle portion of the pile.

For pile 3, all three tests show a minimal change in axial force with tunnelling. For pile 4 in tests CCNM3 and CCNM-R-S, pile head load decreased due to the effect of structure stiffness. Therefore, the axial force along the pile reduced (mechanism 1). For pile 4 in test CCNM-R-L, the pile head load remained unchanged with tunnelling, and the axial force along the pile reduced with tunnelling, the amount of change in axial force was minimal.

Prior to tunnel volume loss, piles were loaded to the designated load, and piles settled during pile loading (see Figure 7.7). To resist pile settlement, upwards shaft friction along the lower portions of the piles is mobilised (discussed in Section 7.2.2). During tunnel volume loss, tunnelling-induced soil movements affect the pre-existing shaft friction along the pile, and to balance the force applied to the pile (affected by the structure stiffness), additional shaft friction along the pile is developed. Figure 7.24 shows the

change in unit shaft friction ($\Delta f_{vl}(z)$) along the pile with tunnel volume loss for centrifuge tests CCNM3, CCNM-R-S and CCNM-R-L. The definition of $\Delta f_{vl}(z)$ is given in Section 6.2.5 (see Equation 6.2). To help understand the development or change in shaft fraction along the pile with tunnelling, Figure 7.25 shows the soil settlements with respect to the pile for all three tests at a tunnel volume loss of $V_{l,t}$=2.8 %. For every test, two cameras were used to capture the soil movements behind the acrylic window. As a result, captured soil movements are not necessarily equal to the soil movements around the pile. In addition, soil settlements with respect to a pile are defined as $S_v - S_p$ (soil settlements along the length of the pile minus pile settlement); if the value is positive then the soil settled more than the pile.

For pile 1 in test CCNM3, the pile settlement is higher than the soil settlement along the depth of the pile. As a result, the pile can be assumed as being "pushed down". For the soil at the upper portion of the pile, to resist the settlement of the pile, the upwards shaft friction is mobilised, and the unit shaft resistance along the upper portion of the pile is increased (Figure 7.24 (a1)). For the soil close to the lower portion of the pile, due to the tunnelling-induced soil movements, the unit shaft friction decreased. For pile 1 in test CCNM-R-S, with the "short" protective wall, soil settlements with respect to the pile are less than in test CCNM3 (black dashed line in Figure 7.25 pile 1), but in general, pile 1 settlement in test CCNM-R-S is still greater than the soil. Therefore, to resist pile settlement, the shaft friction along the upper portion of the pile increased (Figure 7.24 (b1)). In addition, unlike pile 1 in test CCNM3, a small increase in shaft friction at the lower portion of the pile is identified in test CCNM-R-S (Figure 7.24 (b1)). For pile 1 in test CCNM-R-L, the pile head load remains unchanged with tunnelling, while the pile end bearing force reduced. As a consequence, the shaft resistance increased at the lower and upper portion of the pile (Figure 7.24 (c1)). A reduction in shaft resistance is observed along the middle portion of the pile, but the amount is minimal.

For pile 2 in tests CCNM3 and CCNM-R-S, the soil at the upper portion of the pile (close to the soil surface) shows greater settlement than the pile (Figure 7.25 pile 2). As a result, the soil tends to "drag down" the pile, and the shaft friction along the upper portion of the pile increased in the tests CCNM3 and CCNM-R-S (Figure 7.24 (a2, b2)). For pile 2 in test CCNM-R-L, the soil settlements at the upper portion of the pile are less than the pile settlement (Figure 7.25 pile 2 dotted line), similar to pile 1 in test CCNM-R-L. Therefore, the pile is being "pushed down", and to resist the pile settlement, upwards shaft friction is mobilised (an increase in unit shaft resistance at the upper portion of the pile, see Figure 7.24 (c2)). For pile 2 in tests CCNM3 and CCNM-R-S, reductions in unit shaft resistance are identified along the middle portion of the pile (Figure 7.24 (a2, b2)). It is believed that the tunnelling-induced soil movements caused such reductions. In addition, the soil at the lower portion of the pile is not affected

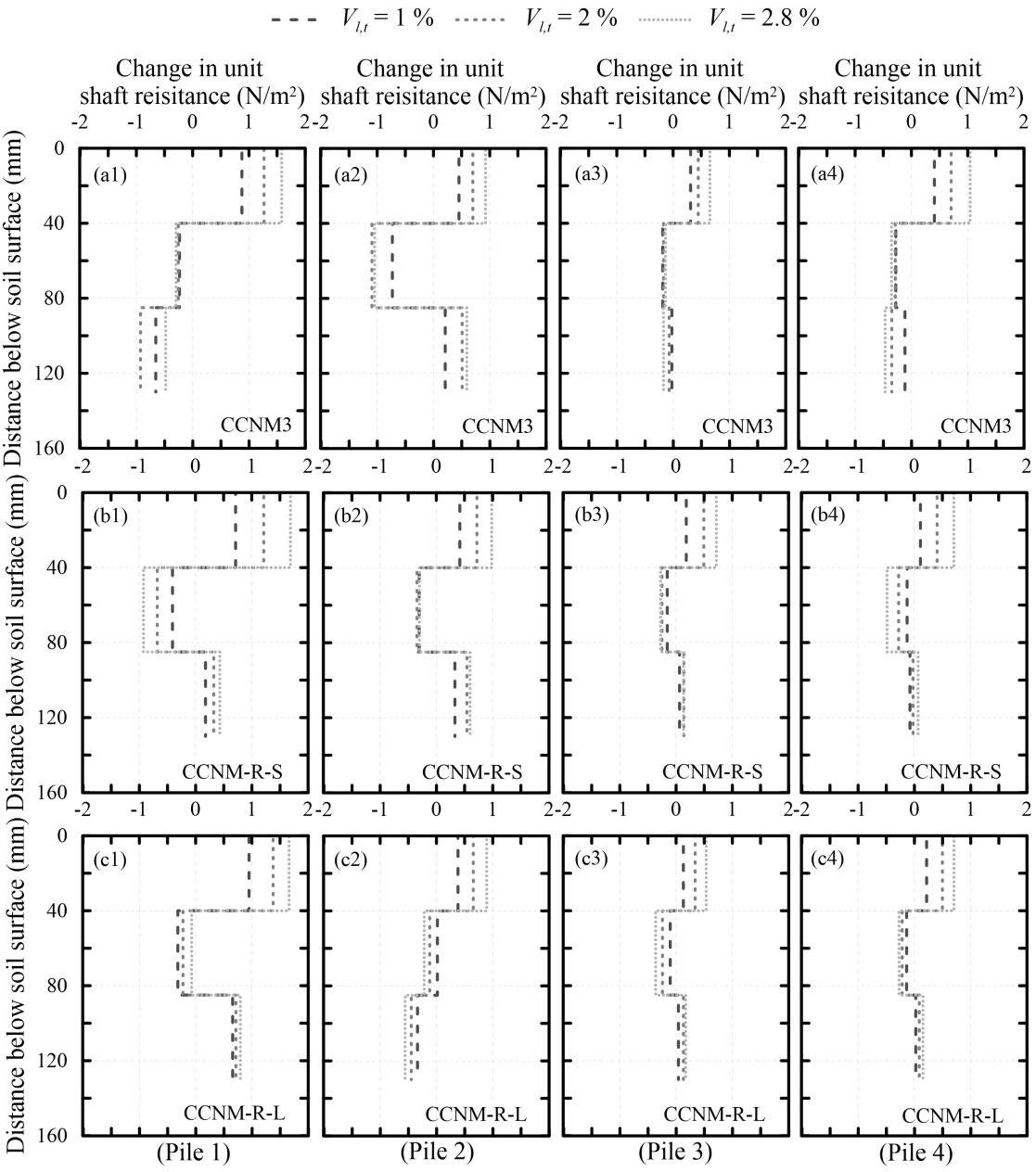


FIGURE 7.24: Change in unit shaft resistance at $V_{l,t} = 0,\ 1,\ 2,$ and 2.8% : (a) CCNM3, (b) CCNM-R-S, (c) CCNM-R-L

by the tunnelling-induced soil movements, and with the increase in pile 2 settlement, upwards shaft friction along the lower portion of the pile increased (Figure 7.24 (a2, b2)). For pile 2 in test CCNM-R-L, the shaft friction along the middle and lower portions of the pile reduced with tunnelling (Figure 7.24 (c2)). Referring back to Figure 7.12, a concentrated zone of horizontal soil displacements was identified at a soil depth of z/z_t =0.5-0.8 (close to the middle and lower portions of the pile) with a horizontal distance between x/D_t=0.8-1.4 (located at the front of pile 2, which has a horizontal distance of x/D_t=1.6). This major horizontal soil movement zone causes the loss of end

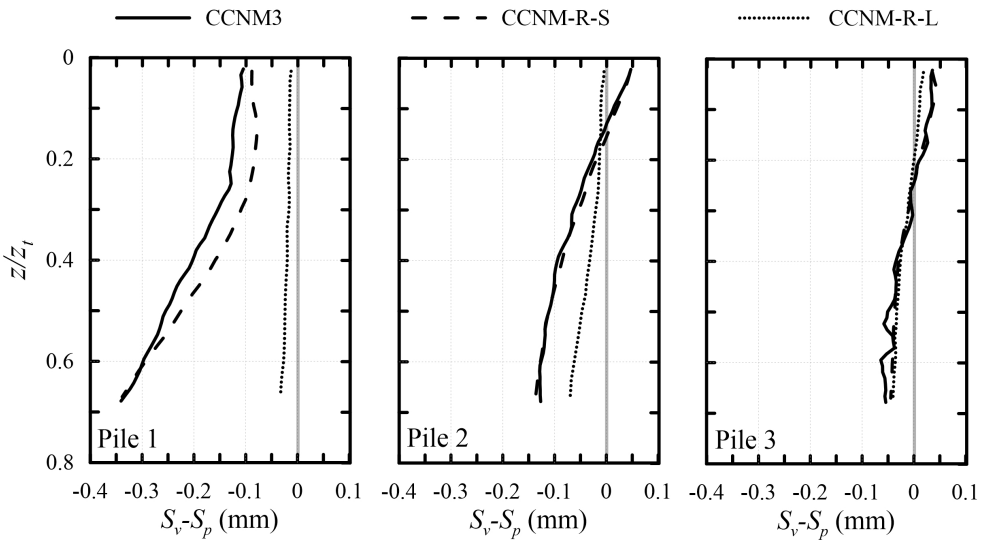


FIGURE 7.25: Soil settlements with respect to the pile along the depth of the pile at a tunnel volume loss of $V_{l,t} = 2.8\%$

bearing force for pile 1 and reduces pile 2 soil confining pressure, therefore decreasing the shaft friction along the middle and lower portions of the pile (Figure 7.24 (c1, c2)).

For pile 3 in all three tests, soil along the upper portion of the pile settles greater than the pile (Figure 7.25 pile 3). Therefore, the soil tends to "drag down" the pile, and the unit shaft resistance at the upper portion of the pile increases. All three tests show a minimal change in pile head load with tunnelling, and the overall change in shaft resistance along the middle and lower portions of the pile is minimal (Figure 7.24 (a3, b3 and c3)).

For pile 4, an increase in shaft friction along the upper portion of the pile is identified for all three tests, similar to pile 3. Therefore, it is believed that the soil settlements close to the soil surface are higher than the settlement of pile 4 in all three tests (soil close to pile 4 was out of the camera field of view). As pile 4 is located furthest away from the tunnel, the effect of tunnelling-induced soil movements on pile shaft resistance is minimal.

7.2.8 The effect of protective walls on post-tunnelling pile jacking response

The shaft resistance along the piles may be affected by the tunnelling-induced soil movements, which could affect the post-tunnelling pile jacking response. Figure 7.26 shows the load-settlement curves for all piles in tests CCNM3, CCNM-R-S and CCNM-R-L, as well as the "greenfield" pile jacking for test PJ (pile 2). Piles were jacked into the soil using a displacement control method, with a jacking rate of 0.1 mm/s; the pile jacking method was discussed in section 6.2.2. In addition, to further investigate the pie jacking

stiffness with increase in pile head load, Figure 7.27 shows the global secant stiffness of the pile versus pile head load. The global secant stiffness was determined as the change in pile head load (ΔQ_t) from the initial pile head load prior to pile driving, divided by the pile head settlement (S_p) (as done in Section 6.2.7).

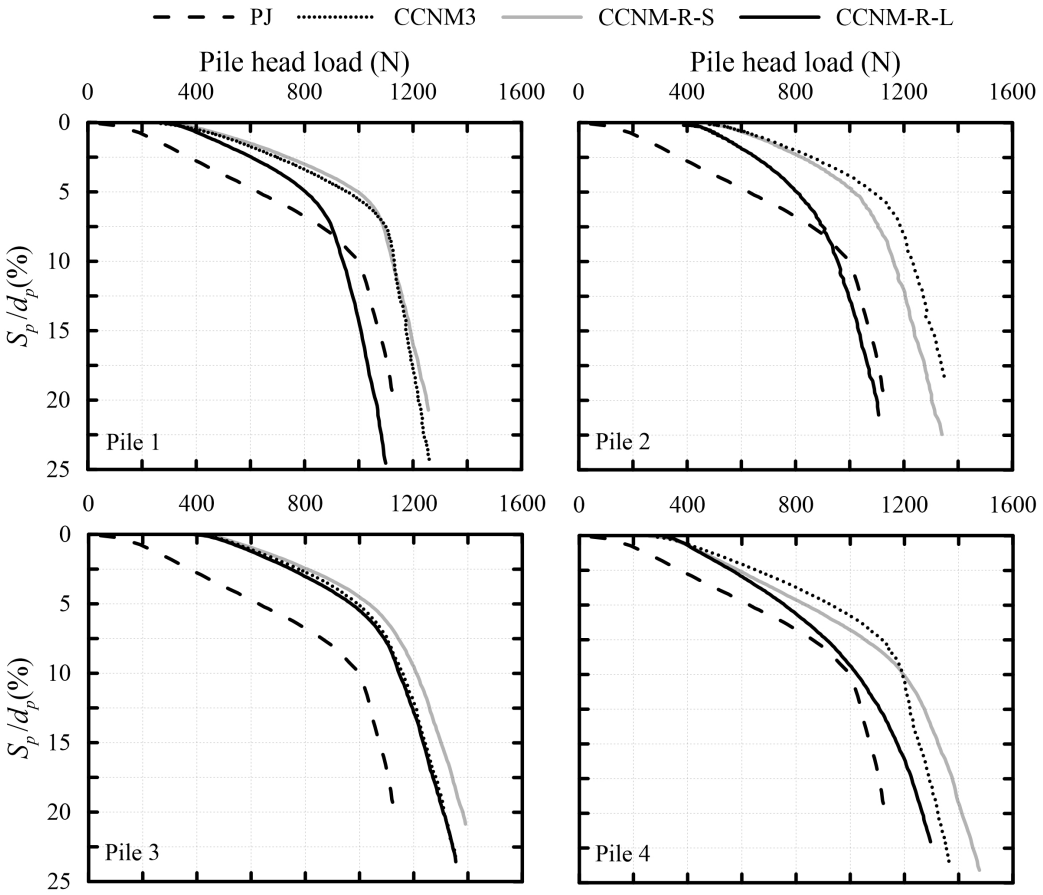


FIGURE 7.26: Load-displacement curves: test PJ, CCNM3, CCNM-R-S and CCNM-R-L

For pile 1, the pile jacking response in Figure 7.26 for tests CCNM3 and CCNM-R-S is similar, as well as the global stiffness curve (Figure 7.27). Pile 1 in test CCNM-R-L shows less pile jacking stiffness than the other two tests (CCNM3 and CCNM-R-S), and the stiffness degrades faster than the other two tests. For pile 2, "greenfield" pile jacking shows the least stiffness, followed by the pile in test CCNM-R-L and CCNM-R-S. Pile 2 in test CCNM-R-L shows similar load-displacement curve to pile 1 in test CCNM-R-L (Figure 7.26), and pile 2 stiffness degrades faster than the other two tests (CCNM3 and CCNM-R-S), see Figure 7.27. For pile 3, all three tests (CCNM3, CCNM-R-S and CCNM-R-L) show similar load-displacement curve shape (Figure 7.26), and under a given pile head load, the pile stiffness in all three tests is greater than the "greenfield" test PJ (Figure 7.27). For pile 4, the load-displacement curve shape varies between the tests, and test CCNM3 shows the greatest pile jacking stiffness compared to the other

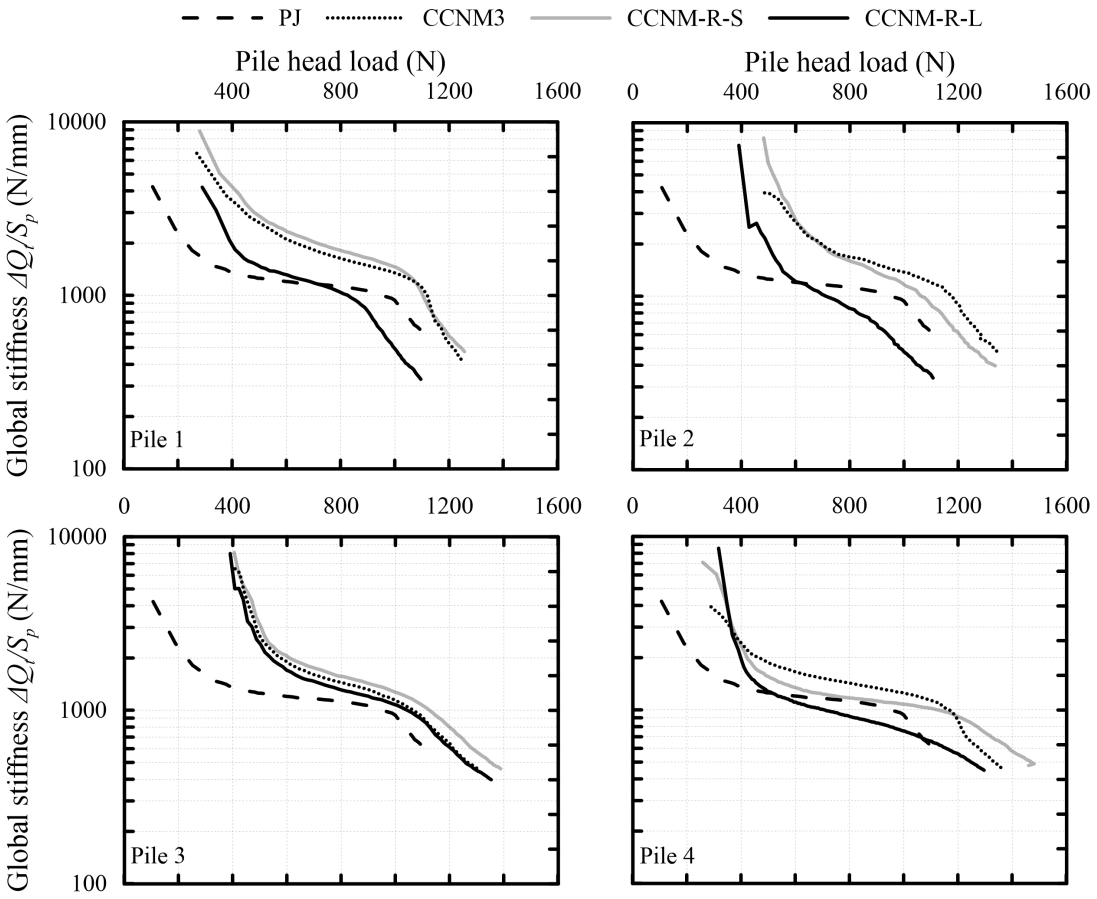


FIGURE 7.27: Post-tunnelling pile global stiffness with pile head load

tests, followed by CCNM-R-S. Pile 4 in test CCNM-R-L shows the most rapid stiffness degradation of all piles.

Based on the above data, it can be summarised that the post-tunnelling pile driving response is affected by the protective wall as well as the position of the pile with respect to the tunnel. The "long" protective wall (CCNM-R-L) shows the lowest pile jacking stiffness, and the stiffness degrades faster in the other tests. For the "short" retailing wall (CCNM-R-S), piles 1, 3 and 4 showed similar load-settlement curve shape to the piles in test CCNM3, and pile 2 showed greater stiffness degradation than the pile in test CCNM3.

After tunnel volume loss, shaft resistance along the pile was affected by the tunnelling-induced soil movements. In Section 6.2.2, pile 1 unit shaft resistance reduced with tunnelling (for tests CCNM2 and CCNM3). During post-tunnelling pile jacking, with the increase in pile settlement, the shaft friction along the pile re-mobilised, and greater pile settlement is required to fully re-mobilised the shaft resistance for the pile which lost greater shaft resistance during tunnelling. Similar logic can be applied to the post-tunnelling pile jacking result in this chapter, where Figure 7.28 shows the pile shaft

resistance with jacking for tests(CCNM3, CCNM-R-S and CCNM-R-L, as well as the data from the "greenfield" pile jacking test PJ (pile 2).

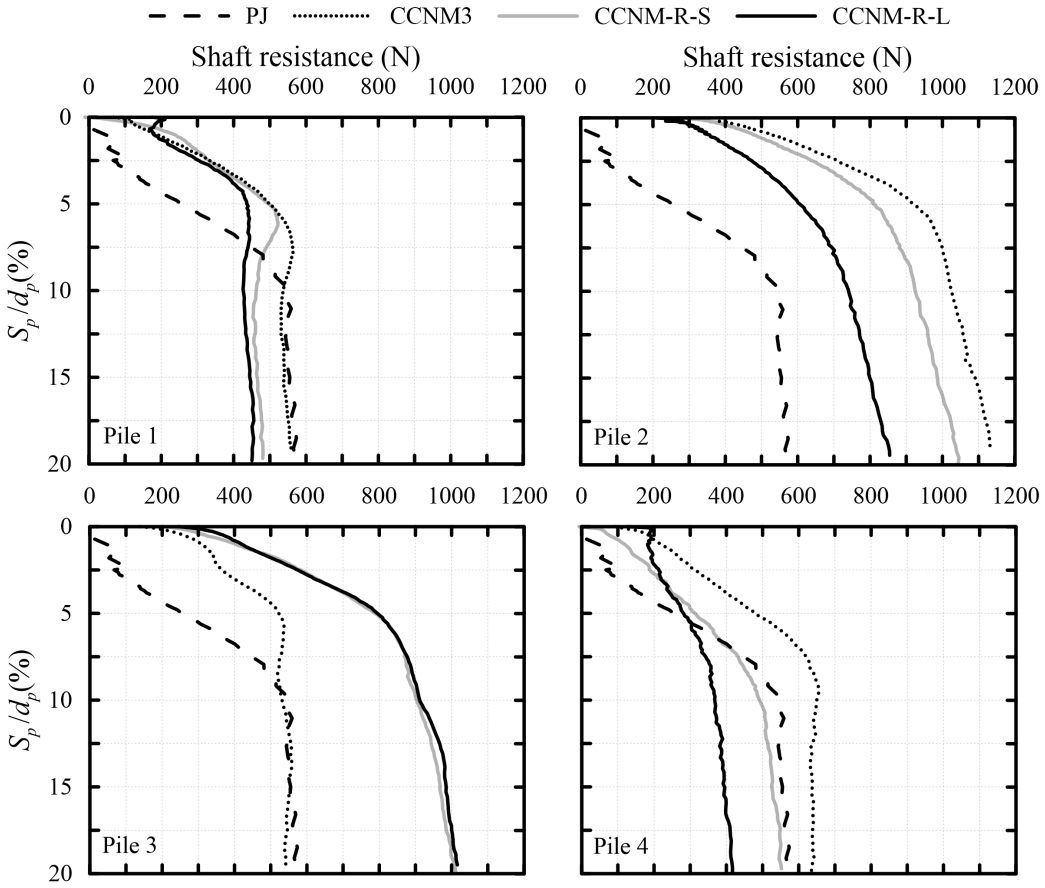


FIGURE 7.28: Shaft resistance of piles: test PJ, CCNM3, CCNM-R-S and CCNM-R-L

For 'greenfield' pile jacking (test PJ) in Figure 7.28 (black dashed line), the shaft resistance was fully mobilised at $S_p/d_p \approx 8$ %. For pile 1, the amount of pile settlement required to fully mobilise the shaft friction is different in three tests (CCNM3, CCNM-R-S and CCNM-R-L). The shaft resistance for pile 1 in test CCNM3 was fully mobilised at $S_p/d_p \approx 7.5$ % (black dotted line in Figure 7.28). In test CCNM-R-S and CCNM-R-L, the resistance was fully mobilised at $S_p/d_p \approx 6$ % and $S_p/d_p \approx 5$ %, respectively (grey and back solid line in Figure 7.28). For pile 1, referring back to Figure 7.24 (a), the unit shaft friction along the depth of the pile reduced most for test CCNM3. For pile 1 in tests CCNM-R-S and CCNM-R-L, despite the fact that the unit shaft friction along the middle portion of the pile shows negative values (reduction in shaft friction), the overall unit shaft friction stays positive. Therefore, during pile jacking, to fully re-mobilise shaft friction along the pile, greater pile settlement ($S_p/d_p \approx 7.5$ %) is required for CCNM3 than the other two tests ($S_p/d_p \approx 6$ % and $S_p/d_p \approx 5$ % for test CCNM-R-S and CCNM-R-L). For piles 2 and 3, all three tests (CCNM3, CCNM-R-S and CCNM-R-L) show a similar amount of pile settlement $S_p/d_p \approx 5$ % to fully mobilise

shaft resistance (Figure 7.28 pile 2 and 3). For pile 4, test CCNM3 shows greater pile settlement ($S_p/d_p \approx 10$ %) than tests CCNM-R-S and CCNM-R-L ($S_p/d_p \approx 7.5$ %) to fully mobilise the shaft resistance.

Figure 7.29 shows the load settlement path history for piles in tests PJ, CCNM3, CCNM-R-S and CCNM-R-L. The centrifuge test procedure as discussed in Section 4.4.6 can be categorised into three stages: (1) Piles loaded to the designated working loads, where detailed loading sequence and magnitudes have been discussed in Subsection 4.3.7; (2) followed by the tunnel volume loss process with a small increments of approximately $V_{l,t} = 0.1\%$; (3) post-tunnelling pile jacking (see Figure 7.29 Pile 1 for reference numbers and load settlement direction).

For pile 1 in test CCNM-R-L (Figure 7.29 black solid line), the amount of settlement during tunnel volume loss is not significant (stage 2), and the post-tunnelling load-settlement curve shows similar shape to the pile in test PJ, but with smaller pile head load value. For pile 1 in tests CCNM3 and CCNM-R-S, during tunnel volume loss, the piles settled greater than the pile in test CCNM-R-L. Despite the fact that the settlement in stage 2 is significant, piles in tests CCNM3 and CCNM-R-S showed relatively consistent response during post-tunnelling pile jacking, and the curve converged to the curve in test PJ after pile settlement is greater than $S_p/d_p = 15\%$.

For pile 2 in test CCNM-R-L, during post-tunnelling pile jacking (stage 3), the pile shows greater settlement than the piles in other three tests (CCNM-R-S, CCNM3 and PJ) under a given pile head load. For pile 3 and 4, the load-settlement curves did not present a significant difference between the tests. It is believed that jacking of a pile will affects the response of the adjacent pile. Hence, the results from pile 2, 3 and 4 are affected by the pile jacking of the previous adjacent pile, and no obvious conclusion can be made based on the current data set.

7.3 Summary and conclusions

The use of a protective wall to protect structures from tunnelling-induced damage was investigated in this chapter. The displacement of the pile head, load transfer between the piles and the axial force changes along the depth of the pile were presented. The effect of a protective wall on tunnelling-induced soil movement mechanisms was investigated using geoPIV_RG data. With the use of FBGs along the depth of the protective wall, the effect of tunnelling-induced soil movements on wall deformation and associated bending moment profiles was measured. Results from four centrifuge tests were presented: a "greenfield" tunnel volume loss test (Test GF), a test with a piled structure (CCNM3),

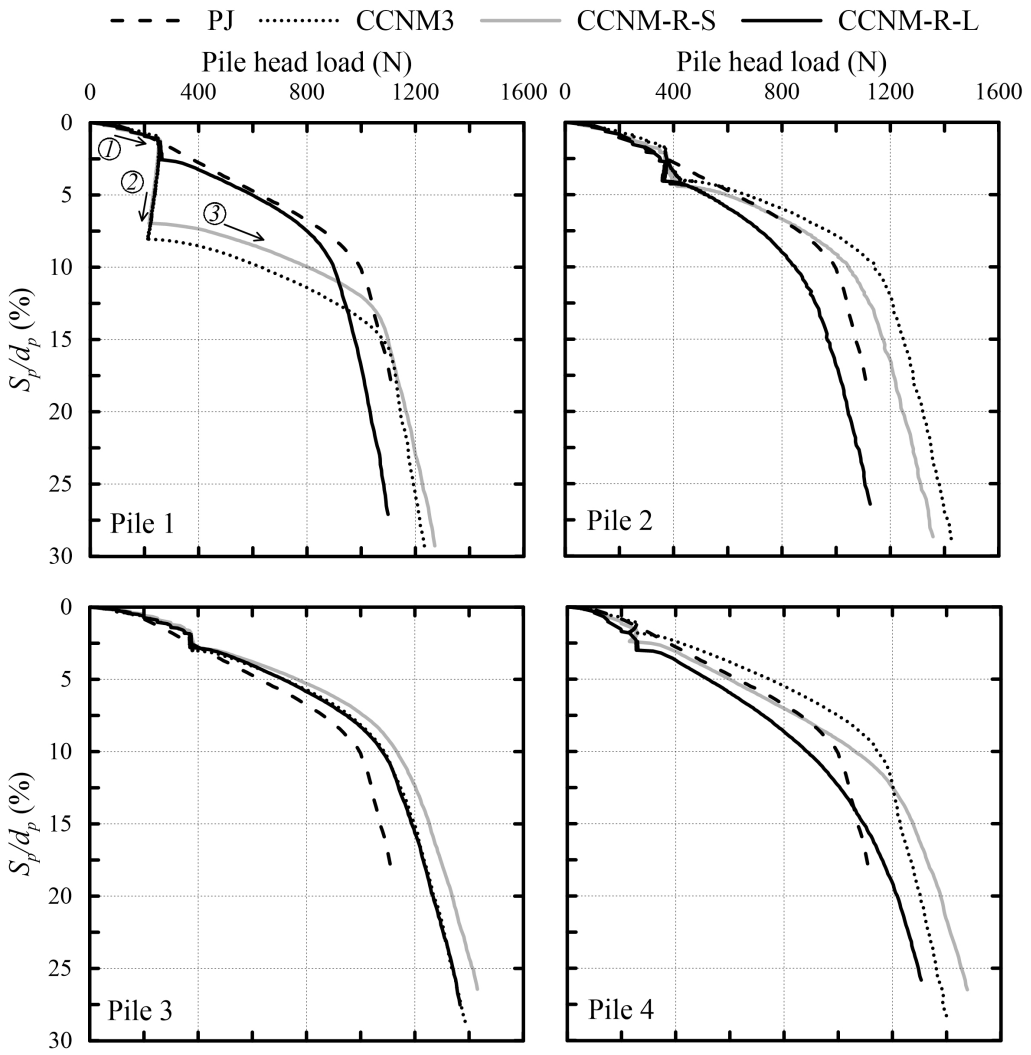


FIGURE 7.29: Load-settlement path history for piles

and two tests involving the use of protective walls (test CCNM-R-S and CCNM-R-L). Based on the obtained results, the following conclusions can be made:

- Pile loading can affect the existing protective wall; after pile 1 loading, the protective walls showed a negative bending moment close to the pile tip, suggesting that the pile loading caused additional soil horizontal pressure towards the wall at the depth around the pile tip. This phenomenon does not relate to reality, where the protective wall does not exist during pile loading (construction of the building). In practice, the protective wall is constructed after the piled structure prior to tunnelling, during the protective wall construction, stress release at the depth of the wall will cause disturbance to the adjacent pile instead. The effect of such differences is unknown and is not the main focus of this research.

- Based on the geoPIV-RG data, it can be concluded that the use of a "long" protective wall can prevent vertical and horizontal soil displacements more efficiently than a "short" wall. The length of the wall could affect the deformation shape of the wall, as well as the bending moment along the depth of the wall. For a "short" wall, where the toe of the wall is located at the tunnel springline, the tunnelling-induced soil movements around the tunnel springline could cause the toe of the wall to move towards the tunnel. For the "long" protective wall, where the toe of the wall is located below the tunnel, a limited amount of displacement is observed at the toe, but the wall moves towards the tunnel around a depth of z/z_t=0.8.

- During tunnel volume loss, the use of a protective wall can prevent tunnelling-induced pile head settlement, and the efficiency of the protective wall to protect tunnelling-induced pile head settlement was evaluated. Based on the current piled structure configuration (4 piles located adjacent to the tunnel), the efficiency ($\eta^{rs}_{V_{l,t}}$) depends mainly on the relative location of the pile with respect to the tunnel (x/D_t) and is less affected by the magnitude of tunnel volume loss. The "long" protective wall provides greater efficiency than the "short" wall in general.

- The settlement of the piles during tunnel volume loss does not necessarily indicate the deformation of the structure, which governs the pile head load distribution. The angular distortion of each frame is calculated to evaluate the distortion of the structure. In general, the most distorted frame is located closest to the tunnel. For tests CCNM2 and CCNM3, the angular distortion of the frame shows similar value with tunnelling, despite the fact that test CCNM2 shows greater pile settlement. For tests CCNM-R-S, the angular distortion of the frame shows a slightly lower value than the frame in test CCNM3, suggesting that the use of a "short" protective wall can reduce the distortion of the frames. Besides, the angular distortion for the frames in test CCNM-R-L shows minimum value with tunnelling, suggested that the use of a "long" protective wall can prevent frame distortion due to tunnelling.

- After pile loading to the designated load (prior to tunnel volume loss), the axial force along the pile increased, and the shaft resistance along the lower portion of the pile increased. During tunnel volume loss, tunnelling-induced soil movements affect the pre-existing shaft friction along the pile, and to balance the force applied to the pile (affected by the structure stiffness), new shaft friction along the pile is developed. For piles located most close to the tunnel (pile 1), the shaft resistance close to the pile tip reduced with tunnelling, and the "long" protective wall can reduce the amount of decrease in shaft resistance along the lower portion of the pile. For the piles located further away from the tunnel (piles 3 and 4), the effect of tunnelling-induced soil movements on pile shaft resistance is minimal.

- After tunnel volume loss, post-tunnelling pile jacking tests were conducted. The shaft resistance along the pile re-mobilised with pile jacking. To fully re-mobilise shaft resistance, greater pile settlement was required for the piles where shaft resistance was more significantly reduced during tunnelling. For "long" protective wall, less shaft resistance was reduced during tunnelling, thus the amount of settlement required to fully mobilise the shaft resistance in test CCNM-R-L was less than in tests CCNM3 and CCNM-R-S.

Chapter 8

Conclusions and recommendations for further research

The rapid increase in urban population requires efficient urban transport systems to reduce traffic congestion and travel time. Utilising underground infrastructure systems is probably the most recognised solution to reduce the congestion of a city, and a large part of these underground systems is made up of tunnels. Nowadays, due to the restricted access and highly occupied underground space, tunnels are being built close to, underneath or even clashing with the existing buried infrastructure and building foundations. Therefore, tunnelling could cause potential damage to the existing assets, and protective structures have been used in practice to reduce such potential damage. However, the high uncertainty regarding the consequence of tunnelling on existing assets and the limited understating of the effect of protective measures on existing assets makes the current protective measures generally costly.

This research aims to improve the understanding of tunnel, soil, piled structure and protective wall interaction (TSPPWI) problems. This research is intended to develop experimental applications and to obtain previously unattainable results, which will enable a better understating of the complex TSPPWI problems. In this research, the coupled centrifuge numeric modelling (CCNM) was used to address the current limitation in modelling piled structure within the geotechnical centrifuge environment, and optical Fibre Bragg Grating (FBG) sensing technique was applied within the CCNM application to overcome the limitations of the conventional strain gauges. This chapter reviews the findings and details presented within the previous chapters and provides some recommendations for future research.

8.1 Conclusions

8.1.1 Experimental methods, equipment, and testing configurations

In general, this research involves three main test packages: (1) greenfield tunnelling in sand, (2) effects of tunnelling on piled structures and (3) the use of protective walls to reduce buildings from tunnelling-induced damage. Chapter 3 provided detailed centrifuge testing developments related to the above three test packages, as well as the testing procedure and experimental set-up.

This research includes some important novel experimental developments, which can be summarised as: (1) a rigid boundary mechanical model tunnel, (2) a modular actuator that enables load/displacement control, (3) further improvement of the current coupling centrifuge numerical modelling system and (4) integration of Fibre Bragg Grating sensors within the centrifuge environment to measure the physical strain. It is believed that this research represents one of the first applications of FBG sensors in a geotechnical centrifuge. The detailed developments and applications have been discussed in Chapter 3.

8.1.2 Tunnelling in sandy ground

As discussed in Chapter 5, there are two different ways to simulate 2D tunnel volume loss in a geotechnical centrifuge, which are fluid-filled flexible membrane (FM) model tunnel and rigid boundary mechanical (RBM) model tunnel. As a result, the ground deformations were affected by the tunnel boundary conditions (flexible or rigid).

Three centrifuge tests were conducted in Chapter 5 using the newly developed eccentric rigid boundary mechanical (eRBM) model tunnel with cover to diameter (C/D) ratios of 1.3, 2.0 and 2.4. The results from the above tests as well as data from other sources (where different types of model tunnels were used) were compared to investigate the effect of tunnel boundary conditions on resulting soil displacement.

Both methods allow the plane-strain tunnel volume loss simulation under centrifuge environment. Unlike the FM model tunnel, the RBM model tunnel boundary is fixed, and the tunnel volume loss shape is pre-defined. For the FM model tunnel, the tunnel boundary displaced shape is unknown. Therefore, during centrifuge spin-up, for FM model tunnels, the internal tunnel pressure of the water is different to the lateral earth pressure of the soil. Such difference in soil displacement around the tunnel during centrifuge spin-up is investigated in this research.

For centrifuge tests, at a given tunnel volume loss ($V_{l,t}$), the eRBM model tunnel showed a similar magnitude and shape in vertical soil settlements to the FM model tunnel. However, for horizontal soil displacements, the eRBM model tunnel provided a greater magnitude than the FM model tunnel. By assessing the horizontal displacement contour, the eRBM model tunnel generated a greater zone of major horizontal displacements located close to the tunnel spring line. The centrifuge results showed that the settlement trough shape developed by the eRBM model tunnel is wider than the FM model tunnel. A set of the equations was developed based on the eRBM model tunnel centrifuge results to predict the settlement trough shape parameter K^* and K^{**}.

The soil volume loss close to the tunnel crown ($V_{l,s}$) was shown to be smaller than tunnel volume loss ($V_{l,t}$), suggesting that the soil close to the tunnel crown underwent dilation with tunnelling. For soil further away from the tunnel crown, an increase in soil volume loss was identified for centrifuge tests. This increase in soil volume loss suggested an overall soil contraction behaviour above the tunnel crown.

The outcome of this work provided a more in-depth understanding of the effect on model tunnel boundary conditions and will help future researchers considering which type of model tunnel to be adopted when developing centrifuge tests related to tunnelling.

8.1.3 The effect of tunnelling on piled structures

Four centrifuge tests are conducted in Chapter 6 to study the effect of tunnelling on piled structures. Two different structure stiffness are investigated: fully flexible (constant load on each pile) and full structure stiffness (structure stiffness simulated using a numerical model within the CCNM application). FBG sensors were used to measure the axial force along with four model piles during centrifuge tests.

The in-flight pile jacking test was carried first to determine the pile axial load capacity; all four piles were jacked into the ground. An assumption was made that the ultimate load capacity of a no-displacement pile is defined at the point when the pile shaft resistance is fully mobilised. Based on axial force along with the pile measured by the FBG sensors, the shaft resistance along the pile was fully mobilised at S_p/d_p (pile head settlement/pile diameter) of about 8%.

Only one piled structure location is considered, where the tunnel is being excavated adjacent to the piled structure. During tunnel volume loss, the pile located closest to the tunnel (pile 1) presented the greatest pile head settlement, and the difference in pile 1 settlement between the tests (centrifuge test with fully flexible structure stiffness and fully structure stiffness) is not significant, and the pile settlement decreased when the

pile is located further away from the tunnel. Based on the pile settlement data between the tests (fully flexible or fully structure stiffness), it seems that the structure stiffness does not have significant effect on pile settlement.

For the centrifuge tests with fully structure stiffness (structure stiffness simulated), pile head load varied with tunnel volume loss (effect of structure stiffness). For the pile located closest to the tunnel (pile 1), pile head load was decreased with tunnelling, where the decreased pile head load from pile 1 will transfer to the other piles, and most of the load from pile 1 was apparently transferred to the adjacent pile (pile 2, see Figure 4.8 for pile numbering). Therefore, the increase in pile 2 head load caused a greater pile head settlement compared with the pile 2 in the installation with flexible structure stiffness (Test CL, constant pile head load).

With the use of FBG sensors, the axial force along the four model piles was measured. The axial force along the piles was mainly affected by two mechanisms: (1) change in pile head load due to structure stiffness, (2) the effect of tunnelling-induced ground movements; there is also pile-pile interaction, but his research focuses on the above two mechanisms. Based on the FBG measurement data, the axial force along the upper portion of piles 1 and 2 was mainly affected by the change in pile head load (mechanism 1), and the axial force along the lower portion of the piles 1 and 2 was affected by tunnelling-induced ground movements (mechanism 2). For pile 3, the effect of mechanisms 1 and 2 was insignificant, and for pile 4, the axial force along the pile was decreased (mechanism 1).

The change in unit shaft resistance along the depth of a pile with tunnel volume loss can be calculated from the variation of axial force measured by the FBG sensors. In addition, the increase in shaft resistance could be caused by upwards shaft resistance or an increase in downwards shaft resistance, and the pile and soil settlements could indicate the direction of the increase in pile shaft resistance. For pile 1 in centrifuge tests with full structure stiffness (test CCNM1 and CCNM2), the increase in unit shaft resistance along the upper portion of the pile is caused by the upwards shaft friction, as the soil tends to resist the downward movement of the pile. For pile 2 in test CCNM1 and CCNM2, the overall change in unit shaft resistance is not significant, and it is believed that the pile base has taken the majority of the increased load from the pile head. For pile 3, the changes in unit shaft friction along the pile are small. For pile 4, the shaft friction at the lower portion of the pile was less affected by tunnelling-induced ground movement than pile 1.

After tunnel volume loss, post-tunnelling pile jacking tests were carried out. During pile jacking, the shaft friction was re-mobilised, and more pile settlement was required for the case where more reduction in shaft resistance had been taken place during tunnelling.

In general, the post-tunnelling pile axial capacity is affected by (1) the pile position with respect to the tunnel, (2) the tunnel volume loss prior to pile jacking, (3) pile-pile interaction, and (4) the initial pile head load before pile jacking.

To summarise, two structure stiffnesses were tested using CCNM system (fully flexible structure stiffens and fully structure stiffness), the work demonstrated the importance of structure stiffness effect on pile settlement and pile head load transfer. The use of FBG sensors provided previously unattainable model pile axial force measurements within the CCNM applications. This work improved the accuracy of superstructure simulation within geotechnical centrifuge tests. It is believed that the outcome of this work could further improve the understating of complex tunnel, pile, structure interaction problems, and offer alternative approaches to simulate superstructure and measure engineering strain within geotechnical centrifuges.

8.1.4 The use of protective structures to reduce buildings from tunnelling-induced damage

In practice, protective walls have been adopted as a barrier between the tunnel and adjacent piled structures to reduce structures from tunnelling-induced damage. In Chapter 7, four centrifuge tests were presented to improve the understanding of the tunnel, soil, piled structures and protective walls interaction (TSPPWI) problems. Two protective walls (made out of aluminium plate) were used with different embedded depths, referred to as "short" (toe of the wall located at the tunnel spring line) and "long" (toe of the wall located below the tunnel invert). FBG sensors were used to measure the bending moment along the walls during tunnel volume loss.

Two cameras were used to "track" the soil displacement. In general, the horizontal soil displacements behind the walls (both "short" and "long" wall) are less than the soil displacements in the centrifuge test without a wall (test CCNM3). For the centrifuge test with a "short" wall (test CCNM-R-S), the major zone of horizontal displacement was located close to the tunnel springline, whereas for the test with a "long" wall (test CCNM-R-L), as the toe of the wall was located below the tunnel invert with limited soil movements, the horizontal displacement close to the tunnel springline is not as significant as in the test CCNM-R-S. The observed soil displacements from the tests suggested that the use of a protective wall can reduce the soil movements on the building side of the wall.

Two cameras were also used to measure the displacement of the protective walls with tunnelling. It was found that the displaced shape of the protective wall was highly

depends on the length of the wall. For test CCNM-R-S (use of "short" wall), tunnelling-induced soil movements caused the toe of the wall to move towards the tunnel, with maximum negative bending moment (see Figure 7.13 for the direction of bending moment) at a depth of $z/z_t = 0.8$. For test CCNM-R-L, soil movements towards the tunnel occurred at a $z/z_t = 0.8$, with limited wall displacement at the toe of the wall, resulting in a clockwise rotation motion at the upper part of the wall.

Based on the pile head settlement data, it is suggested that the use of protective walls can reduce tunnelling-induced pile settlement. The efficiency of the protective walls can be quantified in terms of pile settlement, where the maximum efficiency of a protective wall is assumed to be when the tunnelling-induced pile settlement was fully eliminated, and the other extreme case is when the protective wall had zero protection to pile settlement (wall does not exist). The centrifuge tests CCNM-R-S and CCNM-R-L should fall into these two extreme cases. In general, the variation of efficiency parameter for all four piles was not very sensitive to tunnel volume loss but was more significantly affected by the location of the pile. The efficiency parameter decreases with an increase in pile distance from the tunnel, and CCNM-R-L shows higher efficiency value than test CCCNM-R-S, in general, see Figure 7.17.

The pile head load data indicated that the use of a "long" protective wall significantly reduced the amount of load transferred between the pile during tunnel volume loss. For test CCNM-R-S, the "short" wall reduced the load transfer between the piles, but the pile head settlement with tunnelling is similar to test CCNM3.

Test CCNM-R-S showed less structure settlement than CCNM3, and test CCNM-R-L showed a significant reduction in structure settlement compared to other tests. To quantify the deformation of a structure, the angular distortion for each frame was calculated. The results indicated that for the structure, the most significant angular distortion with tunnel volume loss was experienced at the lowest structure level, see Figure 7.21. With tunnel volume loss, test CCNM-R-L showed minimum structure distortion, followed by test CCNM-R-S. The results in Figure 7.22 suggested that the use of "long" protective wall will significantly reduce the differential settlement between the piles, whereas the use of 'short' protective wall seems to have limited effect on reducing differential pile settlement.

After tunnelling, pile jacking tests were conducted. With the use of the "long" protective wall, less shaft resistance was reduced during tunnelling. Thus the amount of settlement required to fully mobilising shaft resistance during pile jacking was less than in tests CCNM-R-S and CCNM3.

The outcomes from these tests could improve the understanding of the complex tunnel, soil, piled structure and protective walls interaction (TSPPWI) problems. The use of FBG sensors on the protective walls offered the previously unattainable bending moment measurement along the wall, and the use of the CCNM system improved the accuracy of structure simulation within the geotechnical centrifuges. The work presented in Chapter 7 will help engineers to refine their design of protective walls in practice, and enable more efficient and cost-effective protective measures to be adopted.

8.2 Guidance for practical application

From engineering's point of view, to reduce or prevent structures from tunnelling induced damages is important. The works carried out in this research investigated the effect of tunnelling on the adjacent piled structure. In addition, two protective walls were used to reduce uneven settlement. Due to the limited variations (depth of the wall is varied), and only one case of tunnelling location with respect to the piled structure is considered, it is difficult to provide full guidance for practical application. Based on the current data and the investigated geometry, the following suggestions can be provided:

- For the pile located closest to the tunnel, greater pile settlement is expected than other piles during tunnel volume loss. Therefore, it is suggested to increase the size of the pile during the construction of the piled structure to reduce the potential pile failure at the post-construction tunnelling stages.
- Based on the structure deformation data, greatest angular distortion is expected to exist for the frames located closest to the tunnel (in both horizontal and vertical direction). Therefore, it is suggested to add additional braces to the frame located close to the tunnel.
- The use of protective wall can reduce tunnelling induced uneven settlement, therefore reducing the damages to the adjacent structures. Therefore, introducing a protective wall between the tunnel and adjacent piled structure is a reasonable solution in practice.
- Different length protective walls will cause significant differences in the deformed shape of the wall, therefore, it is suggested to take extra consideration of bending moment calculation along the wall during the design stage.
- Figure 7.17 provided the average efficiency parameter $\overline{\eta^{rs}}$ with respect to pile locations. Despite the limited amount of data sets, it is suggested that the depth of the wall should be located below the tunnel invert by one diameter of the tunnel

to allow the protective wall to have a better performance in reducing tunnelling induced soil movements.

8.3 Recommendations for future work

The newly developed eccentric rigid boundary mechanical (eRBM) model tunnel has been successfully implemented within the centrifuge tests. Improvements could be made in terms of the available calibration data for the numerical models. The use of pressure sensors (e.g. Tekscan) in the centrifuge tests would enable the measurement of lateral soil pressure, which improves the understanding of the soil response during spin-up and tunnelling, thereby providing additional data for validation of numerical models.

The newly developed pile loading system (modular actuator) combined with the real time interface allows for relatively quick and easy simulation of different piled structures and testing configurations. So far, only one type of piled structure layout has been tested (piled structure adjacent to the tunnel), hence further research could be conducted to investigate the effect of different locations of the structure with respect to the tunnel, for example, the piled group is located above the tunnel. In addition, different structures can be considered within the numerical model of the CCNM application replicating different buildings (stiffness of the structures), and more advanced structural models could be implemented to consider structural non-linearity (e.g. connections, damage).

The model pile used for this research was an aluminium tube, which can not replicate the brittle failure of a reinforced concrete pile in prototype scale. Simulation of realistic concrete piled foundation behaviour in the centrifuge using "model" piles can be achieved in the future (Knappett et al., 2010), with the FBG sensors integrated within these piles. Further research can be carried out to develop the model concrete piles that can replicate the characteristics of full-scale concrete piles.

The use of protective walls considered in this research only varied the length of the wall, and only one protective wall offset distance (adjacent to the tunnel) was considered. Further research could be conducted to investigate the effect of wall stiffness, type of wall (secant pile wall, or contiguous pile wall) as well as the surface roughness of the wall.

The centrifuge tests and numerical simulations carried out in this thesis considered a row of four piles adjacent to a model tunnel in a 2D plane-strain scenario, and the model tunnel simulated within the centrifuge deforms uniformly along the length of the tunnel, where the tunnel excavation sequence is not considered. Further research could aim to study global 3D tunnel-soil-foundation-superstructure interaction problems. A 3D

model tunnel that can simulate tunnel advancement within the centrifuge is suggested, and the associated 3D surface soil movements could be assessed using three-dimensional imaging system (Le et al., 2018).

Bibliography

Atkinson, J. H., Brown, E. T., and Potts, D. M. (1975). Collapse of shallow unlined tunnels in dense sand. *Tunnels and Tunneling*, 7(3):81–87.

Attewell, P. B. and Yeates, J. (1984). *Ground movements and their effects on structures*. Blackie and Son Ltd.

Bilotta, E. (2008). Use of diaphragm walls to mitigate ground movements induced by tunnelling. *Géotechnique*, 58(2):143–155.

Bolton, M. D., Gui, M. W., Garnier, J., Corte, J. F., Bagge, G., Laue, J., and Renzi, R. (1999). Centrifuge cone penetration tests in sand. *Géotechnique*, 49(4):543–552.

Bolton, M. D., Gui, M. W., and Phillips, R. (1993). Review of miniature soil probes for model tests. In *Proceedings of the 11th Southeast Asian Geotechnical Conference*, pages 85–90. South East Asian Geotechnical Society.

Boonsiri, I. and Takemura, J. (2015a). A centrifuge model study on pile group response to adjacent tunnelling in sand. *Journal of JSCE*, 3(1):1–18.

Boonsiri, I. and Takemura, J. (2015b). Observation of ground movement with existing pile groups due to tunneling in sand using centrifuge modelling. *Geotechnical and Geological Engineering*, 33(3):621–640.

Boonyarak, T. and Ng, C. W. (2015). Effects of construction sequence and cover depth on crossing-tunnel interaction. *Canadian Geotechnical Journal*, 52(7):851–867.

Boscardin, M. D. and Cording, E. J. (1989). Building response to excavation-induced settlement. *Journal of Geotechnical Engineering*, 115(1):1–21.

Burland, J. B. (1995). Assessment of risk of damage to buildings due to tunnelling and excavations. In *Proc 1st Int Conf Earthquake Geotechnical Engineering*, pages 1189–1201. IS-Tokyo'95.

Burland, J. B., Standing, J. R., and Jardine, F. M., editors (2001). *Building Response to Tunnelling: Case studies from Construction of the Jubilee Line Extension, London*, volume 2. Thomas Telford.

Celestino, T. B., Gomes, R. A. M. P., and Bortolucci, A. A. (2000). Errors in ground distortions due to settlement trough adjustment. *Tunnelling and underground space technology*, 15(1):97–100.

Clough, G. W. and Schmidt, B. (1981). Design and performance of excavation and tunnels in soft clays. soft clay engineering. *Developments in geotechnical engineering*, 20:567–634.

Cording, E. (1991). Control of ground movements around tunnels in soil. In *General Report, 9th Pan-American Conference on Soil Mechanics and Foundation Engineering, Chile*, pages 2195–2244.

DeSA, U. et al. (2013). World population prospects: the 2012 revision. *Population division of the department of economic and social affairs of the United Nations Secretariat, New York*, 18.

Di Mariano, A., Gesto, J. M., Gens, A., and Schwarz, H. (2007). Ground deformation and mitigating measures associated with the excavation of a new metro line. In *Proc. XIV European Conference on Soil Mechanics and Geotechnical Engineering, ECSMGE*, pages 1901–1906.

Divall, S. (2013). *Ground movements associated with twin-tunnel construction in clay.* PhD thesis, City University London.

Ellis, E., Cox, C., Yu, H. S., Ainsworth, A., and Baker, N. (2006). A new geotechnical centrifuge at the university of nottingham, uk. In *6th International Conference of Physical Modelling in Geotechnics: ICPMG*, volume 6, pages 129–33.

Farrell, R. P. (2010). *Tunnelling in sands and the response of buildings.* PhD thesis, University of Cambridge.

Franza, A. (2016). *Tunnelling and its effects on piles and piled structures.* PhD thesis, University of Nottingham.

Franza, A., Idinyang, S., Heron, C., Marshall, A. M., and Abdelatif, A. (2016). Development of a coupled centrifuge-numerical model to study soil-structure interaction problems. In *Proceedings of the 3rd European Conference on Physical Modelling in Geotechnics (Eurofuge 2016)*, pages 135–140.

Franza, A. and Marshall, A. M. (2017). A centrifuge modelling study of the response of piled structures to tunnelling. *Journal of Geotechnical and Geoenvironmental Engineering.*

Franza, A. and Marshall, A. M. (2018). Centrifuge modelling study of the response of piled structures to tunnelling. *ASCE Journal of Geotechnical and Geoenvironmental Engineering*, 144(2).

Franza, A., Marshall, A. M., Haji, T. K., Abdelatif, A. O., Carbonari, S., and Morici, M. (2017). A simplified elastic analysis of tunnel-piled structure interaction. *Tunneling and Underground Space Technology*, 61:104–121.

Franza, A., Marshall, A. M., and Zhou, B. (2019). Greenfield tunnelling in sands: the effects of soil density and relative depth. *Geotechnique*.

Goh, K. H. and Mair, R. J. (2012). The horizontal response of framed buildings on individual footings to excavation-induced movements. In *Geotechnical Aspects of Underground Construction in Soft Ground-Proceedings of the 7th International Symposium on Geotechnical Aspects of Underground Construction in Soft Ground*, pages 895–902.

Gudehus, G. and Mašín, D. (2009). Graphical representation of constitutive equations. *Géotechnique*, 59(2):147–151.

Gulvanessian, H., Formichi, P., and Calgaro, J. A. (2009). *Designers' Guide to Eurocode 1: Actions on Buildings: EN1991-1-1 and-1-3 TO-1-7*. Thomas Telford Ltd.

Hagiwara, T., Grant, R. J., Calvello, M., and Taylor, R. N. (1999). The effect of overlying strata on the distribution of ground movements induced by tunnelling in clay. *Soils and Foundations*, 39(3):63–73.

Hibbitt, K. (2002). *ABAQUS/Explicit User's Manual: Version 6.3*. Hibbit, Karlsonn & Sorensen.

Hong, Y., Soomro, M. A., and Ng, C. W. W. (2015). Settlement and load transfer mechanism of pile group due to side-by-side twin tunnelling. *Computers and Geotechnics*, 64:105–119.

Idinyang, S., Franza, A., Heron, C., and Marshall, A. M. (2018). Real-time data coupling for hybrid testing in a geotechnical centrifuge. *International Journal of Physical Modelling in Geotechnics*, pages 1–13.

Jacobsz, S. W. (2003). *The effects of tunnelling on piled foundations*. PhD thesis, University of Cambridge.

Jacobsz, S. W., Standing, J. R., Mair, R. J., Hagiwara, T., and Sugiyama, T. (2004). Centrifuge modelling of tunnelling near driven piles. *Soils and Foundations*, 44(1):49–56.

Kaalberg, F. J., Teunissen, E. A. H., Van Tol, A. F., and Bosch, J. W. (2005). Dutch research on the impact of shield tunnelling on pile foundations. In Klaas Jan Bakker, Adam Bezuijen, W. B. E. K., editor, *Proceedings of the 5th International Symposium on Geotechnical Aspects of Underground Construction in Soft Ground*, pages 123–131. Taylor & Francis Group.

Katoh, Y., Miyake, M., and Wada, M. (1998). Ground deformation around shield tunnel. In *Centrifuge*, volume 98, pages 733–738.

Kersey, A. D., Davis, M. A., Patrick, H. J., LeBlanc, M., Koo, K., Askins, C., Putnam, M., and Friebele, E. J. (1997). Fiber grating sensors. *Journal of lightwave technology*, 15(8):1442–1463.

Knappett, J., Reid, C., Kinmond, S., and O'Reilly, K. (2010). Small-scale modeling of reinforced concrete structural elements for use in a geotechnical centrifuge. *Journal of Structural Engineering*, 137(11):1263–1271.

Kutter, B. L., Chang, J., and Davis, B. (1994). Collapse of cavities in sand and particle size effects. *Proceedings of International Conference Centrifuge '94*, pages 809–815.

Le, B. T., Nadimi, S., Goodey, R. J., and Taylor, R. N. (2018). A study on performance of three-dimensional imaging system for physical models. In *Proceedings of the 9th International Conference on Physical Modelling in Geotechnics*, volume 2, pages 853–858. CRC Press/Balkema.

Ledesma, A. and Alonso, E. E. (2017). Protecting sensitive constructions from tunnelling: the case of world heritage buildings in barcelona. *Géotechnique*, 67(10):914–925.

Lee, C. J. (2012). Numerical analysis of the interface shear transfer mechanism of a single pile to tunnelling in weathered residual soil. *Computers and Geotechnics*, 42:193–203.

Lee, C. J. and Chiang, K. H. (2007). Responses of single piles to tunneling-induced soil movements in sandy ground. *Canadian Geotechnical Journal*, 44(10):1224–1241.

Loganathan, N. and Poulos, H. G. (1998). Analytical prediction for tunneling-induced ground movements in clays. *Journal of Geotechnical and Geoenvironmental Engineering*.

Loganathan, N., Poulos, H. G., and Stewart, D. P. (2000). Centrifuge model testing of tunnelling-induced ground and pile deformations. *Geotechnique*, 50(3):283–294.

Mair, R. J. (2008). Tunnelling and geotechnics: new horizons. *Géotechnique*, 58(9):695–736.

Mair, R. J. and Taylor, R. N. (1997). Theme lecture: Bored tunneling in the urban environment. *Proceedings of the fourteenth international conference on soil mechanics and foundation engineering (Hamburg, 1997), Balkema*, pages 2353–2385.

Mair, R. J., Taylor, R. N., and Bracegirdle, A. (1993). Subsurface settlement profiles above tunnels in clays. *Geotechnique*, 43(2).

Marshall, A. M. (2009). *Tunnelling in sand and its effect on pipelines and piles.* PhD thesis, University of Cambridge.

Marshall, A. M. (2012). Tunnel-pile interaction analysis using cavity expansion methods. *Journal of Geotechnical and Geoenvironmental Engineering*, 138(10):1237–1246.

Marshall, A. M., Farrell, R. P., Klar, A., and Mair, R. J. (2012). Tunnels in sands: the effect of size, depth and volume loss on greenfield displacements. *Géotechnique*, 62(5):385–399.

Marshall, A. M. and Franza, A. (2016). Discussion of "observation of ground movement with existing pile groups due to tunneling in sand using centrifuge modelling" by ittichai boonsiri and jiro takemura. *Geotechnical and Geological Engineering*, pages 1–5.

Marshall, A. M. and Franza, A. (2017). Discussion of "Observation of Ground Movement with Existing Pile Groups Due to Tunneling in Sand Using Centrifuge Modelling" by Ittichai Boonsiri and Jiro Takemura. *Geotechnical and Geological Engineering*, 35(1):535–539.

Marshall, A. M., Klar, A., and Mair, R. J. (2010). Tunneling beneath buried pipes - a view of soil strain and its effect on pipeline behavior. *ASCE Journal of the Geotechnical and Geoenvironmental Engineering*, 136(12):1664–1672.

Marshall, A. M. and Mair, R. J. (2011). Tunneling beneath driven or jacked end-bearing piles in sand. *Canadian Geotechnical Journal*, 48(12):1757–1771.

Moyo, P., Brownjohn, J. M. W., Suresh, R., and Tjin, S. C. (2005). Development of fiber bragg grating sensors for monitoring civil infrastructure. *Engineering structures*, 27(12):1828–1834.

Ng, C. W. W., Hong, Y., and Soomro, M. (2015). Effects of piggyback twin tunnelling on a pile group: 3d centrifuge tests and numerical modelling. *Géotechnique*, 65(1):38–51.

Ng, C. W. W. and Lu, H. (2013). Effects of the construction sequence of twin tunnels at different depths on an existing pile. *Canadian Geotechnical Journal*, 51(2):173–183.

Ng, C. W. W., Lu, H., and Peng, S. Y. (2013). Three-dimensional centrifuge modelling of the effects of twin tunnelling on an existing pile. *Tunnelling and Underground Space Technology*, 35:189–199.

Ng, C. W. W., Soomro, M. A., and Hong, Y. (2014). Three-dimensional centrifuge modelling of pile group responses to side-by-side twin tunnelling. *Tunnelling and underground space technology*, 43:350–361.

Nomoto, T., Imamura, S., Hagiwara, T., Kusakabe, O., and Fujii, N. (1999). Shield tunnel construction in centrifuge. *Journal of geotechnical and geoenvironmental engineering*, 125(4):289–300.

O'reilly, M. and New, B. (1981). Settlements above tunnels in the united kingdom-their magnitude and prediction. In *In Proceedings of the 3rd International Symposium, Tunnelling '82*, pages 173–181. Institution of Mining and Metallurgy.

Peck, R. B. (1969). Deep excavations and tunnelling in soft ground. In *Proc. 7th int. conf. on SMFE*, pages 225–290.

Potts, D. M. (1976). *Behaviour of Lined and Unlined Tunnels in Sand.* PhD thesis, University of Cambridge.

Potts, D. M. and Addenbrooke, T. I. (1997). A structure's influence on tunnellinginduced ground movements. *Proceedings of the Institution of Civil Engineers-Geotechnical Engineering*, 125(2):109–125.

Poulos, H. G. (2006). Pile settlement zones above and around tunnelling operations. In *AGS AUCTA Mini-Symposium: Geotechnical Aspects of Tunnelling for Infrastructure Projects.*

Ritter, S., Giardina, G., DeJong, M. J., and Mair, R. J. (2017). Centrifuge modelling of building response to tunnel excavation. *International Journal of Physical Modelling in Geotechnics*, pages 1–16.

Selemetas, D. (2005). *The response of full-scale piles and piled structures to tunnelling.* PhD thesis, University of Cambridge.

Shahin, H. M., Nakai, T., Zhang, F., Kikumoto, M., and Nakahara, E. (2011). Behavior of ground and response of existing foundation due to tunneling. *Soils and Foundations*, 51(3):395–409.

Son, M. and Cording, E. J. (2005). Estimation of building damage due to excavation-induced ground movements. *Journal of Geotechnical and Geoenvironmental Engineering*, 131(2):162–177.

Song, G., Marshall, A. M., and Heron, C. (2018). A mechanical displacement control model tunnel for simulating eccentric ground loss in the centrifuge. In *9th International Conference of Physical Modelling in Geotechnics: ICPMG*.

Standing, J. R. and Potts, D. M. (2008). Contributions to Géotechnique 1948-2008: Tunnelling. *GÉOTECHNIQUE*, 58(5):391–398.

Stanier, S. A., Blaber, J., Take, W. A., and White, D. (2015). Improved image-based deformation measurement for geotechnical applications. *Canadian Geotechnical Journal*, 53(5):727–739.

Taylor, R. N. (1994). *Geotechnical centrifuge technology*. CRC Press.

Vorster, T. E. B. (2006). *The effects of tunnelling on buried pipes*. PhD thesis, University of Cambridge.

Vorster, T. E. B., Klar, A., Soga, K., and Mair, R. J. (2005). Estimating the effects of tunneling on existing pipelines. *Journal of Geotechnical and Geoenvironmental Engineering*, 131(11):1399–1410.

White, D. J., Take, W. A., and Bolton, M. D. (2003). Soil deformation measurement using particle image velocimetry (PIV) and photogrammetry. *Geotechnique*, 53(7):619–631.

Williamson, M. (2014). *Tunnelling Effect on Bored Piles in Clay*. PhD thesis, University of Cambridge.

Zhou, B. (2015). *Tunnelling-induced ground displacements in sand*. PhD thesis, University of Nottingham.

Zhou, B., Marshall, A. M., and Yu, H. S. (2014). The effect of relative density on greenfield settlements above tunnels in sands. In *Geoshanghai 2014 - International conference on geotechnical engineering*, pages 96–105, Shanghai. ASCE.